MEASUREMENT OF TOP-ANTITOP DIFFERENTIAL CROSS SECTIONS IN THE DI-LEPTON CHANNEL WITH ATLAS IN P-P COLLISIONS AT 7TEV

BY

KI LIE

DISSERTATION

Submitted in partial fulfillment of the requirements
for the degree of Doctor of Philosophy in Physics
in the Graduate College of the
University of Illinois at Urbana-Champaign, 2015

Urbana, Illinois

Doctoral Committee:

Professor Tony M. Liss, Chair
Professor Steven M. Errede, Director of Research
Professor Scott S. Willenbrock
Professor Liang Yang

Abstract

This dissertation presents a measurement of differential cross sections as a function of mass, transverse momentum and rapidity of the top quark pairs using $\sqrt{s} = 7$ TeV proton-proton collision data collected by the ATLAS detector at the Large Hadron Collider. This data corresponds to an integrated luminosity of $4.6\,\mathrm{fb}^{-1}$. Events with top quark pair signatures are selected in the di-lepton channel. The reconstructed differential distributions are subtracted with estimated backgrounds and are corrected for detector response and acceptance to the top parton level. The measured differential cross sections are compared with different Monte Carlo generators of top quark pair production. The results are consistent with the Standard Model predictions and with the differential cross section results measured in the lepton+jets channel.

To my family

and those who love me unconditionally.

Table of Contents

Chapter 1

Introduction

"L'essentiel est invisible pour les yeux. (The essential is invisible to the eyes.)"

- Le Petit Prince (The Little Prince)

"The most incomprehensible thing about the world is that it is comprehensible."

- Albert Einstein

Physicists are puzzle-players. The puzzle given by nature has fascinated many to seek and understand what is behind the seen, and there lies all the unseen laws of nature governing the universe, from the biggest to the smallest. Particle physicists like to play the puzzles of both.

The world of the smallest, where one can relate to the world of the largest by realizing that the largest (i.e. the whole universe) was originated from the smallest at a single point in space and time (i.e. the so-called *Big Bang*), is described by the elementary particles, the most fundamental building blocks of matter discovered and coined by particle physicists. The Standard Model of particle physics is so far the most successful model to describe both the seen (i.e. matter particles observed) and the unseen (i.e. the laws of forces between the matter particles) in the world of the tiniest. Many properties of the fundamental particles have been accurately described, many new particles predicted and verified by experiments, and three of the four known fundamental forces in nature, electromagnetic force, weak force and strong force, are formulated in this framework. It is a great success and a big sense of achievement to solve such complicated and far-reaching pieces of the puzzle to much simpler and comprehensible forms with human minds. We like to hope, that if the last fundamental force in nature, the weakest yet the most familiar one to all beings, gravity, can somehow be described and understood in one framework as well. We humans need not only a sense of achievement, but the sense of completion (especially true and important for Ph.D. graduate students, one may say). The grand puzzle of nature is not yet completely solved.

What is more is that there are still many questions within and outside the Standard Model left unanswered: "Are the fundamental particles we know truly *the most* fundamental ones?", "Why are there three

generations of leptons and quarks and what determines their masses and the hierarchy?", "What causes the asymmetry of matter over antimatter in the visible universe?", "What is their origin of mass?", "Are there other elementary particles beyond the Standard Model", "What is the quantum theory of gravity?", "What is dark matter and what causes dark energy?", "How did our universe begin, evolve and will there be an end?". Among these questions, many are closely related to the top quark and how much we know about it. We may find some light at the modern high energy particle colliding machines - the only laboratories we can find and (re-)produce it.

This dissertation presents measurement of top quark pair ($t\bar{t}$) differential cross sections as a function of the invariant mass ($m_{t\bar{t}}$), the transverse momentum ($p_{\mathrm{T}}^{t\bar{t}}$) and the rapidity ($y_{t\bar{t}}$). The measurements use data collected by the ATLAS detector at the CERN LHC, in Geneva, Switzerland. This dissertation is organized as follows:

- Chapter 2 gives the motivation for this measurement with a brief introduction to the Standard Model and top quark physics.
- Chapter 3 gives a brief overview of the LHC and the ATLAS detector.
- Chapter 4 describes the Monte Carlo simulations used in this analysis.
- Chapter 5 defines the criteria for selecting $t\bar{t}$ events in ATLAS.
- Chapter 6 discusses the background processes and their estimation methods.
- Chapter 7 describes the method for reconstructing the $t\bar{t}$ system and the criteria for improvement.
- Chapter 8 illustrates the use of the method of unfolding in this analysis.
- Chapter 9 discusses the systematic uncertainties and how they are evaluated in this measurement.
- Chapter 10 presents the $t\bar{t}$ differential cross section results in three individual dilepton channels.
- Chapter 11 presents the combined dilepton channel results, and compares them with other measurements in ATLAS.
- Chapter 12 concludes this measurement and some future prospects are discussed in Chapter 13.
- The appendices include detailed studies at the intermediate steps of the measurement.

Chapter 2

Top Quark Physics

2.1 The Standard Model and the Top Quark

The Standard Model (SM) of particle physics has been a well-established and well-tested theory since the early 1970s. There have been various textbooks of particle physics [1–4] thoroughly introducing the theoretical framework. In this chapter I present only some aspects that are relevant to the top quark. The goal is to understand the implications of top quark measurements within the framework of the SM.

2.1.1 The Standard Model

There are 17 elementary particles in the SM: 6 quarks and 6 leptons, 4 vector bosons and 1 scalar boson. The quarks (q) and leptons (l) are fermions and are the building blocks of matter. They can be classified into three generations: the 1st generation consists of the lightest and most stable quarks and leptons, the heavier and the less stable particles constitute the 2nd and 3rd generations. Each generation in the quarks is comprised of an "up-type" and an "down-type" quark and their names may or may not reflect these types: the up quark (u) and the down quark (d) in the 1st generation, the charm quark (c) and the strange quark (s) in the 2nd, and the top quark (t) and the bottom quark (b) in the 3rd generation. Each quark has spin 1/2 (thus is a fermion) and an electric charge of 2/3 (for the up-type) and -1/3 (for the down-type). The leptons are arranged similarly as the quarks in three generations: the electron (e^-), the muon (μ^-) and the tau (τ^-) belong to the 1st, the 2nd and the 3rd generations respectively with their corresponding neutrinos (electron neutrino (ν_e), muon neutrino (ν_μ) and tau neutrino (ν_τ)). The electron, the muon and the tau have mass much smaller than the quarks in the same generation, and all have an electric charge of -1. The neutrinos are electrically neutral. In the SM, neutrinos are assumed massless, while it is experimentally found that the neutrinos have mass but are very small. Each quark and lepton has an antiparticle associated with it with the same mass but an opposite electric charge (if not electrically neutral) in the SM. In the case of neutrinos, whether each neutrino is its own antiparticle remains a question to be answered. The antiquarks are denoted as $\bar{q}$ ($\bar{u}$, $\bar{d}$, $\bar{c}$, $\bar{s}$, $\bar{t}$, $\bar{b}$). The antileptons are l^+ (e^+, μ^+, τ^+) and $\bar{\nu}$ ($\bar{\nu_e}$, $\bar{\nu_\mu}$, $\bar{\nu_\tau}$). Table

2.1 summarizes the quarks and the leptons with their properties.

Quarks				Leptons			
Generation	Name	Charge	Mass [GeV/c^2]	Generation	Name	Charge	Mass [GeV/c^2]
1st	u	+2/3	0.002	1st	e	-1	0.511×10^{-3}
	d	-1/3	0.005		ν_e	0	$< 0.22 \times 10^{-7}$
2nd	c	+2/3	1.28	2nd	μ	-1	105.7×10^{-3}
	s	-1/3	0.95		ν_μ	0	$< 0.19 \times 10^{-3}$
3rd	t	+2/3	173.2	3rd	τ	-1	1776.8×10^{-3}
	b	-1/3	4.2		ν_τ	0	$< 18.2 \times 10^{-3}$

Table 2.1: Quarks and leptons in the Standard Model. The mass values are updated in January, 2014 [5].

The 4 vector bosons represent 3 fundamental forces in nature: the strong force is mediated by the gluon (g), the weak force is mediated by the W and Z bosons and the photon (γ) describes the electromagnetic interaction. They are called vector bosons due to the fact that they all have spin 1 (thus vector) and can occupy the same quantum states (bosons). There are 8 massless gluons as the force-carriers in the strong interaction, known as the "color" forces. Only quarks and gluons possess color charges (or "colors") thus are the only particles coupled by the strong force. The $W^{\pm}$ and Z^0 bosons are with large masses $m_W = 80.4$ GeV and $m_Z = 91.2$ GeV [5], and mediates the weak interaction between the leptons and the quarks. The photon is massless and all electrically charged particles experience the electromagnetic force. Gravitational force is not considered in the SM, but it is the weakest force of all and its effect on massive particles at the quantum scales is very small.

The scalar boson (H), or the Higgs boson, is responsible for giving mass to the elementary particles. A mechanism that breaks the electroweak symmetry (the Brout-Englert-Higgs mechanism) is required in the SM for the vector bosons and the fermions to acquire mass, and the simplest choice introduces a massive, scalar particle of spin 0 that couples to other elementary particles. A scalar boson was recently discovered at the LHC [6, 7] and has a mass of $m_H = 125.09 \pm 0.24$ GeV [8]. Its properties are also found to be consistent with the SM Higgs boson [9–12]. This discovery solves the electroweak symmetry breaking "mystery" in the SM.

2.1.2 The Top Quark

The top quark is by far the most massive particle in the SM ($m_t = 173.2 \pm 0.9$ GeV [5]). It is around 40 times heavier than the b-quark and has a mass comparable to a Gold atom. It is the only quark in the SM that has a mass so close to the electroweak symmetry breaking scale ($v \sim 246$ GeV), which gives a Yukawa coupling $y_t = \sqrt{2}m_t/v$ of almost unity. This special property leads to speculations of its special role in the electroweak symmetry breaking (through which elementary particles acquire mass), and unique sensitivity to

interactions beyond the SM (BSM). A rich number of processes in proposed BSM, if they exist, can modify the production rates of top quarks and the deviations from theoretical calculations can show up in the total (total cross section $\sigma_{t\bar{t}}$) and/or differential (e.g. differential cross sections $d\sigma/dm_{t\bar{t}}$ and $d\sigma/dp_{\mathrm{T}}^{t\bar{t}}$) production rates of top-antitops ($t\bar{t}$).

Top Quark Mass in the SM

The masses of quarks are not predicted in the SM. However, these parameters show up in the calculation of radiative corrections in the electroweak processes. Radiative corrections are higher order contributions in the perturbation series for calculating an electroweak process' cross section, for example. Therefore, even at a time when some particles have not been observed, precise measurements of the known quarks allow indirect predictions of the unseen particles' mass values. The top quark has played an important role in these aspects, due to its largest quark mass in the SM and thus the correction terms have strong dependence on it. One example is the prediction of the mass of scalar boson with the precision EW measurements of W boson and the top quark. Prior to the observation of the scalar boson at the LHC [6, 7], global fits to precision electroweak measurements have indirectly limited the mass of the scalar boson to be $m_H < 158$ GeV at the 95% confidence level [13]. Figure 2.1 shows the global fit with latest direct measurements of m_W and m_t to constrain SM Higgs m_H [14]. The mass range of SM Higgs predicted is consistent with the discovered scalar boson's mass at $m_H = 125.09 \pm 0.24$ GeV [8].

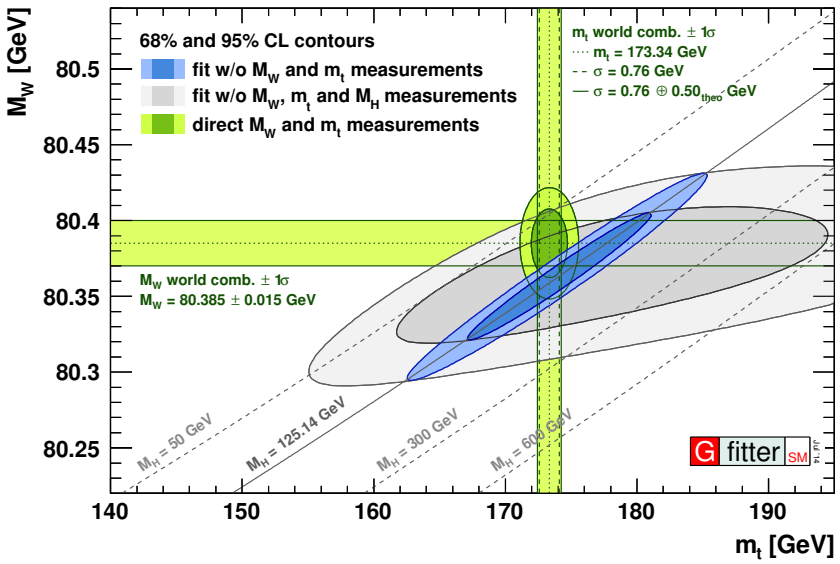

Figure 2.1: Global electroweak fit using latest measurements of m_W and m_t (last updated in July 2014 [14]).

2.2 Top Quark Pair Production

In proton-proton (pp) collisions, top quark pairs ($t\bar{t}$) are produced mainly via the strong interaction. Thus, $t\bar{t}$ production can be described in terms of quantum chromodynamics (QCD), the theory of strong interaction. At the leading order (LO) QCD, quark-antiquark annihilation ($q\bar{q} \to t\bar{t}$) and gluon fusion ($gg \to t\bar{t}$) contribute to $t\bar{t}$ production, shown in Figure 2.2. The relative importance of both processes depends on the center-of-mass collision energy $\sqrt{s}$ and the nature of the beam (pp or $p\bar{p}$ collisions). At the LHC at $\sqrt{s} = 7$ TeV, the gluon fusion process dominates $\sim 85\%$ of the $t\bar{t}$ production, while the quark-antiquark annihilation is the dominant process at the Tevatron. The total inclusive cross section for $pp \to t\bar{t}$ is:

$$\sigma(pp \to t\bar{t}) = \sum_{i,j} \int dx_i dx_j f_{i,p}(x_i, \mu^2) f_{j,p}(x_j, \mu^2) \cdot \hat{\sigma}_{ij}(ij \to t\bar{t}; \hat{s}, m_t^2, \mu^2) \tag{2.1}$$

where p is the colliding proton at the LHC, x_i and x_j are the momentum fractions for partons i and j, f_i and f_j are the parton distribution functions (PDFs) for partons i and j, μ is the renormalization and factorization scale μ and m_t is the pole mass of the top quark. The "hatted" variables $\hat{\sigma}_{ij}$ and $\hat{s} = x_i x_j s$ are the parton cross section and parton center-of-mass energy, respectively. The integral is summed over all relevant partons inside the proton.

The parton cross section $\hat{\sigma}$ depends on the top quark pole mass m_t, the parton center-of-mass energy $\hat{s}$ and the strong coupling constant α_s. It can be expanded in α_s to the next-to-next-to-leading order (NNLO) as

$$\hat{\sigma}_{i,j}(\beta) = \frac{\alpha_s^2}{m_t^2}(\sigma_{i,j}^{(0)} + \alpha_s \sigma_{i,j}^{(1)} + \alpha_s^2 \sigma_{i,j}^{(2)} + \mathcal{O}(\alpha_s^3)). \tag{2.2}$$

where $\beta = \sqrt{1-\rho}$, with $\rho \equiv 4m_t^2/\hat{s}$, is the relative velocity of the final state top quarks. All the partonic processes $ij \to t\bar{t}$ are calculated in QCD at NNLO including resummation of soft gluon terms at the next-to-leading-logarithmic (NNLL) accuracy [15–20]. Table 2.2 shows the NNLO+NNLL QCD calculations of total cross sections for top quark pair production $\sigma_{t\bar{t}}$ at $m_t = 173.3$ GeV with MSTW2008nnlo68cl PDF set [21], at different center-of-mass energies $\sqrt{s}$ corresponding to the conditions at the Tevatron and the LHC.

At the LHC, gluon fusion $gg \to t\bar{t}$ dominates the contribution to $\sigma_{t\bar{t}}$ due to the large gluon density in the proton at small x, as shown in the distributions of the PDFs in figure 2.3. The proton PDFs f_i are determined by several groups with data on deep-inelastic scattering experiments, and are used in generation of the Monte Carlo simulations.

Figure 2.4 shows that the measured $\sigma_{t\bar{t}}$ agrees well in data at the LHC with ATLAS and CMS detectors with the NNLO+NNLL calculations [15–20].

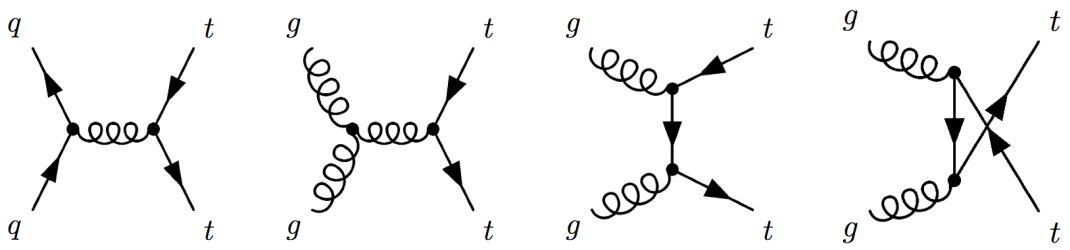

Figure 2.2: Feynman diagrams of $t\bar{t}$ production at the leading order QCD: the quark-antiquark annihilation ($q\bar{q} \to t\bar{t}$) and the gluon fusion ($gg \to t\bar{t}$). The latter is the dominant process for $t\bar{t}$ production at the LHC.

Collider	$\sigma_{t\bar{t}}$ [pb]
Tevatron ($p\bar{p}$) 1.96 TeV	7.164
LHC (pp) 7 TeV	172.0
LHC (pp) 8 TeV	245.8
LHC (pp) 14 TeV	953.6

Table 2.2: QCD NNLO+NNLL [15–20] total cross sections of top quark pair productions at 1.96 TeV, 7 TeV, 8 TeV and 14 TeV at $m_t = 173.3$ GeV with MSTW2008nnlo68cl PDF set [21]. Only the central values are shown.

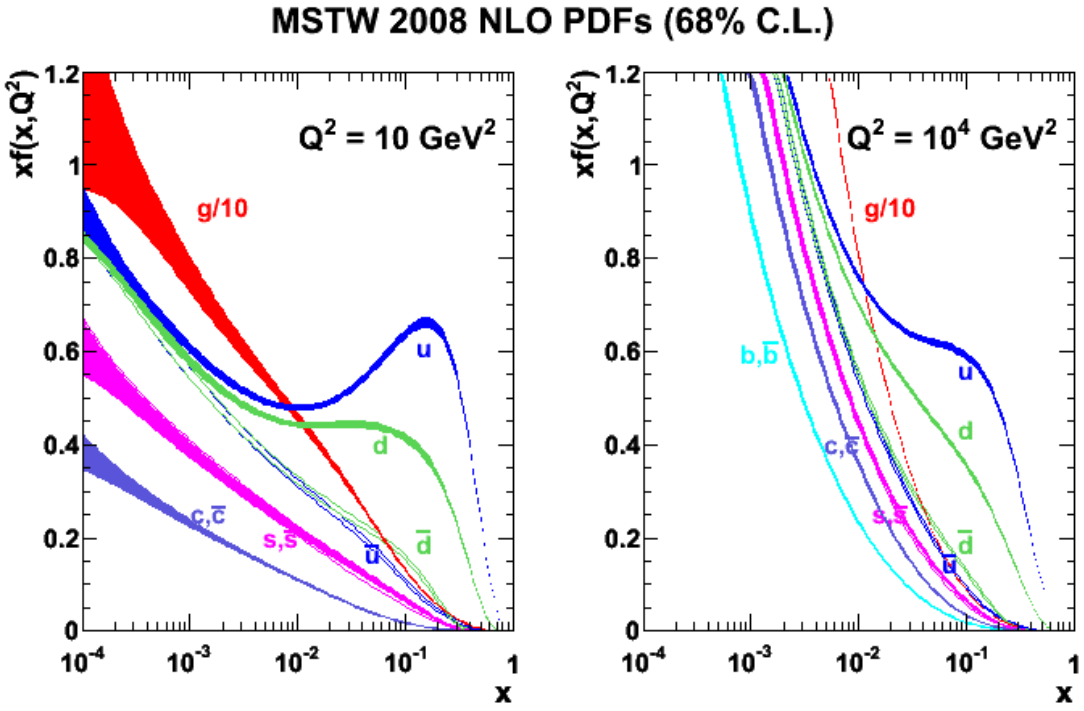

Figure 2.3: MSTW 2008 NLO PDFs at $Q^2 = 10$ GeV^2 and $Q^2 = 10^4$ GeV^2 [21].

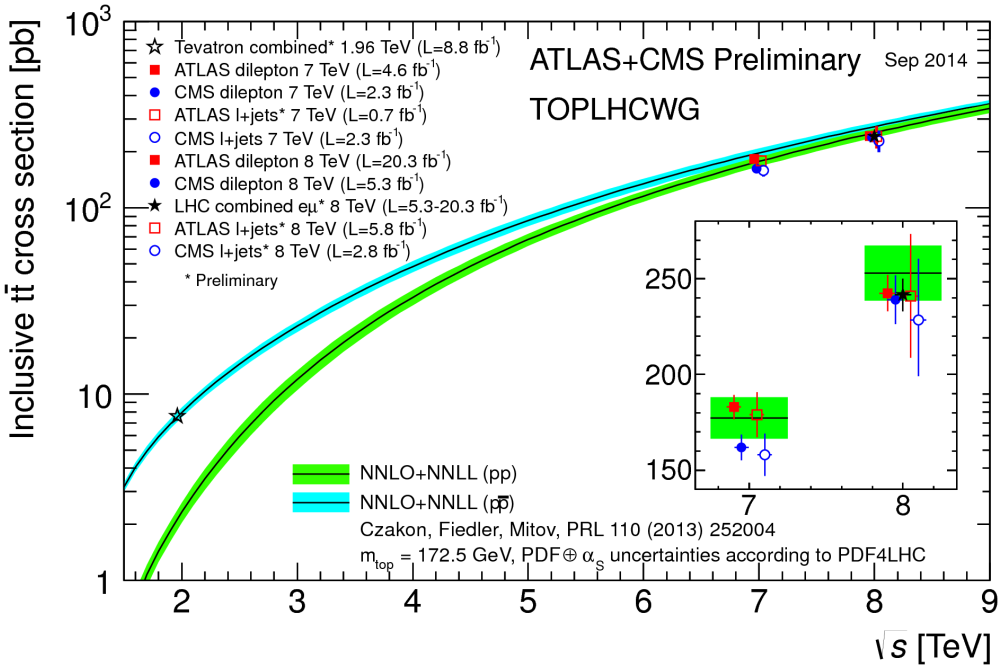

Figure 2.4: Summary of LHC and Tevatron measurements of the top-pair production cross-section as a function of the centre-of-mass energy compared to the NNLO QCD calculation complemented with NNLL resummation (top++2.0). The theory band represents uncertainties due to renormalisation and factorisation scale, parton density functions and the strong coupling. The measurements and the theory calculation is quoted at m_{top}=172.5 GeV. Measurements made at the same centre-of-mass energy are slightly offset for clarity.

2.3 Analysis Overview

In this analysis, the kinematic distributions of $t\bar{t}$ are measured and are corrected for detector, acceptance and reconstruction effects ("unfolded") to the generated-parton (truth) level. Together with the efficiency distributions estimated from the signal MC sample, the absolute (or normalized) differential cross sections are measured. The differential cross section $d\sigma_{t\bar{t}}/dx_{t\bar{t}}$ where $x_{t\bar{t}} = m_{t\bar{t}}$, $p_{\mathrm{T}}^{t\bar{t}}$, $y_{t\bar{t}}$ or $|y_{t\bar{t}}|$ is calculated as

$$(\frac{d\sigma}{dx_{t\bar{t}}})_i = \frac{N_i^{unfolded}}{L \cdot Br \cdot (A \cdot \epsilon)_i \cdot \Delta x_i} \tag{2.3}$$

where $N_i^{unfolded} = (N_{obs,i} - N_{bkg,i})^{unfolded}$ is the unfolded background-subtracted data spectrum in the i^{th} bin; L is the integrated luminosity of measured data; Br is the branching ratio of the $t\bar{t}$ default MC sample, including single-lepton and di-lepton channels, and is taken as $Br^{t\bar{t}\to nofullhad} = 0.543 = 1-(1-(3\times 0.108))^2$; $(A \cdot \epsilon)_i$ is the differential efficiency evaluated from simulation in the i^{th} bin; Δx_i is the bin width at the i-th bin. This differential cross section becomes the inclusive cross section, when all bins are integrated with respect to the individual bin widths. The integrated inclusive cross section is given by

$$\sigma_{t\bar{t}}^{int} = \sum_i (\frac{d\sigma}{dx_{t\bar{t}}})_i (\Delta x_{t\bar{t}})_i \tag{2.4}$$

and the inclusive cross section measured by the cut-and-count method,

$$\sigma_{t\bar{t}}^{inc} = \frac{N_{obs} - N_{bkg}}{L \cdot Br \cdot (A \cdot \epsilon)} \tag{2.5}$$

are both evaluated in this analysis. The measured values and uncertainties in both methods are consistent with each other.

To obtain results with reduced systematic uncertainties, the normalized differential cross section $\frac{1}{\sigma_{t\bar{t}}}\frac{d\sigma}{dx_{t\bar{t}}}$ is evaluated and presented along with the results for the absolute differential cross section. The integrated inclusive $t\bar{t}$ cross section $\sigma_{t\bar{t}}^{int}$ and its associated uncertainties is taken as the normalization of the absolute differential cross section, by which some of the systematic effects in the differential cross section are canceled by the same effects in the inclusive cross section.

The definition of generated top parton in this analysis refers to final-state partons after hard gluon emissions and before top decay. This definition corresponds to the same definition used in another $t\bar{t}$ differential measurement in ATLAS in the lepton+jets channel [22] and is described in section 5.1.1.

Chapter 3

The LHC and the ATLAS Detector

3.1 The LHC

The Large Hadron Collider (LHC) at CERN is the world's largest and most energetic particle accelerator. It consists of a 27-km ring, housed in a tunnel about 100 m underground near Geneva, Switzerland, to accelerate and collide proton beams with a center-of-mass energy of up to 14 TeV, at a designed luminosity of $10^{34} cm^{-2} s^{-1}$. The high energy and luminosity of the particle collisions at the LHC allows a wide range of study from precision measurements to new searches of particles and phenomena beyond our known physics. The four major experiments at the LHC are ATLAS, ALICE, CMS and LHCb, as shown in figure 3.1.

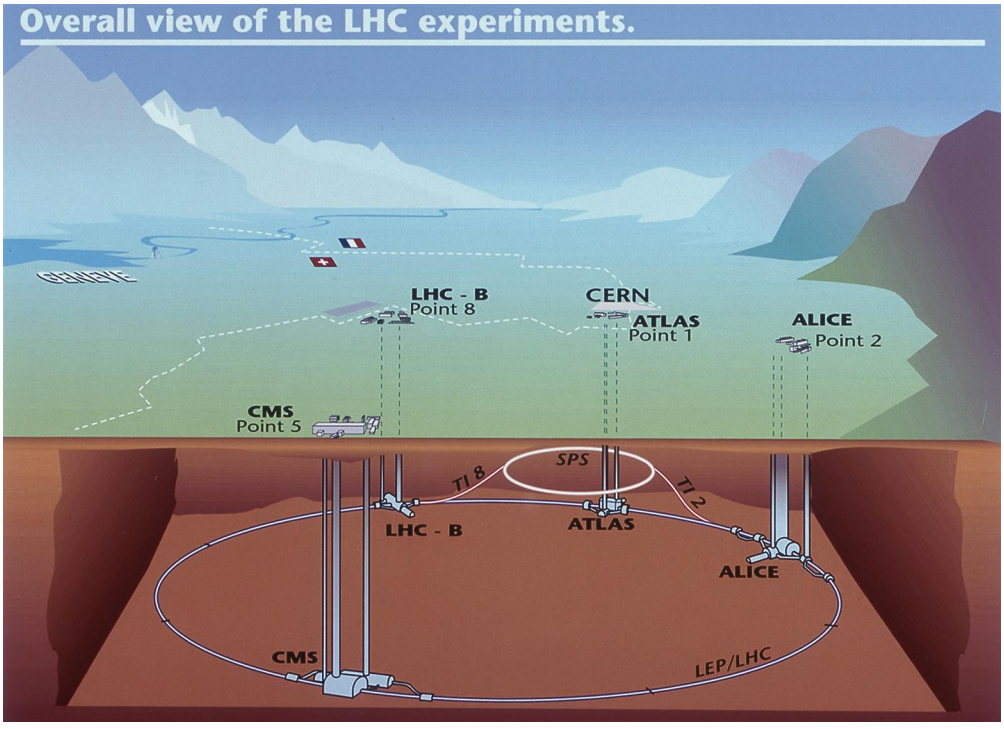

Figure 3.1: The overall view of the four major experiments at the LHC.

3.2 The ATLAS Detector

The ATLAS (A Toroidal LHC ApparatuS) detector is a general purpose detector designed to probe these particle collisions with high resolution, precision and efficiency. These requirements set high standards on the electronics and the software infrastructure developed in the detector, as well as new computing frameworks to handle large data recorded for physics analysis. Figure 3.2 shows a cut-away view and different components of the detector. The integrated luminosity of pp collisions delivered by the LHC and recorded by the ATLAS in 2011 is shown in figure 3.3. The data recording efficiency is over 93%.

Definitions

The ATLAS detector is described by a right-handed coordinate system. The nominal interaction point is defined as the origin of the coordinate system. The counter-clockwise beam direction is taken as the z-axis, the positive x-axis is defined as pointing from the interaction point to the center of the LHC ring, and the positive y-axis is defined as pointing upwards such that the x-y plane is transverse to the beam direction. The azimuthal angle ϕ is measured around the beam axis, and the polar angle θ is the angle from the beam axis. For final state particles, the pseudorapidity variable, defined as $\eta = -\ln\tan(\theta/2)$, is often used instead of the polar angle θ (while in the case of massive objects such as top quarks, W/Z bosons, etc., the rapidity $y = 1/2\ln[(E+p_z)/(E-p_z)]$ is used). A pseudorapidity of 2.5 (-2.5) corresponds to $\theta \sim 10$ (170) degrees. The detector is nominally forward-backward symmetric with respect to the interaction point. The transverse momentum p_{T}, the transverse energy E_{T} and the missing transverse energy $E_{\mathrm{T}}^{\mathrm{miss}}$ are defined in the x-y plane. The angular distance ΔR is defined as $\Delta R = \sqrt{\Delta\eta^2 + \Delta\phi^2}$.

Magnet System

The design of ATLAS is fundamentally driven by the choice of the magnet configuration of the detector. The ATLAS magnet system consists of four superconducting magnets: one solenoid and three toroids (one barrel and two end-caps). The solenoid is aligned on the beam axis and provides a 2 T axial magnetic field for the inner detector for excellent identification and reconstruction of charged particles, while its thickness is minimized to reduce its radiative effects to the barrel electromagnetic calorimeter. The toroids provides a toroidal magnetic field of about 0.5 T in the barrel and 1T in the two end-caps for the muon detectors, in the central and end-cap region, respectively, to generate strong bending power for the muons in a large and open volume. The ATLAS toroids are arranged in an eight-fold azimuthal symmetry around the calorimeters.

Tracker

The inner detector is the innermost part of ATLAS and is surrounded by the solenoid. It is a combination of two high-resolution semiconductor pixel (Pixel) and strip (SCT) detectors in its inner part and a straw-tube tracking detector (TRT) in its outer part, which altogether reconstructs the momentum of charged particles like electrons, muons and hadrons in jets with high efficiency. This overall coverage of the inner detector, $|\eta| < 2.5$, provides tracking measurements in a range matched by the precision measurements of the electromagnetic (EM) calorimeter.

Calorimeters

The calorimeters consist of a number of sampling detectors with full azimuthal symmetry and coverage around the beam axis. High granularity liquid-argon (LAr) electromagnetic sampling calorimeters cover the pseudorapidity range $|\eta| < 3.2$ and provides excellent performance in terms of energy resolution and electron/photon identification. The scintillator-tile calorimeter (TileCal) covers the range $|\eta| < 1.7$ for the hadronic calorimetry, and is separated into a large central barrel and two smaller extended barrel cylinders. For larger pseudorapidity regions, the end-cap (electromagnetic and hadronic) calorimeters and the forward calorimeter extend the pseudorapidity coverage to $|\eta| = 4.9$. The designed calorimeter depths (or thicknesses) also ensure a good containment of electromagnetic and hadronic shower, therefore limit punch-through into the muon system and provide a good resolution for high-energy jets. Together with the large η coverage, a good $E_{\mathrm{T}}^{\mathrm{miss}}$ measurement, which is important for many physics SM and exotic signatures, can also be achieved.

Muon Chamber

The muon spectrometer is the outermost sub-detector of ATLAS, designed exclusively for the detection (identification, triggering and reconstruction) of muons. Muons are minimum ionizing particles and typically pass through the ATLAS detector without depositing a substantial portion of their kinetic energy in the calorimeter. The identification and reconstruction of muons are based on the deflection of muon tracks in the large toroidal magnets, instrumented with separate trigger and high-precision chambers. The muon system identifies tracks in the region $|\eta| < 2.7$, with precision measurements up to $|\eta| = 2.5$ when combined with the inner detector measurements. The stand-alone spectrometer also provides good resolution for high-p_{T} ($p_{\mathrm{T}} = 1$ TeV) muons and excellent charge identification.

Trigger

The ATLAS detector provides highly efficient triggering on low transverse momentum objects to reject sufficient background processes. The ATLAS trigger system has three distinct levels: L1, L2, and the event filter (EF). Each trigger level refines the decisions made at the previous level and applies additional selection criteria where necessary. The first level trigger uses information based on a subset of detectors and reduces the bunch cross frequency (20 MHz) by a factor of about 400 to about 50 kHz. L2 and EF access more detector information and reduce the final trigger rate of 200 Hz. These high level triggers are implemented in software whereas the L1 triggers are implemented in hardware.

Overall Performance

Table 3.1 gives a summary of the general performance of the ATLAS detector.

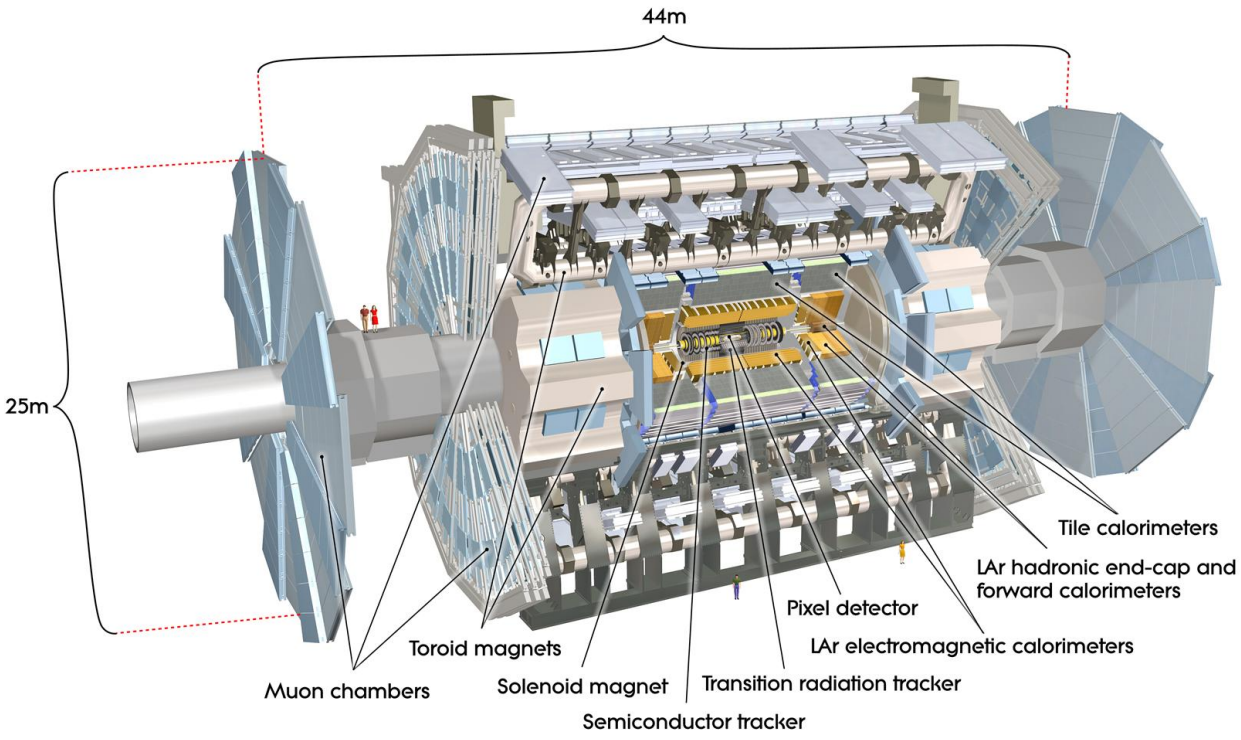

Figure 3.2: The ATLAS detector.

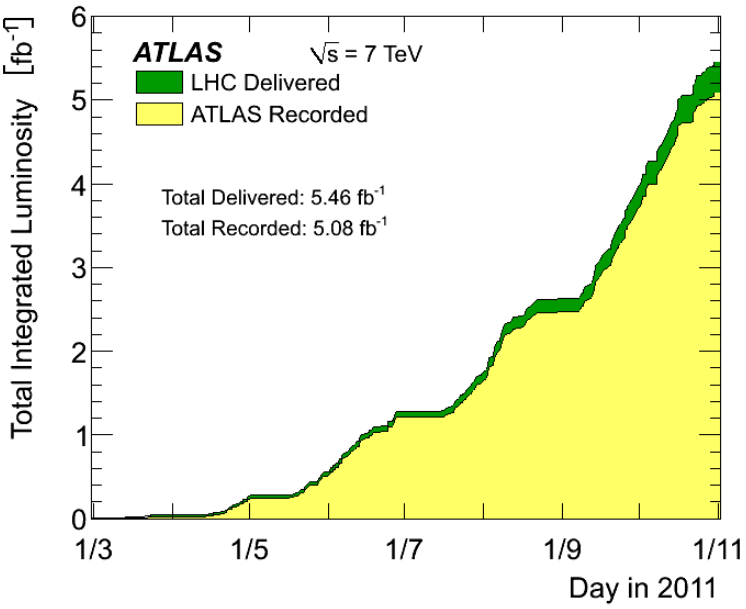

Figure 3.3: Cumulative luminosity versus time delivered by the LHC (green) and recorded by ATLAS (yellow) during stable beams and for pp collisions at 7 TeV centre-of-mass energy in 2011.

Detector component	Required resolution	η coverage	
		Measurement	Trigger
Tracking	$\sigma_{p_{\mathrm{T}}}/p_{\mathrm{T}} = 0.05\% p_{\mathrm{T}} \oplus 1\%$	± 2.5	
EM calorimetry	$\sigma_E/E = 10\%/\sqrt{E} \oplus 0.7\%$	± 3.2	± 2.5
Hadronic calorimetry (jets)			
barrel and end-cap	$\sigma_E/E = 50\%/\sqrt{E} \oplus 3\%$	± 3.2	± 3.2
forward	$\sigma_E/E = 100\%/\sqrt{E} \oplus 10\%$	$3.1 < \lvert\eta\rvert < 4.9$	$3.1 < \lvert\eta\rvert < 4.9$
Muon spectrometer	$\sigma_{p_{\mathrm{T}}}/p_{\mathrm{T}} = 10\%$ at $p_{\mathrm{T}} = 1$ TeV	± 2.7	± 2.4

Table 3.1: General performance of the ATLAS detector [23]. The units for E and p_{T} are in GeV.

Chapter 4

Monte Carlo Simulation

The baseline simulated top quark pair production sample (117050) is generated with 10M events using POWHEG [24] generator with a next-to-leading order (NLO) parton distribution function (PDF) set CT10 [25]. Parton showering and the underlying event are modelled by PYTHIA [26] using the P2011 tune [27]. This sample includes both ℓ+jets and dilepton channels. The top quark mass is set to 172.5 GeV. The $t\bar{t}$ sample is normalized to the NNLO+NNLL cross section of $177.3^{+10.1}_{-10.8} pb$ [15–20].

Single top production samples are generated using POWHEG [24] interfaced to PYTHIA [26] using the P2011C tune with Diagram Removal (DR) scheme. Specifically, W-t associated production dilepton sample (110141) with 0.5M events is used in this analysis. The sample (assuming dileptonic branching ratio of $(3 \times 0.108)^2 = 0.105$ in Monte-Carlo) is normalized to approximate NNLO cross-sections and uncertainties: $15.74^{+1.17}_{-1.21}$ pb [28].

The Z+jets samples (107650-5, 107660-5, 107670-5) include both the Z events and the full Drell-Yan contribution from the $\gamma^* \to ll$ and the interference from Z/γ^*. The samples are generated with dileptons in the invariant mass range of 40 GeV $< m_{ll} <$ 2000 GeV, using ALPGEN interfaced to HERWIG and JIMMY. The cross-sections are normalized to NNLO total Z/Drell-Yan cross-sections recommended in [29].

The diboson samples for WW, WZ and ZZ productions (107101-11) are generated using ALPGEN interfaced to HERWIG [30] and JIMMY [31] with CTEQ6L1 PDF set and with the AUET2 tune [32]. The cross-sections are normalized to NLO in [29].

All the simulation samples are generated with multiple pp interactions per bunch crossing (pile-up). The simulated events are re-weighted such that the distribution of the average number of interactions per pp bunch crossing in simulation matches that in the measured data. The average number of interactions typically has a range between 4 and 16 and varies over different data-taking periods.

All of the samples used in the nominal and $t\bar{t}$ modeling systematics and studies are listed in Tables A.1 and A.2. All samples in the nominal analysis are processed through the full GEANT4 simulation (fullSim, or FS) of the ATLAS detector. Fast simulation of the ATLAS detector (ALTFASTII, or AF2) is used in some samples for $t\bar{t}$ modeling systematics studies (I/FSR, parton shower, color reconnection, underlying event and

renormalization/factorization scale). When a fast simulation sample is used for systematic comparison, it is compared with the fast simulation version of the sample of interest (e.g. AltFastII POWHEG+Herwig 105860 vs AltFastII POWHEG+Pythia 117050).

Chapter 5

Selection of $t\bar{t}$ Events

5.1 Object Selection

5.1.1 Generated top partons

The top quarks are generated at the parton level in the full phase-space, and the measured observables in the visible phase-space are extrapolated to the full phase-space using the acceptance and efficiency from the MC. The simulated top partons in this analysis are final-state partons before decay and after hard gluon emission. This refers to top quarks with status code 155 in HERWIG [33] and status code 3 in PYTHIA samples.

5.1.2 Electrons

Electrons are reconstructed in the central region with energy deposits (clusters) in the EM calorimeter associated to reconstructed tracks in the Inner Detector. The candidates are selected with the following requirements:

- the calorimeter acceptance requires energy clusters (cl) of the electron to be within $|\eta_{cl}| < 2.47$, excluding the transition region $1.37 < |\eta_{cl}| < 1.52$;
- the transverse energy of the reconstructed electron is required to be $E_{\mathrm{T}} > 25$ GeV, where $E_{\mathrm{T}} = E_{cl}/\cosh\eta_{track}$;
- electrons are required to satisfy the `Tight++` criteria, which include stringent selection on calorimeter, tracking and combined variables that ensure good separation between isolated electrons and jets;
- the isolation cuts require a calorimeter isolation cut with 90% efficiency at a cone size of $\Delta R = 0.2$ (`Etcone20@90`) and a track isolation cut with 90% efficiency at a cone size of $\Delta R = 0.3$ (`Ptcone30@90`);
- further isolation of electron requires any jet to be removed in the event when found within $\Delta R = 0.2$ of the electron direction axis (electron-jet overlap removal); after that any electrons within $\Delta R = 0.4$

with a selected jet with $p_{\mathrm{T}}(jet) > 25$ GeV and $|JVF| > 0.75$ are rejected, to remove overlap of jet-like electrons.

Scale factors for electron reconstruction, identification (ID), trigger efficiencies and isolation cuts are applied on all MCs. Efficiencies of electron reconstruction and trigger are measured with the tag-and-probe method using $Z \to ee$ samples [34]. The ID-isolation efficiencies are derived from both Z and W events. The electron energy scale is also corrected in data and in MC, and energy smearing is applied to the MC to match the energy resolution in data.

5.1.3 Muons

Muon objects are defined using the `Muid` algorithm. Following the recommendations from the Muon Combined Performance (MCP) group [35], the muon candidates are selected with the following requirements:

- the muon candidates are required to be "combined", which means they have reconstructed tracks in both the inner detector (ID) and the muon spectrometer (MS);
- the detector acceptance of the ID and MS is required with $|\eta| < 2.5$;
- the transverse momentum p_{T} is required to be above 20 GeV to avoid the trigger turn-on region;
- the MCP ID track quality requirements are passed;
- the isolation of muons from other objects requires a calorimeter isolation cut of $E_{\mathrm{T}}^{0.2} < 4$ GeV, where $E_{\mathrm{T}}^{0.2}$ is the sum of the transverse energy in a cone of $\Delta R = 0.2$ around the muon, together with a track isolation requirement of $p_{\mathrm{T}}^{0.3} < 2.5$ GeV, where $p_{\mathrm{T}}^{0.3}$ is the sum of transverse momentum of ID tracks in a cone of $\Delta R = 0.3$ around the muon;
- and a further isolation requires that a selected muon is away from any selected jet with $p_{\mathrm{T}} > 25$ GeV and $|JVF| > 0.75$ by the distance parameter $\Delta R(\mu, j) > 0.4$, where JVF, the jet vertex fraction, is a variable defined to discriminate jets arising from multiple interactions (pileup).

The muon reconstruction, identification (ID), isolation and trigger scale factors are applied to the MC events to correct the MC to match the data. The efficiencies of isolation and trigger requirements are measured using the tag-and-probe method in the $Z \to \mu\mu$ events in data and MC [36].

5.1.4 Jets

Jets are reconstructed with the anti-k_t algorithm [37] with a distance parameter of 0.4, using topological clusters built from calorimeter cells with significant energy deposits ("topoclusters") at the eletromagnetic (EM) scale. Jets are then calibrated to the hadronic scale with p_{T} and η-dependent correction factors derived from Monte Carlo simulation.

The jets used in this analysis also satisfy the following requirements:

- sufficiently separated from an electron by $\Delta R = 0.2$, otherwise the jet is removed (electron-jet duplicates removal, as mentioned in the requirements for electron candidates above);
- a transverse momentum greater than 25 GeV;
- $|\eta| < 2.5$ for a jet to be reconstructed efficiently using the calorimeter systems;
- $|JVF| > 0.75$ to suppress jets produced from in-time pile-ups / multiple interactions;
- jet quality criteria (jet cleaning) are applied to reject the so-called *bad jets*, meaning jets produced not by in-time real energy deposits in the calorimeters, but produced from hardware problems in the calorimeters, beam-gas interactions in the LHC, and particle showers induced by cosmic rays.

5.1.5 Missing transverse energy

The missing transverse energy ($E_{\mathrm{T}}^{\mathrm{miss}}$) is an object-based quantity derived from physics objects, where the topological clusters are calibrated at the EM scale. This $E_{\mathrm{T}}^{\mathrm{miss}}$ is defined as `MET_RefFinal_em_tightpp` in the Top Group using a similar approach as the `MET_RefFinal` definition recommended by the Jet/ETmiss Performance Working Group, and is calculated from calorimeter cells calibrated to their associated objects. These objects include electrons, jets (above 20 GeV), soft jets (7-20 GeV) and muons, where the order indicates the order of association of the cells to the objects. The remaining energy from cells not included in the clusters used for reconstructing the objects is included as the Cell-Out term, also calibrated at the EM scale. Photons and τ objects are not included in this $E_{\mathrm{T}}^{\mathrm{miss}}$ calculation as their contributions to the measured $E_{\mathrm{T}}^{\mathrm{miss}}$ are small.

5.1.6 b-tagging

The jet selection for reconstructing $t\bar{t}$ system is further enhanced by identifying jets arising from hadronization and weak decays of b-quarks. The specific properties of these jets with long lifetime ($\tau_b \sim 10^{-12}$sec), large B hadron mass and large branching ratio into leptons allow one to discriminate the b's from light quark

jets by exploiting the measurable secondary vertices and impact parameters of the decay products of these jets. The output weights of three b-tagging algorithms are inputs to a neural network (TMVA) to extract a combined tagging discrimination weight for each jet. These algorithms rely on the topology of weak b and c-hadron decays inside the jet, the correlation between the significances of the transverse impact parameter and longitudinal impact parameter, and the search of a good secondary vertex with only tracks associated to the jet. Likelihood ratios are built from the relevant variables to give a tagging discrimination weight in each algorithm. It has been shown that the combined tagger (MV1) has the best performance among the tagging algorithms available in ATLAS [38].

In this analysis, a b-tagged jet is defined as a jet having MV1 weight with > 0.601713, which corresponds to a b-tagging efficiency of 70% [39].

5.2 Event selection

A top quark decays into a b-quark and a W boson with a branching ratio of $\sim 100\%$. The b-quark hadronizes into multiple jets, while the W can decay leptonically into a lepton and a neutrino or hadronically into jets. In the dilepton decay channel of $t\bar{t}$ production, candidates of top quark pairs are selected by requiring two high transverse momentum isolated leptons of opposite charge signs and at least two jets with high momentum in the event. In addition to this jet requirement, we also apply b-tagging requirements to select jets with higher probability of arising from the hadronization of the b-quarks directly from the top quark decay.

5.2.1 Event Selection Requirements

The dilepton channel consists of ee, $\mu\mu$ and $e\mu$ channels. The requirements in each individual channel follow the ATLAS Top Group prescription [38]. The selection requirements are determined so as to optimise the signal-background ratio for each channel. To increase the purity of jets originating from $t\bar{t}$ decays, final selected events are required to have at least 1 b-tagged jet.

In all ee, $\mu\mu$ and $e\mu$ channels, the selected events pass the trigger requirements defined for each data taking period. Exactly two good leptons defined by the above section with opposite charge signs are required. A primary vertex reconstructed from at least five tracks, to be consistent with x-y profile of the beam spot, is required. Events identified as cosmic ray events are rejected. One of the leptons in the events is required to match the lepton Event Filter (EF) triggers used for each data taking period within a ΔR distance of 0.15. Events with a muon overlapped with an electron or vice versa are rejected. Jet cleaning is applied and events having any bad (`LooseBad`) jets are rejected. To suppress backgrounds from Drell-Yan and multijet

processes in the ee and $\mu\mu$ channels, $E_{\mathrm{T}}^{\mathrm{miss}}$ is required to be greater than 60 GeV and the dilepton invariant mass m_{ll} is required to be outside the Z boson mass window $|m_{ll} - 91\ \mathrm{GeV}| < 10$ GeV. m_{ll} is also required to be above 15 GeV in ee and $\mu\mu$ to reject backgrounds from bottom-quark production and vector-meson decays. No missing tranverse energy and dilepton invariant mass requirements are applied in the $e\mu$ channel, but a reconstructed variable, H_{T}, defined to be the scalar sum of p_{T} of all selected leptons and jets in an event, is required to be greater than 130 GeV to suppress remaining background from Z/γ^*+jets processes. In addition, two or more selected good jets defined by the above section are required for each selected event. Among these jets, in each event, it is further required that there are at least one jet that is b-tagged (with MV1 weight > 0.601713), indicating that these jets are identified as originated from a b-quark at a 70% efficiency [39].

After the standard dilepton event selection, a further selection using jet-lepton mass variable (m_{jl}) is applied to reject events where "unwanted" jets, which are not associated with $t\bar{t}$ decay, are selected by the jet selection algorithm (Section 7.2). The use and the optimisation of this variable is described in section 7.3. Events that passed the requirement of ($m_{l^+j}/172.5\ \mathrm{GeV} < 0.8$ OR $m_{l^-j}/172.5\ \mathrm{GeV} < 0.8$), while j is the sub-leading MV1-weight jet, give the final event sample for this analysis.

Table 5.1 shows the event selection cuts in data events.

	Cut	ee	$\mu\mu$	$e\mu$
0	Total	469616920	469616920	469616920
1	GRL	427615766	427615766	427615766
2	Trigger	164644802	170040212	334535406
3	Good vertex	163927865	169146797	332925446
4	Cosmic rejection	163927865	169146794	332925443
5	≥ 2 leptons	681767	1814143	12921
6	one of the leptons matches the trigger	681767	1814084	12917
7	e-μ overlap removal	681752	1814084	12863
8	Jet cleaning	678564	1804240	12806
9	MET$>$ 60 GeV (ee,$\mu\mu$); $H_{\mathrm{T}} > 130$ GeV ($e\mu$)	1695	4990	7504
10	≥ 2 jets with $p_{\mathrm{T}} > 25$ GeV, $\lvert\eta\rvert > 2.5$, $\lvert JVF\rvert > 0.75$	1005	2844	5441
11	Exactly 2 leptons	1000	2832	5424
12	Opposite-sign leptons	988	2811	5320
13	$M_{ee,\mu\mu} > 15$ GeV	983	2788	5320
14	$\lvert M_{ee,\mu\mu} - 91\rvert > 10$ GeV	738	2057	5320
15	Both leptons matched to truth leptons	738	2057	5320
16	LAr error flag (done in GRL)	738	2057	5320
17	≥ 1 tagged jets with MV1 $w > 0.601713$	574	1600	4344
18	jet-lepton mass cut	532	1509	4038

Table 5.1: Event selection cuts and selected events in data, in the ee, $\mu\mu$ and $e\mu$ channels. This selection is compared and cross-checked with other dilepton-channel analysis teams in the Top group for 2011 data analyses. There are good agreements ($< 1\%$ differences) in all three channels.

5.2.2 Event Yields for Data and Monte Carlo Samples

Event yields for the estimated backgrounds, estimated signal and data, passing all cuts in Table 5.1, are summarized in Table 5.2. The fraction for each of the estimated background and signal of the total estimated yield are also shown.

	ee		$\mu\mu$		$e\mu$	
$Z \to ee/\mu\mu$+jets	2.1	0.4%	5.8	0.4%	0.2	0.0%
$Z \to \tau\tau$+jets	0.4	0.1%	2.6	0.2%	5.8	0.1%
Single top (W-t)	20.4	3.9%	57.9	3.9%	154.8	3.9%
Diboson	1.0	0.2%	3.2	0.2%	9.0	0.2%
Fake leptons	12.2	2.3%	11.4	0.8%	50.2	1.3%
Total bkg.	36.1	6.9%	80.9	5.4%	219.9	5.6%
$t\bar{t}$	484.6	93.1%	1421.4	94.6%	3738.5	94.4%
Total	520.8	100%	1502.3	100%	3958.4	100%
Observed	532		1509		4038	

Table 5.2: Yields and fractions of expected $t\bar{t}$ signal and backgrounds compared to observed events, in the ee, $\mu\mu$ and $e\mu$ channels. Background yields are broken down into each background process.

Chapter 6

Background Processes in $t\bar{t}$ Selection

After the event selection requirement in this analysis, the estimated backgrounds contribute to only up to 7% of the total estimated yields.

The background processes mimicking $t\bar{t}$ dilepton signature are significantly suppressed by the two identified lepton requirements and the at least one b-tagged jet requirement. The two measured lepton requirement suppresses multijet background processes (dominated by QCD, W+jets, $t\bar{t}$ single lepton and hadronic channels), while the ≥ 1 b-tagged jet requirement further rejects the Z boson production in association with jets to $< 0.5\%$ of the total estimated yields. The irreducible backgrounds are single top W-t production and the diboson (WW, WZ, ZZ) production, which the former has the largest contribution in total background. Misidentified (fake) leptons due to inefficiencies in the detector also contribute to a fraction (33% for ee, 15% for $\mu\mu$ and 23% for $e\mu$) of the total background.

In this analysis, both the Z+jets background and the fake leptons are estimated from the data. The single top Wt production and WW, WZ, ZZ diboson production are estimated from Monte-Carlo simulations.

6.1 Z+jets background

The Z+jets backgrounds in ee and $\mu\mu$ channels are estimated first from Monte-Carlo samples and then normalized to data using $Z \to ll$ events. A control region (CR) populated with Z events is defined, as shown in Figure 6.1, and a normalization factor is extracted in CR by requiring the invariant mass of the lepton pair within 10 GeV of m_Z and a lowered $E_{\mathrm{T}}^{\mathrm{miss}}$cut ($E_{\mathrm{T}}^{\mathrm{miss}} > 30$ GeV). This normalisation factor is then applied to MC Z+jets in signal region (SR) in the corresponding channel as follows:

$$N_{Z+jets} = \frac{Data(CR) - MC_{other}(CR)}{MC_{Z+jets}(CR)} \times MC_{Z+jets}(SR) \tag{6.1}$$

The normalization in the control region in ee and $\mu\mu$ channels are found to be 1.89(4) and 2.07(7) respectively. The control regions in m_{ll} and $E_{\mathrm{T}}^{\mathrm{miss}}$ before and after the normalization applied are shown in the Figures 6.2 and 6.3. The Z+jets background yields estimated with this procedure is shown in Table 6.1.

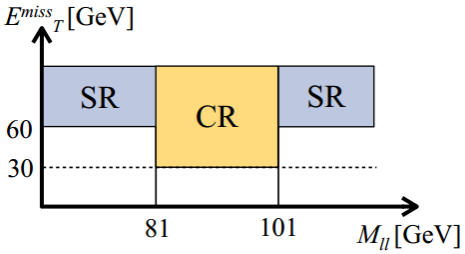

Figure 6.1: Definition of control region (CR) and signal region (SR) for estimating Z+jets background normalization. These regions are defined in ee and $\mu\mu$ channels.

The Z($\rightarrow \tau^+\tau^-$)+jets background and Z+jets background in the $e\mu$ channel is estimated from MC only.

The summary of Z+jets background estimates in ee, $\mu\mu$ and $e\mu$ channels are shown in Table 6.3.

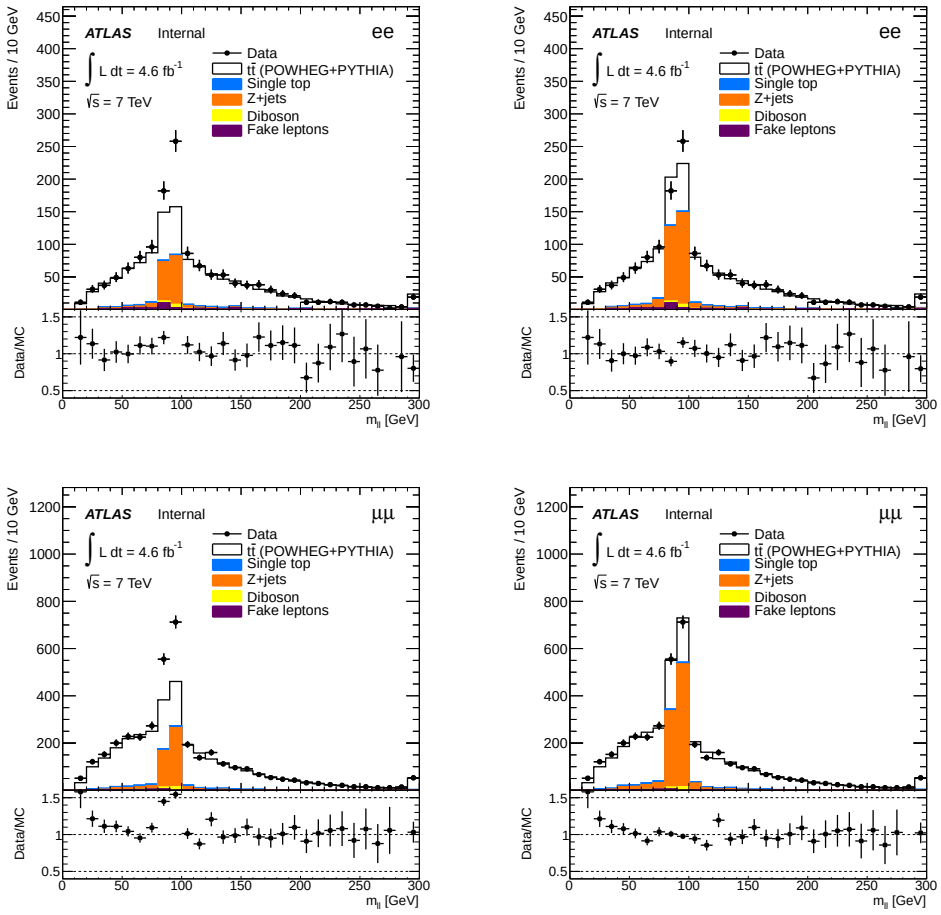

Figure 6.2: Dilepton invariant mass (m_{ll}) without (left) and with (right) data-driven Z+jets normalization applied in the ee (top) and $\mu\mu$ (bottom) channels in the control region (CR) with $E_{\mathrm{T}}^{\mathrm{miss}} > 30$ GeV. This analysis uses events in these channels with $E_{\mathrm{T}}^{\mathrm{miss}} > 60$ GeV and $|m_{ll} - m_Z| > 10$ GeV (where m_Z is 91 GeV).

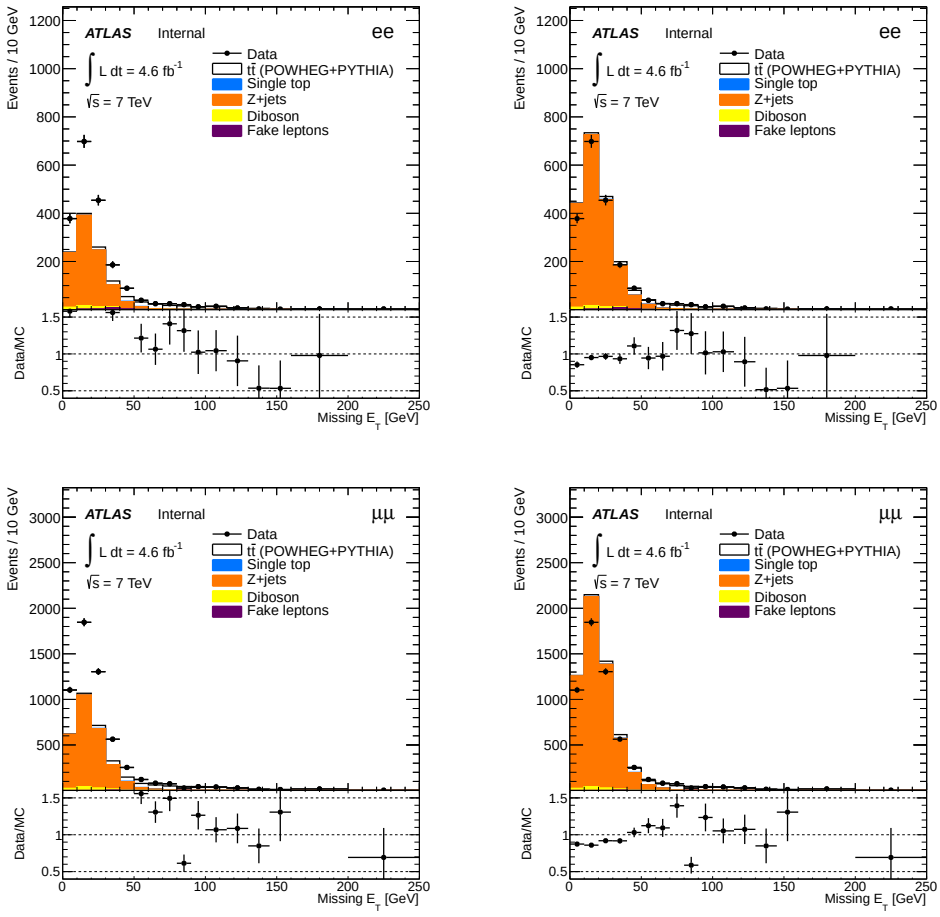

Figure 6.3: Missing transverse energy ($E_{\mathrm{T}}^{\mathrm{miss}}$) without (left) and with (right) data-driven Z+jets normalization applied in the ee (top) and $\mu\mu$ (bottom) channels in the control region (CR) with $|m_{ll} - m_Z| \leq 10$ GeV. This analysis uses events in these channels with $E_{\mathrm{T}}^{\mathrm{miss}} > 60$ GeV and $|m_{ll} - m_Z| > 10$ GeV (where m_Z is 91 GeV).

	ee	$\mu\mu$
Z($\rightarrow ee/\mu\mu$)+jets (Monte-Carlo)	1.1 $\pm$ 0.4(stat.) $\pm$ 0.6(syst.)	2.8 $\pm$ 0.8(stat.) $\pm$ 1.9(syst.)
Z($\rightarrow ee/\mu\mu$)+jets (Data-driven)	2.1 $\pm$ 0.7(stat.) $\pm$ 1.1(syst.)	5.8 $\pm$ 1.7(stat.) $\pm$ 4.0(syst.)

Table 6.1: Yields and uncertainties for Z+jets backgrounds in the ee and $\mu\mu$ channels. The systematic uncertainties include all object modelling 1-σ variations in the MC Z+jets samples.

6.2 Fake lepton background

The fake lepton background is evaluated in the dilepton channel from the data using a matrix method [38].

In the matrix method, two samples of events are selected using the loose and the tight lepton identification

requirements. The fractions (or the efficiencies) of the real (ε_{real}) and fake (ε_{fake}) loose leptons being selected as tight leptons are measured in the data. Z-boson decays to two leptons control samples are used to measure ε_{real}, while samples with control regions dominated by the fake leptons contributions are used to measure ε_{fake}. In the dilepton channel, contributions from QCD multijet processes, W+jets processes, other channels of $t\bar{t}$ and single top productions are included in this fake lepton estimation.

The estimated yield and uncertainties of the fake lepton events are shown in Figure 6.2. The total number of events in the loose di-lepton sample used to measure the real and fake efficiencies are included and broken down into the number of events with one loose (tight) lepton and another tight (loose) lepton and events with both leptons being tight (passing the standard lepton cuts).

Channel	Total	LL	LT	TL	TT	Fake leptons
ee	1002	79	192	204	527	12.2 ± 7.3
$\mu\mu$	1708	7	77	125	1499	11.4 ± 4.6
$e\mu$	5862	155	848	834	4025	50.2 ± 26.1

Table 6.2: Yields and uncertainties of fake lepton background events in the ee, $\mu\mu$ and $e\mu$ channels. The total events and events with loose-loose (LL), loose-tight (LT), tight-loose (TL), tight-tight (TT) di-lepton are shown in each channel. The uncertainties are derived from 1-σ variation of measured real and fake efficiencies.

6.3 Single top background

Single top W-t associated production has the same dilepton signature same as the $t\bar{t}$ dilepton decay channel. It also produces a b-jet that passes our nominal selection cuts with ≥ 1 b-tagged jets. Thus, W-t channel is the largest background in this analysis (more than half of the total background processes). The estimated uncertainties also include the scale uncertainty given by approximate NNLO calculations in W-t cross section [28]: $15.74^{+1.17}_{-1.21}$ pb. Therefore, k-factors of 1.07 and 0.92 are applied for the up and down scale variation of the normalization of W-t sample. The yield and estimated uncertainties are listed in Table 6.3.

6.4 Diboson background

The diboson production is a small background in this analysis (0.2% of the total estimated yields; $< 5\%$ of the total estimated backgrounds). The WW, WZ and ZZ processes are rejected due to the b-tagging requirement. The yield and estimated uncertainties are listed in Table 6.3.

6.5 Summary

The predicted signal process, the total background processes described above and the observed events in the dilepton (ee, $\mu\mu$ and $e\mu$) channels are summarized in Table 6.3.

	ee	$\mu\mu$	$e\mu$
$t\bar{t}$ (dilepton)	484.6±55.2	1 421.4±77.5	3 738.5±248.8
Single top	20.4±2.5	57.9±5.8	154.8±15.1
$Z(\rightarrow ee/\mu\mu)$+jets	2.1±0.9	5.8±4.3	0.2±0.2
$Z(\rightarrow \tau\tau)$+jets	0.4±0.3	2.6±1.2	5.8±1.2
Diboson	1.0±0.3	3.2±0.6	9.0±1.5
Fake leptons	12.2±7.4	11.4±4.7	50.2±26.1
Predicted	520.8±38.6	1 502.3±59.8	3 958.4±178.2
Observed	532	1509	4038

Table 6.3: Yields and uncertainties of expected $t\bar{t}$ signal and backgrounds compared to observed events, in the ee, $\mu\mu$ and $e\mu$ channels. All systematic uncertainties (except PDF uncertainties) are included.

Chapter 7

Reconstruction of $t\bar{t}$ System

7.1 Reconstruction method

The $t\bar{t}$ system cannot be fully solved (i.e. to obtain the 4-vectors of the two top quarks) easily in the dilepton channel due to the presence of the two neutrinos in the undetected missing energy. Therefore, we reconstruct an approximate $t\bar{t}$ system, using all measured $t\bar{t}$ dilepton decay objects: two jets, two leptons and $E_{\mathrm{T}}^{\mathrm{miss}}$, in the following. The measured $t\bar{t}$ system variable and is then unfolded to parton level using Monte Carlo generated $t\bar{t}$ system variable and the corresponding response matrix.

$$\begin{aligned} E &= E(l_1) + E(l_2) + E(j_1) + E(j_2) + E_T^{miss} \\ p_x &= p_x(l_1) + p_x(l_2) + p_x(j_1) + p_x(j_2) + E_x^{miss} \\ p_y &= p_y(l_1) + p_y(l_2) + p_y(j_1) + p_y(j_2) + E_y^{miss} \\ p_z &= p_z(l_1) + p_z(l_2) + p_z(j_1) + p_z(j_2) \end{aligned} \tag{7.1}$$

where (E, p_x, p_y, p_z) is the 4-momentum of the reconstructed $t\bar{t}$ system. The $t\bar{t}$ system variables $m_{t\bar{t}}$, $p_{\mathrm{T}}^{t\bar{t}}$ and $y_{t\bar{t}}$ are defined from the $t\bar{t}$ system 4-momentum as usual as:

$$m_{t\bar{t}} = \sqrt{E^2 - p^2} = \sqrt{E^2 - p_x^2 - p_y^2 - p_z^2} \tag{7.2}$$

$$p_{\mathrm{T}}^{t\bar{t}} = \sqrt{p_x^2 + p_y^2} \tag{7.3}$$

$$y_{t\bar{t}} = \frac{1}{2} ln \frac{E + p_z}{E - p_z} \tag{7.4}$$

This reconstructed $t\bar{t}$ system is an approximate one in the sense that the z-component of the neutrinos' energy is absent, due to the unmeasured "missing E_z" in the detector. This results in an overall shift towards below the true value for the $t\bar{t}$ system variables $m_{t\bar{t}}$ and $y_{t\bar{t}}$, which contains longitudinal information of the $t\bar{t}$

4-momentum. However, $p_{\mathrm{T}}^{t\bar{t}}$ is not affected by the longitudinal information and is thus a fully reconstructed variable. With a generally diagonal response matrix (meaning the reconstructed values are reasonably well correlated to the true values), the approximations in the reconstruction can be seen as an acceptance effect and can be corrected to the truth distribution by unfolding procedure.

An important factor that affects the quality of the reconstruction is whether the selected measured objects are originated from $t\bar{t}$ decay, or arise from objects recoiling against the $t\bar{t}$ system from the $t\bar{t}$ production at the vertex or initial-state radiations (ISR) or other multi-jet events. In the di-lepton channel, two jets are chosen in a way to best describe jets decayed from a $t\bar{t}$ event. A jet selection algorithm applied previously in this analysis,

- two highest p_{T} b-tagged jets when available or one b-tagged jet and one highest p_{T} untagged jet for events with only one b-tagged jet (p_{T}-*based* algorithm)

is found to be selecting a significant number of jets not associated with b-quarks from $t\bar{t}$, and thus resulting in an inaccurate reconstructed $t\bar{t}$ system. The current jet selection criteria is:

- two jets with the highest MV1 weights (*MV1-based* algorithm)

This criteria is seen to give the best recontruction of the $t\bar{t}$ system. It also shows a higher purity of selected $t\bar{t}$-jets than the p_{T}-based algorithm. The study and comparison of the jet selection algorithms are described in Section 7.2.

It should be noted that in this $t\bar{t}$ reconstruction and jet selection criteria, if there is a gluon radiation from one of the b-quarks in the final state, this will not be considered part of the $t\bar{t}$ system, even though it contains part of the $t\bar{t}$ 4-momentum. Ideally, one would include final-state radiations (FSR) into the reconstructed $t\bar{t}$ system but not ISR, but this is difficult to do and thus practically, all the other jets (but the two carrying most of the b-quark momenta) are excluded.

7.2 Jet selection algorithm study

The two selection algorithms mentioned above are studied using $t\bar{t}$ Monte-Carlo sample and the jet selection efficiencies from each case are compared. The $t\bar{t}$ jet purity is defined as

$$\text{jet purity} = \frac{N_{\text{correct jets}}}{N_{\text{selected jets}}} \tag{7.5}$$

where $N_{\text{correct jets}}$ are jets originated from b-quarks of the top decay and are assigned using the `jet_trueflav` variable (`jet_trueflav==5` indicates a jet is matched to b-quarks).

In both algorithms, the first selected jet correctly matches with b-quarks almost all the time (98.7% for p_{T}-based selection and 99.1% for MV1-based selection in ee events). While for the second jet, the MV1-based selection has a 2-3% higher $t\bar{t}$ jet purity than the p_{T}-based selection (68.0% for p_{T}-based selection and 71.6% for MV1-based selection in ee events). The values of $t\bar{t}$ jet purity are similar in the ee, $\mu\mu$ and $e\mu$ channels.

The migration matrix of $p_{\mathrm{T}}^{t\bar{t}}$ in both cases is also compared, in Figure 7.1. It is seen that the MV1-based algorithm of selecting jets gives a more diagonal migration matrix of $p_{\mathrm{T}}^{t\bar{t}}$, which indicates a more accurate reconstruction of the $t\bar{t}$ system.

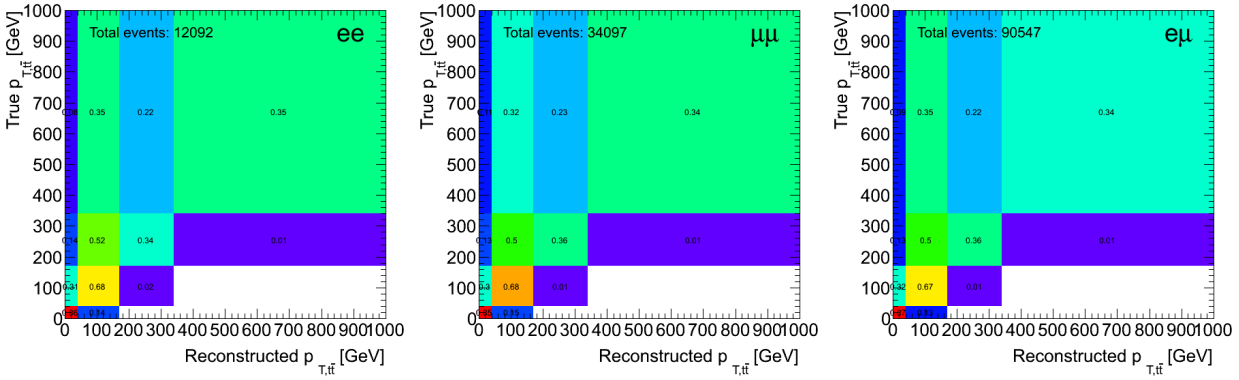

(a) p_{T}-based jet selection

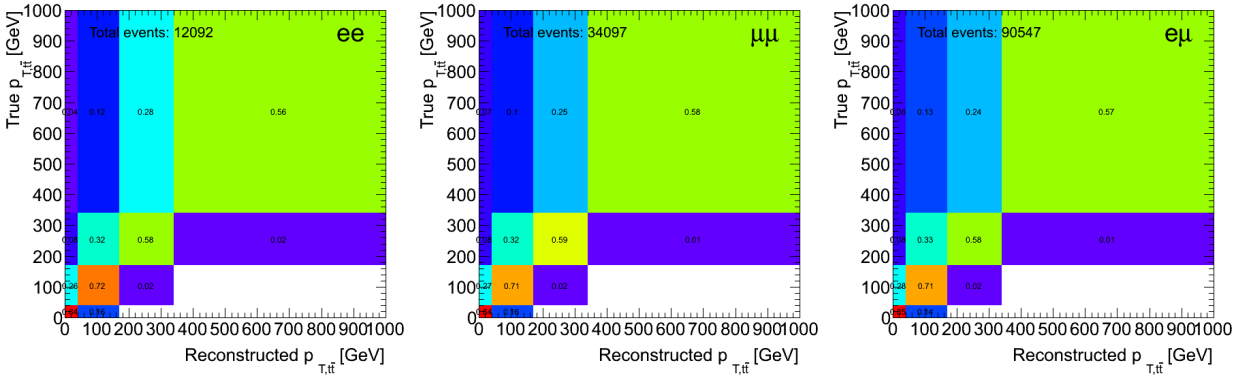

(b) MV1-based jet selection

Figure 7.1: Migration matrix of $p_{\mathrm{T}}^{t\bar{t}}$ in p_{T}-based 7.1a and MV1-based 7.1b algorithms of jet selection. Both cases use the same standard dilepton events with at least 1 b-tagged jets.

7.3 An optimised event selection based on the invariant mass of a jet and a lepton

An additional event selection cut based on jet-lepton invariant mass is chosen to be applied in this analysis. The effect and the optimisation of the cut is discussed in this section.

Kinematically, the invariant mass of all decayed products of the top quark is constrained by the top quark mass at particle level. In the dilepton channel, specifically, the invariant mass of a selected jet and the lepton must be lower than the top quark mass within detector resolution ($x_{jl} \equiv m_{jl}/m_{top} < 1$). An "incorrect" jet selection may result in a jet-lepton mass higher than the m_{top}.

From the jet selection algorithm study above, the second selected jet (either ordering by p_{T} or MV1-weight) is incorrect for about 30% of the time (the first selected jet is almost always correct/originated from b-quark). Figure 7.2 shows the 2D histograms of the jet-lepton invariant mass using the second selected (sub-leading MV1-weight) jet paired with the negatively charged lepton (m_{jl^-}) versus the jet-lepton invariant mass using the *same* selected jet paired with the positively charged lepton (m_{jl^+}). The difference of the pattern of this plot using the correct and incorrect jets show discriminating power against events with unwanted jets, and suggest a possible cut on ($m_{jl^-} < m_{jl}^{cut}$ OR $m_{jl^+} < m_{jl}^{cut}$) to increase $t\bar{t}$ jet purity of the event sample.

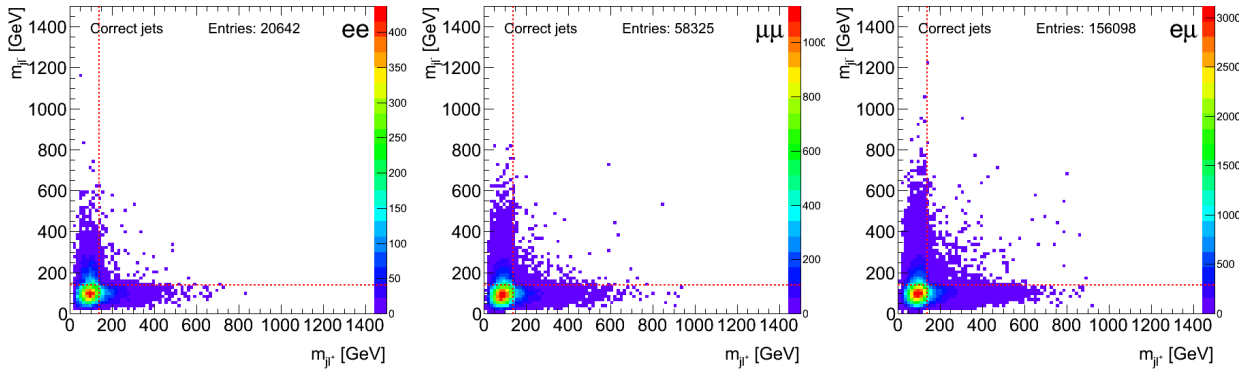

(a) Correct jets (jets matched to b-quarks)

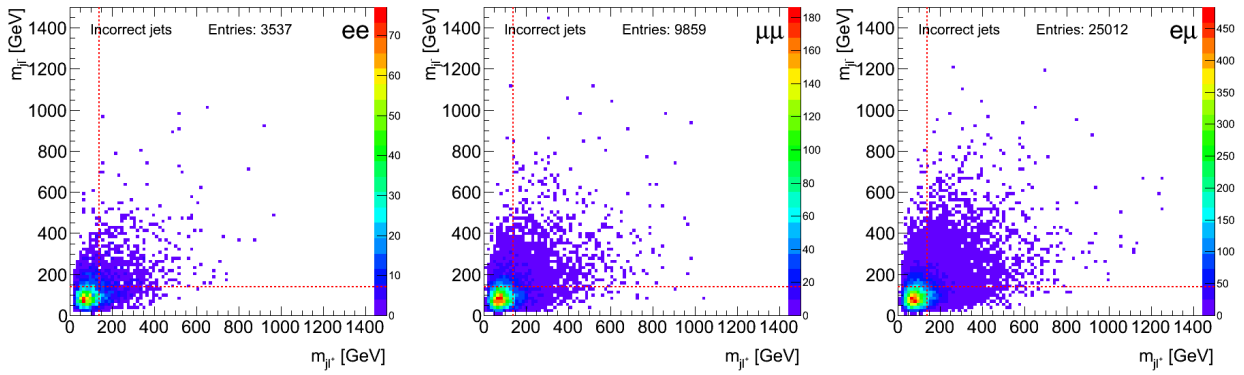

(b) Incorrect jets (jets not matched to b-quarks)

Figure 7.2: m_{jl^-} vs m_{jl^+} using the second highest MV1 jet. The top (bottom) plot uses the jets (not) matched with b-quarks. The red dotted line indicates the $x_{jl} = m_{jl}/172.5$ GeV < 0.8 cut as used in the analysis to reject events picking up wrong jets. The total number of events is the sum of events from the two plots.

An optimisation study for the use of a jet-lepton mass cut is done by evaluating the balance between the $t\bar{t}$ jet purity and event selection efficiency. Cut values x_{jl}^{cut} at $x_{jl} = 0.2$ to 6.0 on the second selected jet are studied at reconstructed level. The $t\bar{t}$ jet purity for both selected jets is found to be maximum at x_{lj} cut of 0.8 (87.1%), with an event selection efficiency of 92.7% (in the ee channel). Figure 7.3 shows the effect on m_{jl} and the $t\bar{t}$ jet purity after applying the selection $x_{jl^-} < 0.8$ OR $x_{jl^+} < 0.8$ (where j is the second jet) from the at-least-1-btagged sample with MV1-based jet selection. The effect of this cut is also reflected in a more diagonal migration matrix of $p_{\mathrm{T}}^{t\bar{t}}$ and is shown in figure 7.4 (c.f. migration matrix of $p_{\mathrm{T}}^{t\bar{t}}$ before this cut in Figure 7.1b). The increase in the probability of the diagonal element for the last (second last) $p_{\mathrm{T}}^{t\bar{t}}$ bin is about 14% (10%), across the ee, $\mu\mu$ and $e\mu$ channels. The effect of this cut significantly improves the resolutions on $t\bar{t}$ kinematic variables $m_{t\bar{t}}$, $p_{\mathrm{T}}^{t\bar{t}}$, $y_{t\bar{t}}$ and $|y_{t\bar{t}}|$, as will be shown in section 7.4.1.

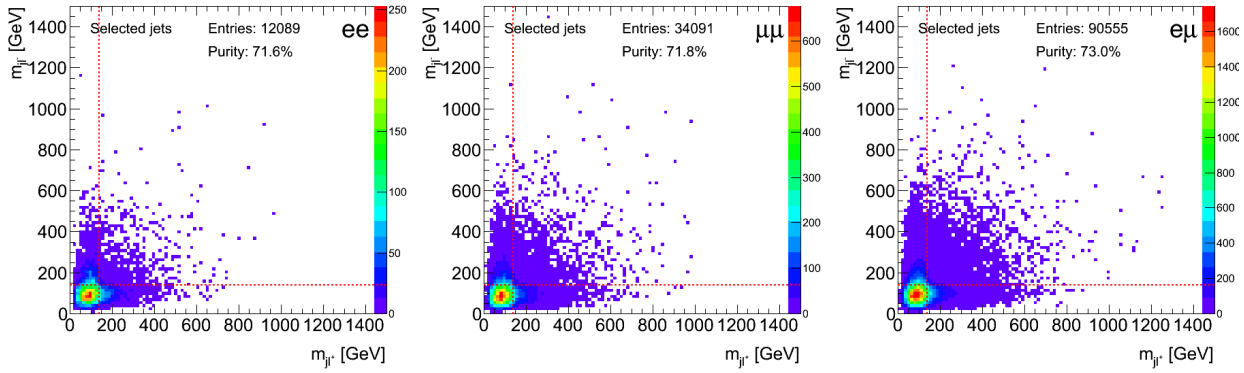

(a) Before $m_{l^+j}/172.5$ GeV < 0.8 OR $m_{l^-j}/172.5$ GeV < 0.8 cut on event selection

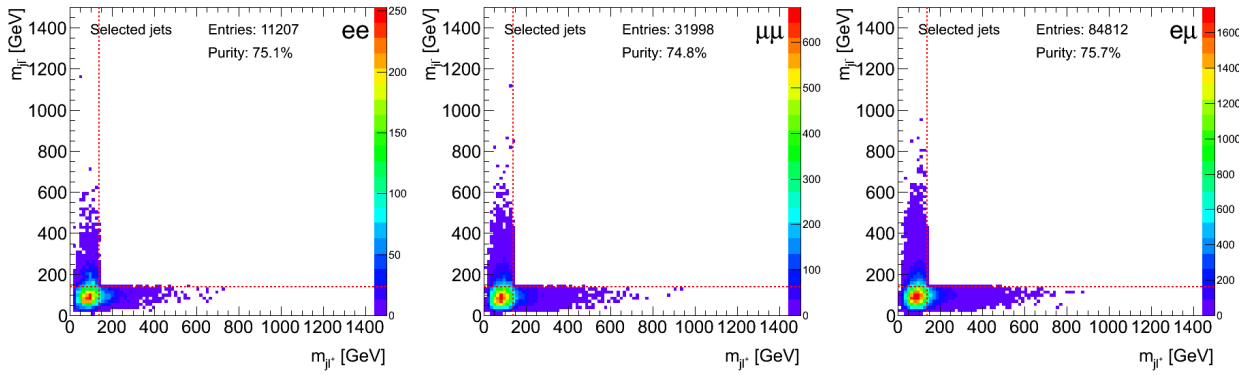

(b) After $m_{l^+j}/172.5$ GeV < 0.8 OR $m_{l^-j}/172.5$ GeV < 0.8 cut on event selection

Figure 7.3: m_{jl^-} vs m_{jl^+} and $t\bar{t}$ jet purity of the second selected jet in the MV1-based selection algorithm. The top (bottom) plot is before (after) applying the $m_{l^+j}/172.5$ GeV < 0.8 OR $m_{l^-j}/172.5$ GeV < 0.8 event selection, where j is the second selected jet. The red dotted line indicates the $x_{jl} = m_{jl}/172.5$ GeV < 0.8 cut as used in the analysis to reject events picking up wrong jets. The $t\bar{t}$ jet purity changes from 71.6% to 75.1% after applying the selection.

We apply this cut and require a final selection of dilepton events with $x_{jl^-} < 0.8$ OR $x_{jl^+} < 0.8$, where j

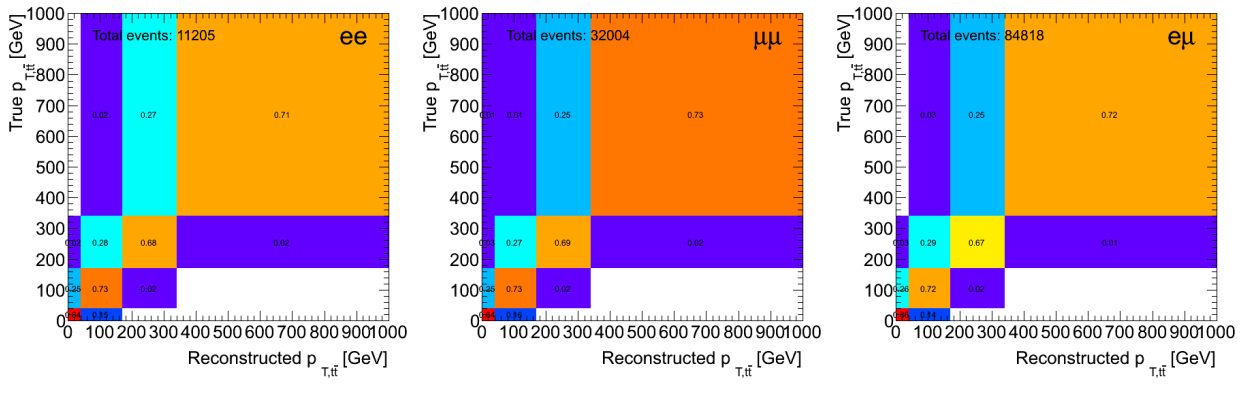

Figure 7.4: Migration matrix of $p_{\mathrm{T}}^{t\bar{t}}$ in MV1-based algorithms of jet selection in the ee (left), $\mu\mu$ (center) and $e\mu$ (right) channels, after an event selection of $m_{l^+j}/172.5$ GeV < 0.8 OR $m_{l^-j}/172.5$ GeV < 0.8, where j is the second selected jet.

is the sub-leading MV1-weight jet and $x_{jl} \equiv m_{jl}/m_{top}$ with $m_{top} = 172.5$ GeV, to increase the purity of the measured objects for a more accurate reconstruction of the $t\bar{t}$ system. By applying this selection, it is seen that there is improvement in the resolution of the $t\bar{t}$ system variables and the total systematic uncertainties (which is associated with the migration matrix and unfolding) are reduced.

When considering the kinematic constraint $m_{jl}/m_{top} < 1$, one may also consider defining a cut m_{jl}^{cut} on both m_{jl^-} and m_{jl^+} ($m_{jl^-} < m_{jl}^{cut}$ AND $m_{jl^+} < m_{jl}^{cut}$) instead of an "OR" cut to reject unwanted events. This cut should also have a high rejection power on the events with a wrong second jet. Figure 7.2 shows that events in all but the bottom left quadrant (defined by $x_{jl} = m_{jl}/m_{top} < 0.8$ with the red dotted lines) are rejected by this cut. However, in Figure 7.2 the rejected regions in fact have the best discriminating power between events with correct second jet assignment and events with the wrong second jet assignment. This cut would therefore overkill some good events. Futhermore, rejecting events in the high mass regions (the bottom right and top left regions in each plot in Figure 7.2) would also suppress events with high $m_{t\bar{t}}$, a main region of interest in our measurement.

The final selection of jets and events for the reconstruction of $t\bar{t}$ system is therefore chosen to be 2 leading-MV1 jets with $x_{jl^-} < 0.8$ OR $x_{jl^+} < 0.8$ event cut on the second selected jet in this analysis.

7.4 Resolution and binning

7.4.1 Resolution

A properly determined binning can give physically useful results and avoid large statistical fluctuations in each bin. The binnings of $X_{t\bar{t}}$ ($X_{t\bar{t}} = m_{t\bar{t}}$, $p_{\mathrm{T}}^{t\bar{t}}$ or $y_{t\bar{t}}$) are chosen by considering the resolutions and the statistics in each bin of the reconstructed variables. The resolution of each $X_{t\bar{t}}$ is shown in Figure 7.5. The resolutions are estimated from Monte Carlo $t\bar{t}$ POWHEG +PYTHIA 117050 sample by comparing the reconstructed variables with the generated ones. The RMS value of the difference between the reconstructed and the generated $X_{t\bar{t}}$ in an arbitrarily chosen bin is then fitted with a 2nd-order polynomial function and provides an estimation of the resolution and thus the bin size. The bin sizes are primarily chosen to be the same as the resolution at the bin centers, while in bins where the data statistics are small (less than 10 events in the most populated channel), those bins are merged. A common binning is chosen for all dilepton ee, $\mu\mu$ and $e\mu$ channels for each $t\bar{t}$ variable.

Resolutions in different algorithms (jet selection, event selection) of each $t\bar{t}$ system variable are compared and summarized in Figure 7.6. The jet and event selection algorithms used in this comparison are:

- 2 leading-p_{T} jets
- 2 btag jets or 1 btag jet+leading-p_{T} jet (used in pre-approval study)
- 2 leading-MV1 jets
- 2 leading-MV1 jets with $x_{jl^-} < 0.8$ OR $x_{jl^+} < 0.8$ event cut on the second selected jet (used in current analysis)

The last criteria (the selection requirement for $t\bar{t}$ events used in this analysis), using both MV1-based jet selection and jet-lepton mass event cut, shows the best resolutions in all $t\bar{t}$ system variables in comparision to the other requirements listed above.

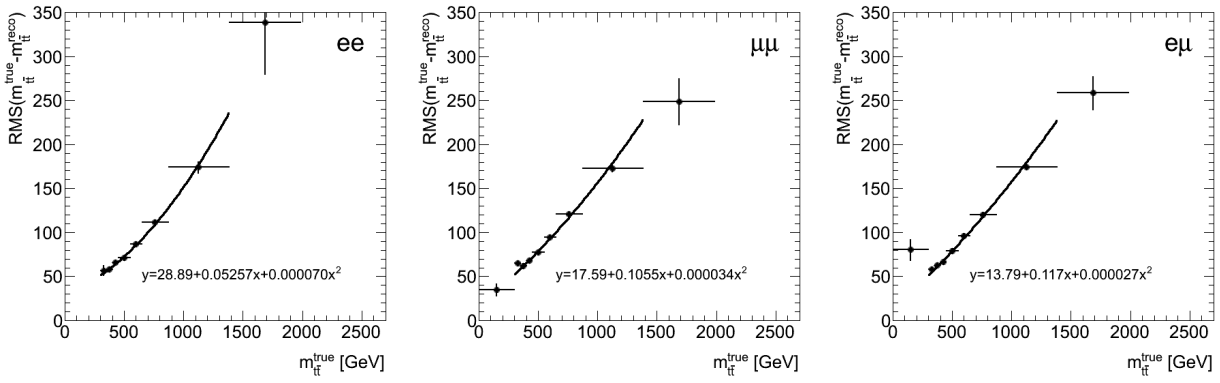

(a) $m_{t\bar{t}}$

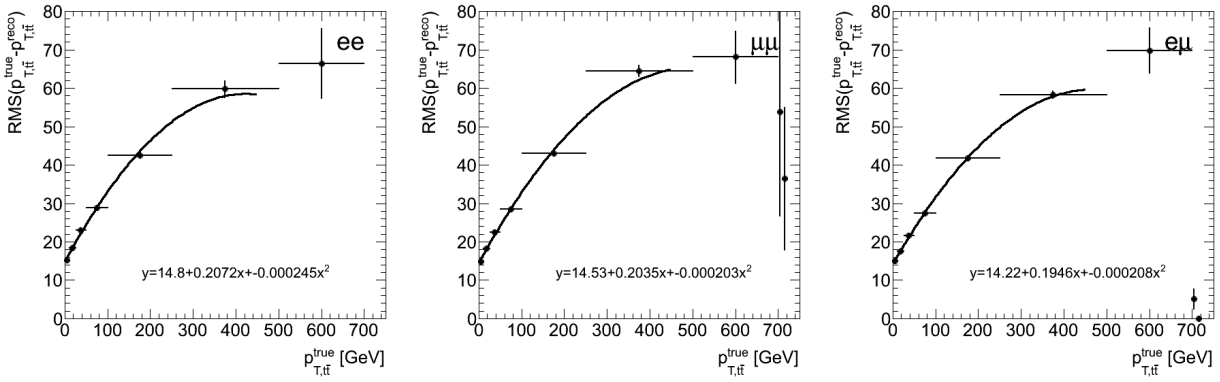

(b) $p_{\mathrm{T}}^{t\bar{t}}$

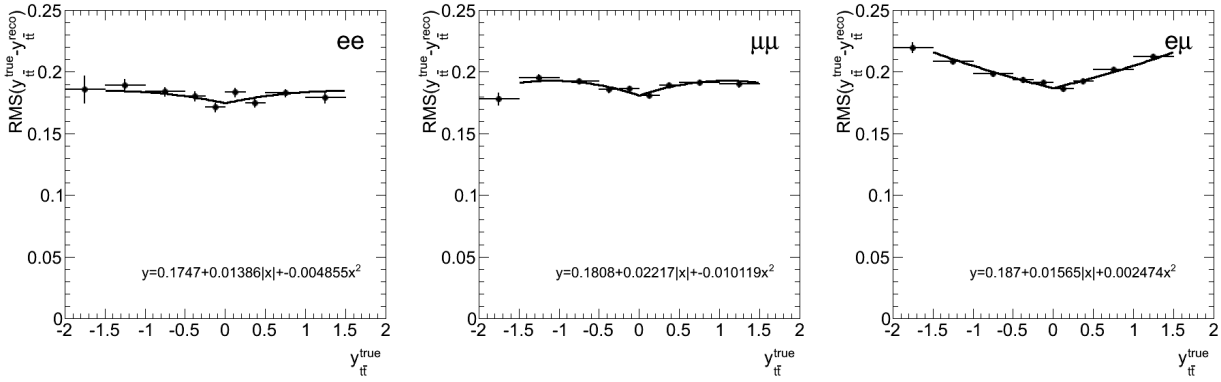

(c) $y_{t\bar{t}}$

Figure 7.5: Resolutions of (a)$m_{t\bar{t}}$, (b)$p_{\mathrm{T}}^{t\bar{t}}$ and (c)$y_{t\bar{t}}$ in ee (left), $\mu\mu$ (center) and $e\mu$ (right) channels.

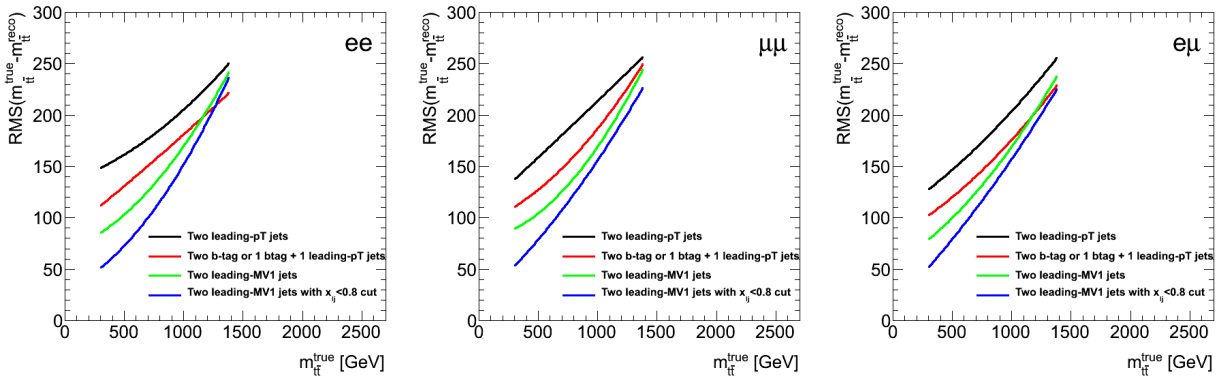

(a) $m_{t\bar{t}}$

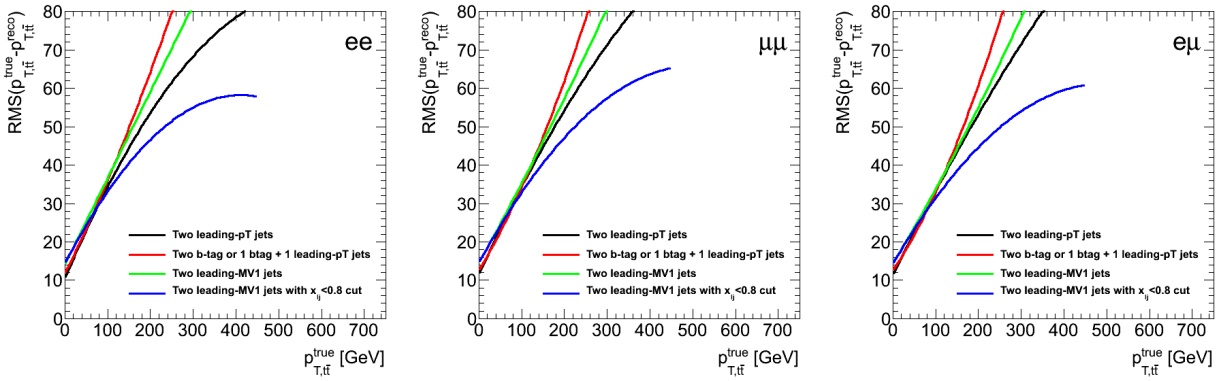

(b) $p_{\mathrm{T}}^{t\bar{t}}$

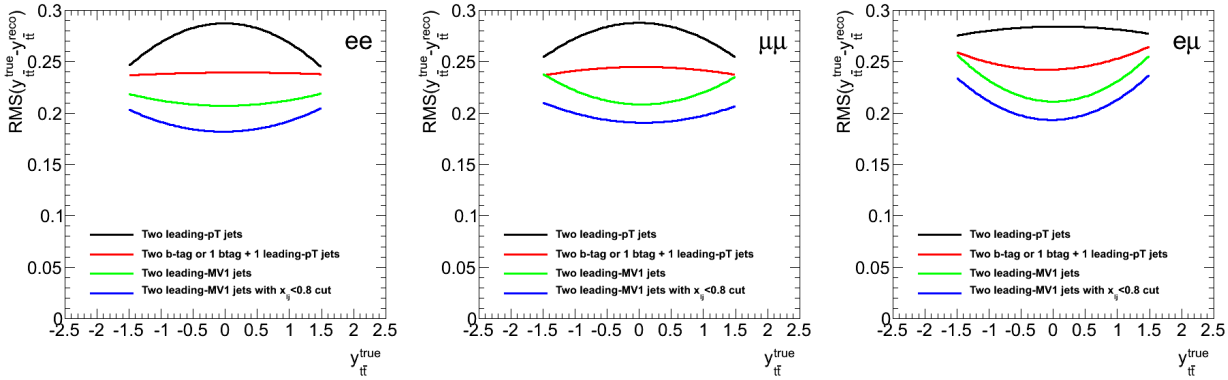

(c) $y_{t\bar{t}}$

Figure 7.6: Resolution of (a)$m_{t\bar{t}}$, (b)$p_{\mathrm{T}}^{t\bar{t}}$ and (c)$y_{t\bar{t}}$ with respect to different jet selection algorithms.

7.4.2 Binning

For the purpose of comparison, the results in this analysis are given in the binnings used by the lepton+jets measurement [22], as shown in Table 7.1. The resolutions in the dilepton channel in all $t\bar{t}$ system variables are found to be either at similar level or smaller than the ones estimated in the lepton+jets channel.

	$m_{t\bar{t}}$ [GeV]	
Bin	Bin range	Bin width
1	0 - 250	250
2	250 - 450	200
3	450 - 550	100
4	550 - 700	150
5	700 - 950	250
6	950 - 2700	1750

(a) $m_{t\bar{t}}$

	$p_{\mathrm{T}}^{t\bar{t}}$ [GeV]	
Bin	Bin range	Bin width
1	0 - 40	40
2	40 - 170	130
3	170 - 340	170
4	340 - 1000	660

(b) $p_{\mathrm{T}}^{t\bar{t}}$

	$y_{t\bar{t}}$	
Bin	Bin range	Bin width
1	-2.5 - -1.0	1.5
2	-1.0 - -0.5	0.5
3	-0.5 - 0	0.5
4	0 - 0.5	0.5
5	0.5 - 1.0	0.5
6	1.0 - 2.5	1.5

(c) $y_{t\bar{t}}$

	$\lvert y_{t\bar{t}} \rvert$	
Bin	Bin range	Bin width
1	0 - 0.5	0.5
2	0.5 - 1.0	0.5
3	1.0 - 2.5	1.5

(d) $|y_{t\bar{t}}|$

Table 7.1: Binnings of (a)$m_{t\bar{t}}$, (b)$p_{\mathrm{T}}^{t\bar{t}}$, (c)$y_{t\bar{t}}$ and (d)$|y_{t\bar{t}}|$ applied in this analysis. The same binnings are used in the lepton+jets analysis [22].

7.5 Data/MC comparison of $t\bar{t}$ system kinematic variables

Using the reconstruction method, jet selection algorithm and additional event selection, together with the binning choice described above, the reconstructed $t\bar{t}$ system kinematic variables $m_{t\bar{t}}$, $p_{\mathrm{T}}^{t\bar{t}}$, $y_{t\bar{t}}$ and $|y_{t\bar{t}}|$ are measured and shown in Figures 7.7 and 7.8. Tables 7.2, 7.3, 7.4 and 7.5 summarize the total and individual yields for the data, estimated backgrounds and signal for each of $t\bar{t}$ system variables in measurement in each of the dilepton channels, at the reconstructed level (i.e. before unfolding). The uncertainty band in the figures includes all systematic uncertainties except $t\bar{t}$ modelling uncertainties; the uncertainty in the tables includes all systematic uncertainties except PDF uncertainties. The systematic uncertainties considered in this analysis is described in chapter 9.

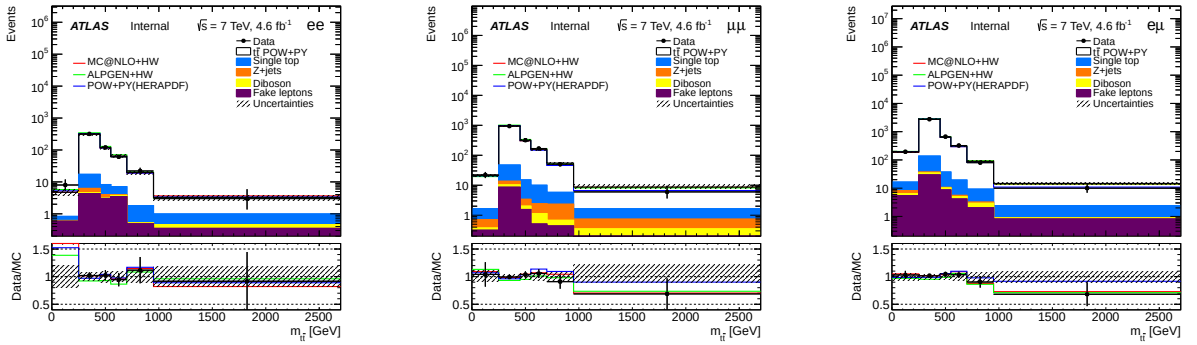

(a) $m_{t\bar{t}}$

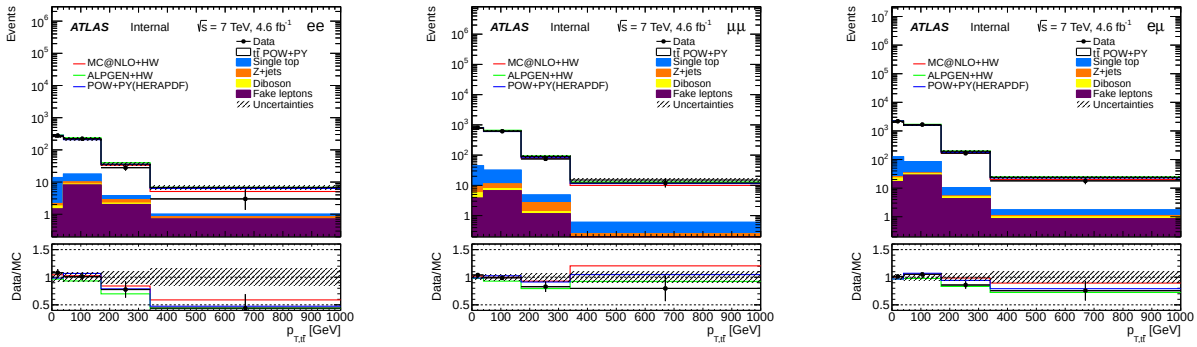

(b) $p_{\mathrm{T}}^{t\bar{t}}$

Figure 7.7: Reconstructed (a)$m_{t\bar{t}}$ and (b)$p_{\mathrm{T}}^{t\bar{t}}$ in the ee (left), $\mu\mu$ (center) and $e\mu$ (right) channels. The error band includes all systematic uncertainties except $t\bar{t}$ modeling uncertainties. Simulated $t\bar{t}$ samples are normalized to NNLO+NNLL calculations.

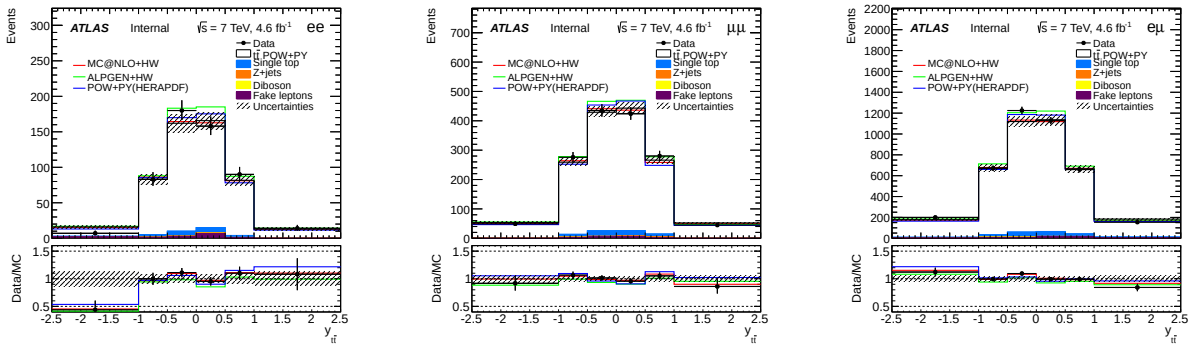

(a) $y_{t\bar{t}}$

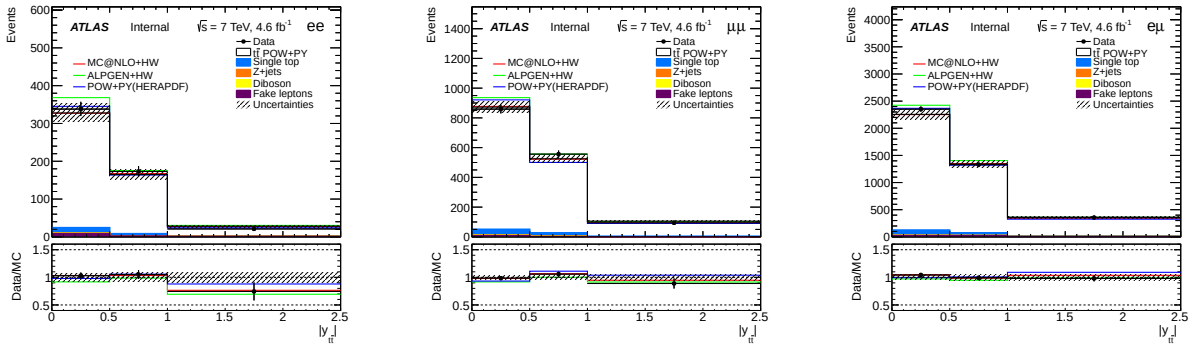

(b) $|y_{t\bar{t}}|$

Figure 7.8: Reconstructed (a)$y_{t\bar{t}}$ and (b)$|y_{t\bar{t}}|$ in the ee (left), $\mu\mu$ (center) and $e\mu$ (right) channels. The error band includes all systematic uncertainties except $t\bar{t}$ modeling uncertainties. Simulated $t\bar{t}$ samples are normalized to NNLO+NNLL calculations.

$m_{t\bar{t}}$ (ee)	Bins [GeV]					
	0-250	250-450	450-550	550-700	700-950	950-2700
$t\bar{t}$ (dilepton)	3.90±1.43	294.24±33.64	108.85±14.67	57.44±9.45	17.89±3.42	2.29±1.26
$Z(\to ee/\mu\mu)$+jets	0.00±0.00	1.34±0.69	0.80±0.58	0.00±0.19	0.00±0.00	0.00±0.00
$Z(\to \tau\tau)$+jets	0.00±0.00	0.26±0.30	0.00±0.00	0.17±0.15	0.00±0.00	0.00±0.00
Single top	0.21±0.11	10.97±1.27	4.25±0.68	3.13±0.50	1.29±0.22	0.53±0.13
Diboson	0.03±0.03	0.36±0.17	0.18±0.29	0.31±0.16	0.03±0.08	0.11±0.11
Fake leptons	0.59±0.45	4.26±5.21	3.03±2.05	3.45±2.47	0.49±0.36	0.35±0.34
Predicted	4.73±0.92	311.44±21.91	117.12±10.97	64.50±5.98	19.69±2.16	3.27±0.58
Observed	8	318	120	61	22	3

(a) $m_{t\bar{t}}$, ee channel

$m_{t\bar{t}}$ ($\mu\mu$)	Bins [GeV]					
	0-250	250-450	450-550	550-700	700-950	950-2700
$t\bar{t}$ (dilepton)	19.51±3.29	903.30±45.82	293.18±28.57	149.07±16.29	49.20±9.91	7.09±1.83
$Z(\to ee/\mu\mu)$+jets	0.22±0.33	2.17±2.15	0.82±0.93	0.87±0.69	1.46±1.21	0.23±1.01
$Z(\to \tau\tau)$+jets	0.12±0.13	1.16±0.89	0.57±0.51	0.37±0.30	0.18±0.20	0.16±0.15
Single top	0.93±0.21	33.43±3.33	11.62±1.29	7.58±0.94	3.47±0.45	0.90±0.18
Diboson	0.06±0.08	1.62±0.30	0.44±0.31	0.63±0.22	0.24±0.15	0.24±0.14
Fake leptons	0.31±0.10	8.54±2.93	1.55±1.16	0.51±0.56	0.44±0.14	0.10±0.03
Predicted	21.15±2.17	950.21±35.11	308.17±17.81	159.02±10.49	54.98±3.85	8.72±1.45
Observed	22	943	320	168	50	6

(b) $m_{t\bar{t}}$, $\mu\mu$ channel

$m_{t\bar{t}}$ ($e\mu$)	Bins [GeV]					
	0-250	250-450	450-550	550-700	700-950	950-2700
$t\bar{t}$ (dilepton)	171.88±16.35	2584.22±158.05	597.90±69.85	292.76±43.48	79.50±8.98	12.27±3.41
$Z(\to ee/\mu\mu)$+jets	0.20±0.16	0.00±0.00	0.00±0.00	0.00±0.00	0.00±0.00	0.00±0.00
$Z(\to \tau\tau)$+jets	1.67±0.53	2.78±0.92	0.56±0.37	0.47±0.30	0.28±0.19	0.00±0.00
Single top	8.17±0.79	98.92±9.59	26.41±2.61	13.73±1.72	6.01±0.78	1.54±0.23
Diboson	0.86±0.21	4.75±0.85	1.44±0.47	0.95±0.26	0.88±0.25	0.07±0.08
Fake leptons	5.40±2.90	29.28±17.86	8.61±4.55	4.11±2.41	2.01±1.55	0.80±0.59
Predicted	188.18±12.07	2719.96±120.75	634.91±36.41	312.02±19.98	88.68±7.26	14.68±1.52
Observed	194	2766	665	323	80	10

(c) $m_{t\bar{t}}$, $e\mu$ channel

Table 7.2: Yields of selected events expected $m_{t\bar{t}}$ (at the reconstructed level) signal and backgrounds compared to observed selected events, in the ee, $\mu\mu$ and $e\mu$ channels. Background yields are broken down into each background process. Systematic uncertainties except PDF uncertainties are included. The binning is the same as in the unfolded results.

$p_{\mathrm{T}}^{t\bar{t}}$ (ee)	Bins [GeV]			
	0-40	40-170	170-340	340-1000
$t\bar{t}$ (dilepton)	244.32±37.49	202.25±23.36	32.22±6.13	5.82±2.56
$Z(\rightarrow ee/\mu\mu)$+jets	0.38±0.32	1.28±0.67	0.36±0.32	0.12±0.20
$Z(\rightarrow \tau\tau)$+jets	0.00±0.00	0.17±0.28	0.26±0.18	0.00±0.00
Single top	11.67±1.37	7.53±1.12	1.00±0.25	0.17±0.06
Diboson	0.32±0.24	0.53±0.18	0.18±0.10	0.00±0.04
Fake leptons	1.45±5.09	8.01±4.69	2.01±1.38	0.71±0.58
Predicted	258.15±38.37	219.76±22.91	36.02±6.32	6.82±2.58
Observed	279	222	28	3

(a) $p_{\mathrm{T}}^{t\bar{t}}$, ee channel

$p_{\mathrm{T}}^{t\bar{t}}$ ($\mu\mu$)	Bins [GeV]			
	0-40	40-170	170-340	340-1000
$t\bar{t}$ (dilepton)	728.74±74.06	592.43±43.83	85.73±13.98	14.45±6.88
$Z(\rightarrow ee/\mu\mu)$+jets	2.31±2.03	2.15±2.84	1.13±0.64	0.18±0.29
$Z(\rightarrow \tau\tau)$+jets	1.08±0.76	1.24±0.70	0.23±0.19	0.00±0.00
Single top	35.01±3.19	20.50±2.78	2.07±0.48	0.35±0.08
Diboson	1.85±0.36	1.10±0.39	0.19±0.09	0.07±0.05
Fake leptons	3.75±1.66	6.58±2.49	1.14±0.46	0.00±0.08
Predicted	772.74±75.62	624.00±39.20	90.50±13.60	15.05±6.89
Observed	804	618	75	12

(b) $p_{\mathrm{T}}^{t\bar{t}}$, $\mu\mu$ channel

$p_{\mathrm{T}}^{t\bar{t}}$ ($e\mu$)	Bins [GeV]			
	0-40	40-170	170-340	340-1000
$t\bar{t}$ (dilepton)	2032.95±223.61	1500.58±101.15	182.93±31.95	22.07±6.36
$Z(\rightarrow ee/\mu\mu)$+jets	0.20±0.16	0.00±0.00	0.00±0.00	0.00±0.00
$Z(\rightarrow \tau\tau)$+jets	2.89±0.99	2.36±0.78	0.38±0.24	0.13±0.15
Single top	98.48±9.18	50.59±6.25	5.08±0.71	0.63±0.14
Diboson	5.25±0.87	3.00±0.71	0.58±0.17	0.13±0.08
Fake leptons	16.90±15.05	28.19±13.80	4.29±2.80	0.85±0.60
Predicted	2156.68±226.94	1584.71±97.19	193.25±31.66	23.80±6.21
Observed	2187	1667	166	18

(c) $p_{\mathrm{T}}^{t\bar{t}}$, $e\mu$ channel

Table 7.3: Yields of selected events expected $p_{\mathrm{T}}^{t\bar{t}}$ (at the reconstructed level) signal and backgrounds compared to observed selected events, in the ee, $\mu\mu$ and $e\mu$ channels. Background yields are broken down into each background process. Systematic uncertainties except PDF uncertainties are included. The binning is the same as in the unfolded results.

$y_{t\bar{t}}$ (ee)	Bins					
	-2.5–1.0	-1.0–0.5	-0.5-0.0	0.0-0.5	0.5-1.0	1.0-2.5
$t\bar{t}$ (dilepton)	13.22±3.01	78.12±9.22	152.17±17.21	150.85±20.97	77.80±11.85	12.44±2.34
$Z(\to ee/\mu\mu)$+jets	0.36±0.47	0.46±0.33	0.19±0.21	0.84±0.85	0.30±0.54	0.00±0.00
$Z(\to \tau\tau)$+jets	0.00±0.00	0.00±0.00	0.26±0.18	0.00±0.24	0.17±0.15	0.00±0.00
Single top	0.39±0.11	3.04±0.47	6.44±0.94	7.24±0.93	2.76±0.36	0.50±0.12
Diboson	0.07±0.06	0.14±0.08	0.27±0.18	0.52±0.17	0.03±0.04	0.00±0.03
Fake leptons	1.91±1.59	1.34±1.33	2.70±2.61	6.31±3.70	0.62±2.00	0.00±1.02
Predicted	15.96±3.43	83.11±9.47	162.03±17.32	165.75±21.41	81.68±12.02	12.94±2.55
Observed	7	83	180	158	90	14

(a) $y_{t\bar{t}}$, ee channel

$y_{t\bar{t}}$ ($\mu\mu$)	Bins					
	-2.5–1.0	-1.0–0.5	-0.5-0.0	0.0-0.5	0.5-1.0	1.0-2.5
$t\bar{t}$ (dilepton)	51.25±5.86	245.94±20.13	403.92±26.93	417.70±23.67	251.83±17.27	50.70±5.29
$Z(\to ee/\mu\mu)$+jets	0.69±1.17	0.45±0.57	0.89±0.87	0.76±1.27	2.98±2.36	0.00±0.68
$Z(\to \tau\tau)$+jets	0.00±0.00	0.70±0.53	0.11±0.14	1.32±0.62	0.16±0.24	0.27±0.26
Single top	1.39±0.41	9.23±1.02	18.59±1.93	17.88±1.77	9.53±1.12	1.31±0.35
Diboson	0.10±0.10	0.90±0.31	1.02±0.27	0.73±0.22	0.44±0.20	0.03±0.03
Fake leptons	0.00±0.54	1.84±0.93	4.52±1.34	4.74±1.45	1.07±1.07	0.00±0.34
Predicted	53.43±6.26	259.07±20.35	429.04±26.03	443.14±23.63	266.01±17.76	52.31±5.38
Observed	49	276	435	424	280	45

(b) $y_{t\bar{t}}$, $\mu\mu$ channel

$y_{t\bar{t}}$ ($e\mu$)	Bins					
	-2.5–1.0	-1.0–0.5	-0.5-0.0	0.0-0.5	0.5-1.0	1.0-2.5
$t\bar{t}$ (dilepton)	169.42±17.90	639.04±49.63	1060.84±64.05	1072.01±72.09	624.40±44.16	172.82±21.30
$Z(\to ee/\mu\mu)$+jets	0.00±0.00	0.00±0.00	0.00±0.00	0.00±0.00	0.20±0.16	0.00±0.00
$Z(\to \tau\tau)$+jets	0.26±0.22	0.55±0.28	1.46±0.63	1.59±0.58	0.94±0.48	0.97±0.46
Single top	5.80±0.76	25.02±2.51	46.69±4.75	47.15±4.48	24.41±2.45	5.70±0.64
Diboson	0.51±0.24	2.28±0.47	2.55±0.44	1.68±0.38	1.49±0.39	0.45±0.16
Fake leptons	2.34±1.34	7.50±4.15	7.77±8.77	14.17±7.58	14.35±7.01	4.10±2.38
Predicted	178.32±18.28	674.39±50.83	1119.31±66.14	1136.59±74.24	665.78±45.57	184.04±21.73
Observed	200	671	1225	1128	659	155

(c) $y_{t\bar{t}}$, $e\mu$ channel

Table 7.4: Yields of selected events expected $y_{t\bar{t}}$ (at the reconstructed level) signal and backgrounds compared to observed selected events, in the ee, $\mu\mu$ and $e\mu$ channels. Background yields are broken down into each background process. Systematic uncertainties except PDF uncertainties are included. The binning is the same as in the unfolded results.

$\lvert y_{t\bar{t}}\rvert$ (ee)	Bins		
	0.0-0.5	0.5-1.0	1.0-2.5
$t\bar{t}$ (dilepton)	303.02±37.12	155.93±19.70	25.66±4.37
$Z(\rightarrow ee/\mu\mu)$+jets	1.02±0.84	0.76±0.66	0.36±0.47
$Z(\rightarrow \tau\tau)$+jets	0.26±0.30	0.17±0.15	0.00±0.00
Single top	13.68±1.78	5.81±0.76	0.89±0.16
Diboson	0.78±0.27	0.17±0.09	0.07±0.07
Fake leptons	9.01±5.45	1.96±3.18	1.20±0.70
Predicted	327.78±37.52	164.79±19.97	28.19±4.38
Observed	338	173	21

(a) $\lvert y_{t\bar{t}}\rvert$, ee channel

$\lvert y_{t\bar{t}}\rvert$ ($\mu\mu$)	Bins		
	0.0-0.5	0.5-1.0	1.0-2.5
$t\bar{t}$ (dilepton)	821.62±44.91	497.78±31.81	101.95±9.97
$Z(\rightarrow ee/\mu\mu)$+jets	1.65±1.90	3.43±2.53	0.69±1.75
$Z(\rightarrow \tau\tau)$+jets	1.43±0.66	0.86±0.64	0.27±0.26
Single top	36.47±3.53	18.76±2.06	2.71±0.73
Diboson	1.75±0.38	1.34±0.31	0.12±0.12
Fake leptons	9.26±2.78	2.91±1.98	0.00±0.87
Predicted	872.18±43.66	525.08±32.33	105.74±10.42
Observed	859	556	94

(b) $\lvert y_{t\bar{t}}\rvert$, $\mu\mu$ channel

$\lvert y_{t\bar{t}}\rvert$ ($e\mu$)	Bins		
	0.0-0.5	0.5-1.0	1.0-2.5
$t\bar{t}$ (dilepton)	2132.85±131.27	1263.44±91.96	342.25±37.45
$Z(\rightarrow ee/\mu\mu)$+jets	0.00±0.00	0.20±0.16	0.00±0.00
$Z(\rightarrow \tau\tau)$+jets	3.04±0.90	1.49±0.55	1.22±0.55
Single top	93.85±9.05	49.43±4.88	11.50±1.31
Diboson	4.23±0.67	3.77±0.75	0.96±0.32
Fake leptons	21.94±14.94	21.85±10.34	6.43±3.24
Predicted	2255.91±135.42	1340.18±94.44	362.36±38.23
Observed	2353	1330	355

(c) $\lvert y_{t\bar{t}}\rvert$, $e\mu$ channel

Table 7.5: Yields of selected events expected $\lvert y_{t\bar{t}}\rvert$ (at the reconstructed level) signal and backgrounds compared to observed selected events, in the ee, $\mu\mu$ and $e\mu$ channels. Background yields are broken down into each background process. Systematic uncertainties except PDF uncertainties are included. The binning is the same as in the unfolded results.

Chapter 8

Unfolding

Measured kinematic distributions with a detector need to be corrected for the instrumentation's acceptance and resolution effects, as well as biases in reconstructed-level observables, in order to allow direct comparisons with theory predictions and across experiments. The procedure of this correction of data from detector-reconstructed level to generator ("true") level is called unfolding. This procedure generally involves inverting the response matrix that is derived from the response of the detector, and often "regularisation", an algorithm to suppress fluctuating contributions to the unfolded data and thus to regulate the associated uncertainties. Two unfolding methods adopting regularisation are the Bayesian (or Iterative) and the Singular Value Decomposition (SVD) methods. In this measurement of $t\bar{t}$ differential cross-sections, the Bayesian algorithm is chosen as the default unfolding method, while both methods were considered and compared in the development of the analysis. Correlations among bins in an unfolded spectrum often arise due to the migrations of bin contents during the unfolding procedure, thus are also measured and shown along with the unfolded results.

The theory prediction from the MC generator refers to the top-parton-level prediction, as defined and described in section 5.1.1.

8.1 Response matrix

Effects of smearing and shifting of a true value of the measured variable are induced by the response of the detector. The response matrix (or migration matrix) is a 2-dimensional representation of how the true value of an observable is mapped into the measured value, according to the characteristic response of the detector or other acceptance effects. Thus the true (or generator) level and the reconstructed level of a MC sample can be used to construct the response matrix through an event-by-event basis. The response matrix represented by a 2D histogram can be represented in terms of the number of events or in terms of probability - each bin (i,j) is normalized by the total number of events in a true bin j, thus showing the probability of a true bin being re-distributed across reconstructed bins. The response matrix in number of events is used as

input in the unfolding, while the probability matrix is often shown in plots instead. The probability matrix allows one to see the proportions of diagonal versus off-diagonal bins, despite the sometimes large order-of-magnitude differences across bins. It also allows one to compare the response matrices among different measurements.

The response matrices of the $t\bar{t}$ system variables used in this measurement in terms of probability are shown in Figure 8.1 and 8.2. These are constructed from the default MC $t\bar{t}$ POWHEG +PYTHIA 117050 sample.

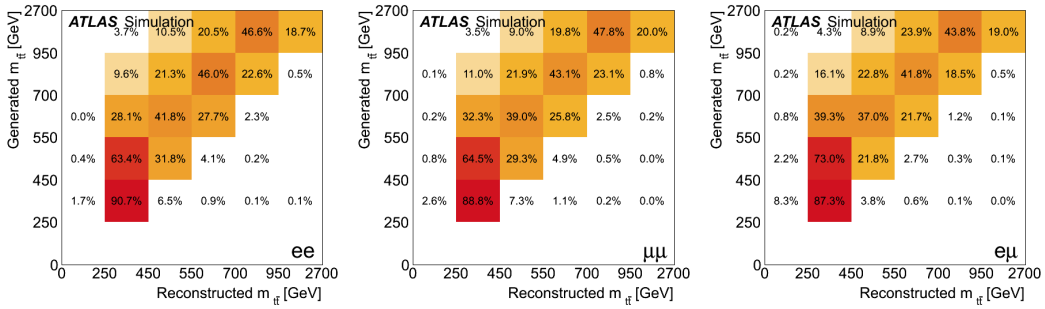

(a) $m_{t\bar{t}}$

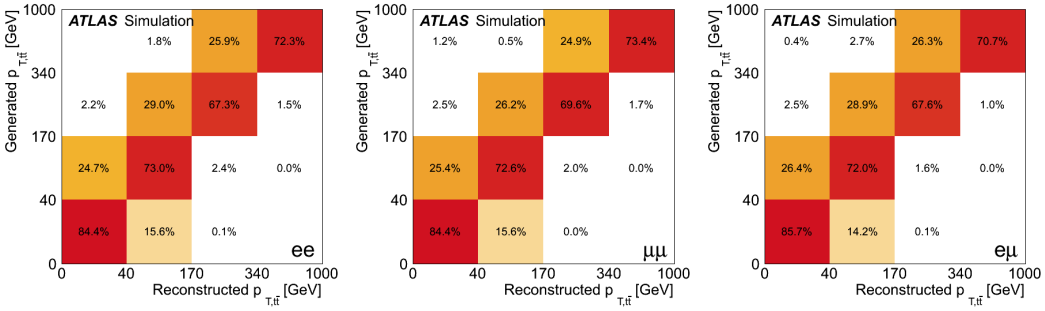

(b) $p_{\mathrm{T}}^{t\bar{t}}$

Figure 8.1: The probability response matrix of true and reconstructed (a)$m_{t\bar{t}}$ and (b)$p_{\mathrm{T}}^{t\bar{t}}$ in the ee (left), $\mu\mu$ (center) and $e\mu$ (right) channels. The actual response matrix is in number of events. Cells with no probability shown indicate that for a cell (i,j), no events are reconstructed in bin i correspond to the generated events bin j in the MC sample.

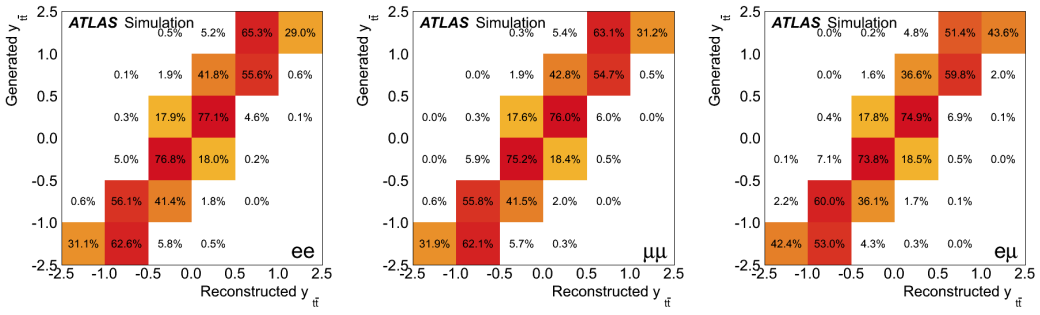

(a) $y_{t\bar{t}}$

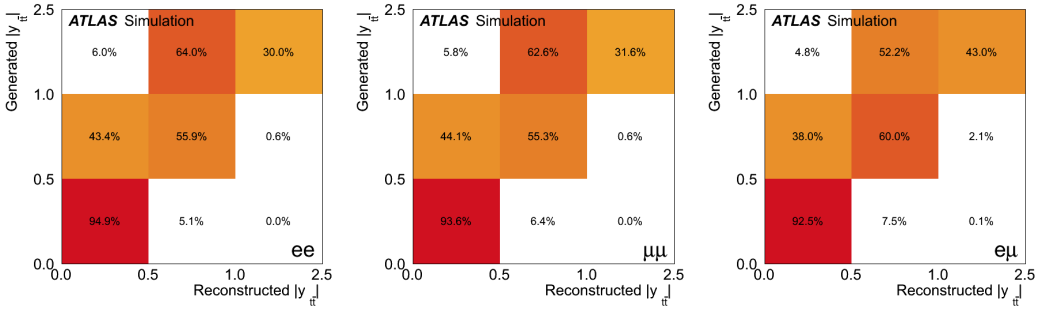

(b) $|y_{t\bar{t}}|$

Figure 8.2: The probability response matrix of true and reconstructed (a)$y_{t\bar{t}}$ and (b)$|y_{t\bar{t}}|$ in the ee (left), $\mu\mu$ (center) and $e\mu$ (right) channels. The actual response matrix is in number of events. Cells with no probability shown indicate that for a cell (i,j), no events are reconstructed in bin i correspond to the generated events bin j in the MC sample.

8.2 Unfolding method

The method of iterative Bayesian unfolding [40] is chosen in this analysis to unfold the measured reconstructed $t\bar{t}$ system variables to the generated (truth) ones. The method applies an iterative procedure using Bayes' theorem. It assumes a first intial probability of the truth and iterates the calculation by updating the probability with the obtained final probability from the Bayes formula. The iteration terminates when the χ^2 is sufficiently small when compared to the truth probability obtained from MC (see determination of unfolding parameter in 8.3). With a reasonably chosen number of iterations, this method gives a stable result against statistical fluctuations and correlations across bins. It is also noted and shown that the method does not produce biased results or suppress deviations (e.g. strong peaks) in data (section 6.3 in [40], 8.4.2 in this note).

The implementation and test of the method is in the RooUnfold framework [41, 42].

8.3 Choice and determination of the unfolding parameter

8.3.1 Study of unfolding parameter and χ^2

A parameter of regularization in the Bayesian unfolding is the number of iterations. One way to systematically optimise the choice is to compare the levels of agreement between the unfolded and the truth distributions at different number of iterations. The optimised choice should be reasonably consistent also at different input data conditions (i.e. shape of the measured data). Two approaches to test the goodness of unfolded-truth agreement are shown in the study below: the relative bias and the χ^2 of the unfolded spectrum for each iteration. Both quantities are extracted from the unfolded and the true test-data distributions.

A series of MC $t\bar{t}$ samples are used as the test-data samples to emulate possible data conditions in $m_{t\bar{t}}$, $p_{\mathrm{T}}^{t\bar{t}}$, $y_{t\bar{t}}$ and $|y_{t\bar{t}}|$. First, we study 3 test-data samples that are relatively close to the nominal one (Powheg +Pythia P2011C $t\bar{t}$ 117050): half of the default POWHEG+PYTHIA P2011C sample, MC@NLO+HERWIG (105200) and ALPGEN+HERWIG dilepton (105890-2; 117897-9). These are samples used in studies of $t\bar{t}$ signal modeling uncertainties in Section 9.1. To emulate the unfolding setup (i.e. same/similar migration matrix) in treating real data, we use the default Powheg +Pythia P2011C 117050 sample to train the migration matrix (thus same in unfolding real data) in the second and third case, while in the last case, the other half of the default sample not used as test is used to train the unfolding. Statistical independence between the test and the training samples is ensured in all cases. Secondly, we study the samples used in the stress tests, as described in Section 8.4.2. The unfolded distributions are compared to the stressed true

distributions. The case of a good agreement with the truth should show a small value both in the relative bias and χ^2.

All the test samples are re-weighted to the luminosity of data, while the statistics of the training sample inherits from the MC POWHEG+PYTHIA P2011C sample. Each $t\bar{t}$ system variable, $m_{t\bar{t}}$, $p_{\mathrm{T}}^{t\bar{t}}$, $y_{t\bar{t}}$ and $|y_{t\bar{t}}|$, in each of the ee, $\mu\mu$ and $e\mu$ channels with the lep+jets binning are studied independently. In this study, the unfolded spectra of the first 5 iterations are tested and compared (10 iterations are shown in the χ^2 study for some cases).

Figures C.1-C.3 show the relative bias ((unfolded-true)/true) of each of the first 5 iterations of unfolded spectra in the cases of half POWHEG+PYTHIA, MC@NLO+HERWIG and ALPGEN+HERWIG samples. Figures C.4-C.7 show the same for the stressed test-data samples, in $m_{t\bar{t}}$, $p_{\mathrm{T}}^{t\bar{t}}$, $y_{t\bar{t}}$ and $|y_{t\bar{t}}|$ respectively. The relative bias shows visually how much an unfolded spectrum deviates from the true one. The uncertainty of each bias value shows the statistical uncertainty estimated in each iteration of the unfolding.

Figure C.8-C.14 shows the χ^2 as a function of number of iterations for each $t\bar{t}$ system variable in each dilepton channel. In the closure tests, the total χ^2, the χ^2's of the 2nd last and the last bins are shown and studied, while the total χ^2 and the χ^2's of the most stressed bin are studied in the stress tests. The total χ^2 is a generalized χ^2, taking the covariances across bins into account and calculated using the covariance matrix derived from the unfolding as: $\chi^2 = (x-\bar{x})^T V^{-1}(x-\bar{x})$, where V^{-1} is the inverse of the covariance matrix and x and $\bar{x}$ are the unfolded and true values, respectively. The χ^2 for individual bins cannot include the covariance terms, thus is calculated in the usual way as the sum of (residuals/uncertainty)-squared (and thus is independent from the neighboring bins): $\sum_i \frac{(x_i-\bar{x}_i)^2}{\sigma_i^2}$, where x_i and $\bar{x}_i$ are the unfolded and true values respectively at bin i, and σ_i is the statistical uncertainty of bin i (taken as the square root of the i-th diagonal element of the covariance matrix from unfolding).

Table 8.1 summarizes the number of iterations with minimum χ^2 ($n_{\min.\chi^2}$) from the above closure tests using different MCs similar to the training sample as the test data. Generally, the χ^2's of the bulk and the tail regions are significantly suppressed after 2-3 iterations for all $t\bar{t}$ system variables (in some cases when the χ^2's are already minimal at the 1st iteration). In $m_{t\bar{t}}$, the minimum χ^2's of all bins per number of degrees of freedom (n.d.f.) are already at the level of or less than 1 starting at the 2nd iterations, while for other variables the all-bin-χ^2's are generally very small (χ^2 much less than n.d.f.) from the first and for all further iterations. These closure tests therefore do not seem to show obvious choices of the optimized numbers of iterations for the variables in consideration, due to the little differences between the training samples and the test data, and the often trivially small χ^2 values at each iteration.

Tables 8.2 summarizes the number of iterations with minimum χ^2 ($n_{\min.\chi^2}$) from the stress tests discussed

in 8.4.2. In $m_{t\bar{t}}$, the stress test with $m_{Z\prime} = 1.6$ TeV indicates $n_{\min.\chi^2}$= 3 for all bins and $n_{\min.\chi^2}$= 2 for the most stressed bin in all ee, $\mu\mu$ and $e\mu$ channels, while in the $m_{Z\prime} = 0.6$ TeV case there is no $n_{\min.\chi^2}$ indicated in general. In the latter case the χ^2's are suppressed to similar to or below the number of degrees of freedom (5) at 2 or 3 iterations. In $p_{\mathrm{T}}^{t\bar{t}}$, both stress tests using Alpgen+HW lnln Np3 and Alpgen+HW lnln Np4 samples show an $n_{\min.\chi^2}$ at 2 for all bins and for the most stressed bin in all dilepton channels. In the cases of $y_{t\bar{t}}$ and $|y_{t\bar{t}}|$, the $m_{Z\prime} = 1.6$ TeV stress test does not show a clear mininum χ^2, but the tests with Alpgen+HW lnln Np0 sample as stressed data indicate a $n_{\min.\chi^2}$ at 1 or 2. The χ^2's at the first two number of iterations for the tests in $y_{t\bar{t}}$ and $|y_{t\bar{t}}|$ are close to or less than the number of degrees of freedom.

Test: half1 POW+PY	$m_{t\bar{t}}$			$p_{\mathrm{T}}^{t\bar{t}}$			$y_{t\bar{t}}$			$\lvert y_{t\bar{t}}\rvert$		
channel	ee	$\mu\mu$	$e\mu$	ee	$\mu\mu$	$e\mu$	ee	$\mu\mu$	$e\mu$	ee	$\mu\mu$	$e\mu$
$n_{\min.\chi^2}$: all bins	-	-	-	-	-	-	-	-	3	-	-	4
$n_{\min.\chi^2}$: 2nd last bin	1	1	1	-	-	-	-	-	3	1	-	4
$n_{\min.\chi^2}$: last bin	-	4	2	-	-	-	-	1	2	5	-	1

(a) Half of POWHEG +PYTHIA $t\bar{t}$

Test: MC@NLO+HW	$m_{t\bar{t}}$			$p_{\mathrm{T}}^{t\bar{t}}$			$y_{t\bar{t}}$			$\lvert y_{t\bar{t}}\rvert$		
channel	ee	$\mu\mu$	$e\mu$	ee	$\mu\mu$	$e\mu$	ee	$\mu\mu$	$e\mu$	ee	$\mu\mu$	$e\mu$
$n_{\min.\chi^2}$: all bins	-	-	8	3	-	-	-	3	4	-	5	3
$n_{\min.\chi^2}$: 2nd last bin	4	1	4	5	5	-	-	1	2	1	3	2
$n_{\min.\chi^2}$: last bin	-	2	5	-	-	4	-	3	4	1	-	4

(b) MC@NLO +HERWIG $t\bar{t}$

Test: ALPGEN+HW	$m_{t\bar{t}}$			$p_{\mathrm{T}}^{t\bar{t}}$			$y_{t\bar{t}}$			$\lvert y_{t\bar{t}}\rvert$		
channel	ee	$\mu\mu$	$e\mu$	ee	$\mu\mu$	$e\mu$	ee	$\mu\mu$	$e\mu$	ee	$\mu\mu$	$e\mu$
$n_{\min.\chi^2}$: all bins	-	-	9	5	-	-	-	-	5	7	3	2
$n_{\min.\chi^2}$: 2nd last bin	2	2	5	7	3	-	2	2	6	6	1	1
$n_{\min.\chi^2}$: last bin	-	1	4	-	-	7	4	1	2	7	4	2

(c) ALPGEN +HERWIG $t\bar{t}$

Table 8.1: The summary of the number of iterations with minimum χ^2 ($n_{\min.\chi^2}$) in the unfolding tests of each $t\bar{t}$ system variable in the ee, $\mu\mu$ and $e\mu$ channels when using (a) half of POWHEG +PYTHIA $t\bar{t}$ as test data, (b)MC@NLO +HERWIG $t\bar{t}$ and (c)ALPGEN +HERWIG $t\bar{t}$. The χ^2's are calculated for all bins (inclusive, with bin-to-bin covariances), the 2nd last bin and the last bin (isolated bins, no bin-to-bin covariance). A null entry indicates there is no mininum of χ^2 in the range of the number of iterations except for the last number of iterations considered in the study (10 in this case).

Test: $m_{Z\prime} = 0.6$ TeV	$m_{t\bar{t}}$		
channel	ee	$\mu\mu$	$e\mu$
$n_{\min.\chi^2}$: all bins	-	-	-
$n_{\min.\chi^2}$: most stressed bin:	-	-	-

Test: $m_{Z\prime} = 1.6$ TeV	$m_{t\bar{t}}$		
channel	ee	$\mu\mu$	$e\mu$
$n_{\min.\chi^2}$: all bins	3	3	3
$n_{\min.\chi^2}$: most stressed bin:	2	2	2

(a) $m_{t\bar{t}}$

Test: Alpgen+HW lnln Np3	$p_{\mathrm{T}}^{t\bar{t}}$		
channel	ee	$\mu\mu$	$e\mu$
$n_{\min.\chi^2}$: all bins	2	2	2
$n_{\min.\chi^2}$: most stressed bin:	2	2	2

Test: Alpgen+HW lnln Np4	$p_{\mathrm{T}}^{t\bar{t}}$		
channel	ee	$\mu\mu$	$e\mu$
$n_{\min.\chi^2}$: all bins	2	2	2
$n_{\min.\chi^2}$: most stressed bin:	2	2	2

(b) $p_{\mathrm{T}}^{t\bar{t}}$

Test: $m_{Z\prime} = 1.6$ TeV	$y_{t\bar{t}}$		
channel	ee	$\mu\mu$	$e\mu$
$n_{\min.\chi^2}$: all bins	-	-	4
$n_{\min.\chi^2}$: most stressed bin:	-	-	2

Test: Alpgen+HW lnln Np0	$y_{t\bar{t}}$		
channel	ee	$\mu\mu$	$e\mu$
$n_{\min.\chi^2}$: all bins	2	2	1
$n_{\min.\chi^2}$: most stressed bin:	2	2	1

(c) $y_{t\bar{t}}$

Test: $m_{Z\prime} = 1.6$ TeV	$\lvert y_{t\bar{t}}\rvert$		
channel	ee	$\mu\mu$	$e\mu$
$n_{\min.\chi^2}$: all bins	-	-	4
$n_{\min.\chi^2}$: most stressed bin:	-	-	-

Test: Alpgen+HW lnln Np0	$\lvert y_{t\bar{t}}\rvert$		
channel	ee	$\mu\mu$	$e\mu$
$n_{\min.\chi^2}$: all bins	2	2	1
$n_{\min.\chi^2}$: most stressed bin:	2	1	1

(d) $|y_{t\bar{t}}|$

Table 8.2: The summary of the number of iterations with minimum χ^2 ($n_{\min.\chi^2}$) in the unfolding stress tests of each $t\bar{t}$ system variable in the ee, $\mu\mu$ and $e\mu$ channels. The χ^2's are calculated for all bins (inclusive, with bin-to-bin covariances) and the most stressed bin (isolated bin, no bin-to-bin covariance). A null entry indicates there is no mininum of χ^2 in the range of the number of iterations except for the last number of iterations considered in the study (5 in this case).

8.3.2 Preservation of total variance in unfolding and its dependence on unfolding parameter

A general property of the iterative Bayesian unfolding algorithm is that the total number of events should be preserved before and after the unfolding procedure. The unfolding "maps" events from one bin to another ones, introducing bin-to-bin correlations, and the variances in individual bins are also modified. But since the total number of events (or the overall normalization) is unchanged, the *total variance* of the measured events is preserved. In other words, the total variance of the measured and reconstructed spectrum

$$\sigma^2_{\text{obs}}(\text{total}) = \sum_{i=1}^{n} \sigma^2_{\text{obs}}(i) \tag{8.1}$$

is equal to

$$\sigma^2_{\text{unf}}(\text{total}) = \sum_{i \neq j}^{n} \sigma^2_{\text{unf}}(i) + \text{cov}(i,j) \tag{8.2}$$

in the unfolding. In a quick check of the unfolded results, one can show that this indeed is the case.

We use one half of the nominal POWHEG+PYTHIA sample is taken as the test data and is unfolded using the other half of the sample as the training and unfolding matrix construction. The ratio of the total variance integrated from the unfolded spectrum, including all covariance terms (i.e. non-diagonal terms in the covariance matrix), with the total variance in the measured and reconstructed spectrum is evaluated and compared across 10 iterations in the Bayesian unfolding. In this test, the input test data uses the statistics from the MC and is not scaled to data luminosity. The check for each $t\bar{t}$ system variable in each dilepton channel is shown in Figure 8.3. It is seen that the unfolded spectrum does preserve the total variance of the measured events, regardless of the iteration number of the unfolding.

While presenting the results, nevertheless, often only the variance terms of the covariance matrix (i.e. the diagonal elements) are shown, as their square roots are taken and presented as the statistical uncertainties. The numerial values of the 1D statistical errors for each bin of the unfolded variable do not (and cannot easily be presented to) carry the 2D, bin-to-bin covariance information, and the presentation of these numbers and error bars can be quite misleading about the actual covariance and degree of uncertainty in the differential result in the 1D histogram, especially when correlations between any bins are are significant. To minimize this kind of possible biases in one's interpretation of the results, we study the total variance of the unfolded spectrum again, but *without* taking the covariance terms into the integral sum:

$$\sigma^2_{\text{unf}}(\text{total, no cov.}) = \sum_{i \neq j}^{n} \sigma^2_{\text{unf}}(i) \tag{8.3}$$

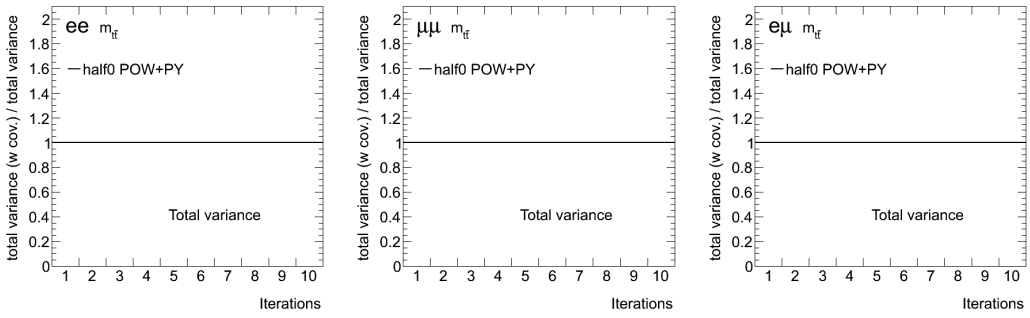

(a) $m_{t\bar{t}}$

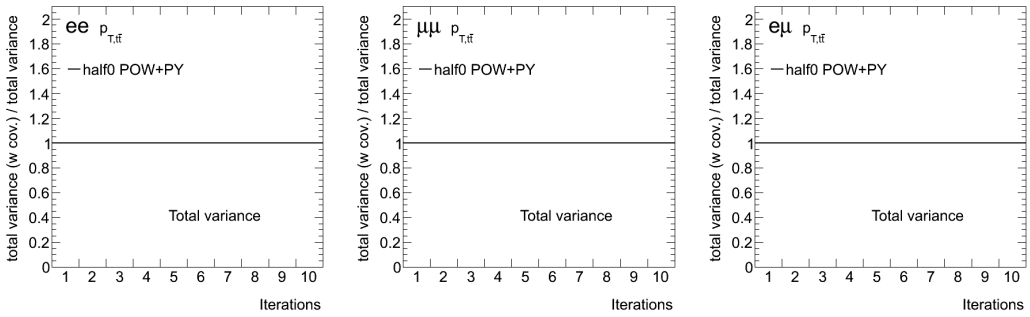

(b) $p_{\mathrm{T}}^{t\bar{t}}$

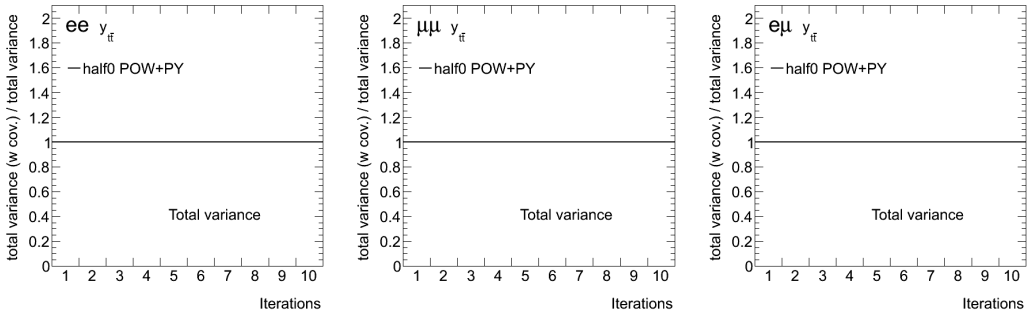

(c) $y_{t\bar{t}}$

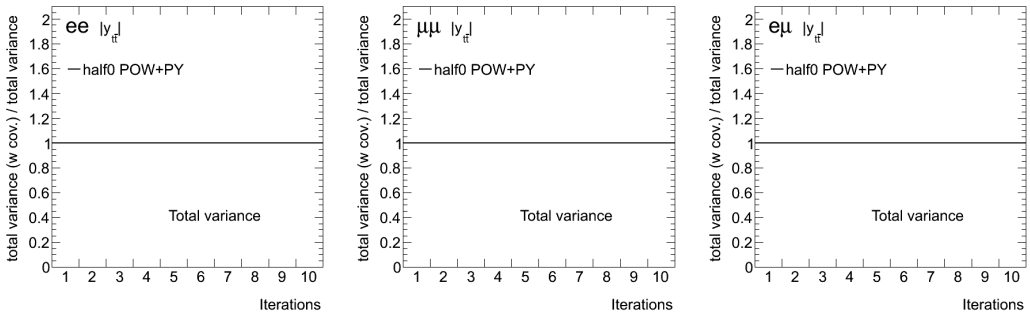

(d) $|y_{t\bar{t}}|$

Figure 8.3: The ratio of the total variance integrated from unfolded spectrum with covariances and the total variance in measured and reconstructed spectrum, as a function of number of iterations in Bayesian unfolding of (a)$m_{t\bar{t}}$, (b)$p_{\mathrm{T}}^{t\bar{t}}$, (c)$y_{t\bar{t}}$ and (d)$|y_{t\bar{t}}|$ in the ee (left), $\mu\mu$ (center) and $e\mu$ (right) channels. Test data using half of the POWHEG +PYTHIA $t\bar{t}$ sample as input is compared. The other half of the POWHEG +PYTHIA $t\bar{t}$ is used as the training sample. The input test data uses the statistics from the MC (not scaled to data luminosity).

This total variance without covariance is our estimator. We then impose the criteria that this estimator is approximately equal to the actual total covariance,

$$\sigma^2_{\text{unf}}(\text{total, no cov.}) \approx \sigma^2_{\text{obs}}(\text{total}) \tag{8.4}$$

for an iteration n in the Bayesian unfolding. This criteria serves as a constraint to impose limits on the allowed numerical values of the statistical error for each bin of the unfolded variable, for/at each iteration n.

Figure 8.4 shows the ratio of this estimator (total variance without covariance) from the unfolded spectrum and the total variance in the measured and reconstructed spectrum for each $t\bar{t}$ system variable, and is compared across 10 iterations in the Bayesian unfolding.

From these results, it can be seen that the choices of iteration numbers shown in Table 8.3 best suit the above criteria in this MC test using the POWHEG+PYTHIA $t\bar{t}$ sample. One may observe that the differences in these choices for $m_{t\bar{t}}$ (4), $p_{\text{T}}^{t\bar{t}}$ (2) and $y_{t\bar{t}}$ or $|y_{t\bar{t}}|$ (3) are consistent with the level of diagonality of the migration matrices of these variables, as shown in Figures 8.1 and 8.2. The response matrix is the most diagonal in the $p_{\text{T}}^{t\bar{t}}$ case, due to the fact that our $t\bar{t}$ reconstruction method fully reconstructs the $t\bar{t}$ system in the transverse region, while in the $m_{t\bar{t}}$ and $y_{t\bar{t}}$ (or $|y_{t\bar{t}}|$ cases, the off-diagonal elements reflects the 'under-reconstruction' of $t\bar{t}$ in the longitudinal region, due to the unmeasured neutrinos' p_z (see discussion in the reconstruction method, Section 7.1). $m_{t\bar{t}}$ is the variable most sensitive to this loss of the z-components of the neutrinos' 3-momenta, and is reflected in a higher number of iterations in the Bayesian unfolding to reach the optimal result (good closure, minimum bin-to-bin correlations).

Variable	Iterations
$m_{t\bar{t}}$	4
$p_{\text{T}}^{t\bar{t}}$	2
$y_{t\bar{t}}$	3
$\lvert y_{t\bar{t}}\rvert$	3

Table 8.3: The summary of the number of iterations at which the total variance of the unfolded spectrum without covariance is approximately equal to the total variance for each $t\bar{t}$ system variable.

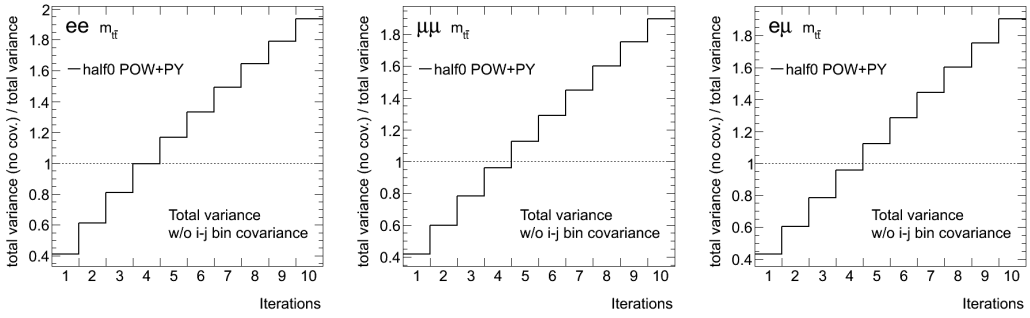

(a) $m_{t\bar{t}}$

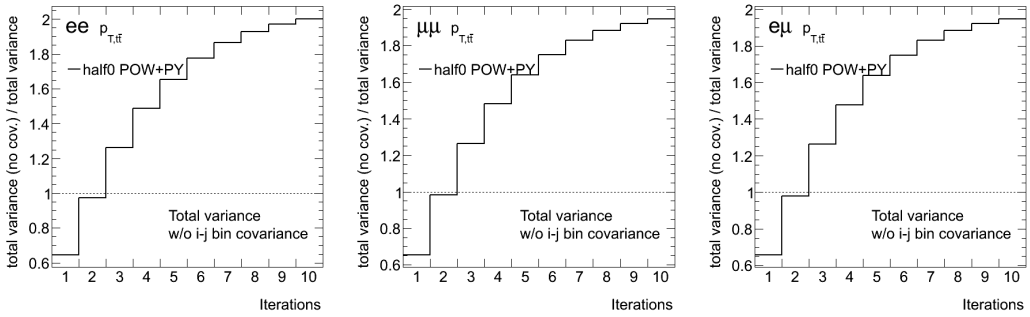

(b) $p_{\mathrm{T}}^{t\bar{t}}$

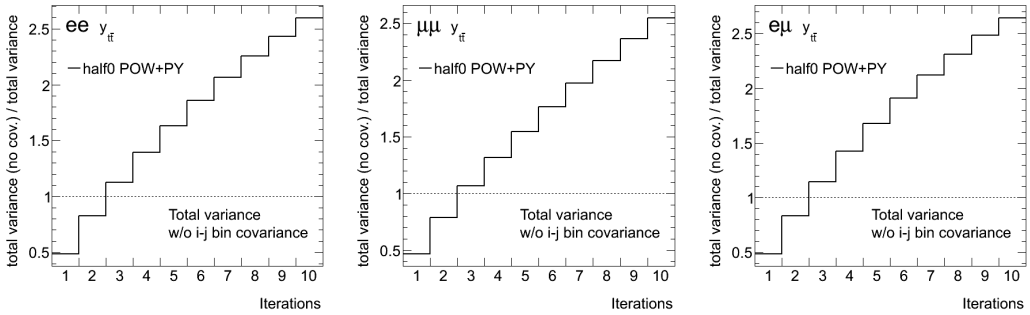

(c) $y_{t\bar{t}}$

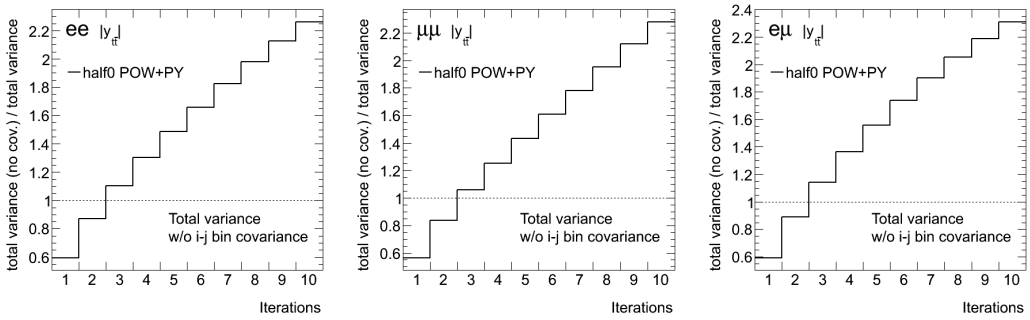

(d) $|y_{t\bar{t}}|$

Figure 8.4: The ratio of the total variance integrated from unfolded spectrum *without* covariances and the total variance in measured and reconstructed spectrum, as a function of number of iterations in Bayesian unfolding of (a)$m_{t\bar{t}}$, (b)$p_{\mathrm{T}}^{t\bar{t}}$, (c)$y_{t\bar{t}}$ and (d)$|y_{t\bar{t}}|$ in the ee (left), $\mu\mu$ (center) and $e\mu$ (right) channels. Test data using half of the POWHEG +PYTHIA $t\bar{t}$ sample as input is compared. The other half of the POWHEG +PYTHIA $t\bar{t}$ is used as the training sample. The input test data uses the statistics from the MC (not scaled to data luminosity).

8.4 Tests with simulated data

The unfolding method is desired to give consistent and unbiased results that retain sufficient sensitivity to shape alterations from the simulated truth spectrum. To understand the performance of the unfolding algorithm when it is applied to data, simulated tests are performed on Monte Carlo samples to emulate different conditions possible in real data. In the following study, closure and stress tests are designed to evaluate the expected performance of the unfolding in this analysis.

8.4.1 Closure tests

A training sample and a test sample are used in a closure test. The training sample is used as the expected signal simulation where the simulated truth spectra and the response matrix are extracted ("trained") from. The response matrix is a 2D matrix showing the event migration from one bin to another between the truth and reconstructed distributions. The test sample mimics the data and is unfolded with the truth spectra and the response matrix from the training sample to give the resulted spectra.

To show that the unfolded spectra returns a reasonable closure, two closure tests with different choices of the training and the test samples are studied:

1. the test sample is identical to the training sample (using the default $t\bar{t}$ sample)
2. the default $t\bar{t}$ sample is divided into two halves: one as the training sample and the other as the test sample.

In the first case, shown in Figure 8.5, the truth and reconstructed distributions are identical in the test and training samples, and thus the unfolded truth spectrum is expected to be perfectly close or identical to the training truth spectrum. This test checks for any systematic bias due to the unfolding algorithm and the response matrix.

In the second case, shown in Figure 8.6, statistical independence is ensured between the training and test samples. Good (but not perfect) closures are expected in the unfolded spectra when compared to the truth distributions of the test sample.

In both cases, the test samples are reweighted to the same luminosity as in real data to emulate the data condition. The normalization of the test samples is reflected in the similar level of statistical uncertainties of the unfolded spectra between the two closure tests.

The following closure tests use 4 iterations in Bayesian unfolding of $m_{t\bar{t}}$, 3 iterations for $y_{t\bar{t}}$ and $|y_{t\bar{t}}|$, and 2 iterations for $p_{\mathrm{T}}^{t\bar{t}}$ (see Section 8.3 for study and determination). In the following tests we show that these numbers of iterations are sufficient for the unfolding with respect to the truth of the test data, while the

statistical uncertainties are kept within a reasonable range (Section 8.3.2 discusses the effect of iterations on the variance). The goodness of the closure is reflected from the overall χ^2 between the unfolded and the simulated truth histograms.

Pseudo-experiments are also performed to test the stability of the closures. The number of events in both the response matrix and the test data distribution are Poisson-randomized, emulating 1000 different test and training pseudo-samples with the same truth. A summary of the resulting pull distributions, defined by $x - \mu/\sigma$ where x, μ and σ are the unfolded content, the truth value and the statistical uncertainty of the measured value and from the unfolding, respectively, is shown in Figure 8.7. The result shows that the unfolding with our input distributions is unbiased (indicated by the RMS values of the pull, or the error bars in the plots). The results of the pseudo-experiments are also found to be stable with respect to the number of pseudo-experiments used in the test.

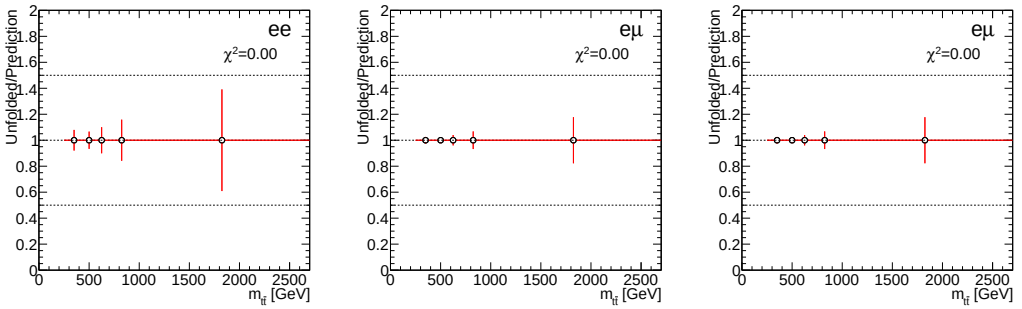

(a) $m_{t\bar{t}}$

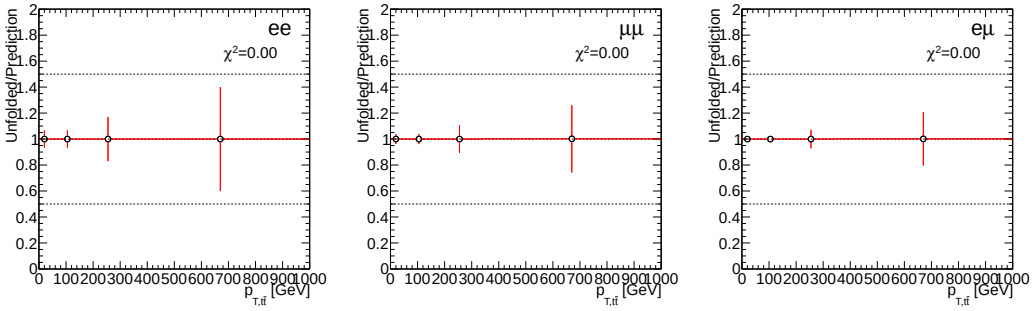

(b) $p_{\mathrm{T}}^{t\bar{t}}$

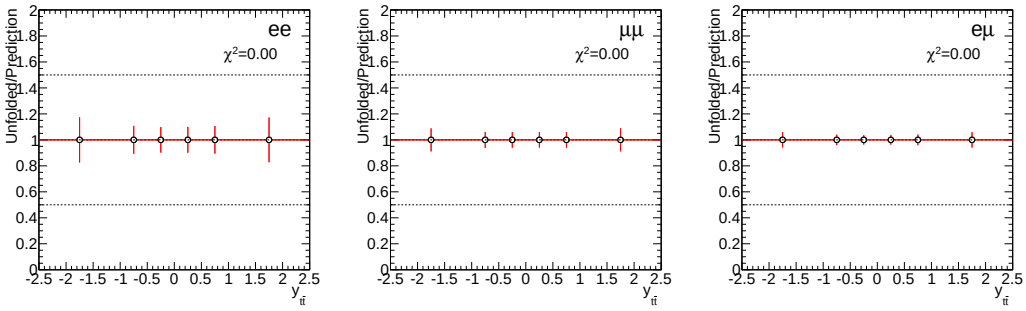

(c) $y_{t\bar{t}}$

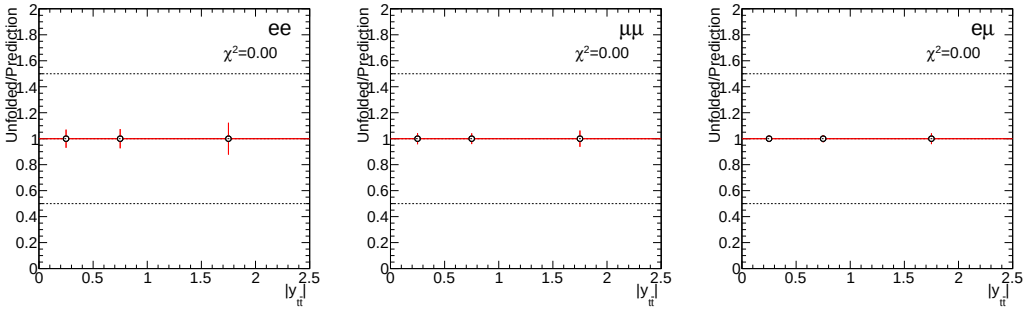

(d) $|y_{t\bar{t}}|$

Figure 8.5: Closure in the $t\bar{t}$ system variables in the ee, $\mu\mu$ and $e\mu$ channels after Bayesian unfolding with 4 ($m_{t\bar{t}}$), 2 ($p_{\mathrm{T}}^{t\bar{t}}$) or 3 ($y_{t\bar{t}}$ and $|y_{t\bar{t}}|$) iterations. The same default POWHEG +PYTHIA $t\bar{t}$ sample is used as the *training* and *test data* sample (training sample = test sample).

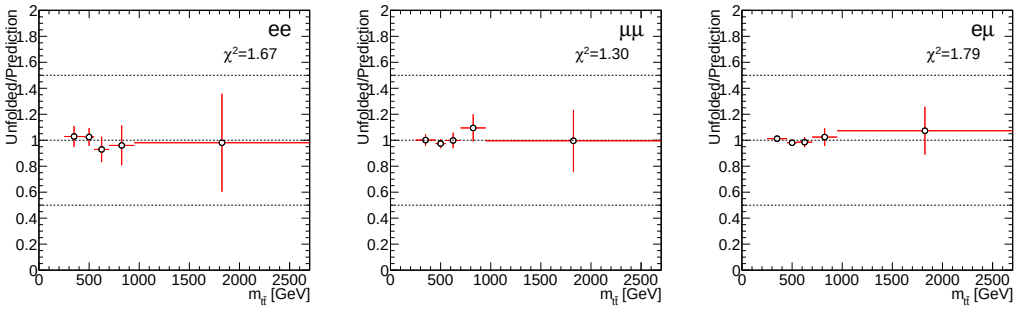

(a) $m_{t\bar{t}}$

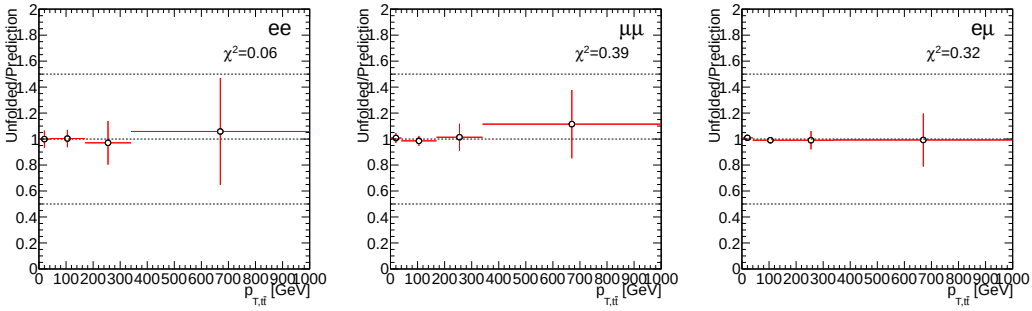

(b) $p_{\mathrm{T}}^{t\bar{t}}$

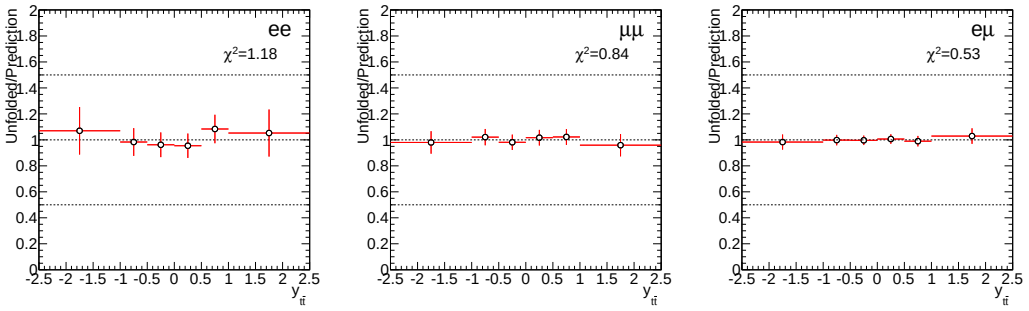

(c) $y_{t\bar{t}}$

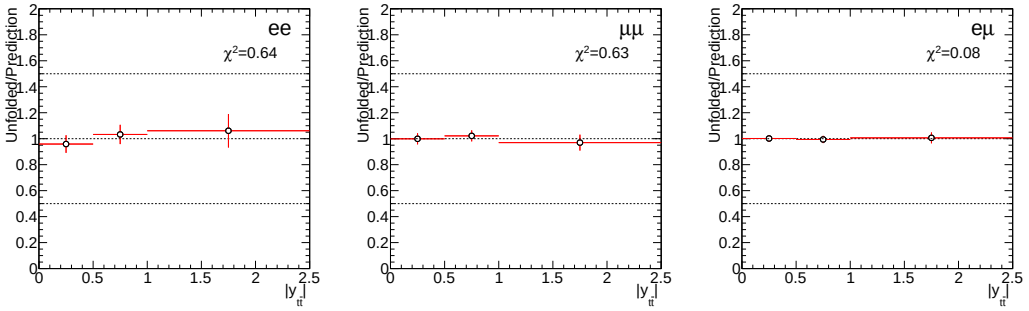

(d) $|y_{t\bar{t}}|$

Figure 8.6: Closure in the $t\bar{t}$ system variables in the ee, $\mu\mu$ and $e\mu$ channels after Bayesian unfolding with 4 ($m_{t\bar{t}}$), 2 ($p_{\mathrm{T}}^{t\bar{t}}$) or 3 ($y_{t\bar{t}}$ and $|y_{t\bar{t}}|$) iterations. The default POWHEG +PYTHIA $t\bar{t}$ sample is divided into two halves, one as the *training* sample and another as the *test data* sample.

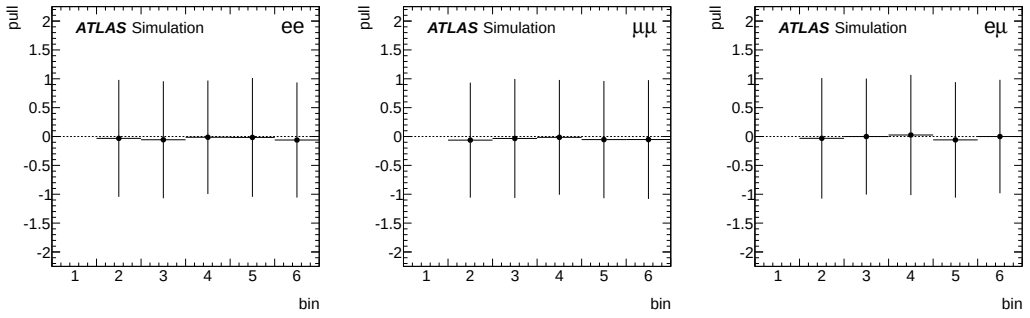

(a) $m_{t\bar{t}}$

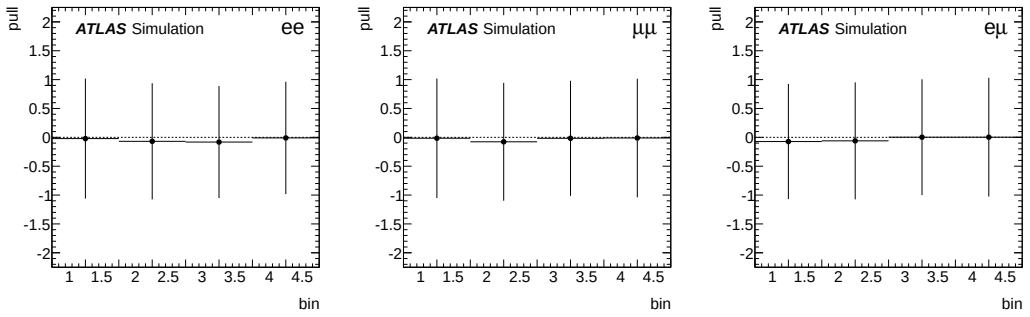

(b) $p_{\mathrm{T}}^{t\bar{t}}$

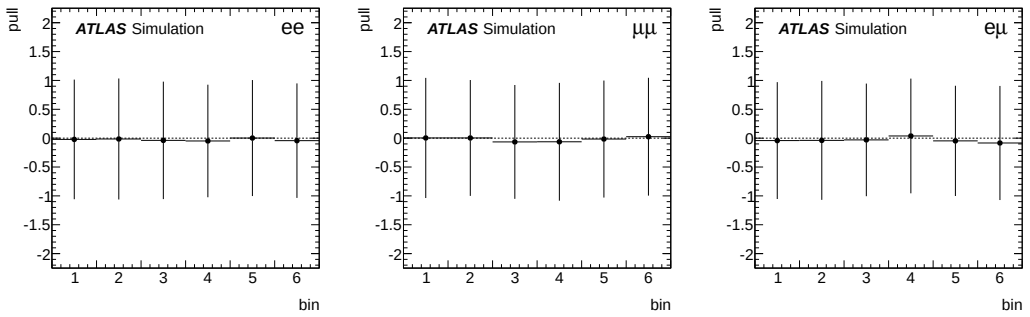

(c) $y_{t\bar{t}}$

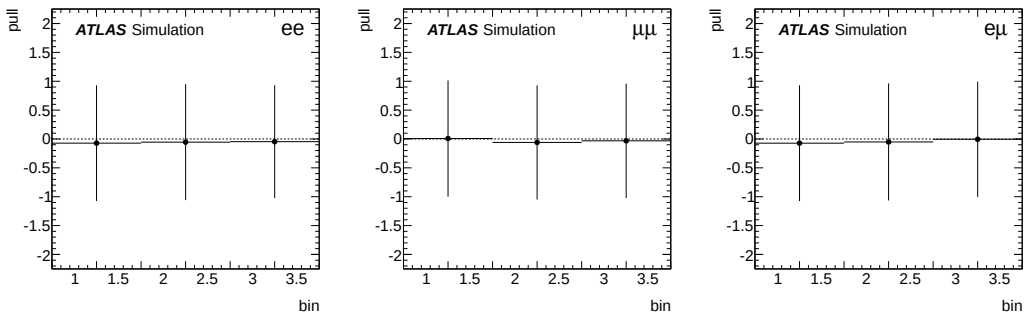

(d) $|y_{t\bar{t}}|$

Figure 8.7: Pull values in the $t\bar{t}$ system variables in the ee, $\mu\mu$ and $e\mu$ channels after Bayesian unfolding with 4 ($m_{t\bar{t}}$), 2 ($p_{\mathrm{T}}^{t\bar{t}}$) or 3 ($y_{t\bar{t}}$ and $|y_{t\bar{t}}|$) iterations in 1000 pseudo-experiments. The error bars denote the RMS values of the pull distributions. An RMS of the pull at 1 indicates an unbiased result.

8.4.2 Stress tests

The sensitivity of the unfolded spectra to the shape of the test data is studied in the stress tests as follows.

Ideally, the unfolded spectra are desired to reflect shape variations in the truth spectra in data. In other words, a chosen regularisation should not be biased towards the truth distribution in the training sample (MC) and suppress the extra shape information (e.g. resonance, dip ... etc), if any, in the real truth in data.

Reconstructed and truth distributions from simulated $t\bar{t}$ resonance samples and multi-leg $t\bar{t}$ production samples are used to emulate these shape alternations from the SM $t\bar{t}$ process. In particular, the reconstructed and truth mass distributions obtained from these samples are added to the reconstructed and truth mass spectra of the SM $t\bar{t}$ respectively to give the "stressed" spectra. The stressed reconstructed spectrum is used as the test data, while the migration matrix is built from the nominal POWHEG +PYTHIA $t\bar{t}$ sample (117050 fullsim), the same as in the closure tests. The unfolded spectrum is then compared to the stressed truth distribution.

The scenarios emulated in the stress tests for each of the $t\bar{t}$ system variables are:

- for $m_{t\bar{t}}$: low and high mass narrow resonances. These cases test altered spectra as peaks in different regions of $m_{t\bar{t}}$. For the low mass resonance, a $m_{Z'} = 0.6$ TeV $Z' \to t\bar{t}$ sample (PYTHIA standalone, 105598) is used, while a $m_{Z'} = 1.6$ TeV $Z' \to t\bar{t}$ sample (PYTHIA standalone, 105594) is used for the high mass resonance. The signal strength is set/scaled to be 20% of the most stressed bin in both cases.

- for $p_{\mathrm{T}}^{t\bar{t}}$: increased events in high $p_{\mathrm{T}}^{t\bar{t}}$ region. $t\bar{t}$ ALPGEN+HERWIG lnln Np3 and Np4 samples (117897 and 117898) are used. The signal strength is set/scaled to be 20% of the most stressed bin in both cases.

- for $y_{t\bar{t}}$ and $|y_{t\bar{t}}|$: more populated central and more populated high rapidity regions. For the more populated central rapidity case, the $m_{Z'} = 1.6$ TeV $Z' \to t\bar{t}$ sample (PYTHIA standalone, 105594) is used, and for the more populated high rapidity case, the $t\bar{t}$ ALPGEN+HERWIG lnln Np0 sample (105890) is used. In the case of emulating a more populated high rapidity, the stressed distributions are normalized to the unstressed ones to better visualize the shape differences. The signal strength is set/scaled to be 20% of the most stressed bin in the first case, and for the second case, the signal strength is about 15% after the normalization.

All stress tests are done in all ee, $\mu\mu$ and $e\mu$ dilepton channels. The test data spectra are re-weighted to data luminosity, and the difference of acceptance among channels are reflected in statistical uncertainties of the unfolded spectra.

It should be noted that these MC-based tests illustrate the level (and the limit) of sensitivity of the unfolding algorithm. The aim is not to show that the unfolding method always correctly describes the attributes in the truth data *quantitatively*, instead, is to show that the unfolding with the regularisation parameter chosen is not overly biasing the data towards the training MC sample - we anticipate satisfactory results by observing unfolded spectra being affected by the altered truth spectra, in a *qualitatively* consistent manner (e.g. a peak in the truth is shown in a peak in the unfolded around the same bin region). The limit of the unfolding should be covered by the statistical uncertainties from the unfolding (which accounts for the data statistics *and* the MC statistics of the migration matrix).

Figures 8.8 and 8.9 show the stress test results for $m_{t\bar{t}}$ in the low mass and high mass regions, respectively. In the low-mass resonance tests, the most stressed bin mostly populates the 3rd bin, and the unfolded spectra are seen to be sensitive to the resonance by recovering up to 90% of the most stressed bin (about 50% of the resonance) with respect to the truth spectra. The sensitivity is also reflected in neighboring bins of the most stressed bin, where the bin contents are affected by the stressed structure as a smeared peak. All 3 dilepton channels show a similar and consistent behavior, with the ee ($e\mu$) channel having the largest (smallest) statistical uncertainties. In the high mass case, the resonance populates exclusively the last bin in $m_{t\bar{t}}$. The resonance is seen almost fully recovered by the unfolding in the tail bin in the central values and statistical uncertainties, while the other unstressed bins remained unaltered.

Stress test results for $p_{\mathrm{T}}^{t\bar{t}}$ are shown in Figures 8.10 and 8.11. In both cases, the spectra are increasingly altered towards the tail region, but with sligltly different shapes. For both cases the unfolded spectra agree well with the stressed truth spectra within statistical uncertainties of all $p_{\mathrm{T}}^{t\bar{t}}$ bins. This good sensitivity can attribute to the highly correlated reconstructed and true values of $p_{\mathrm{T}}^{t\bar{t}}$, as reflected in the diagonal elements of its migration matrices **??**.

The results for $y_{t\bar{t}}$ ($|y_{t\bar{t}}|$) are shown in Figures 8.12 and 8.13 (8.14 and 8.15). The two cases test the stressed spectra towards a lower absolute rapidity $|y|$ (in the first case) and a higher one (second case). In the first case, the unfolded spectra is seen to recover well the stressed spectra in the lower $|y|$ regions, for both $y_{t\bar{t}}$ and $|y_{t\bar{t}}|$, well within statistical uncertainties for all dilepton channels. In the second case, the unfolded spectra also show good sensitivity to the altered true spectra emphasised in the high $|y|$ bins, by recovering up to 7% difference from the true spectra in the most stressed bins (within 2σ).

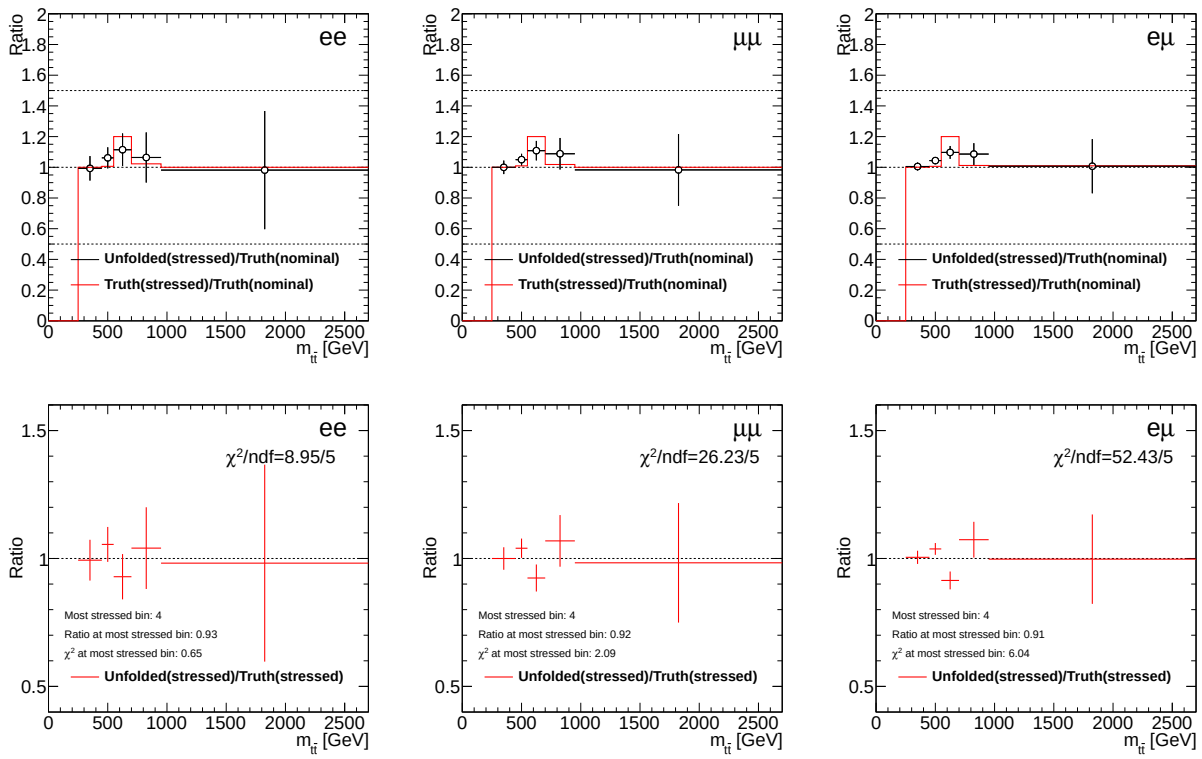

Figure 8.8: Stress test in $m_{t\bar{t}}$ with $Z' \to t\bar{t}$ resonance at $m_{Z'} = 0.6$ TeV in the ee, $\mu\mu$ and $e\mu$ channels. The signal strength is 20% at the most stressed bin. 4 iterations in Bayesian unfolding is used for this test. The ratio of stressed unfolded and stressed truth at most stressed bin is ≈ 0.9.

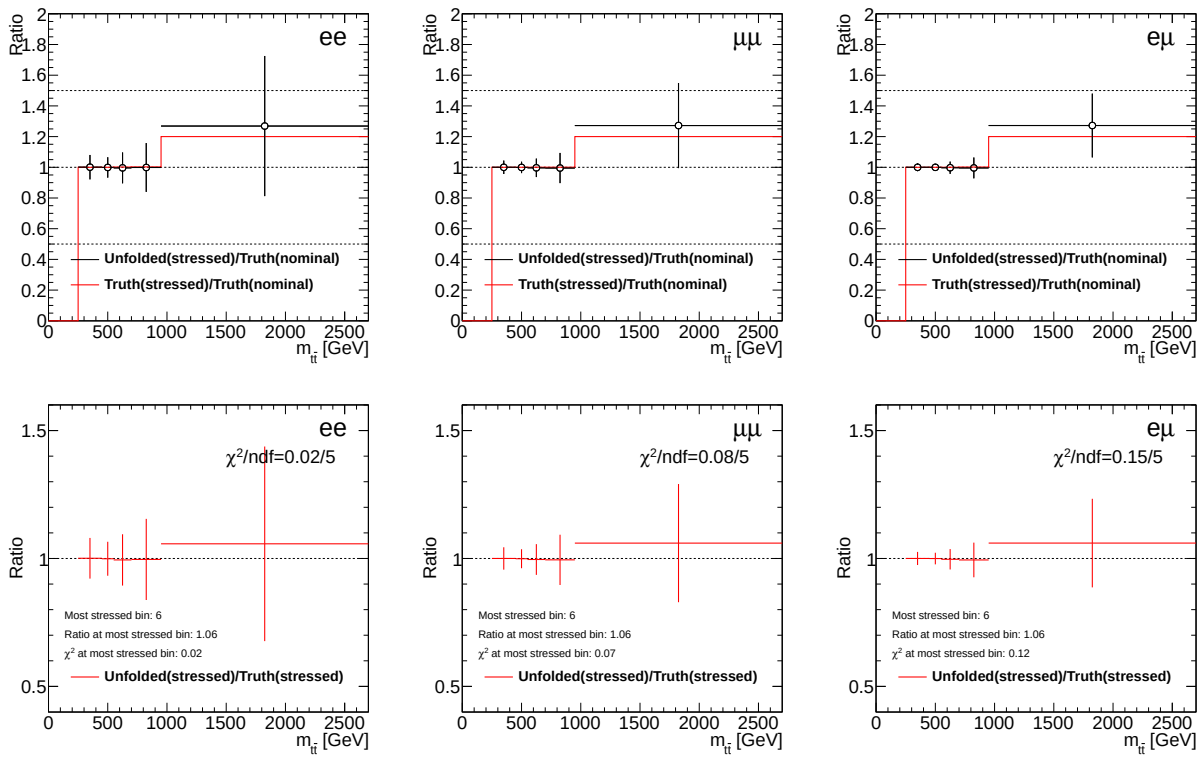

Figure 8.9: Stress test in $m_{t\bar{t}}$ with $Z' \to t\bar{t}$ resonance at $m_{Z'} = 1.6$ TeV in the ee, $\mu\mu$ and $e\mu$ channels. The signal strength is 20% at the most stressed bin. 4 iterations in Bayesian unfolding is used for this test. The ratio of stressed unfolded and stressed truth at most stressed bin is ≈ 1.0.

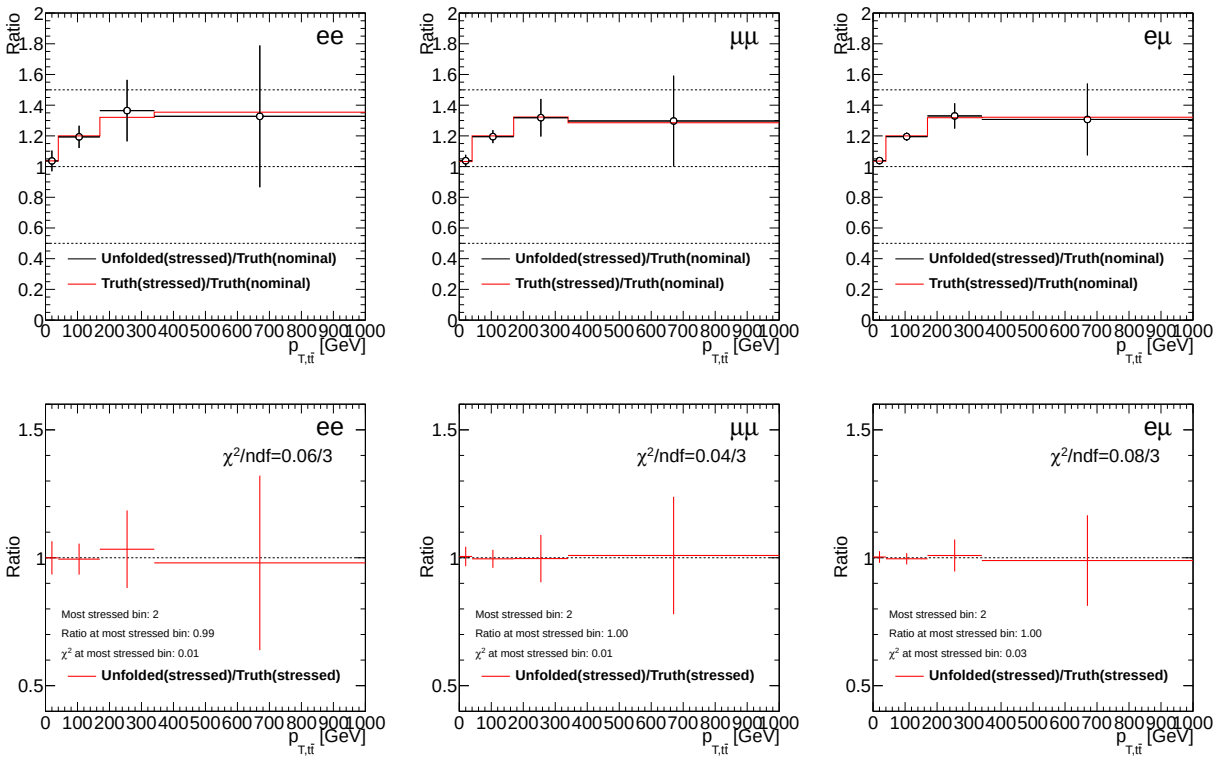

Figure 8.10: Stress test in $p_{\mathrm{T}}^{t\bar{t}}$ with $t\bar{t}$ ALPGEN+HERWIG lnln Np3 sample in the ee, $\mu\mu$ and $e\mu$ channels. The signal strength is 20% at the most stressed bin. 2 iterations in Bayesian unfolding is used for this test. The ratio of stressed unfolded and stressed truth at most stressed bin is ≈ 1.0.

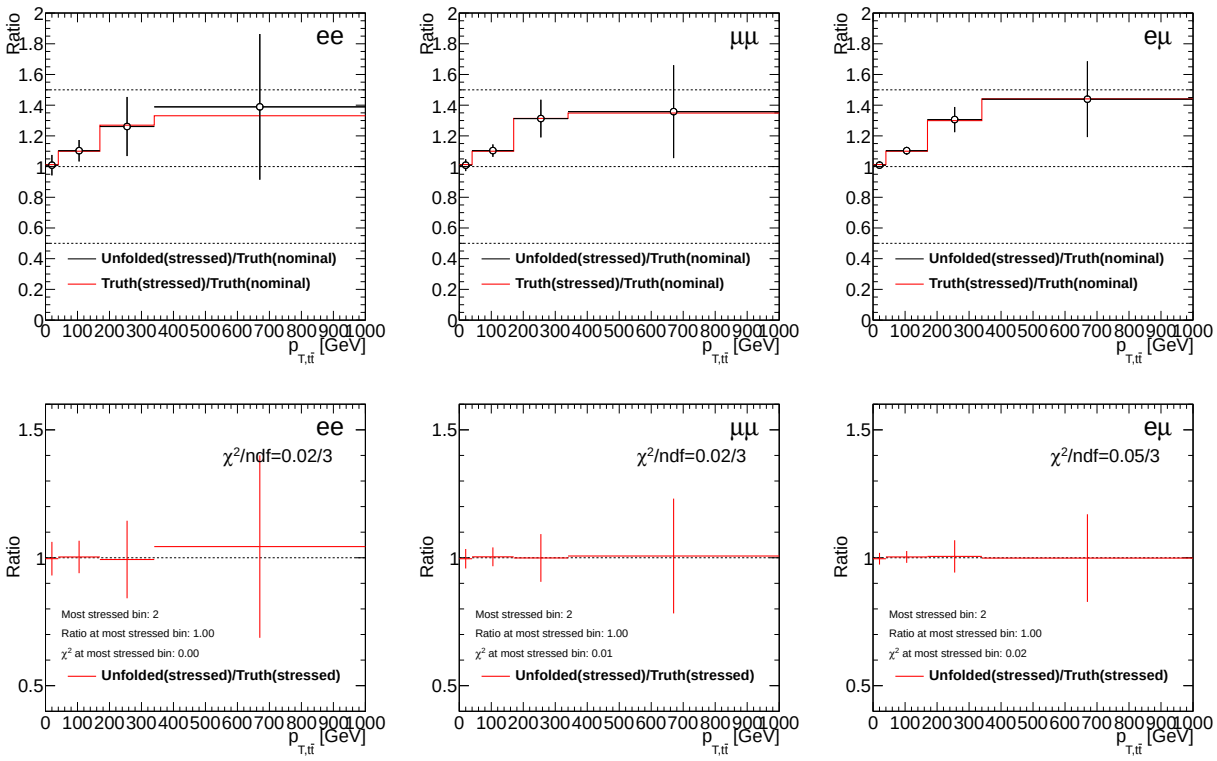

Figure 8.11: Stress test in $p_{\mathrm{T}}^{t\bar{t}}$ with $t\bar{t}$ ALPGEN+HERWIG lnln Np4 sample in the ee, $\mu\mu$ and $e\mu$ channels. The signal strength is 20% at the most stressed bin. 2 iterations in Bayesian unfolding is used for this test. The ratio of stressed unfolded and stressed truth at most stressed bin is ≈ 1.0.

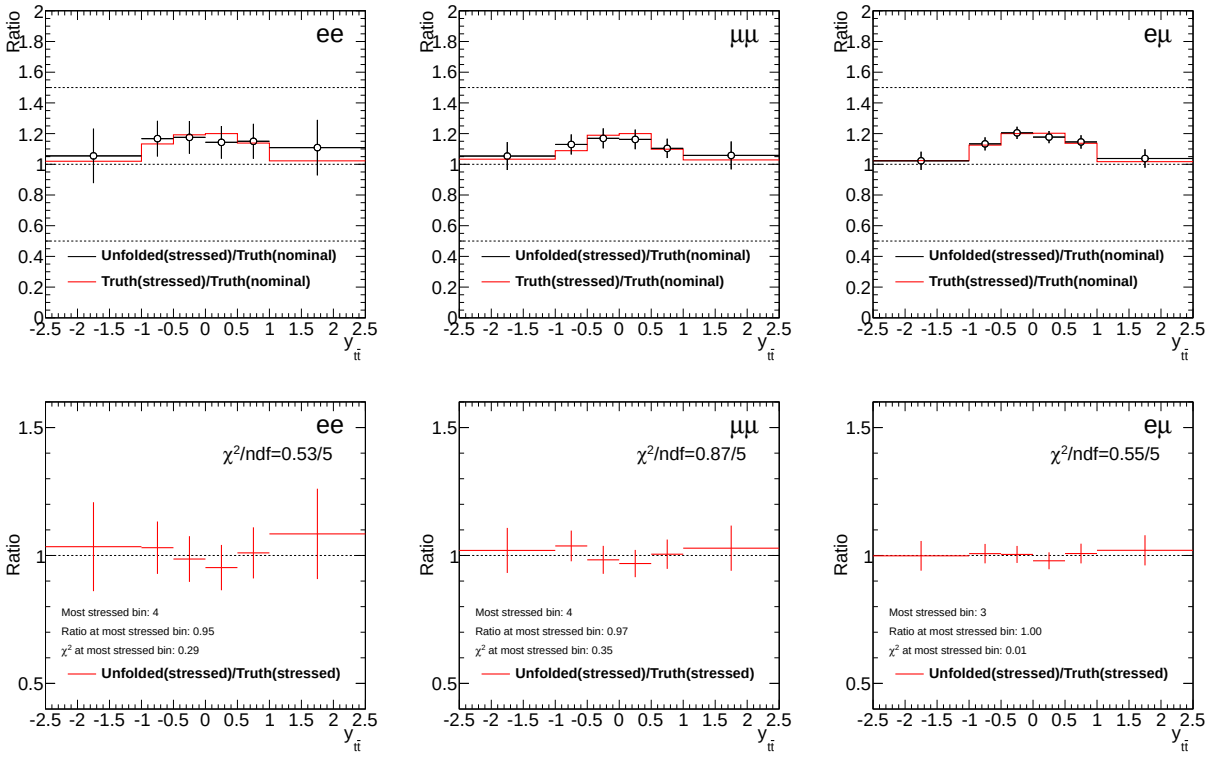

Figure 8.12: Stress test of $y_{t\bar{t}}$ with $Z' \to t\bar{t}$ resonance at $m_{Z'} = 1.6$ TeV in the ee, $\mu\mu$ and $e\mu$ channels. The signal strength is 20% at the most stressed bin. 3 iterations in Bayesian unfolding is used for this test. The ratio of stressed unfolded and stressed truth at most stressed bin is ≈ 1.0.

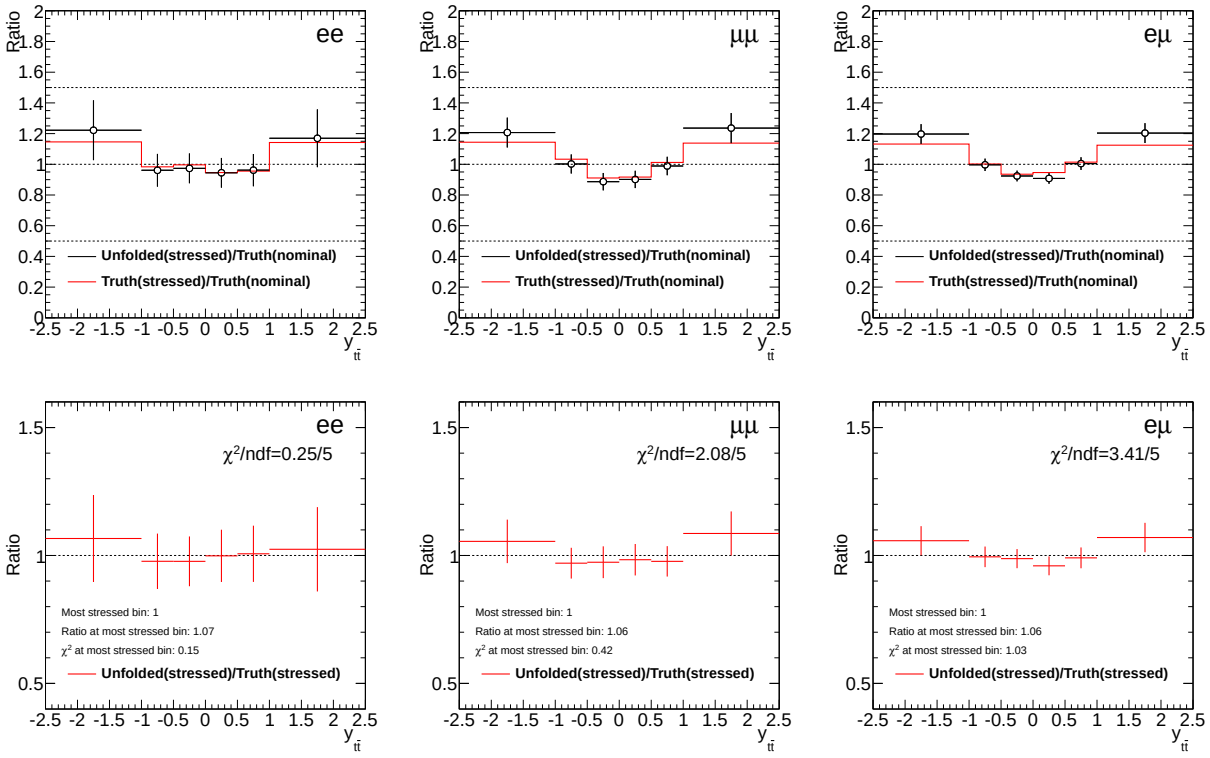

Figure 8.13: Stress test of $y_{t\bar{t}}$ with $t\bar{t}$ ALPGEN+HERWIG lnln Np0 sample in the ee, $\mu\mu$ and $e\mu$ channels. The signal strength is about 15% at the most stressed bin. 3 iterations in Bayesian unfolding is used for this test. The ratio of stressed unfolded and stressed truth at most stressed bin is ≈ 1.1.

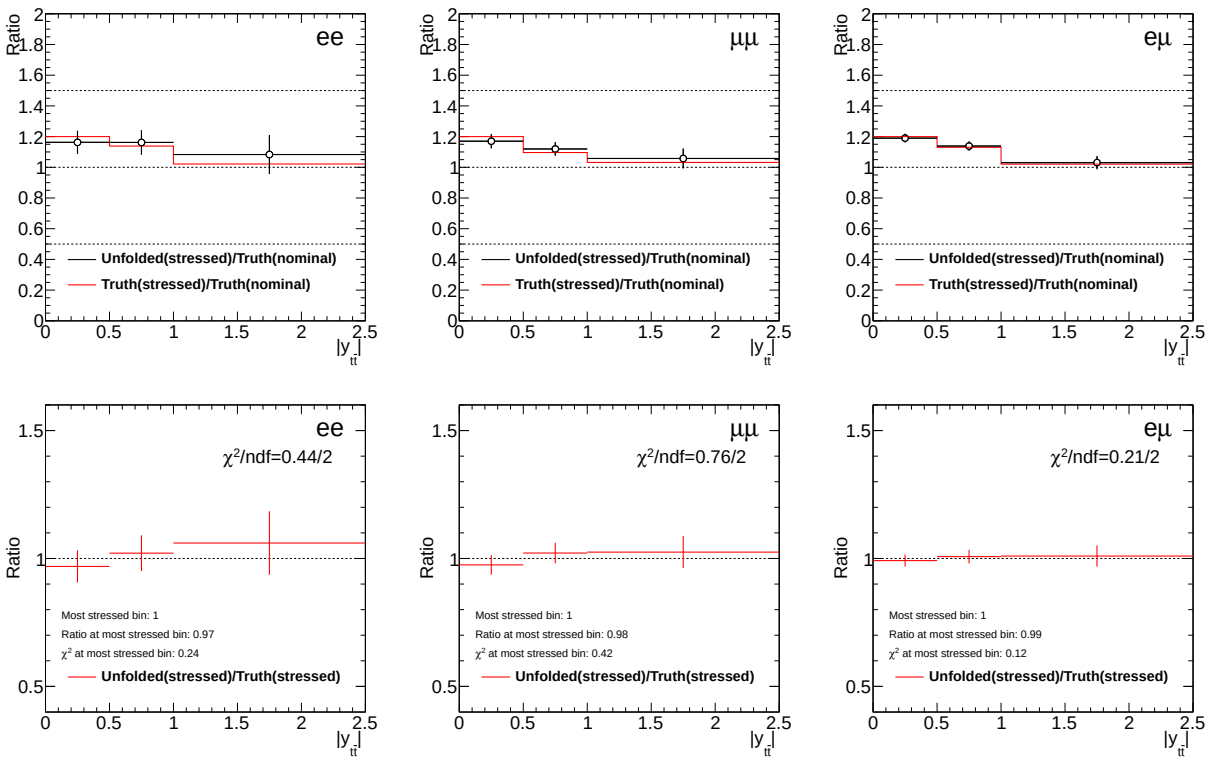

Figure 8.14: Stress test of $|y_{t\bar{t}}|$ with $Z' \to t\bar{t}$ resonance at $m_{Z'} = 1.6$ TeV in the ee, $\mu\mu$ and $e\mu$ channels. The signal strength is 20% at the most stressed bin. 3 iterations in Bayesian unfolding is used for this test. The ratio of stressed unfolded and stressed truth at most stressed bin is ≈ 1.0.

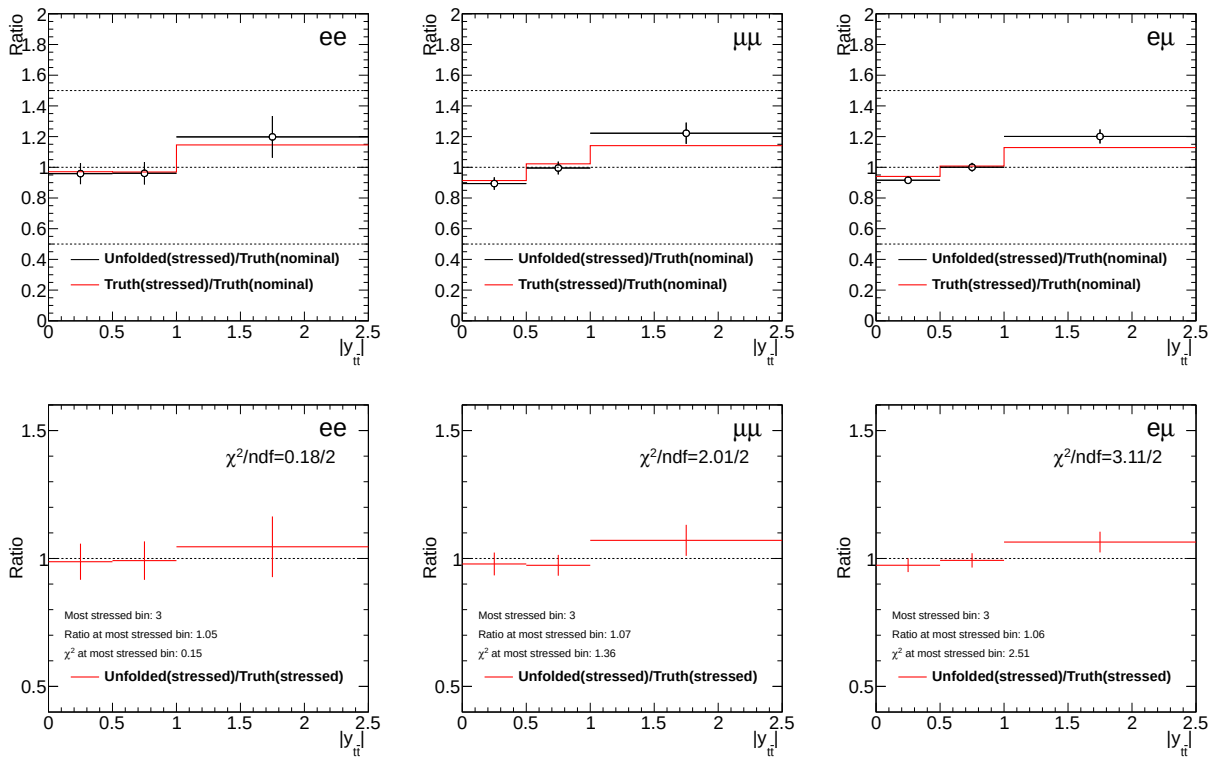

Figure 8.15: Stress test of $|y_{t\bar{t}}|$ with $t\bar{t}$ ALPGEN+HERWIG lnln Np0 sample in the ee, $\mu\mu$ and $e\mu$ channels. The signal strength is about 15% at the most stressed bin. 3 iterations in Bayesian unfolding is used for this test. The ratio of stressed unfolded and stressed truth at most stressed bin is ≈ 1.1.

8.5 Unfolded data

Figure 8.16 shows measured reconstructed $m_{t\bar{t}}$, $p_{\mathrm{T}}^{t\bar{t}}$, $y_{t\bar{t}}$ and $|y_{t\bar{t}}|$ distributions subtracted with predicted backgrounds. Figure 8.17 shows the background-subtracted data spectra unfolded to the number of events in the true spectra. The hatched error band includes the total statistical and systematic uncertainties. The statistical uncertainty is taken as square root of the diagonal elements of the data statistical convariance matrix. The systematic contributions include all (the detector modelling, background modelling, $t\bar{t}$ modelling, unfolding uncertainties and luminosity uncertainty) as discussed in chapter 9. The unfolded spectra is to be corrected by acceptance and efficiency per bin to differential cross sections.

The choices of number of iterations in Table 8.3 are used to unfold the data, i.e. for n=4 for $m_{t\bar{t}}$, n=2 for $p_{\mathrm{T}}^{t\bar{t}}$, n=3 for $y_{t\bar{t}}$ and $|y_{t\bar{t}}|$. The same n's are used across the dilepton ee, $\mu\mu$ and $e\mu$ channels. The study of the number of iterations in the Bayesian unfolding in discussed in the Section 8.3.

Figures 8.18 and 8.19 show the covariance and correlation matrix of each $t\bar{t}$ system variable after unfolding, respectively.

Figure 8.20 shows the ratio of the total variance without covariance from the unfolded data spectrum and the total variance in the measured and reconstructed data spectrum for each $t\bar{t}$ system variable, compared across 10 iterations in the Bayesian unfolding. This is to show that the best choices of number of iterations discussed in Section 8.3.2 and Table 8.3 are applicable when unfolding data, which has a different statistics for the input data. One may infer that these choices of iteration number has little dependence on or is independent of the data statistics, but depends on the conditions (shape of spectrum, migration matrix) of the unfolded variables of interest.

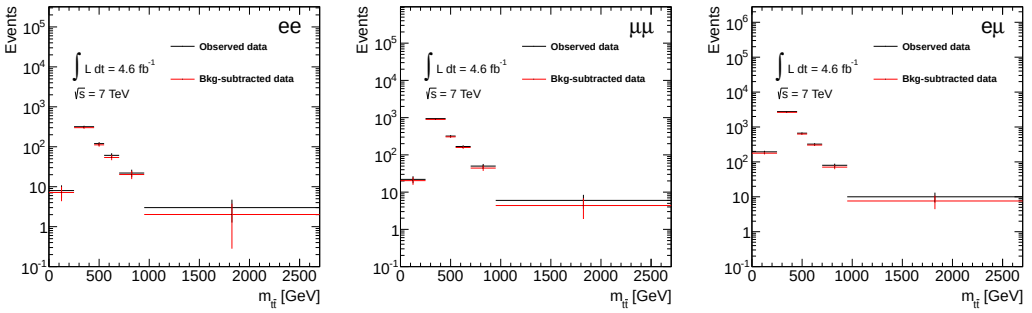

(a) $m_{t\bar{t}}$

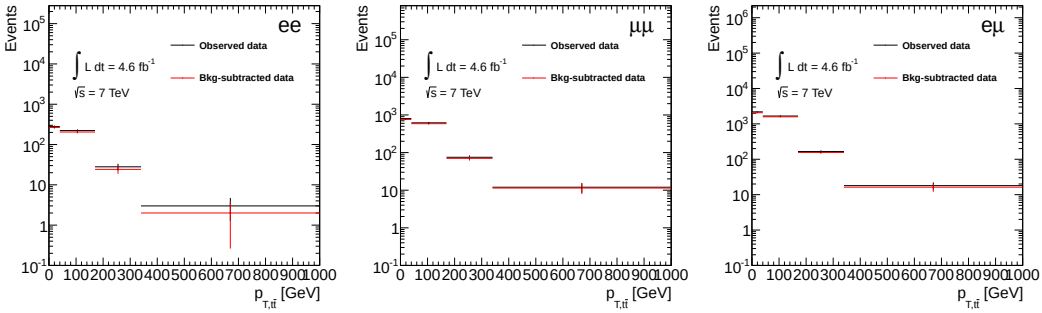

(b) $p_{\mathrm{T}}^{t\bar{t}}$

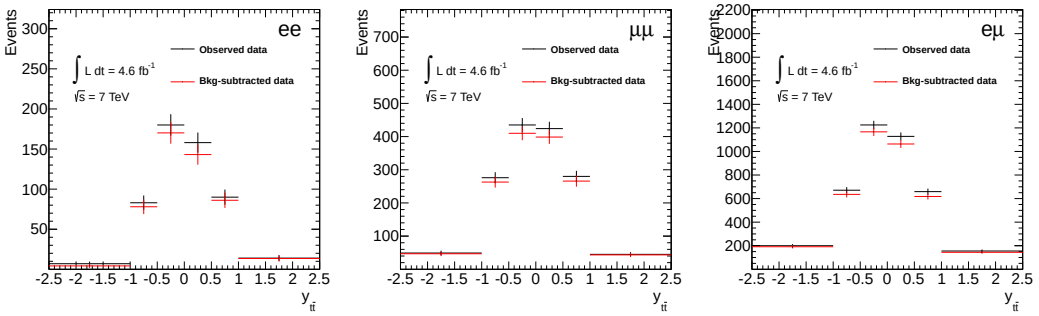

(c) $y_{t\bar{t}}$

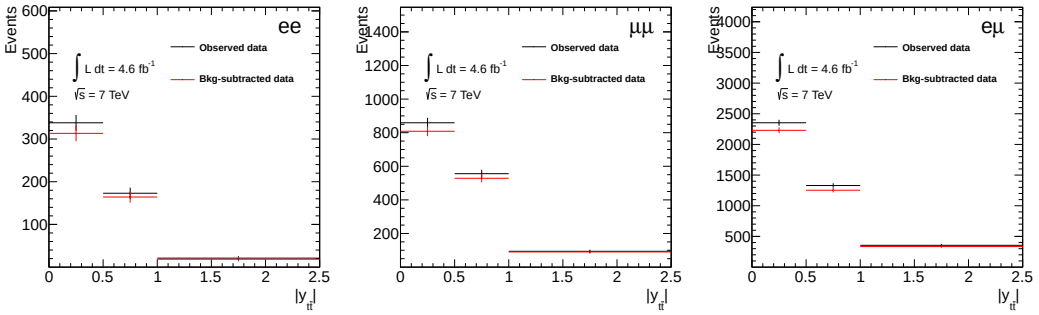

(d) $|y_{t\bar{t}}|$

Figure 8.16: The background-subtracted data (a)$m_{t\bar{t}}$, (b)$p_{\mathrm{T}}^{t\bar{t}}$, (c)$y_{t\bar{t}}$ and (d)$|y_{t\bar{t}}|$ spectrum in the ee (left), $\mu\mu$ (center) and $e\mu$ (right) channels.

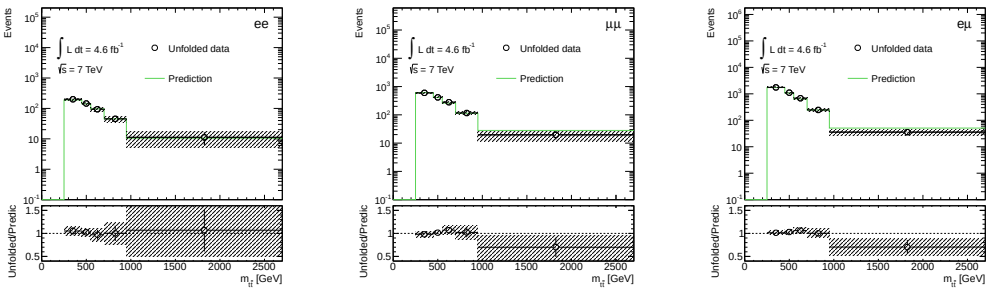

(a) $m_{t\bar{t}}$

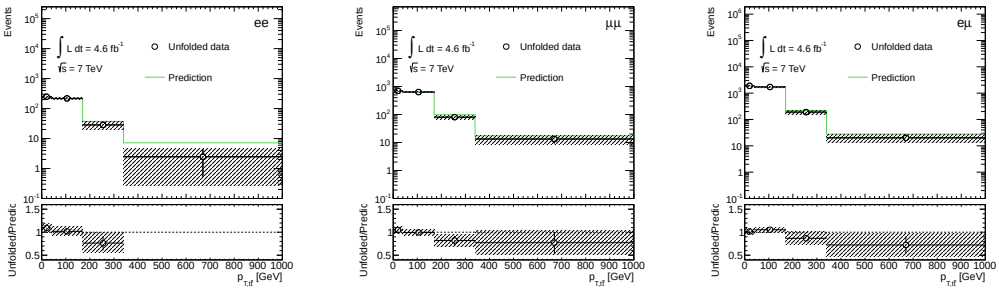

(b) $p_{\mathrm{T}}^{t\bar{t}}$

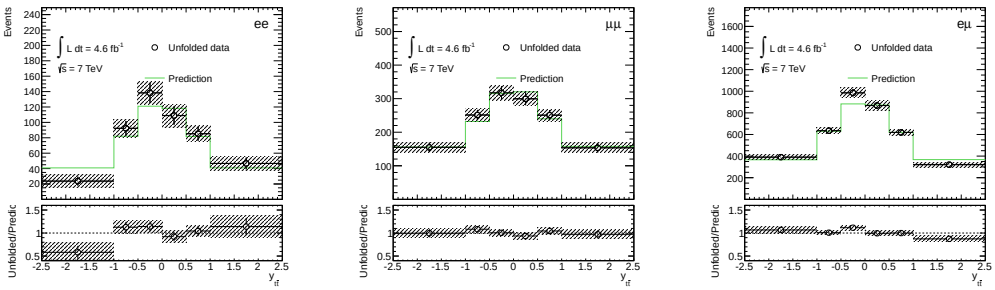

(c) $y_{t\bar{t}}$

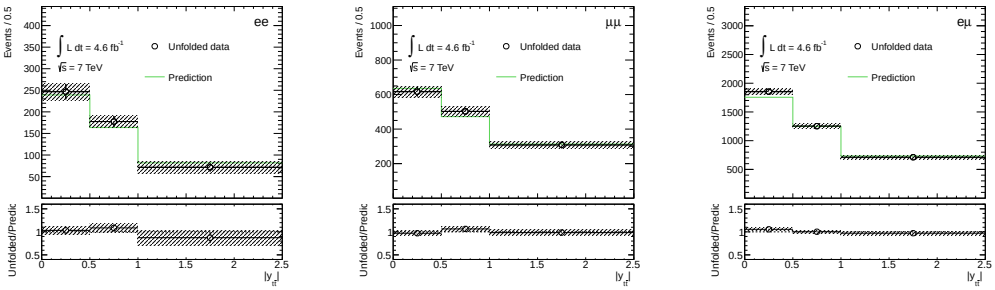

(d) $|y_{t\bar{t}}|$

Figure 8.17: The unfolded data (a)$m_{t\bar{t}}$, (b)$p_{\mathrm{T}}^{t\bar{t}}$, (c)$y_{t\bar{t}}$ and (d)$|y_{t\bar{t}}|$ spectrum in the ee (left), $\mu\mu$ (center) and $e\mu$ (right) channels. The unfolded data is overlayed and compared with the prediction: the baseline $t\bar{t}$ Powheg+Pythia P2011C sample. The error bars include the unfolded data statistical uncertainties.

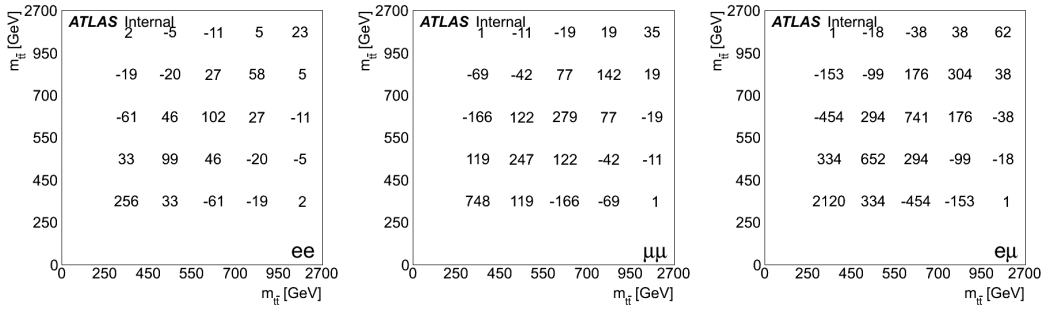

(a) $m_{t\bar{t}}$

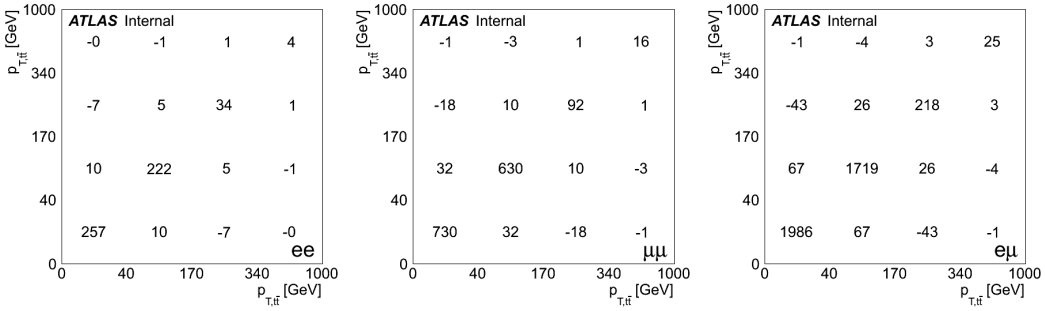

(b) $p_{\mathrm{T}}^{t\bar{t}}$

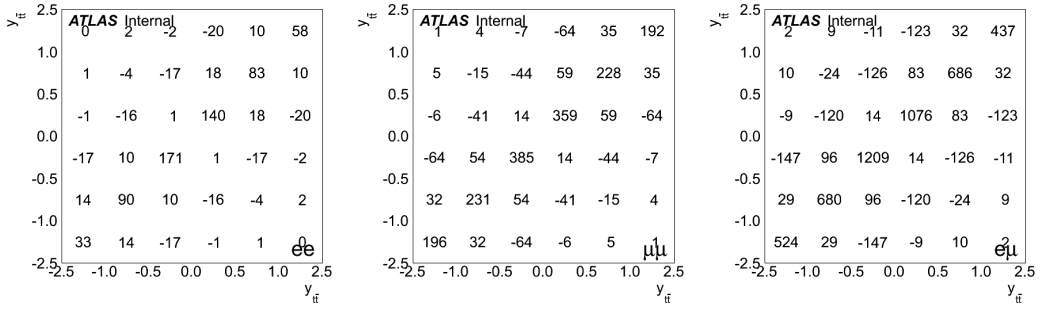

(c) $y_{t\bar{t}}$

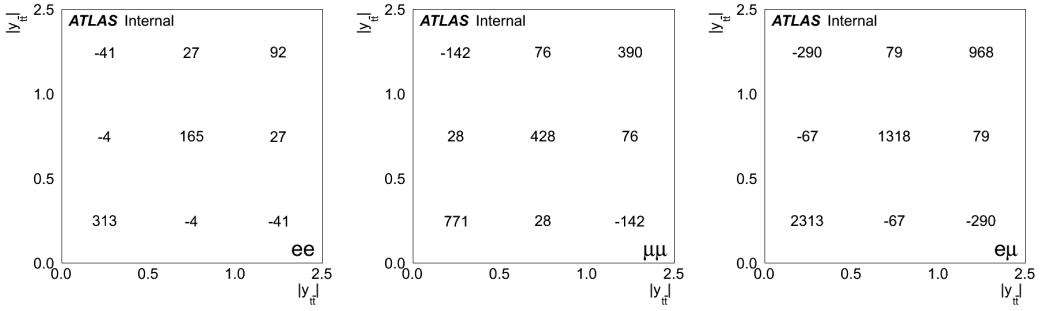

(d) $|y_{t\bar{t}}|$

Figure 8.18: The covariance matrix of (a)$m_{t\bar{t}}$, (b)$p_{\mathrm{T}}^{t\bar{t}}$, (c)$y_{t\bar{t}}$ and (d)$|y_{t\bar{t}}|$ in the ee (left), $\mu\mu$ (center) and $e\mu$ (right) channels.

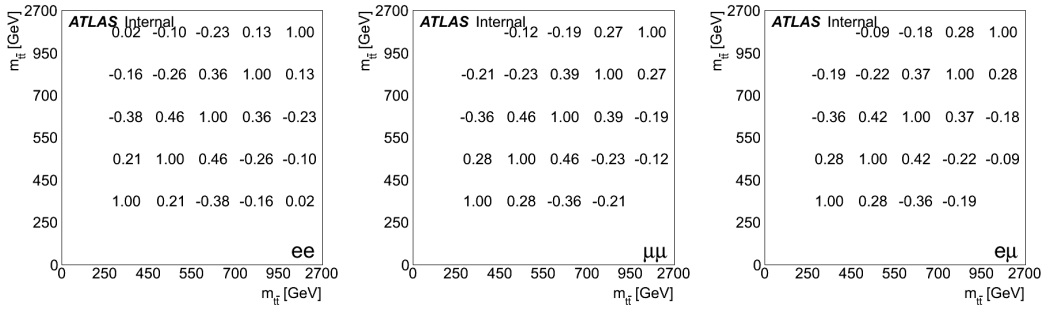

(a) $m_{t\bar{t}}$

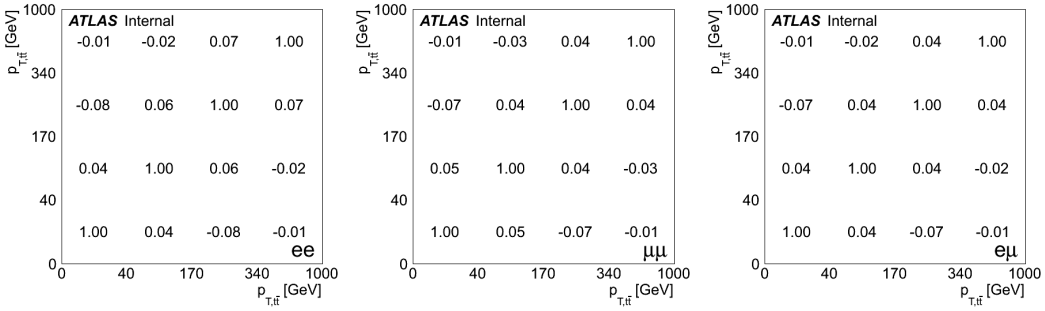

(b) $p_{\mathrm{T}}^{t\bar{t}}$

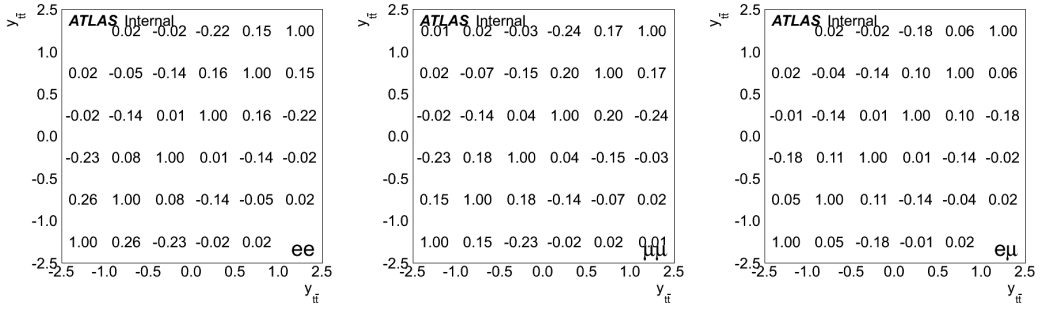

(c) $y_{t\bar{t}}$

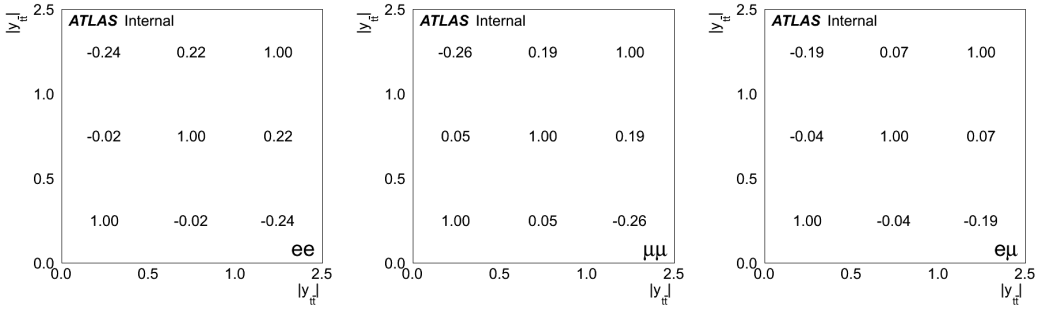

(d) $|y_{t\bar{t}}|$

Figure 8.19: The correlation matrix of (a)$m_{t\bar{t}}$, (b)$p_{\mathrm{T}}^{t\bar{t}}$, (c)$y_{t\bar{t}}$ and (d)$|y_{t\bar{t}}|$ in the ee (left), $\mu\mu$ (center) and $e\mu$ (right) channels.

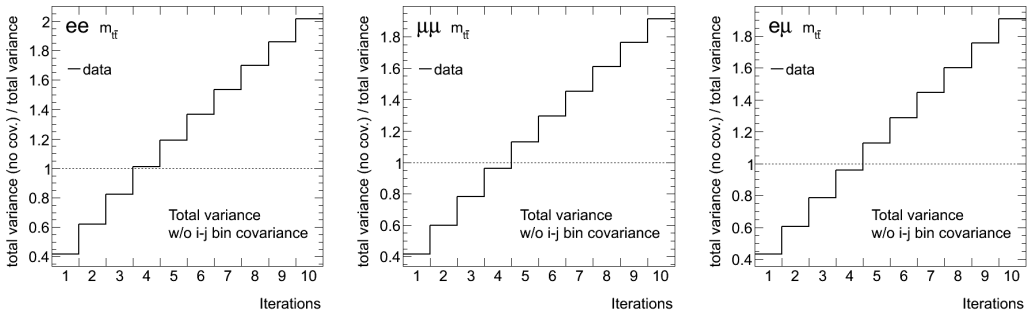

(a) $m_{t\bar{t}}$

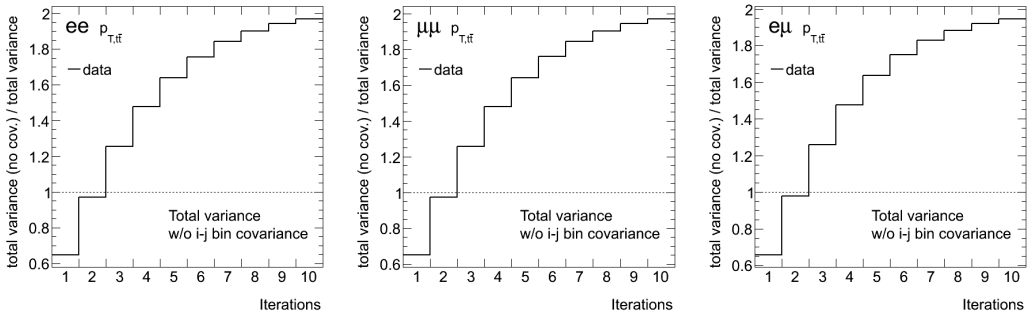

(b) $p_{\mathrm{T}}^{t\bar{t}}$

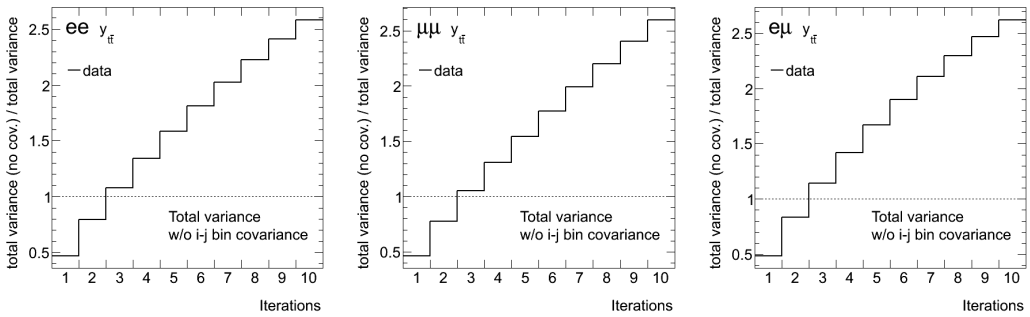

(c) $y_{t\bar{t}}$

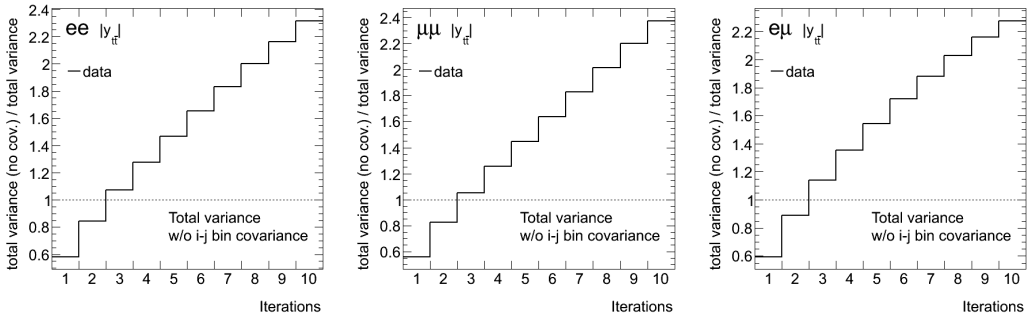

(d) $|y_{t\bar{t}}|$

Figure 8.20: The ratio of the total variance integrated from unfolded spectrum *without* covariances and the total variance in measured spectrum, as a function of number of iterations in Bayesian unfolding of (a)$m_{t\bar{t}}$, (b)$p_{\mathrm{T}}^{t\bar{t}}$, (c)$y_{t\bar{t}}$ and (d)$|y_{t\bar{t}}|$ in the ee (left), $\mu\mu$ (center) and $e\mu$ (right) channels. Test data using half of the POWHEG +PYTHIA $t\bar{t}$ sample as input is compared. The other half of the POWHEG +PYTHIA $t\bar{t}$ is used as the training sample. The input test data uses the statistics from the MC (not scaled to data luminosity).

Chapter 9

Systematic Uncertainties

The evaluation of systematic uncertainties in this analysis follows the standard tools (`TopRootCore` packages) and Top group recommendation for systematic uncertainties in 2011 analyses ([38] and `https://twiki.cern.ch/twiki/bin/viewauth/AtlasProtected/TopSystematicUncertainties2011`).

Each systematic contribution corresponds to 1σ of the uncertainty contribution, and is first evaluated at the reconstructed level. The shifted spectra are propagated into unfolding and then compared with the unfolded result without systematics. Individual and total systematic uncertainties at both reconstructed and unfolded levels are evaluated and examined. All of the individual systematic contributions are assumed to be uncorrelated, and are summed in quadrature to obtain the total systematic uncertainty.

The systematic uncertainty evaluation in this analysis adopts the *data-based* method (as discussed in the ATLAS internal analysis note of the l+jets channel $t\bar{t}$ differential cross section measurement [43], section 11.3) as the default method. This method uses measured data as *the* input to unfolding and compares the unfolded data with a systematic-shifted setting in unfolding (i.e. a different migration matrix) to the unfolded data with the nominal setting. The difference between the two spectra is taken as the uncertainty for the systematic component. Another method, defined as the *MC-based* method (discussed in [43], section 11.3), uses a systematic-varied MC as input, unfolds it with the nominal unfolding matrix (from the nominal MC), and compares the unfolded spectrum with the true spectrum of the varied MC. The relative uncertainty (syst-true/true) is computed and then applied to unfolded data as the systematic uncertainty for each systematic component. The two methods of evaluating systematic uncertainties are compared in Section F.2 for $t\bar{t}$ modeling systematics, which involve different MC $t\bar{t}$ samples with varied MC statistics. The differences between the two methods in each bin of $m_{t\bar{t}}$, $p_{\mathrm{T}}^{t\bar{t}}$, $y_{t\bar{t}}$ and $|y_{t\bar{t}}|$ in each dilepton chanel are small, and neither methods show a generally smaller uncertainty in each of the individual $t\bar{t}$ modeling systematic uncertainties (especially when focusing on the low statistics bins in high $m_{t\bar{t}}$, $p_{\mathrm{T}}^{t\bar{t}}$ and $|y_{t\bar{t}}|$). Based on this study, the default data-based method is chosen to be applied to the uncertainty evaluation for all systematic components. The sum in quadrature of all systematic components gives the total systematic uncertainty.

9.1 Signal Modeling

- *MC generator*

  Predictions from the default signal sample POWHEG +PYTHIA (117050, fullSim) are compared with MC@NLO +HERWIG (105200) fullSim sample to account for the uncertainty in MC generators. Both samples are produced with next-to-leading order (NLO) generators. This choice of comparison is favored in this analysis rather than a comparison with ALPGEN +HERWIG samples due to the predicted higher acceptance in the leading order (LO) ALPGEN samples when compared to data at reconstructed level and to NLO MCs at truth level. The NLO-to-LO comparison, using the fullSim POWHEG +PYTHIA (117050) sample and fullSim ALPGEN +HERWIG samples (105890-2 and 117897-9 for dilepton, 105894-6 and 117887-9 for single lepton), are shown as a reference in detailed tables of systematic uncertainties, but is not taken into account in the estimation of total uncertainty.

- *Parton showering and hadronization*

  The effects of parton shower modelling are evaluated by comparing POWHEG AF2 samples interfaced to HERWIG (105860) and PYTHIA (117050). Both POWHEG + HERWIG (105860) and POWHEG + PYTHIA (117050) ALTFASTII samples are vetoed with events in generator-level with leptons (e, μ's) decayed from taus, since tau polarisation is neglected by Tauola during the tau decay in the POWHEG + HERWIG sample. In addition, dedicated ALTFASTII ALPGEN samples (117525-9 and 117535-9) interfaced to PYTHIA are generated with different initial state and final state radiation (ISR and FSR) settings to monitor effects of higher and lower parton shower activities. The radiation settings in these samples adopt simultaneous variations of `kT` factors and the parton shower tune from the baseline PYTHIA Perugia 2011 tune.

- *Parton Distribution Functions*

  The effect of different choices of parton distribution functions (PDF) in simulation is studied by reweighting the generated events by different NLO PDF sets. The procedure in evaluating the uncertainty follows the PDF4LHC working group recommendations [44].

  The detailed evaluations of the PDF uncertainties are described in Section F.1.

- *Color reconnection*

  The impact of different models of colour reconnection (CR) are studied by comparing POWHEG +PYTHIA AF2 samples in Perugia 2011 tune (117428) and Perugia 2011 no CR tune [45] (117429).

- *Underlying events*

  The effect of underlying events (UE) is also studied with POWHEG +PYTHIAALTFASTII samples in Perugia tune [45]. AF2 samples in Perugia 2011 (117428) and Perugia 2011 mpiHI tunes (117430) are compared to extract this systematic uncertainty.

- *Renormalization and factorization scales*

  The effect of matrix element renormalization (μ_R) and factorization (μ_F) scales is studied with MC@NLO +HERWIG AF2 samples with different renormalization/factorization scale variations. Differences between the mudown (110006) and muup (110007) samples are taken as the systematic uncertainties. This systematic uncertainty is shown in results only to be compared with the MC generator systematics, but is not taken into account in the total systematic uncertainty estimation.

9.2 Detector modeling

Standard tools (`TopRootCore` packages) and recommendations in TopSystematicUncertainties2011 twiki [46] and in [38] for final 2011 analyses are used to evaluate the all detector modeling uncertainties in this analysis.

- *Lepton scale and resolution*

  Lepton energy or momentum scale and resolution are corrected for the detector conditions to match the simulated data with the measured data. The transverse energy of electrons is scaled in data and smeared in MC; the muon transverse momentum is scaled and smeared both in MC. All lepton energy or momentum scale and resolution corrections, and their uncertainties, are provided by egammaAnalysisUtils-00-02-81 for the electron and MuonMomentumCorrections-00-05-03 and for the muon. The systematic uncertainties are applied to MC data.

- *Lepton ID, reconstruction, trigger and isolation scale factors*

  All electron scale factors and uncertainties are integrated in TopElectronSFUtils-00-00-18 developed by the top working group. Efficiencies and their uncertainties are parametrised in η and E_{T} in electron ID, isolation and trigger SFs, while the electron reconstruction SF is η-dependent. The uncertainties of isolation SFs include pileup effects (1%), underlying events ($< 1\%$) and the difference between top and W/Z electrons (close-by jets and ISR/FSR effects), and are added in quadrature to the statistical uncertainties to an overall a few percent [38]. The SFs and their uncertainties are evaluated with both full simulation and AFII samples, with the latter resulting in a slightly larger uncertainty due to pileup effects. The ID, reco and isolation SFs are combined in the TopElectronSFUtils tool.

Muon reconstruction efficiency is provided by MuonEfficiencyCorrections-01-01-00 developed by Muon Combined Performance (MCP) group, while muon top-ID, isolation and trigger efficiencies are available in TopMuonSFUtils-00-00-14 provided by the top working group is used. Muon reconstruction SFs use a p_{T}-η-ϕ map of efficiency measurements; muon ID and isolation SFs are evaluated according to different data periods; the muon trigger SFs are a function of η and ϕ and also data periods. The uncertainty on the resulting reco-id-isolation scale factors are within 1% [38], while the uncertainty on the trigger scale factors is typically 1% [38].

- *Jet energy scale (JES)*

  The jet energy scale (JES) uncertainty is evaluated using the recommended tool JetUncertainties-00-08-06.

  The total JES uncertainty is a linear sum of JES uncertainties in the $t\bar{t}$ signal and background samples (they are highly correlated). In the signal $t\bar{t}$ sample, the JES uncertainty is evaluated from a total of 22 components of sources independently. The total JES uncertainty in signal events is the sum of all components (according to the positive and negative directions shifted from the nominal) in quadrature. The background JES uncertainty is evaluated in the background MC samples using the overall uncertainty instead of individual JES components, due to small differences between overall- and individual-component-based evaluation in backgrounds and technical simplicity.

  A more specific treatment is done in the $t\bar{t}$ sample to better describe the assumption of the jet condition in $t\bar{t}$ events. The gluon fractions of jets in the $t\bar{t}$ sample are parametrised in the dilepton channel in η and in p_{T} and are used as input (`MJESttbarDi_rel16.root` in `MultiJesInputFiles`) in the evaluation of JES uncertainty in signal events. The quark-gluon composition for the background samples are assumed to be the default one (50%-50%). Figure 9.1 shows the two configurations used for estimating the jet flavor composition uncertainties.

- *Jet energy resolution*

  Systematic uncertainties of the smearing of jet transverse energy are provided by JetResolution-01-00-00. The systematics are applied to MC data.

- *Jet reconstruction efficiency*

  Systematic uncertainties of jet reconstruction efficiency is provided by JetEffiProvider-00-00-05.

- *Jet vertex fraction (JVF) scale factors*

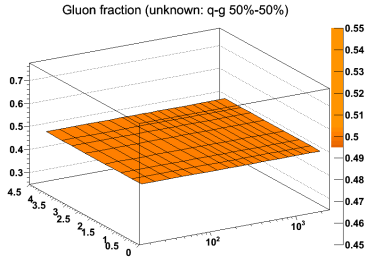

(a) Gluon fractions (50%)

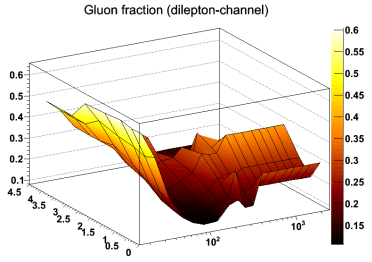

(b) Gluon fractions (parametrised in dilepton)

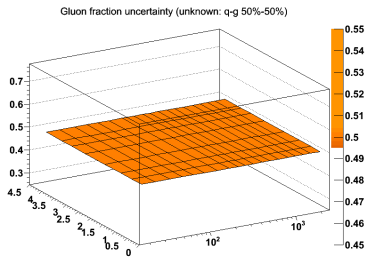

(c) Uncertainties in gluon fractions (50%)

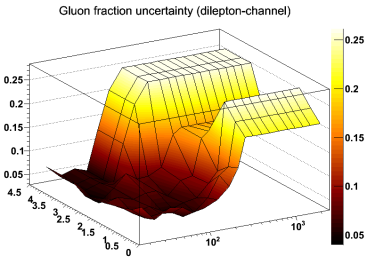

(d) Uncertainties in gluon fractions (parametrised in dilepton)

Figure 9.1: Gluon fractions and uncertainties in η and p_{T} used as inputs to estimate jet flavor composition uncertainties. In background samples, unknown composition (50%-50% quark-gluon fractions) (left) is assumed, while a parametrised fraction in $t\bar{t}$ dilepton events (right) is used for $t\bar{t}$ signal events.

JVF scale factors and uncertainties are provided by TopJetUtils-00-00-07, and are both applied to MC data.

- *Missing transverse energy*

  Uncertainty contributions from out-of-cluster calorimeter cells and low-p_{T} jets from soft interactions are evaluated, and are added in quadrature with uncertainties evaluated from corrections of pile-up effects. The calculations are done in MissingETUtility-01-00-09.

- *b-tagging efficiency*

  The uncertainties of the scale factors of b-tagging and mis-tag rates of the MV1 tagger are obtained from the Calibration Data Interface file `2014-Winter-7TeV-MC11-CDI.root` for 2011 data. The calibration scheme used is `ttbar_pdf_dijet`, derived from a combination of the ttbar PDF, system8 and pTrel calibration analyses. It is the latest default calibration recommended by the top b-tagging working group [47].

9.3 Background modeling

- *Fake leptons*

  The fake lepton estimation is varied with the uncertainties of the real and fake rates of each lepton, and the variations are summed in quadrature to give the uncertainty in fake estimation. Uncertainties in normalization and shape are evaluated. The standard and recommended tool (`FakesMacros-00-00-32`) is used to calculate the fake lepton estimation and its variations from data.

- *Single top normalization*

  Variations in the cross-sections of single top background processes based on theoretical approximate NNLO calculations [28] are applied on the overall normalization of the single top MC samples. The effect of this contribution is less than 1% in the measured inclusive and differential $t\bar{t}$ cross sections.

9.4 MC statistics

The uncertainty of MC statistics accounts for the finiteness of MC samples. In the measurement of reconstructed spectra, the $\sqrt{(N)}$ of each sample is weighted and summed in quadrature with all other samples in each bin. For measurements involving unfolding, the uncertainty from $t\bar{t}$ sample is obtained from the MC statistical covariance matrix after the unfolding. This matrix is evaluated by doing 1000 toy experiments with the unfolding, each with a poisson-randomized response matrix derived from the $t\bar{t}$ MC. The variances (diagonal elements) reflect the finiteness of the MC sample after unfolding (with the choice of unfolding parameter for regularization).

9.5 Luminosity Uncertainty

A flat uncertainty of 1.8% [38] (Section 5.2) is applied to all backgrounds and signal MC samples and propagated to the measured inclusive and differential cross-sections. In the case of normalized differential cross-sections, the effects are mostly suppressed due to the same uncertainty in the inclusive cross-section measurement.

Chapter 10

$t\bar{t}$ Differential Cross Sections Measurements

In this section, the summarized results of the unfolded differential cross-sections $d\sigma/dm_{t\bar{t}}$, $d\sigma/dp_{\mathrm{T}}^{t\bar{t}}$, $d\sigma/dy_{t\bar{t}}$ and $d\sigma/d|y_{t\bar{t}}|$ are presented in the ee, $\mu\mu$ and $e\mu$ channels, respectively. For each $t\bar{t}$ system variable, the absolute and normalized differential cross-sections are calculated as described in Section 2.3 and are presented in summary tables (10.1,10.2,10.6,10.7,10.11,10.12,10.16,10.17) and in figures (10.1,10.2,10.3,10.4) with the nominal measured values and the associated uncertainties. The integrated inclusive $t\bar{t}$ cross section $\sigma_{t\bar{t}}^{int}$ and the integral of the normalized differential cross-sections are also shown in the summary tables. The integrated inclusive cross-section is obtained from the differential cross-section results by summing all the bin contents of the unfolded differential cross-section distributions multiplying their respective bin widths. This $\sigma_{t\bar{t}}^{int}$ is consistent with the value obtained by a cut-and-count method (see Appendix E) using the same data and background events as in the differential measurements, and is consistent across the $t\bar{t}$ system variables. The result summary is followed by a summarized table of the breakdown of each systematic uncertainty for each of the absolute and normalized measurements.

The unfolded differential cross-section results are compared with various Monte-Carlo $t\bar{t}$ models beside the default Powheg +Pythia MC: MC@NLO +Herwig, Alpgen +Herwig and Powheg +Pythia with HeraPDF. The result figures show the generated parton-level differential cross-sections of these MC models overlayed with the measured unfolded differential cross-sections, and their respective ratios.

Bin-to-bin correlations in each measured distributions are also shown in Tables 10.5, 10.10, 10.15 and 10.20. These correlations are due to migrations of bin contents during unfolding.

10.1 Results for $m_{t\bar{t}}$

From equation 2.3, the unfolded absolute and normalized differential cross sections are measured as shown in Tables 10.1 and 10.2. The systematic and statistical uncertainty components of the absolute and normlized differential measurements for each dilepton channel are shown in Tables 10.3 and 10.4. Figure 10.1 shows the measured results compared with different MCs.

4 iterations are used to unfold the $m_{t\bar{t}}$ spectrum, as discussed in Sections 8.3.2 and 8.5.

The correlation matrix is shown in table 10.5.

$m_{t\bar{t}}$ [GeV]	$d\sigma/dm_{t\bar{t}}$ [pb/GeV]	Stat. [%]	Syst. [%]
250-450	$0.454^{+0.065}_{-0.064}$	± 7.9	$^{+12}_{-12}$
450-550	$0.501^{+0.075}_{-0.072}$	± 6.9	$^{+13}_{-13}$
550-700	$0.181^{+0.032}_{-0.032}$	± 11	$^{+14}_{-14}$
700-950	$0.045^{+0.011}_{-0.011}$	± 17	$^{+17}_{-17}$
950-2700	$0.0017^{+0.0009}_{-0.0009}$	± 43	$^{+28}_{-27}$
$\sigma^{int}_{t\bar{t}}$ [pb]	$182.3^{+16.0}_{-15.7}$	± 4.8	$^{+7.3}_{-7.1}$

(a) ee

$m_{t\bar{t}}$ [GeV]	$d\sigma/dm_{t\bar{t}}$ [pb/GeV]	Stat. [%]	Syst. [%]
250-450	$0.423^{+0.029}_{-0.029}$	± 4.5	$^{+5.0}_{-5.0}$
450-550	$0.497^{+0.034}_{-0.033}$	± 3.8	$^{+5.7}_{-5.5}$
550-700	$0.200^{+0.021}_{-0.021}$	± 5.9	$^{+8.7}_{-8.7}$
700-950	$0.046^{+0.008}_{-0.008}$	± 10	$^{+14}_{-13}$
950-2700	$0.0011^{+0.0004}_{-0.0005}$	± 30	$^{+23}_{-29}$
$\sigma^{int}_{t\bar{t}}$ [pb]	$177.7^{+7.7}_{-7.6}$	± 2.7	$^{+3.3}_{-3.3}$

(b) $\mu\mu$

$m_{t\bar{t}}$ [GeV]	$d\sigma/dm_{t\bar{t}}$ [pb/GeV]	Stat. [%]	Syst. [%]
250-450	$0.437^{+0.032}_{-0.032}$	± 2.6	$^{+6.9}_{-6.8}$
450-550	$0.504^{+0.038}_{-0.037}$	± 2.3	$^{+7.2}_{-7.0}$
550-700	$0.198^{+0.022}_{-0.021}$	± 4.0	$^{+10}_{-10}$
700-950	$0.045^{+0.006}_{-0.006}$	± 7.0	$^{+12}_{-11}$
950-2700	$0.0011^{+0.0003}_{-0.0003}$	± 22	$^{+18}_{-17}$
$\sigma^{int}_{t\bar{t}}$ [pb]	$180.8^{+8.3}_{-8.2}$	± 1.6	$^{+4.3}_{-4.2}$

(c) $e\mu$

Table 10.1: Unfolded absolute differential cross section of $t\bar{t}$ as a function of $m_{t\bar{t}}$ in the ee, $\mu\mu$ and $e\mu$ channels with the total, statistical only and systematic only uncertainties in each bin. The bottom row shows the total $\sigma_{t\bar{t}}$ integrated from the differential measurements.

$m_{t\bar{t}}$ [GeV]	$(1/\sigma)d\sigma/dm_{t\bar{t}}$ [TeV^{-1}]	Stat. [%]	Syst. [%]
250-450	$2.49^{+0.22}_{-0.22}$	± 8.0	$^{+3.9}_{-4.0}$
450-550	$2.75^{+0.23}_{-0.22}$	± 6.8	$^{+4.7}_{-4.4}$
550-700	$0.99^{+0.12}_{-0.12}$	± 11	$^{+5.8}_{-6.1}$
700-950	$0.25^{+0.06}_{-0.06}$	± 17	$^{+17}_{-17}$
950-2700	$0.0094^{+0.0045}_{-0.0045}$	± 43	$^{+23}_{-22}$
Integrated	$1^{+0.06}_{-0.06}$	± 4.9	$^{+2.7}_{-2.7}$

(a) ee

$m_{t\bar{t}}$ [GeV]	$(1/\sigma)d\sigma/dm_{t\bar{t}}$ [TeV^{-1}]	Stat. [%]	Syst. [%]
250-450	$2.38^{+0.14}_{-0.14}$	± 4.6	$^{+3.6}_{-3.6}$
450-550	$2.80^{+0.12}_{-0.12}$	± 3.7	$^{+2.1}_{-2.0}$
550-700	$1.12^{+0.09}_{-0.09}$	± 6.0	$^{+5.2}_{-5.2}$
700-950	$0.26^{+0.04}_{-0.04}$	± 10	$^{+11}_{-10.0}$
950-2700	$0.0063^{+0.0023}_{-0.0025}$	± 30	$^{+21}_{-26}$
Integrated	$1^{+0.03}_{-0.03}$	± 2.7	$^{+2.1}_{-2.1}$

(b) $\mu\mu$

$m_{t\bar{t}}$ [GeV]	$(1/\sigma)d\sigma/dm_{t\bar{t}}$ [TeV^{-1}]	Stat. [%]	Syst. [%]
250-450	$2.42^{+0.09}_{-0.10}$	± 2.6	$^{+2.9}_{-3.0}$
450-550	$2.79^{+0.11}_{-0.11}$	± 2.3	$^{+3.0}_{-3.0}$
550-700	$1.10^{+0.07}_{-0.07}$	± 4.0	$^{+5.0}_{-4.9}$
700-950	$0.25^{+0.03}_{-0.02}$	± 7.1	$^{+7.5}_{-7.0}$
950-2700	$0.0062^{+0.0017}_{-0.0016}$	± 22	$^{+15}_{-14}$
Integrated	$1^{+0.03}_{-0.03}$	± 1.7	$^{+1.9}_{-1.9}$

(c) $e\mu$

Table 10.2: Unfolded normalized differential cross section of $t\bar{t}$ as a function of $m_{t\bar{t}}$ in the ee, $\mu\mu$ and $e\mu$ channels with the total, statistical only and systematic only uncertainties in each bin. The last entry of each table is the integrated sum of the normalized differential cross sections, and is consistent with unity.

$d\sigma/dm_{t\bar{t}}$ (ee)	Bins [GeV]				
Uncertainties [%]	250-450	450-550	550-700	700-950	950-2700
Total	14.23 / -14.02	15.00 / -14.44	17.64 / -17.50	23.89 / -23.86	51.37 / -51.06
Stat. only	7.94 / -7.94	6.92 / -6.92	10.76 / -10.76	16.75 / -16.75	43.26 / -43.26
Syst. only	11.80 / -11.55	13.31 / -12.67	13.98 / -13.81	17.03 / -16.99	27.71 / -27.13
Jet	1.96 / -2.44	4.70 / -3.70	6.01 / -6.42	3.50 / -5.17	8.51 / -7.92
Tagging	1.84 / -1.72	1.78 / -1.65	2.20 / -2.01	3.17 / -2.88	5.39 / -4.27
Lepton	6.17 / -5.61	6.87 / -6.31	7.49 / -6.95	8.06 / -7.21	7.75 / -7.23
$E_{\mathrm{T}}^{\mathrm{miss}}$	0.67 / -0.27	0.14 / -0.50	0.08 / -0.51	0.38 / -0.17	0.95 / -0.38
Fake leptons	2.04 / -2.02	1.43 / -1.48	3.25 / -3.07	3.04 / -2.96	5.55 / -5.34
Other backgrounds	0.27 / -0.26	0.26 / -0.25	0.34 / -0.33	0.44 / -0.43	1.18 / -1.14
$t\bar{t}$ modelling	9.16 / -9.15	9.80 / -9.79	8.90 / -8.88	13.40 / -13.39	22.66 / -22.66
MC stat.	1.28 / -1.28	1.62 / -1.62	2.14 / -2.14	3.06 / -3.06	7.38 / -7.38
Luminosity	1.93 / -1.86	1.94 / -1.87	2.01 / -1.94	2.04 / -1.97	2.30 / -2.22

(a) ee

$d\sigma/dm_{t\bar{t}}$ ($\mu\mu$)	Bins [GeV]				
Uncertainties [%]	250-450	450-550	550-700	700-950	950-2700
Total	6.78 / -6.75	6.79 / -6.69	10.48 / -10.54	17.19 / -16.70	37.75 / -41.50
Stat. only	4.55 / -4.55	3.76 / -3.76	5.92 / -5.92	10.22 / -10.22	29.58 / -29.58
Syst. only	5.03 / -4.99	5.65 / -5.54	8.65 / -8.72	13.82 / -13.21	23.45 / -29.10
Jet	2.82 / -2.85	2.57 / -2.50	5.55 / -5.81	7.65 / -6.91	7.79 / -16.09
Tagging	1.74 / -1.61	1.91 / -1.76	2.49 / -2.24	3.88 / -3.19	3.78 / -10.54
Lepton	1.75 / -1.71	1.75 / -1.71	1.82 / -1.78	1.81 / -1.77	2.68 / -2.64
$E_{\mathrm{T}}^{\mathrm{miss}}$	0.26 / -0.67	0.31 / -0.44	0.29 / -0.34	0.40 / -0.31	4.76 / -5.10
Fake leptons	0.35 / -0.35	0.34 / -0.34	0.40 / -0.40	0.34 / -0.34	0.56 / -0.56
Other backgrounds	0.28 / -0.27	0.27 / -0.26	0.31 / -0.30	0.47 / -0.45	1.18 / -1.14
$t\bar{t}$ modelling	2.60 / -2.59	3.71 / -3.70	5.37 / -5.36	10.28 / -10.26	20.23 / -20.22
MC stat.	0.69 / -0.69	0.96 / -0.96	1.26 / -1.26	2.03 / -2.03	5.35 / -5.35
Luminosity	1.93 / -1.86	1.92 / -1.85	1.92 / -1.85	2.00 / -1.93	2.34 / -2.26

(b) $\mu\mu$

$d\sigma/dm_{t\bar{t}}$ ($e\mu$)	Bins [GeV]				
Uncertainties [%]	250-450	450-550	550-700	700-950	950-2700
Total	7.38 / -7.26	7.55 / -7.36	11.04 / -10.79	13.80 / -13.33	28.27 / -27.65
Stat. only	2.61 / -2.61	2.35 / -2.35	4.01 / -4.01	7.02 / -7.02	21.90 / -21.90
Syst. only	6.91 / -6.77	7.18 / -6.98	10.29 / -10.02	11.89 / -11.34	17.88 / -16.88
Jet	2.53 / -2.57	2.04 / -1.90	4.46 / -4.17	6.97 / -6.42	9.80 / -8.70
Tagging	1.79 / -1.66	1.95 / -1.81	2.40 / -2.21	3.74 / -3.38	6.29 / -5.55
Lepton	3.31 / -3.12	3.52 / -3.32	3.74 / -3.51	4.09 / -3.81	4.28 / -4.11
$E_{\mathrm{T}}^{\mathrm{miss}}$	0.19 / -0.22	0.04 / -0.02	0.35 / -0.35	0.35 / -0.34	0.44 / -0.26
Fake leptons	0.66 / -0.69	0.70 / -0.73	0.79 / -0.80	0.91 / -0.90	5.10 / -4.91
Other backgrounds	0.29 / -0.28	0.29 / -0.28	0.31 / -0.30	0.45 / -0.43	1.19 / -1.15
$t\bar{t}$ modelling	4.76 / -4.74	5.15 / -5.14	7.81 / -7.79	7.40 / -7.38	10.78 / -10.71
MC stat.	0.42 / -0.42	0.56 / -0.56	0.83 / -0.83	1.46 / -1.46	4.06 / -4.06
Luminosity	1.94 / -1.87	1.93 / -1.86	1.93 / -1.86	1.99 / -1.92	2.28 / -2.20

(c) $e\mu$

Table 10.3: Contribution of each systematic uncertainty in unfolded $d\sigma/dm_{t\bar{t}}$ as percentage of the cross section in each bin in the ee, $\mu\mu$ and $e\mu$ channels.

$(1/\sigma)d\sigma/dm_{t\bar{t}}$ (ee)	Bins [GeV]				
Uncertainties [%]	250-450	450-550	550-700	700-950	950-2700
Total	8.93 / -8.98	8.28 / -8.11	12.05 / -12.21	23.59 / -23.76	48.31 / -48.11
Stat. only	8.03 / -8.03	6.81 / -6.81	10.55 / -10.55	16.68 / -16.68	42.53 / -42.53
Syst. only	3.90 / -4.02	4.70 / -4.40	5.81 / -6.15	16.69 / -16.92	22.91 / -22.48
Jet	2.16 / -2.45	2.04 / -1.04	3.84 / -4.17	2.77 / -4.09	7.41 / -6.49
Tagging	0.17 / -0.20	0.22 / -0.23	0.25 / -0.23	1.14 / -1.06	3.31 / -2.47
Lepton	0.79 / -0.63	0.34 / -0.57	0.99 / -1.44	1.67 / -1.32	2.64 / -2.41
$E_{\mathrm{T}}^{\mathrm{miss}}$	0.41 / -0.11	0.27 / -0.39	0.21 / -0.77	0.20 / -0.04	0.72 / -0.27
Fake leptons	0.11 / -0.13	0.77 / -0.80	1.08 / -0.98	0.92 / -0.92	3.42 / -3.37
Other backgrounds	0.03 / -0.04	0.04 / -0.04	0.04 / -0.03	0.14 / -0.13	0.87 / -0.85
$t\bar{t}$ modelling	2.84 / -2.84	3.80 / -3.80	3.51 / -3.51	16.01 / -16.01	19.59 / -19.59
MC stat.	1.27 / -1.27	1.63 / -1.63	2.11 / -2.11	3.08 / -3.08	7.44 / -7.44
Luminosity	0.03 / -0.03	0.02 / -0.02	0.05 / -0.05	0.08 / -0.08	0.33 / -0.33

(a) ee

$(1/\sigma)d\sigma/dm_{t\bar{t}}$ $(\mu\mu)$	Bins [GeV]				
Uncertainties [%]	250-450	450-550	550-700	700-950	950-2700
Total	5.83 / -5.82	4.29 / -4.27	7.90 / -7.94	14.69 / -14.31	36.91 / -40.05
Stat. only	4.60 / -4.60	3.75 / -3.75	5.96 / -5.96	10.24 / -10.24	30.07 / -30.07
Syst. only	3.58 / -3.57	2.09 / -2.04	5.18 / -5.23	10.53 / -9.99	21.42 / -26.46
Jet	2.83 / -2.82	0.88 / -0.76	4.29 / -4.38	6.37 / -5.58	7.36 / -14.65
Tagging	0.34 / -0.32	0.19 / -0.15	0.44 / -0.32	1.79 / -1.30	2.53 / -9.07
Lepton	0.26 / -0.26	0.09 / -0.09	0.40 / -0.40	0.28 / -0.28	1.62 / -1.63
$E_{\mathrm{T}}^{\mathrm{miss}}$	0.07 / -0.15	0.17 / -0.14	0.33 / -0.09	0.26 / -0.19	4.52 / -5.03
Fake leptons	0.01 / -0.01	0.10 / -0.10	0.09 / -0.09	0.04 / -0.04	0.39 / -0.39
Other backgrounds	0.02 / -0.02	0.03 / -0.03	0.00 / -0.00	0.16 / -0.16	0.87 / -0.85
$t\bar{t}$ modelling	2.03 / -2.03	1.62 / -1.62	2.53 / -2.53	7.92 / -7.92	18.61 / -18.61
MC stat.	0.69 / -0.69	0.96 / -0.96	1.26 / -1.26	2.05 / -2.05	5.26 / -5.26
Luminosity	0.00 / -0.00	0.02 / -0.02	0.01 / -0.01	0.06 / -0.06	0.40 / -0.40

(b) $\mu\mu$

$(1/\sigma)d\sigma/dm_{t\bar{t}}$ $(e\mu)$	Bins [GeV]				
Uncertainties [%]	250-450	450-550	550-700	700-950	950-2700
Total	3.90 / -3.99	3.78 / -3.78	6.41 / -6.29	10.27 / -9.97	26.62 / -26.21
Stat. only	2.65 / -2.65	2.30 / -2.30	3.98 / -3.98	7.06 / -7.06	22.09 / -22.09
Syst. only	2.86 / -2.98	3.00 / -3.01	5.03 / -4.87	7.46 / -7.04	14.85 / -14.10
Jet	2.26 / -2.40	0.54 / -0.58	3.66 / -3.45	6.35 / -5.90	9.38 / -8.42
Tagging	0.29 / -0.31	0.13 / -0.15	0.29 / -0.28	1.60 / -1.47	4.15 / -3.72
Lepton	0.28 / -0.32	0.05 / -0.05	0.46 / -0.41	0.97 / -0.83	1.18 / -1.37
$E_{\mathrm{T}}^{\mathrm{miss}}$	0.18 / -0.21	0.05 / -0.02	0.36 / -0.36	0.36 / -0.35	0.45 / -0.26
Fake leptons	0.13 / -0.14	0.03 / -0.03	0.05 / -0.04	0.25 / -0.24	4.57 / -4.44
Other backgrounds	0.02 / -0.02	0.02 / -0.02	0.00 / -0.00	0.14 / -0.13	0.88 / -0.85
$t\bar{t}$ modelling	1.64 / -1.64	2.89 / -2.89	3.28 / -3.28	3.09 / -3.08	8.71 / -8.68
MC stat.	0.41 / -0.41	0.57 / -0.57	0.83 / -0.83	1.45 / -1.45	4.02 / -4.02
Luminosity	0.00 / -0.00	0.01 / -0.01	0.01 / -0.01	0.05 / -0.05	0.33 / -0.33

(c) $e\mu$

Table 10.4: Contribution of each systematic uncertainty in unfolded $\frac{1}{\sigma_{t\bar{t}}}\frac{d\sigma}{dm_{t\bar{t}}}$ as percentage of the cross section in each bin in the ee, $\mu\mu$ and $e\mu$ channels.

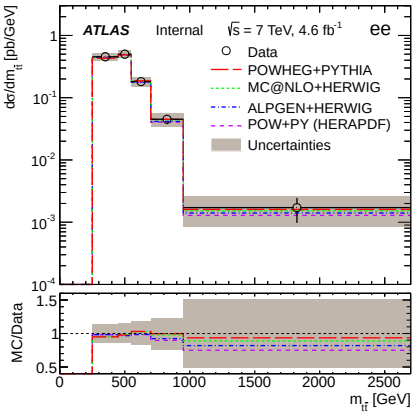

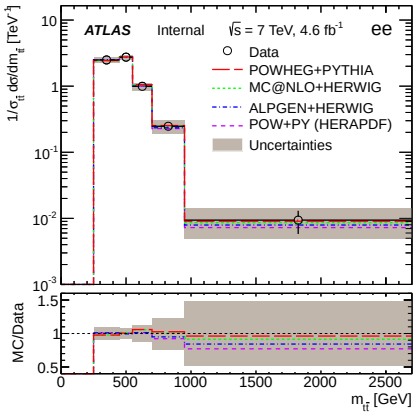

(a) ee

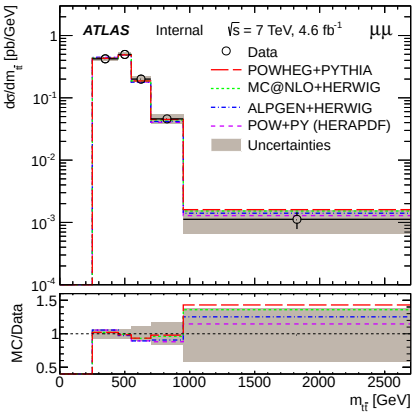

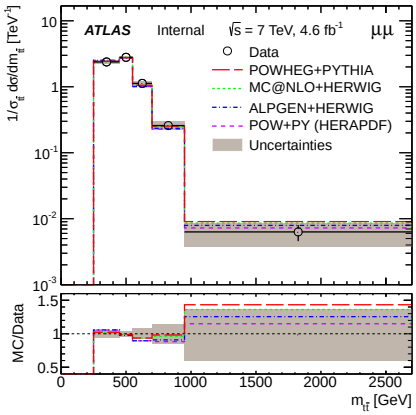

(b) $\mu\mu$

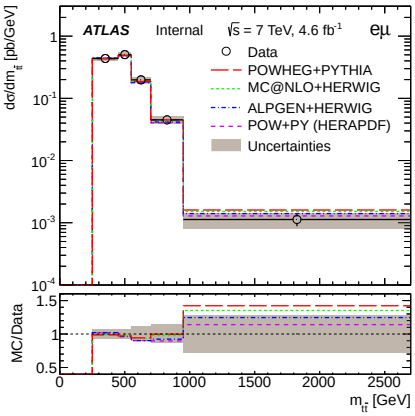

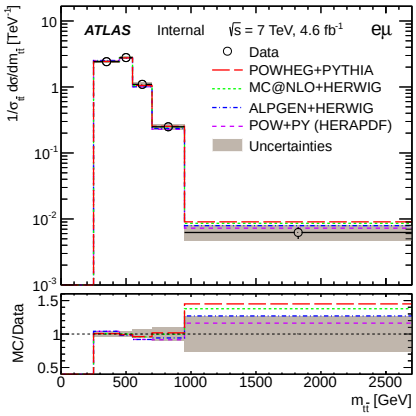

(c) $e\mu$

Figure 10.1: Unfolded $d\sigma/dm_{t\bar{t}}$ (left) and $\frac{1}{\sigma_{t\bar{t}}}\frac{d\sigma}{dm_{t\bar{t}}}$ (right) in the ee (top), $\mu\mu$ (middle) and $e\mu$ (bottom) channels. Different Monte-Carlos are compared with data. The hatched error bands include all statistical and systematic uncertainties.

$m_{t\bar{t}}$ [GeV] (ee)	250-450	450-550	550-700	700-950	950-2700
250-450	1.00	0.21	−0.38	−0.16	0.02
450-550	0.21	1.00	0.46	−0.26	−0.10
550-700	−0.38	0.46	1.00	0.36	−0.23
700-950	−0.16	−0.26	0.36	1.00	0.13
950-2700	0.02	−0.10	−0.23	0.13	1.00

(a) ee

$m_{t\bar{t}}$ [GeV] ($\mu\mu$)	250-450	450-550	550-700	700-950	950-2700
250-450	1.00	0.28	−0.36	−0.21	0.00
450-550	0.28	1.00	0.46	−0.23	−0.12
550-700	−0.36	0.46	1.00	0.39	−0.19
700-950	−0.21	−0.23	0.39	1.00	0.27
950-2700	0.00	−0.12	−0.19	0.27	1.00

(b) $\mu\mu$

$m_{t\bar{t}}$ [GeV] ($e\mu$)	250-450	450-550	550-700	700-950	950-2700
250-450	1.00	0.28	−0.36	−0.19	0.00
450-550	0.28	1.00	0.42	−0.22	−0.09
550-700	−0.36	0.42	1.00	0.37	−0.18
700-950	−0.19	−0.22	0.37	1.00	0.28
950-2700	0.00	−0.09	−0.18	0.28	1.00

(c) $e\mu$

Table 10.5: Bin-to-bin correlations in unfolded $d\sigma/dm_{t\bar{t}}$ and $\frac{1}{\sigma_{t\bar{t}}}\frac{d\sigma}{dm_{t\bar{t}}}$ in the ee, $\mu\mu$ and $e\mu$ channels. These correlations are present due to bin migrations in unfolding.

10.2 Results for $p_{\mathrm{T}}^{t\bar{t}}$

From equation 2.3, the unfolded absolute and normalized differential cross sections are measured as shown in Table 10.6 and 10.7. The systematic and statistical uncertainty components of the absolute and normlized differential measurements for each dilepton channel are shown in Tables 10.8 and 10.9. Figure 10.2 shows the measured results compared with different MCs.

2 iterations are used to unfold the $p_{\mathrm{T}}^{t\bar{t}}$ spectrum, as discussed in Sections 8.3.2 and 8.5.

The correlation matrix is shown in table 10.10.

$p_{\mathrm{T}}^{t\bar{t}}$ [GeV]	$d\sigma/dp_{T,t\bar{t}}$ [pb/GeV]	Stat. [%]	Syst. [%]
0-40	$2.58^{+0.35}_{-0.34}$	± 6.5	$^{+12}_{-12}$
40-170	$0.56^{+0.10}_{-0.09}$	± 6.9	$^{+16}_{-15}$
170-340	$0.044^{+0.014}_{-0.013}$	± 20	$^{+24}_{-21}$
340-1000	$0.0008^{+0.0007}_{-0.0007}$	± 78	$^{+45}_{-44}$
$\sigma_{t\bar{t}}^{int}$ [pb]	$184.0^{+18.8}_{-18.5}$	± 4.6	$^{+9.1}_{-8.9}$

(a) ee

$p_{\mathrm{T}}^{t\bar{t}}$ [GeV]	$d\sigma/dp_{T,t\bar{t}}$ [pb/GeV]	Stat. [%]	Syst. [%]
0-40	$2.48^{+0.18}_{-0.18}$	± 3.9	$^{+6.3}_{-6.2}$
40-170	$0.55^{+0.06}_{-0.06}$	± 4.0	$^{+9.8}_{-10}$
170-340	$0.047^{+0.010}_{-0.010}$	± 12	$^{+16}_{-16}$
340-1000	$0.0018^{+0.0007}_{-0.0007}$	± 30	$^{+27}_{-27}$
$\sigma_{t\bar{t}}^{int}$ [pb]	$179.2^{+10.6}_{-10.7}$	± 2.7	$^{+5.2}_{-5.3}$

(b) $\mu\mu$

$p_{\mathrm{T}}^{t\bar{t}}$ [GeV]	$d\sigma/dp_{T,t\bar{t}}$ [pb/GeV]	Stat. [%]	Syst. [%]
0-40	$2.40^{+0.22}_{-0.21}$	± 2.4	$^{+8.7}_{-8.5}$
40-170	$0.58^{+0.06}_{-0.06}$	± 2.4	$^{+10}_{-10}$
170-340	$0.050^{+0.008}_{-0.008}$	± 7.8	$^{+14}_{-14}$
340-1000	$0.0017^{+0.0007}_{-0.0007}$	± 25	$^{+34}_{-34}$
$\sigma_{t\bar{t}}^{int}$ [pb]	$180.8^{+11.9}_{-11.7}$	± 1.7	$^{+6.4}_{-6.3}$

(c) $e\mu$

Table 10.6: Unfolded absolute differential cross section of $t\bar{t}$ as a function of $p_{\mathrm{T}}^{t\bar{t}}$ in the ee, $\mu\mu$ and $e\mu$ channels with the total, statistical only and systematic only uncertainties in each bin. The bottom row shows the total $\sigma_{t\bar{t}}$ integrated from the differential measurements.

$p_{\mathrm{T}}^{t\bar{t}}$ [GeV]	$(1/\sigma)d\sigma/dp_{T,t\bar{t}}$ [TeV^{-1}]	Stat. [%]	Syst. [%]
0-40	$14.0^{+1.3}_{-1.3}$	$\pm$6.5	$^{+6.2}_{-6.2}$
40-170	$3.04^{+0.30}_{-0.31}$	$\pm$6.8	$^{+7.3}_{-7.5}$
170-340	$0.239^{+0.066}_{-0.062}$	$\pm$21	$^{+18}_{-16}$
340-1000	$0.0043^{+0.0039}_{-0.0039}$	$\pm$80	$^{+40}_{-39}$
Integrated	$1^{+0.06}_{-0.07}$	$\pm$4.6	$^{+4.6}_{-4.6}$

(a) ee

$p_{\mathrm{T}}^{t\bar{t}}$ [GeV]	$(1/\sigma)d\sigma/dp_{T,t\bar{t}}$ [TeV^{-1}]	Stat. [%]	Syst. [%]
0-40	$13.8^{+0.9}_{-0.9}$	$\pm$3.8	$^{+5.2}_{-5.1}$
40-170	$3.04^{+0.21}_{-0.22}$	$\pm$4.0	$^{+5.7}_{-5.9}$
170-340	$0.264^{+0.049}_{-0.049}$	$\pm$12	$^{+14}_{-14}$
340-1000	$0.0100^{+0.0040}_{-0.0040}$	$\pm$30	$^{+26}_{-26}$
Integrated	$1^{+0.05}_{-0.05}$	$\pm$2.7	$^{+3.7}_{-3.7}$

(b) $\mu\mu$

$p_{\mathrm{T}}^{t\bar{t}}$ [GeV]	$(1/\sigma)d\sigma/dp_{T,t\bar{t}}$ [TeV^{-1}]	Stat. [%]	Syst. [%]
0-40	$13.3^{+0.8}_{-0.8}$	$\pm$2.4	$^{+5.8}_{-5.8}$
40-170	$3.19^{+0.20}_{-0.20}$	$\pm$2.4	$^{+5.8}_{-5.9}$
170-340	$0.276^{+0.041}_{-0.041}$	$\pm$7.8	$^{+13}_{-12}$
340-1000	$0.0093^{+0.0038}_{-0.0038}$	$\pm$25	$^{+33}_{-33}$
Integrated	$1^{+0.04}_{-0.04}$	$\pm$1.7	$^{+4.0}_{-4.0}$

(c) $e\mu$

Table 10.7: Unfolded normalized differential cross section of $t\bar{t}$ as a function of $p_{\mathrm{T}}^{t\bar{t}}$ in the ee, $\mu\mu$ and $e\mu$ channels with the total, statistical only and systematic only uncertainties in each bin. The last entry of each table is the integrated sum of the normalized differential cross sections, and is consistent with unity.

$d\sigma/dp_{T,t\bar{t}}$ (ee)	Bins [GeV]			
Uncertainties [%]	0-40	40-170	170-340	340-1000
Total	13.50 / -13.25	17.13 / -16.86	31.29 / -29.54	90.39 / -89.70
Stat. only	6.48 / -6.48	6.93 / -6.93	20.48 / -20.48	78.26 / -78.26
Syst. only	11.85 / -11.56	15.67 / -15.36	23.66 / -21.29	45.23 / -43.85
Jet	2.15 / -2.64	4.73 / -4.48	11.82 / -6.79	15.27 / -13.31
Tagging	2.15 / -1.98	2.05 / -1.89	1.75 / -1.55	3.46 / -3.09
Lepton	6.62 / -6.09	6.97 / -6.28	7.14 / -6.61	6.60 / -5.95
$E_{\mathrm{T}}^{\mathrm{miss}}$	1.87 / -1.33	1.75 / -2.56	1.86 / -1.29	0.13 / -0.28
Fake leptons	2.01 / -2.07	2.11 / -2.01	5.78 / -5.53	27.45 / -26.44
Other backgrounds	0.34 / -0.33	0.29 / -0.28	0.31 / -0.30	0.63 / -0.61
$t\bar{t}$ modelling	8.68 / -8.67	12.56 / -12.56	17.77 / -17.77	30.65 / -30.63
MC stat.	0.84 / -0.84	0.98 / -0.98	2.97 / -2.97	7.52 / -7.52
Luminosity	1.93 / -1.86	1.99 / -1.91	2.12 / -2.04	2.71 / -2.62

(a) ee

$d\sigma/dp_{T,t\bar{t}}$ ($\mu\mu$)	Bins [GeV]			
Uncertainties [%]	0-40	40-170	170-340	340-1000
Total	7.36 / -7.28	10.54 / -10.79	20.12 / -20.21	40.39 / -40.69
Stat. only	3.85 / -3.85	3.97 / -3.97	11.97 / -11.97	30.08 / -30.08
Syst. only	6.28 / -6.18	9.76 / -10.03	16.17 / -16.28	26.95 / -27.40
Jet	2.06 / -2.01	3.56 / -4.08	7.42 / -7.64	7.39 / -9.28
Tagging	2.13 / -2.06	2.08 / -1.93	2.16 / -1.94	3.13 / -2.81
Lepton	1.76 / -1.72	1.75 / -1.71	1.77 / -1.73	1.98 / -2.09
$E_{\mathrm{T}}^{\mathrm{miss}}$	1.12 / -1.05	1.65 / -2.26	0.55 / -1.42	1.30 / -1.58
Fake leptons	0.21 / -0.21	0.41 / -0.41	0.67 / -0.67	0.75 / -0.75
Other backgrounds	0.36 / -0.35	0.28 / -0.27	0.22 / -0.21	0.23 / -0.22
$t\bar{t}$ modelling	4.70 / -4.69	8.26 / -8.25	13.83 / -13.83	25.32 / -25.19
MC stat.	0.49 / -0.49	0.56 / -0.56	1.64 / -1.64	3.35 / -3.35
Luminosity	1.94 / -1.87	1.93 / -1.86	1.96 / -1.89	1.93 / -1.86

(b) $\mu\mu$

$d\sigma/dp_{T,t\bar{t}}$ ($e\mu$)	Bins [GeV]			
Uncertainties [%]	0-40	40-170	170-340	340-1000
Total	9.05 / -8.86	10.62 / -10.55	16.06 / -15.91	42.07 / -41.96
Stat. only	2.35 / -2.35	2.45 / -2.45	7.76 / -7.76	25.24 / -25.24
Syst. only	8.74 / -8.54	10.34 / -10.26	14.06 / -13.89	33.66 / -33.52
Jet	2.00 / -1.87	2.80 / -2.84	6.17 / -6.10	8.73 / -8.44
Tagging	2.16 / -2.00	2.00 / -1.84	2.34 / -2.11	3.90 / -3.54
Lepton	3.54 / -3.34	3.47 / -3.26	3.32 / -3.12	3.45 / -3.26
$E_{\mathrm{T}}^{\mathrm{miss}}$	1.84 / -1.72	1.76 / -1.92	1.33 / -0.95	0.73 / -1.15
Fake leptons	0.75 / -0.79	0.83 / -0.83	1.77 / -1.70	3.78 / -3.67
Other backgrounds	0.37 / -0.36	0.25 / -0.25	0.24 / -0.23	0.29 / -0.28
$t\bar{t}$ modelling	6.87 / -6.85	8.68 / -8.67	11.53 / -11.53	31.66 / -31.65
MC stat.	0.30 / -0.30	0.34 / -0.34	1.13 / -1.13	2.91 / -2.91
Luminosity	1.94 / -1.87	1.93 / -1.86	1.95 / -1.88	2.03 / -1.96

(c) $e\mu$

Table 10.8: Contribution of each systematic uncertainty in unfolded $d\sigma/dp_{\mathrm{T}}^{t\bar{t}}$ as percentage of the cross section in each bin in the ee, $\mu\mu$ and $e\mu$ channels.

$(1/\sigma)d\sigma/dp_{T,t\bar{t}}$ (ee)	Bins [GeV]			
Uncertainties [%]	0-40	40-170	170-340	340-1000
Total	8.94 / -8.98	10.03 / -10.14	27.53 / -26.13	89.24 / -88.94
Stat. only	6.49 / -6.49	6.83 / -6.83	20.51 / -20.51	79.85 / -79.85
Syst. only	6.16 / -6.20	7.34 / -7.49	18.37 / -16.19	39.85 / -39.15
Jet	1.79 / -2.33	2.32 / -2.05	9.82 / -4.78	13.72 / -12.08
Tagging	0.11 / -0.13	0.12 / -0.11	0.66 / -0.60	1.53 / -1.42
Lepton	0.12 / -0.19	0.21 / -0.14	0.82 / -1.22	2.00 / -1.03
$E_{\mathrm{T}}^{\mathrm{miss}}$	1.88 / -1.35	1.74 / -2.55	1.84 / -1.28	0.14 / -0.30
Fake leptons	0.30 / -0.40	0.67 / -0.61	3.56 / -3.47	24.93 / -24.75
Other backgrounds	0.02 / -0.02	0.03 / -0.03	0.01 / -0.01	0.31 / -0.30
$t\bar{t}$ modelling	5.50 / -5.50	6.63 / -6.63	14.66 / -14.66	26.70 / -26.69
MC stat.	0.84 / -0.84	0.98 / -0.98	2.96 / -2.96	7.65 / -7.65
Luminosity	0.03 / -0.03	0.03 / -0.03	0.16 / -0.16	0.74 / -0.74

(a) ee

$(1/\sigma)d\sigma/dp_{T,t\bar{t}}$ $(\mu\mu)$	Bins [GeV]			
Uncertainties [%]	0-40	40-170	170-340	340-1000
Total	6.50 / -6.37	6.95 / -7.11	18.72 / -18.77	39.84 / -40.12
Stat. only	3.83 / -3.83	4.02 / -4.02	11.93 / -11.93	30.21 / -30.21
Syst. only	5.25 / -5.09	5.67 / -5.86	14.42 / -14.49	25.98 / -26.41
Jet	2.00 / -1.81	1.83 / -2.10	6.10 / -6.19	6.73 / -8.41
Tagging	0.05 / -0.08	0.12 / -0.07	0.15 / -0.07	1.09 / -0.92
Lepton	0.02 / -0.01	0.05 / -0.05	0.43 / -0.43	0.69 / -0.99
$E_{\mathrm{T}}^{\mathrm{miss}}$	1.47 / -1.13	1.56 / -1.92	0.50 / -1.08	1.11 / -1.47
Fake leptons	0.10 / -0.10	0.10 / -0.10	0.36 / -0.37	0.57 / -0.57
Other backgrounds	0.04 / -0.04	0.04 / -0.04	0.10 / -0.10	0.09 / -0.09
$t\bar{t}$ modelling	4.60 / -4.60	5.09 / -5.10	12.94 / -12.94	24.81 / -24.73
MC stat.	0.49 / -0.49	0.56 / -0.56	1.65 / -1.65	3.32 / -3.32
Luminosity	0.00 / -0.00	0.00 / -0.00	0.02 / -0.02	0.00 / -0.00

(b) $\mu\mu$

$(1/\sigma)d\sigma/dp_{T,t\bar{t}}$ $(e\mu)$	Bins [GeV]			
Uncertainties [%]	0-40	40-170	170-340	340-1000
Total	6.28 / -6.24	6.30 / -6.37	14.74 / -14.70	41.35 / -41.30
Stat. only	2.36 / -2.36	2.42 / -2.42	7.77 / -7.77	25.00 / -25.00
Syst. only	5.83 / -5.78	5.82 / -5.89	12.52 / -12.48	32.94 / -32.88
Jet	1.86 / -1.80	1.66 / -1.73	5.30 / -5.29	8.52 / -8.28
Tagging	0.06 / -0.07	0.12 / -0.12	0.25 / -0.19	1.76 / -1.63
Lepton	0.06 / -0.08	0.06 / -0.06	0.39 / -0.20	0.57 / -0.55
$E_{\mathrm{T}}^{\mathrm{miss}}$	1.71 / -1.59	1.89 / -2.05	1.45 / -1.08	0.64 / -1.20
Fake leptons	0.07 / -0.10	0.14 / -0.13	1.00 / -0.97	3.07 / -3.02
Other backgrounds	0.06 / -0.05	0.06 / -0.06	0.08 / -0.08	0.02 / -0.02
$t\bar{t}$ modelling	5.24 / -5.24	5.23 / -5.23	11.14 / -11.14	31.47 / -31.47
MC stat.	0.30 / -0.30	0.34 / -0.34	1.13 / -1.13	2.93 / -2.93
Luminosity	0.00 / -0.00	0.01 / -0.01	0.01 / -0.01	0.09 / -0.09

(c) $e\mu$

Table 10.9: Contribution of each systematic uncertainty in unfolded $\frac{1}{\sigma_{t\bar{t}}}\frac{d\sigma}{dp_{\mathrm{T}}^{t\bar{t}}}$ as percentage of the cross section in each bin in the ee, $\mu\mu$ and $e\mu$ channels.

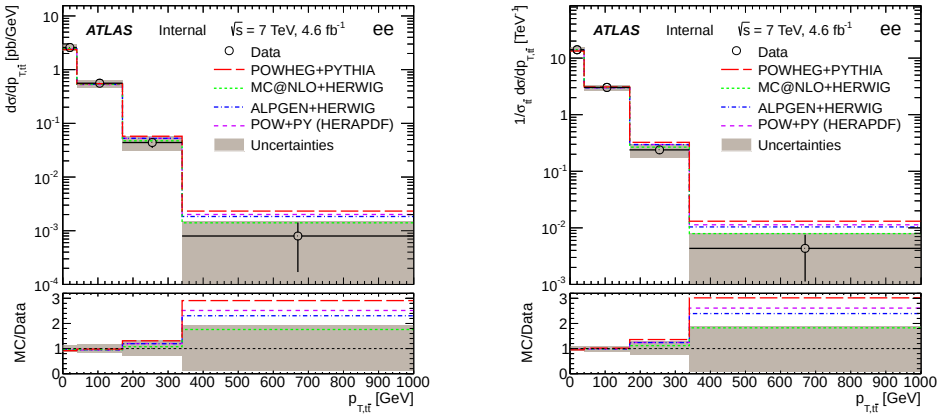

(a) ee

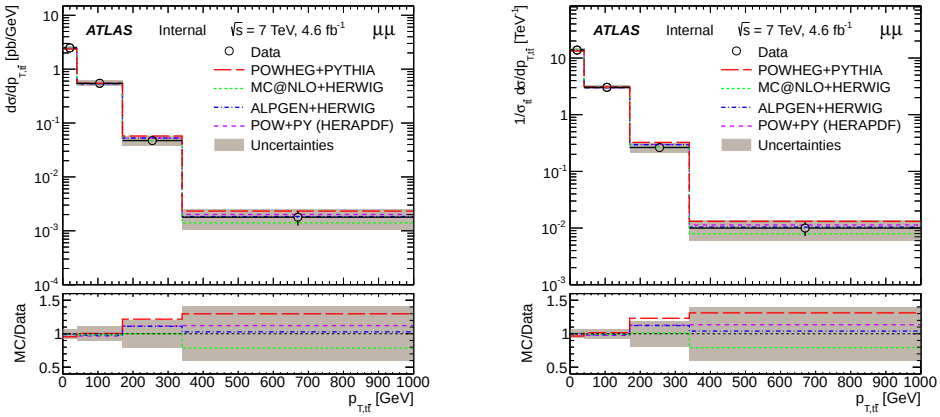

(b) $\mu\mu$

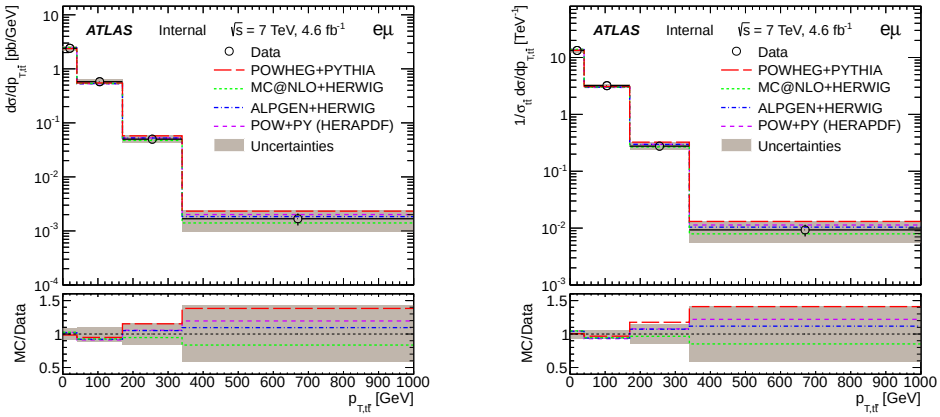

(c) $e\mu$

Figure 10.2: Unfolded $d\sigma/dp_{\mathrm{T}}^{t\bar{t}}$ (left) and $\frac{1}{\sigma_{t\bar{t}}}\frac{d\sigma}{dp_{\mathrm{T}}^{t\bar{t}}}$ (right) in the ee (top), $\mu\mu$ (middle) and $e\mu$ (bottom) channels. Different Monte-Carlos are compared with data. The hatched error bands include all statistical and systematic uncertainties.

$p_{\mathrm{T}}^{t\bar{t}}$ [GeV] (ee)	0-40	40-170	170-340	340-1000
0-40	1.00	0.04	−0.07	−0.01
40-170	0.04	1.00	0.06	−0.02
170-340	−0.07	0.06	1.00	0.07
340-1000	−0.01	−0.02	0.07	1.00

(a) ee

$p_{\mathrm{T}}^{t\bar{t}}$ [GeV] ($\mu\mu$)	0-40	40-170	170-340	340-1000
0-40	1.00	0.05	−0.07	−0.01
40-170	0.05	1.00	0.04	−0.03
170-340	−0.07	0.04	1.00	0.04
340-1000	−0.01	−0.03	0.04	1.00

(b) $\mu\mu$

$p_{\mathrm{T}}^{t\bar{t}}$ [GeV] ($e\mu$)	0-40	40-170	170-340	340-1000
0-40	1.00	0.04	−0.07	−0.01
40-170	0.04	1.00	0.04	−0.02
170-340	−0.07	0.04	1.00	0.04
340-1000	−0.01	−0.02	0.04	1.00

(c) $e\mu$

Table 10.10: Bin-to-bin correlations in unfolded $d\sigma/dp_{\mathrm{T}}^{t\bar{t}}$ and $\frac{1}{\sigma_{t\bar{t}}}\frac{d\sigma}{dp_{\mathrm{T}}^{t\bar{t}}}$ in the ee, $\mu\mu$ and $e\mu$ channels. These correlations are present due to bin migrations in unfolding.

10.3 Results for $y_{t\bar{t}}$

From equation 2.3, the unfolded absolute and normalized differential cross sections are measured as shown in Table 10.11 and 10.12. The systematic and statistical uncertainty components of the absolute and normlized differential measurements for each dilepton channel are shown in Tables 10.13 and 10.14. Figure 10.3 shows the measured results compared with different MCs.

3 iterations are used to unfold the $y_{t\bar{t}}$ spectrum, as discussed in Sections 8.3.2 and 8.5.

The correlation matrix is shown in table 10.15.

$y_{t\bar{t}}$	$d\sigma/dy_{t\bar{t}}$ [pb]	Stat. [%]	Syst. [%]
-2.5–1	$9.5^{+3.5}_{-3.5}$	± 24	$^{+28}_{-27}$
-1–0.5	$63.3^{+9.9}_{-9.8}$	± 10	$^{+12}_{-12}$
-0.5-0	$81.9^{+12.5}_{-12.2}$	± 9.5	$^{+12}_{-12}$
0-0.5	$66.1^{+12.6}_{-12.3}$	± 11	$^{+16}_{-15}$
0.5-1	$58.8^{+11.3}_{-11.2}$	± 11	$^{+16}_{-16}$
1-2.5	$18.7^{+4.1}_{-4.0}$	± 16	$^{+14}_{-14}$
$\sigma^{int}_{t\bar{t}}$ [pb]	$177.5^{+14.2}_{-13.9}$	± 5.1	$^{+6.1}_{-6.0}$

(a) ee

$y_{t\bar{t}}$	$d\sigma/dy_{t\bar{t}}$ [pb]	Stat. [%]	Syst. [%]
-2.5–1	$16.3^{+2.1}_{-2.1}$	± 9.1	$^{+9.3}_{-9.0}$
-1–0.5	$60.9^{+6.1}_{-6.2}$	± 6.1	$^{+8.0}_{-8.2}$
-0.5-0	$72.0^{+6.6}_{-6.7}$	± 6.2	$^{+6.7}_{-7.0}$
0-0.5	$67.2^{+6.0}_{-5.9}$	± 6.3	$^{+6.2}_{-6.1}$
0.5-1	$58.8^{+5.5}_{-5.4}$	± 6.1	$^{+7.0}_{-6.8}$
1-2.5	$16.0^{+2.0}_{-2.0}$	± 9.1	$^{+8.5}_{-8.5}$
$\sigma^{int}_{t\bar{t}}$ [pb]	$177.9^{+7.5}_{-7.5}$	± 2.9	$^{+3.1}_{-3.1}$

(b) $\mu\mu$

$y_{t\bar{t}}$	$d\sigma/dy_{t\bar{t}}$ [pb]	Stat. [%]	Syst. [%]
-2.5–1	$17.5^{+2.0}_{-2.0}$	± 6.0	$^{+10}_{-9.8}$
-1–0.5	$56.7^{+5.0}_{-4.9}$	± 4.1	$^{+7.8}_{-7.6}$
-0.5-0	$80.0^{+5.7}_{-5.6}$	± 3.5	$^{+6.2}_{-6.0}$
0-0.5	$71.4^{+6.1}_{-6.0}$	± 3.8	$^{+7.6}_{-7.5}$
0.5-1	$56.2^{+4.8}_{-4.7}$	± 4.2	$^{+7.4}_{-7.3}$
1-2.5	$14.3^{+1.7}_{-1.7}$	± 6.5	$^{+10}_{-9.8}$
$\sigma^{int}_{t\bar{t}}$ [pb]	$179.9^{+6.7}_{-6.6}$	± 1.8	$^{+3.3}_{-3.2}$

(c) $e\mu$

Table 10.11: Unfolded absolute differential cross section of $t\bar{t}$ as a function of $y_{t\bar{t}}$ in the ee, $\mu\mu$ and $e\mu$ channels with the total, statistical only and systematic only uncertainties in each bin. The bottom row shows the total $\sigma_{t\bar{t}}$ integrated from the differential measurements.

$y_{t\bar{t}}$	$(1/\sigma)d\sigma/dy_{t\bar{t}}$ [$\times 10^{-3}$]	Stat. [%]	Syst. [%]
-2.5–1	$53.7^{+19.1}_{-18.9}$	± 24	$^{+26}_{-26}$
-1–0.5	357^{+41}_{-41}	± 10	$^{+5.3}_{-5.5}$
-0.5-0	462^{+49}_{-49}	± 9.4	$^{+4.7}_{-4.7}$
0-0.5	373^{+53}_{-53}	± 11	$^{+9.3}_{-9.2}$
0.5-1	331^{+45}_{-45}	± 11	$^{+8.3}_{-8.2}$
1-2.5	$106^{+19.6}_{-19.8}$	± 16	$^{+8.7}_{-9.2}$
Integrated	$1^{+0.06}_{-0.06}$	± 5.1	$^{+3.6}_{-3.6}$

(a) ee

$y_{t\bar{t}}$	$(1/\sigma)d\sigma/dy_{t\bar{t}}$ [$\times 10^{-3}$]	Stat. [%]	Syst. [%]
-2.5–1	$91.9^{+10.0}_{-10.0}$	± 9.0	$^{+6.1}_{-6.0}$
-1–0.5	342^{+29}_{-29}	± 6.1	$^{+6.1}_{-6.1}$
-0.5-0	405^{+33}_{-34}	± 6.2	$^{+5.4}_{-5.5}$
0-0.5	377^{+26}_{-26}	± 6.3	$^{+2.8}_{-2.7}$
0.5-1	331^{+24}_{-24}	± 6.1	$^{+3.8}_{-3.8}$
1-2.5	$89.8^{+9.7}_{-9.7}$	± 9.1	$^{+6.0}_{-5.9}$
Integrated	$1^{+0.04}_{-0.04}$	± 2.8	$^{+2.1}_{-2.1}$

(b) $\mu\mu$

$y_{t\bar{t}}$	$(1/\sigma)d\sigma/dy_{t\bar{t}}$ [$\times 10^{-3}$]	Stat. [%]	Syst. [%]
-2.5–1	$97.4^{+7.2}_{-7.2}$	± 5.9	$^{+4.5}_{-4.5}$
-1–0.5	315^{+16}_{-16}	± 4.1	$^{+3.0}_{-3.0}$
-0.5-0	444^{+19}_{-19}	± 3.6	$^{+2.3}_{-2.4}$
0-0.5	397^{+19}_{-19}	± 3.8	$^{+2.8}_{-2.8}$
0.5-1	313^{+16}_{-16}	± 4.3	$^{+2.8}_{-2.9}$
1-2.5	$79.7^{+6.8}_{-6.7}$	± 6.5	$^{+5.6}_{-5.4}$
Integrated	$1^{+0.02}_{-0.02}$	± 1.9	$^{+1.4}_{-1.4}$

(c) $e\mu$

Table 10.12: Unfolded normalized differential cross section of $t\bar{t}$ as a function of $y_{t\bar{t}}$ in the ee, $\mu\mu$ and $e\mu$ channels with the total, statistical only and systematic only uncertainties in each bin. The last entry of each table is the integrated sum of the normalized differential cross sections, and is consistent with unity.

$d\sigma/dy_{t\bar{t}}$ (ee)	Bins					
Uncertainties [%]	-2.5–1.0	-1.0–0.5	-0.5-0.0	0.0-0.5	0.5-1.0	1.0-2.5
Total	37.07 / -36.36	15.63 / -15.44	15.25 / -14.95	19.03 / -18.67	19.29 / -18.99	21.69 / -21.58
Stat. only	24.15 / -24.15	10.23 / -10.23	9.46 / -9.46	10.91 / -10.91	10.62 / -10.62	16.37 / -16.37
Syst. only	28.12 / -27.19	11.81 / -11.57	11.96 / -11.58	15.59 / -15.15	16.10 / -15.74	14.22 / -14.06
Jet	9.89 / -7.85	3.27 / -3.66	3.30 / -3.29	3.44 / -2.63	4.62 / -4.27	3.12 / -4.35
Tagging	2.52 / -2.35	2.23 / -2.02	2.04 / -1.87	2.21 / -2.04	1.89 / -1.74	2.03 / -1.85
Lepton	6.38 / -5.92	6.97 / -6.40	6.76 / -6.18	6.23 / -5.69	7.37 / -6.84	8.20 / -7.42
$E_{\mathrm{T}}^{\mathrm{miss}}$	1.04 / -1.32	0.46 / -0.79	0.74 / -0.23	0.56 / -0.37	0.09 / -0.56	0.61 / -0.50
Fake leptons	12.20 / -11.83	2.39 / -2.39	1.70 / -1.70	3.26 / -3.10	1.72 / -1.68	5.64 / -5.60
Other backgrounds	0.43 / -0.42	0.27 / -0.26	0.29 / -0.28	0.42 / -0.40	0.29 / -0.28	0.23 / -0.22
$t\bar{t}$ modelling	21.69 / -21.68	7.87 / -7.87	8.51 / -8.51	13.00 / -13.00	12.99 / -12.99	8.80 / -8.78
MC stat.	4.45 / -4.45	1.93 / -1.93	1.59 / -1.59	1.79 / -1.79	2.08 / -2.08	2.83 / -2.83
Luminosity	2.30 / -2.22	1.90 / -1.83	1.94 / -1.87	2.05 / -1.97	1.95 / -1.89	1.88 / -1.81

(a) ee

$d\sigma/dy_{t\bar{t}}$ ($\mu\mu$)	Bins					
Uncertainties [%]	-2.5–1.0	-1.0–0.5	-0.5-0.0	0.0-0.5	0.5-1.0	1.0-2.5
Total	13.00 / -12.76	10.07 / -10.25	9.16 / -9.36	8.88 / -8.79	9.32 / -9.12	12.41 / -12.42
Stat. only	9.07 / -9.07	6.14 / -6.14	6.21 / -6.21	6.32 / -6.32	6.13 / -6.13	9.07 / -9.07
Syst. only	9.31 / -8.97	7.98 / -8.20	6.73 / -7.00	6.25 / -6.11	7.02 / -6.75	8.47 / -8.49
Jet	4.07 / -3.54	1.85 / -2.79	1.79 / -2.79	2.87 / -2.73	3.35 / -2.73	2.64 / -2.77
Tagging	2.37 / -2.19	2.18 / -2.01	2.14 / -1.96	2.20 / -2.00	1.89 / -1.96	1.97 / -2.01
Lepton	1.73 / -1.68	1.75 / -1.71	1.78 / -1.74	1.78 / -1.74	1.77 / -1.72	1.84 / -1.80
$E_{\mathrm{T}}^{\mathrm{miss}}$	0.63 / -0.32	0.18 / -0.67	0.18 / -0.56	0.26 / -0.65	0.52 / -0.71	0.50 / -0.78
Fake leptons	0.77 / -0.77	0.33 / -0.33	0.36 / -0.36	0.40 / -0.40	0.34 / -0.34	0.65 / -0.65
Other backgrounds	0.23 / -0.22	0.30 / -0.29	0.37 / -0.35	0.36 / -0.35	0.30 / -0.29	0.24 / -0.23
$t\bar{t}$ modelling	7.38 / -7.34	6.85 / -6.85	5.41 / -5.41	4.18 / -4.18	5.07 / -5.07	7.13 / -7.10
MC stat.	1.51 / -1.51	1.23 / -1.23	1.01 / -1.01	1.03 / -1.03	1.18 / -1.18	1.48 / -1.48
Luminosity	1.92 / -1.85	1.93 / -1.86	1.95 / -1.88	1.95 / -1.89	1.94 / -1.87	1.91 / -1.84

(b) $\mu\mu$

$d\sigma/dy_{t\bar{t}}$ ($e\mu$)	Bins					
Uncertainties [%]	-2.5–1.0	-1.0–0.5	-0.5-0.0	0.0-0.5	0.5-1.0	1.0-2.5
Total	11.66 / -11.52	8.82 / -8.60	7.13 / -6.99	8.52 / -8.38	8.56 / -8.42	12.06 / -11.74
Stat. only	5.99 / -5.99	4.10 / -4.10	3.54 / -3.54	3.78 / -3.78	4.25 / -4.25	6.51 / -6.51
Syst. only	10.01 / -9.85	7.81 / -7.56	6.19 / -6.03	7.63 / -7.47	7.43 / -7.28	10.15 / -9.77
Jet	1.80 / -1.92	2.07 / -1.71	1.60 / -1.52	1.78 / -1.62	1.80 / -1.93	2.67 / -2.09
Tagging	2.32 / -2.16	2.15 / -1.99	2.04 / -1.87	2.12 / -1.96	2.07 / -1.91	2.09 / -1.94
Lepton	3.82 / -3.58	3.65 / -3.43	3.09 / -2.93	3.15 / -3.00	3.76 / -3.51	4.31 / -3.99
$E_{\mathrm{T}}^{\mathrm{miss}}$	0.10 / -0.19	0.10 / -0.02	0.07 / -0.08	0.14 / -0.11	0.08 / -0.12	0.46 / -0.19
Fake leptons	0.69 / -0.72	0.64 / -0.67	0.81 / -0.85	0.70 / -0.72	1.08 / -1.06	1.59 / -1.53
Other backgrounds	0.25 / -0.24	0.31 / -0.30	0.31 / -0.30	0.35 / -0.34	0.31 / -0.30	0.30 / -0.29
$t\bar{t}$ modelling	8.48 / -8.43	5.82 / -5.82	4.16 / -4.16	5.99 / -5.99	5.28 / -5.28	8.09 / -8.04
MC stat.	0.85 / -0.85	0.79 / -0.79	0.59 / -0.59	0.63 / -0.63	0.73 / -0.73	0.94 / -0.94
Luminosity	1.92 / -1.86	1.93 / -1.86	1.92 / -1.85	1.94 / -1.87	1.95 / -1.88	1.97 / -1.90

(c) $e\mu$

Table 10.13: Contribution of each systematic uncertainty in unfolded $d\sigma/dy_{t\bar{t}}$ as percentage of the cross section in each bin in the ee, $\mu\mu$ and $e\mu$ channels.

$(1/\sigma)d\sigma/dy_{t\bar{t}}$ (ee)	Bins					
Uncertainties [%]	-2.5–1.0	-1.0–0.5	-0.5-0.0	0.0-0.5	0.5-1.0	1.0-2.5
Total	35.50 / -35.21	11.43 / -11.49	10.56 / -10.56	14.20 / -14.11	13.70 / -13.65	18.58 / -18.81
Stat. only	24.27 / -24.27	10.10 / -10.10	9.44 / -9.44	10.74 / -10.74	10.88 / -10.88	16.41 / -16.41
Syst. only	25.90 / -25.51	5.35 / -5.48	4.72 / -4.73	9.29 / -9.16	8.31 / -8.23	8.71 / -9.19
Jet	8.27 / -6.52	2.04 / -2.35	1.54 / -1.76	1.82 / -1.49	2.40 / -2.12	2.08 / -2.89
Tagging	0.74 / -0.75	0.21 / -0.19	0.16 / -0.15	0.11 / -0.13	0.23 / -0.29	0.23 / -0.11
Lepton	0.91 / -1.49	0.69 / -0.57	0.45 / -0.34	1.35 / -0.84	0.47 / -0.65	1.26 / -2.46
$E_{\mathrm{T}}^{\mathrm{miss}}$	1.20 / -1.47	0.52 / -0.70	0.58 / -0.07	0.40 / -0.25	0.21 / -0.41	0.76 / -0.40
Fake leptons	8.58 / -8.79	1.03 / -1.07	1.98 / -1.91	0.69 / -0.63	2.27 / -2.17	2.34 / -2.48
Other backgrounds	0.12 / -0.12	0.04 / -0.04	0.02 / -0.02	0.10 / -0.10	0.02 / -0.02	0.08 / -0.08
$t\bar{t}$ modelling	22.50 / -22.49	4.35 / -4.35	3.61 / -3.61	8.79 / -8.79	7.33 / -7.33	7.47 / -7.47
MC stat.	4.44 / -4.44	1.90 / -1.90	1.56 / -1.56	1.82 / -1.82	2.05 / -2.05	2.81 / -2.81
Luminosity	0.32 / -0.32	0.07 / -0.07	0.04 / -0.04	0.07 / -0.07	0.02 / -0.02	0.09 / -0.09

(a) ee

$(1/\sigma)d\sigma/dy_{t\bar{t}}$ $(\mu\mu)$	Bins					
Uncertainties [%]	-2.5–1.0	-1.0–0.5	-0.5-0.0	0.0-0.5	0.5-1.0	1.0-2.5
Total	10.91 / -10.84	8.58 / -8.60	8.21 / -8.30	6.90 / -6.87	7.16 / -7.13	10.85 / -10.82
Stat. only	9.04 / -9.04	6.06 / -6.06	6.20 / -6.20	6.32 / -6.32	6.05 / -6.05	9.05 / -9.05
Syst. only	6.11 / -5.99	6.08 / -6.11	5.39 / -5.51	2.77 / -2.68	3.83 / -3.77	5.98 / -5.93
Jet	2.51 / -2.37	0.65 / -0.91	1.02 / -1.55	0.91 / -0.57	1.54 / -1.34	1.46 / -1.11
Tagging	0.26 / -0.19	0.14 / -0.08	0.16 / -0.07	0.13 / -0.07	0.16 / -0.37	0.13 / -0.26
Lepton	0.40 / -0.40	0.08 / -0.09	0.11 / -0.10	0.27 / -0.27	0.04 / -0.04	0.53 / -0.53
$E_{\mathrm{T}}^{\mathrm{miss}}$	0.84 / -0.42	0.04 / -0.14	0.03 / -0.09	0.08 / -0.13	0.30 / -0.26	0.26 / -0.72
Fake leptons	0.37 / -0.37	0.16 / -0.16	0.09 / -0.09	0.05 / -0.05	0.23 / -0.23	0.22 / -0.22
Other backgrounds	0.07 / -0.08	0.01 / -0.01	0.06 / -0.06	0.05 / -0.05	0.01 / -0.01	0.07 / -0.07
$t\bar{t}$ modelling	5.26 / -5.24	5.91 / -5.91	5.19 / -5.19	2.39 / -2.39	3.28 / -3.29	5.56 / -5.55
MC stat.	1.50 / -1.50	1.24 / -1.24	1.02 / -1.02	1.03 / -1.03	1.17 / -1.17	1.49 / -1.49
Luminosity	0.02 / -0.02	0.01 / -0.01	0.01 / -0.01	0.02 / -0.02	0.00 / -0.00	0.02 / -0.02

(b) $\mu\mu$

$(1/\sigma)d\sigma/dy_{t\bar{t}}$ $(e\mu)$	Bins					
Uncertainties [%]	-2.5–1.0	-1.0–0.5	-0.5-0.0	0.0-0.5	0.5-1.0	1.0-2.5
Total	7.43 / -7.43	5.11 / -5.09	4.26 / -4.27	4.73 / -4.74	5.15 / -5.17	8.57 / -8.46
Stat. only	5.90 / -5.90	4.14 / -4.14	3.56 / -3.56	3.82 / -3.82	4.29 / -4.29	6.52 / -6.52
Syst. only	4.52 / -4.52	2.99 / -2.96	2.34 / -2.36	2.80 / -2.81	2.85 / -2.88	5.56 / -5.39
Jet	0.57 / -0.81	0.52 / -0.31	0.88 / -0.91	0.60 / -0.60	0.30 / -0.50	1.54 / -1.07
Tagging	0.19 / -0.20	0.03 / -0.03	0.10 / -0.10	0.02 / -0.02	0.05 / -0.05	0.06 / -0.06
Lepton	0.30 / -0.29	0.18 / -0.11	0.43 / -0.46	0.37 / -0.41	0.25 / -0.23	0.76 / -0.70
$E_{\mathrm{T}}^{\mathrm{miss}}$	0.07 / -0.17	0.09 / -0.04	0.08 / -0.10	0.15 / -0.13	0.09 / -0.13	0.43 / -0.17
Fake leptons	0.34 / -0.34	0.28 / -0.28	0.18 / -0.21	0.28 / -0.28	0.26 / -0.25	0.77 / -0.73
Other backgrounds	0.06 / -0.06	0.00 / -0.00	0.00 / -0.00	0.04 / -0.04	0.01 / -0.01	0.01 / -0.01
$t\bar{t}$ modelling	4.37 / -4.33	2.82 / -2.82	2.02 / -2.04	2.61 / -2.62	2.71 / -2.72	5.13 / -5.10
MC stat.	0.84 / -0.84	0.78 / -0.78	0.59 / -0.59	0.62 / -0.62	0.73 / -0.73	0.94 / -0.94
Luminosity	0.01 / -0.01	0.01 / -0.01	0.02 / -0.02	0.00 / -0.00	0.01 / -0.01	0.03 / -0.03

(c) $e\mu$

Table 10.14: Contribution of each systematic uncertainty in unfolded $\frac{1}{\sigma_{t\bar{t}}}\frac{d\sigma}{dy_{t\bar{t}}}$ as percentage of the cross section in each bin in the ee, $\mu\mu$ and $e\mu$ channels.

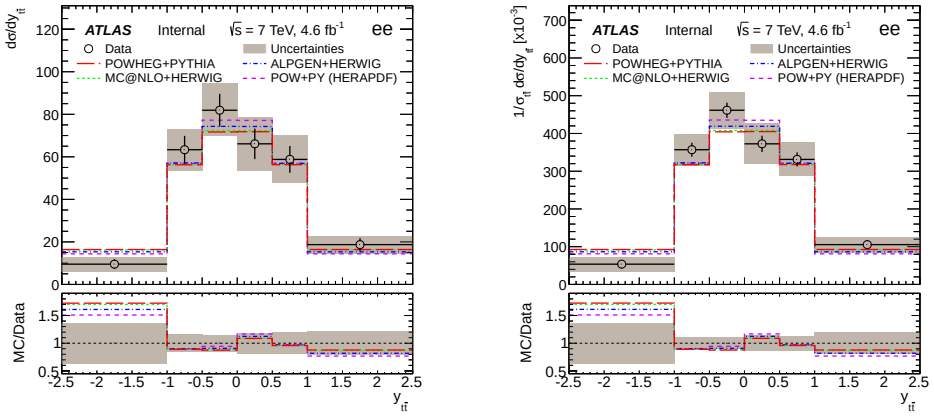

(a) ee

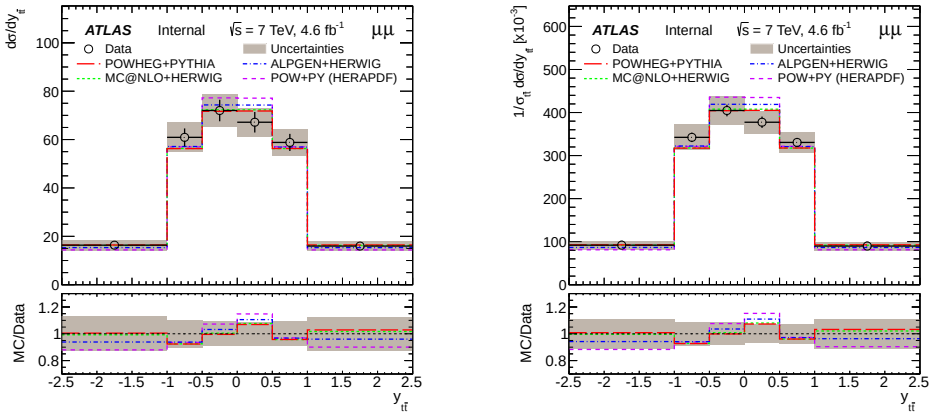

(b) $\mu\mu$

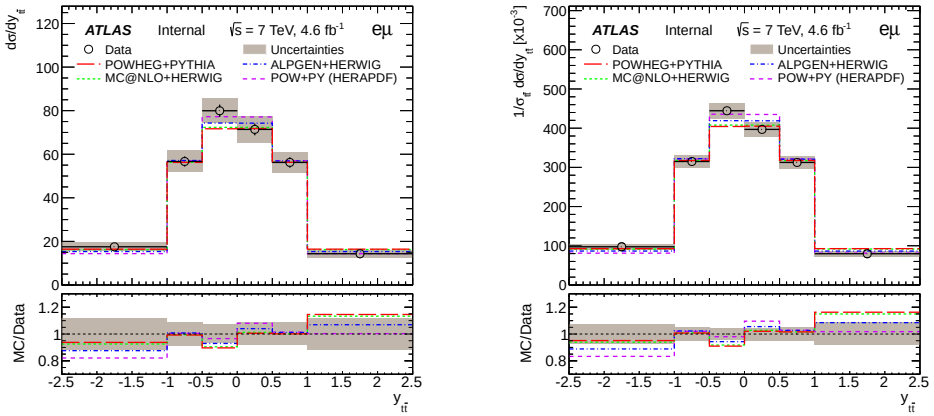

(c) $e\mu$

Figure 10.3: Unfolded $d\sigma/dy_{t\bar{t}}$ (left) and $\frac{1}{\sigma_{t\bar{t}}}\frac{d\sigma}{dy_{t\bar{t}}}$ (right) in the ee (top), $\mu\mu$ (middle) and $e\mu$ (bottom) channels. Different Monte-Carlos are compared with data. The hatched error bands include all statistical and systematic uncertainties.

$y_{t\bar{t}}$ (ee)	-2.5–1.0	-1.0–0.5	-0.5-0.0	0.0-0.5	0.5-1.0	1.0-2.5
-2.5–1.0	1.00	0.26	−0.23	−0.02	0.02	0.00
-1.0–0.5	0.26	1.00	0.08	−0.14	−0.05	0.02
-0.5-0.0	−0.23	0.08	1.00	0.01	−0.14	−0.02
0.0-0.5	−0.02	−0.14	0.01	1.00	0.16	−0.22
0.5-1.0	0.02	−0.05	−0.14	0.16	1.00	0.15
1.0-2.5	0.00	0.02	−0.02	−0.22	0.15	1.00

(a) ee

$y_{t\bar{t}}$ ($\mu\mu$)	-2.5–1.0	-1.0–0.5	-0.5-0.0	0.0-0.5	0.5-1.0	1.0-2.5
-2.5–1.0	1.00	0.15	−0.23	−0.02	0.02	0.01
-1.0–0.5	0.15	1.00	0.18	−0.14	−0.07	0.02
-0.5-0.0	−0.23	0.18	1.00	0.04	−0.15	−0.03
0.0-0.5	−0.02	−0.14	0.04	1.00	0.20	−0.24
0.5-1.0	0.02	−0.07	−0.15	0.20	1.00	0.17
1.0-2.5	0.01	0.02	−0.03	−0.24	0.17	1.00

(b) $\mu\mu$

$y_{t\bar{t}}$ ($e\mu$)	-2.5–1.0	-1.0–0.5	-0.5-0.0	0.0-0.5	0.5-1.0	1.0-2.5
-2.5–1.0	1.00	0.05	−0.18	−0.01	0.02	0.00
-1.0–0.5	0.05	1.00	0.11	−0.14	−0.04	0.02
-0.5-0.0	−0.18	0.11	1.00	0.01	−0.14	−0.02
0.0-0.5	−0.01	−0.14	0.01	1.00	0.10	−0.18
0.5-1.0	0.02	−0.04	−0.14	0.10	1.00	0.06
1.0-2.5	0.00	0.02	−0.02	−0.18	0.06	1.00

(c) $e\mu$

Table 10.15: Bin-to-bin correlations in unfolded $d\sigma/dy_{t\bar{t}}$ and $\frac{1}{\sigma_{t\bar{t}}}\frac{d\sigma}{dy_{t\bar{t}}}$ in the ee, $\mu\mu$ and $e\mu$ channels. These correlations are present due to bin migrations in unfolding.

10.4 Results for $|y_{t\bar{t}}|$

From equation 2.3, the unfolded absolute and normalized differential cross sections are measured as shown in Table 10.16 and 10.17. The systematic and statistical uncertainty components of the absolute and normlized differential measurements for each dilepton channel are shown in Tables 10.18 and 10.19. Figure 10.4 shows the measured results compared with different MCs.

3 iterations are used to unfold the $|y_{t\bar{t}}|$ spectrum, as discussed in Sections 8.3.2 and 8.5.

The correlation matrix is shown in table 10.20.

$\lvert y_{t\bar{t}}\rvert$	$d\sigma/d\lvert y_{t\bar{t}}\rvert$ [pb]	Stat. [%]	Syst. [%]
0-0.5	148^{+22}_{-21}	± 7.1	$^{+13}_{-13}$
0.5-1	122^{+18}_{-18}	± 7.2	$^{+13}_{-13}$
1-2.5	$28.7^{+5.9}_{-5.8}$	± 14	$^{+15}_{-15}$
$\sigma^{int}_{t\bar{t}}$ [pb]	$178.1^{+16.7}_{-16.4}$	± 5.0	$^{+7.9}_{-7.7}$

(a) ee

$\lvert y_{t\bar{t}}\rvert$	$d\sigma/d\lvert y_{t\bar{t}}\rvert$ [pb]	Stat. [%]	Syst. [%]
0-0.5	139^{+10}_{-10}	± 4.5	$^{+5.6}_{-5.7}$
0.5-1	120^{+9}_{-9}	± 4.1	$^{+6.0}_{-6.1}$
1-2.5	$32.3^{+3.3}_{-3.2}$	± 6.4	$^{+7.8}_{-7.6}$
$\sigma^{int}_{t\bar{t}}$ [pb]	$177.9^{+8.2}_{-8.2}$	± 2.8	$^{+3.7}_{-3.7}$

(b) $\mu\mu$

$\lvert y_{t\bar{t}}\rvert$	$d\sigma/d\lvert y_{t\bar{t}}\rvert$ [pb]	Stat. [%]	Syst. [%]
0-0.5	151^{+11}_{-11}	± 2.6	$^{+6.6}_{-6.5}$
0.5-1	113^{+9}_{-9}	± 2.9	$^{+7.5}_{-7.3}$
1-2.5	$31.9^{+3.4}_{-3.3}$	± 4.3	$^{+9.7}_{-9.4}$
$\sigma^{int}_{t\bar{t}}$ [pb]	$180.0^{+8.7}_{-8.5}$	± 1.8	$^{+4.5}_{-4.3}$

(c) $e\mu$

Table 10.16: Unfolded absolute differential cross section of $t\bar{t}$ as a function of $|y_{t\bar{t}}|$ in the ee, $\mu\mu$ and $e\mu$ channels with the total, statistical only and systematic only uncertainties in each bin. The bottom row shows the total $\sigma_{t\bar{t}}$ integrated from the differential measurements.

$\lvert y_{t\bar{t}}\rvert$	$(1/\sigma)d\sigma/d\lvert y_{t\bar{t}}\rvert$ [$\times 10^{-3}$]	Stat. [%]	Syst. [%]
0-0.5	831^{+78}_{-78}	± 7.2	$^{+6.0}_{-5.9}$
0.5-1	686^{+57}_{-57}	± 7.3	$^{+4.1}_{-4.1}$
1-2.5	161^{+30}_{-30}	± 13	$^{+13}_{-13}$
Integrated	$1^{+0.07}_{-0.07}$	± 5.1	$^{+4.2}_{-4.2}$

(a) ee

$\lvert y_{t\bar{t}}\rvert$	$(1/\sigma)d\sigma/d\lvert y_{t\bar{t}}\rvert$ [$\times 10^{-3}$]	Stat. [%]	Syst. [%]
0-0.5	782^{+41}_{-41}	± 4.4	$^{+2.8}_{-2.9}$
0.5-1	673^{+32}_{-32}	± 4.1	$^{+2.5}_{-2.5}$
1-2.5	182^{+14}_{-14}	± 6.5	$^{+4.2}_{-4.1}$
Integrated	$1^{+0.03}_{-0.03}$	± 2.8	$^{+1.8}_{-1.8}$

(b) $\mu\mu$

$\lvert y_{t\bar{t}}\rvert$	$(1/\sigma)d\sigma/d\lvert y_{t\bar{t}}\rvert$ [$\times 10^{-3}$]	Stat. [%]	Syst. [%]
0-0.5	841^{+26}_{-26}	± 2.6	$^{+1.7}_{-1.7}$
0.5-1	627^{+24}_{-24}	± 2.9	$^{+2.6}_{-2.6}$
1-2.5	177^{+11}_{-11}	± 4.4	$^{+4.3}_{-4.3}$
Integrated	$1^{+0.02}_{-0.02}$	± 1.8	$^{+1.6}_{-1.6}$

(c) $e\mu$

Table 10.17: Unfolded normalized differential cross section of $t\bar{t}$ as a function of $|y_{t\bar{t}}|$ in the ee, $\mu\mu$ and $e\mu$ channels with the total, statistical only and systematic only uncertainties in each bin. The last entry of each table is the integrated sum of the normalized differential cross sections, and is consistent with unity.

$d\sigma/d\lvert y_{t\bar{t}}\rvert$ (ee)	Bins		
Uncertainties [%]	0.0-0.5	0.5-1.0	1.0-2.5
Total	14.81 / -14.42	14.93 / -14.68	20.43 / -20.26
Stat. only	7.09 / -7.09	7.23 / -7.23	13.50 / -13.50
Syst. only	13.00 / -12.55	13.06 / -12.77	15.34 / -15.10
Jet	3.22 / -2.78	3.39 / -3.50	4.14 / -4.61
Tagging	2.11 / -1.94	2.06 / -1.88	2.15 / -1.98
Lepton	6.51 / -5.94	7.17 / -6.60	7.07 / -6.38
$E_{\mathrm{T}}^{\mathrm{miss}}$	0.64 / -0.28	0.23 / -0.69	0.75 / -0.38
Fake leptons	2.01 / -1.93	1.79 / -1.80	1.79 / -1.79
Other backgrounds	0.35 / -0.34	0.28 / -0.27	0.30 / -0.29
$t\bar{t}$ modelling	10.12 / -10.12	9.72 / -9.72	12.26 / -12.24
MC stat.	0.91 / -0.91	1.42 / -1.42	2.31 / -2.31
Luminosity	1.99 / -1.92	1.93 / -1.86	1.99 / -1.92

(a) ee

$d\sigma/d\lvert y_{t\bar{t}}\rvert$ ($\mu\mu$)	Bins		
Uncertainties [%]	0.0-0.5	0.5-1.0	1.0-2.5
Total	7.17 / -7.28	7.28 / -7.31	10.07 / -9.93
Stat. only	4.49 / -4.49	4.09 / -4.09	6.42 / -6.42
Syst. only	5.59 / -5.73	6.02 / -6.05	7.77 / -7.58
Jet	2.26 / -2.75	2.50 / -2.62	3.28 / -3.01
Tagging	2.17 / -1.98	2.03 / -1.97	2.17 / -2.10
Lepton	1.78 / -1.73	1.76 / -1.72	1.73 / -1.69
$E_{\mathrm{T}}^{\mathrm{miss}}$	0.22 / -0.61	0.35 / -0.69	0.08 / -0.23
Fake leptons	0.38 / -0.38	0.32 / -0.32	0.71 / -0.71
Other backgrounds	0.36 / -0.35	0.30 / -0.29	0.23 / -0.23
$t\bar{t}$ modelling	3.71 / -3.71	4.24 / -4.24	6.05 / -6.01
MC stat.	0.58 / -0.58	0.88 / -0.88	1.03 / -1.03
Luminosity	1.95 / -1.88	1.94 / -1.87	1.91 / -1.85

(b) $\mu\mu$

$d\sigma/d\lvert y_{t\bar{t}}\rvert$ ($e\mu$)	Bins		
Uncertainties [%]	0.0-0.5	0.5-1.0	1.0-2.5
Total	7.10 / -6.94	8.07 / -7.88	10.62 / -10.38
Stat. only	2.56 / -2.56	2.94 / -2.94	4.32 / -4.32
Syst. only	6.62 / -6.45	7.52 / -7.31	9.70 / -9.43
Jet	1.63 / -1.49	1.94 / -1.82	2.12 / -1.88
Tagging	2.08 / -1.91	2.11 / -1.95	2.21 / -2.05
Lepton	3.12 / -2.96	3.71 / -3.47	4.06 / -3.78
$E_{\mathrm{T}}^{\mathrm{miss}}$	0.09 / -0.09	0.02 / -0.03	0.25 / -0.20
Fake leptons	0.70 / -0.73	0.76 / -0.77	0.99 / -0.98
Other backgrounds	0.33 / -0.32	0.31 / -0.30	0.27 / -0.26
$t\bar{t}$ modelling	4.77 / -4.77	5.46 / -5.46	7.93 / -7.87
MC stat.	0.32 / -0.32	0.55 / -0.55	0.67 / -0.67
Luminosity	1.93 / -1.86	1.94 / -1.87	1.95 / -1.88

(c) $e\mu$

Table 10.18: Contribution of each systematic uncertainty in unfolded $d\sigma/d|y_{t\bar{t}}|$ as percentage of the cross section in each bin in the ee, $\mu\mu$ and $e\mu$ channels.

$(1/\sigma)d\sigma/d\lvert y_{t\bar{t}}\rvert$ (ee)	Bins		
Uncertainties [%]	0.0-0.5	0.5-1.0	1.0-2.5
Total	9.36 / -9.35	8.35 / -8.38	18.69 / -18.69
Stat. only	7.22 / -7.22	7.29 / -7.29	13.46 / -13.46
Syst. only	5.96 / -5.94	4.08 / -4.13	12.97 / -12.97
Jet	1.18 / -1.27	0.91 / -0.95	2.32 / -2.23
Tagging	0.08 / -0.09	0.06 / -0.08	0.19 / -0.18
Lepton	0.67 / -0.51	0.34 / -0.54	0.58 / -1.17
$E_{\mathrm{T}}^{\mathrm{miss}}$	0.54 / -0.12	0.33 / -0.53	0.92 / -0.48
Fake leptons	0.18 / -0.13	0.34 / -0.37	0.32 / -0.32
Other backgrounds	0.04 / -0.03	0.03 / -0.03	0.01 / -0.01
$t\bar{t}$ modelling	5.70 / -5.71	3.67 / -3.67	12.50 / -12.49
MC stat.	0.90 / -0.90	1.42 / -1.42	2.32 / -2.32
Luminosity	0.02 / -0.02	0.04 / -0.04	0.02 / -0.02

(a) ee

$(1/\sigma)d\sigma/d\lvert y_{t\bar{t}}\rvert$ $(\mu\mu)$	Bins		
Uncertainties [%]	0.0-0.5	0.5-1.0	1.0-2.5
Total	5.24 / -5.27	4.82 / -4.83	7.75 / -7.68
Stat. only	4.43 / -4.43	4.12 / -4.12	6.51 / -6.51
Syst. only	2.80 / -2.86	2.50 / -2.51	4.20 / -4.06
Jet	0.79 / -0.97	0.69 / -0.68	1.73 / -1.45
Tagging	0.14 / -0.04	0.05 / -0.13	0.05 / -0.11
Lepton	0.13 / -0.13	0.05 / -0.06	0.15 / -0.16
$E_{\mathrm{T}}^{\mathrm{miss}}$	0.03 / -0.11	0.14 / -0.19	0.32 / -0.16
Fake leptons	0.06 / -0.05	0.23 / -0.23	0.31 / -0.31
Other backgrounds	0.06 / -0.06	0.01 / -0.01	0.07 / -0.07
$t\bar{t}$ modelling	2.61 / -2.62	2.23 / -2.23	3.65 / -3.62
MC stat.	0.59 / -0.59	0.87 / -0.87	1.04 / -1.04
Luminosity	0.02 / -0.02	0.00 / -0.00	0.02 / -0.02

(b) $\mu\mu$

$(1/\sigma)d\sigma/d\lvert y_{t\bar{t}}\rvert$ $(e\mu)$	Bins		
Uncertainties [%]	0.0-0.5	0.5-1.0	1.0-2.5
Total	3.11 / -3.12	3.90 / -3.90	6.16 / -6.11
Stat. only	2.60 / -2.60	2.90 / -2.90	4.37 / -4.37
Syst. only	1.70 / -1.73	2.60 / -2.61	4.34 / -4.27
Jet	0.61 / -0.62	0.28 / -0.33	0.87 / -0.74
Tagging	0.05 / -0.05	0.01 / -0.01	0.08 / -0.09
Lepton	0.40 / -0.44	0.18 / -0.15	0.51 / -0.48
$E_{\mathrm{T}}^{\mathrm{miss}}$	0.11 / -0.12	0.02 / -0.04	0.23 / -0.18
Fake leptons	0.08 / -0.10	0.10 / -0.10	0.20 / -0.18
Other backgrounds	0.02 / -0.02	0.00 / -0.00	0.04 / -0.04
$t\bar{t}$ modelling	1.49 / -1.51	2.52 / -2.53	4.16 / -4.12
MC stat.	0.33 / -0.33	0.55 / -0.55	0.67 / -0.67
Luminosity	0.01 / -0.01	0.00 / -0.00	0.01 / -0.01

(c) $e\mu$

Table 10.19: Contribution of each systematic uncertainty in unfolded $\frac{1}{\sigma_{t\bar{t}}}\frac{d\sigma}{d|y_{t\bar{t}}|}$ as percentage of the cross section in each bin in the ee, $\mu\mu$ and $e\mu$ channels.

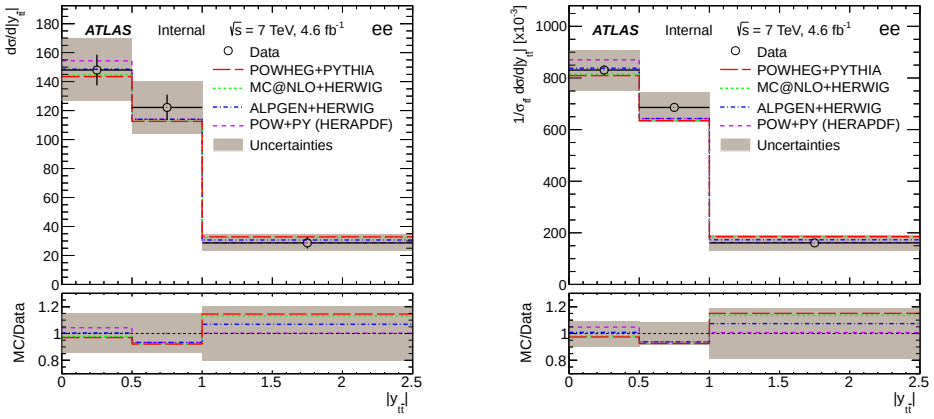

(a) ee

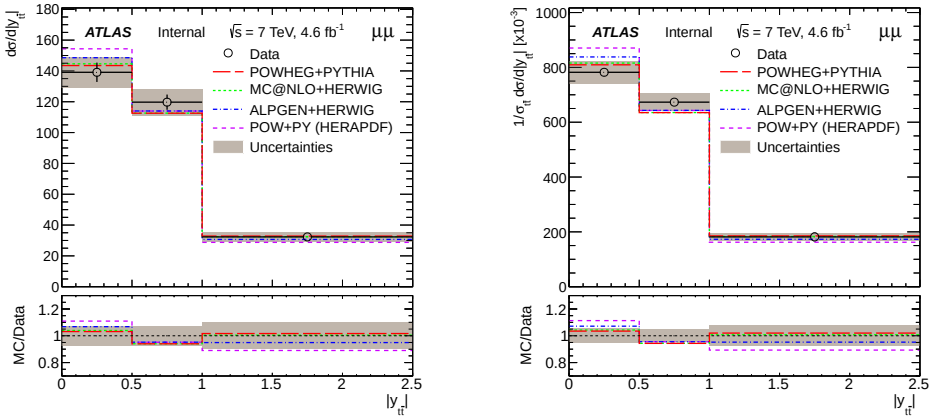

(b) $\mu\mu$

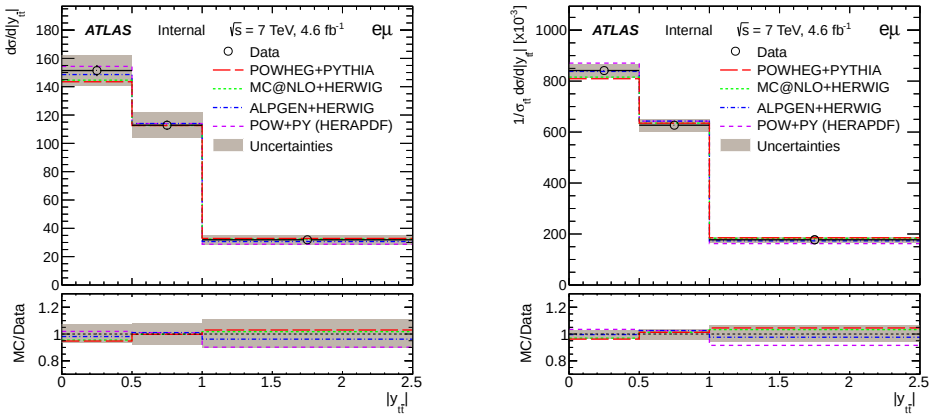

(c) $e\mu$

Figure 10.4: Unfolded $d\sigma/d|y_{t\bar{t}}|$ (left) and $\frac{1}{\sigma_{t\bar{t}}}\frac{d\sigma}{d|y_{t\bar{t}}|}$ (right) in the ee (top), $\mu\mu$ (middle) and $e\mu$ (bottom) channels. Different Monte-Carlos are compared with data. The hatched error bands include all statistical and systematic uncertainties.

$\lvert y_{t\bar{t}}\rvert$ (ee)	0.0-0.5	0.5-1.0	1.0-2.5
0.0-0.5	1.00	−0.02	−0.24
0.5-1.0	−0.02	1.00	0.22
1.0-2.5	−0.24	0.22	1.00

(a) ee

$\lvert y_{t\bar{t}}\rvert$ ($\mu\mu$)	0.0-0.5	0.5-1.0	1.0-2.5
0.0-0.5	1.00	0.05	−0.26
0.5-1.0	0.05	1.00	0.19
1.0-2.5	−0.26	0.19	1.00

(b) $\mu\mu$

$\lvert y_{t\bar{t}}\rvert$ ($e\mu$)	0.0-0.5	0.5-1.0	1.0-2.5
0.0-0.5	1.00	−0.04	−0.19
0.5-1.0	−0.04	1.00	0.07
1.0-2.5	−0.19	0.07	1.00

(c) $e\mu$

Table 10.20: Bin-to-bin correlations in unfolded $d\sigma/d|y_{t\bar{t}}|$ and $\frac{1}{\sigma_{t\bar{t}}}\frac{d\sigma}{d|y_{t\bar{t}}|}$ in the ee, $\mu\mu$ and $e\mu$ channels. These correlations are present due to bin migrations in unfolding.

Chapter 11

Combination of Channels

The procedure of combining the three $t\bar{t}$ dilepton channel results and the combined results are described in this section.

The individual dilepton ee, $\mu\mu$ and $e\mu$ channel results for the differential cross sections for each of the $t\bar{t}$ system variables ($m_{t\bar{t}}$, $p_{\mathrm{T}}^{t\bar{t}}$, $y_{t\bar{t}}$ and $|y_{t\bar{t}}|$) are in reasonably good agreement with each other (within their uncertainties with respect to each other). The results therefore verify lepton universality of the SM for electroweak interactions.

A combination of the dilepton channels can be done at the *number-of-events* level.

Recall equation 2.3,

$$(\frac{d\sigma}{dx_{t\bar{t}}})_i = \frac{N_i^{unfolded}}{L \cdot Br \cdot (A \cdot \epsilon)_i \cdot \Delta x_i}$$

where $N_i^{unfolded} = (N_{obs,i} - N_{bkg,i})^{unfolded}$ is the unfolded background-subtracted data spectrum in the i^{th} bin; L is the integrated luminosity of measured data; Br is the branching ratio of the $t\bar{t}$ default MC sample, including single-lepton and di-lepton channels, and taken as $Br^{t\bar{t}\to nofullhad} = 0.543 = 1-(1-(3\times 0.108))^2$; $(A \cdot \epsilon)_i$ is the differential efficiency evaluated from simulation in the i^{th} bin; Δx_i is the bin width at the i-th bin. If we re-write the equation in number of observed $t\bar{t}$ events (total observed events background-subtracted and unfolded), we have

$$\begin{aligned} N_i^{unfolded}(ee) &= L \cdot (\tfrac{d\sigma}{dx_{t\bar{t}}})_i \cdot Br \cdot (A \cdot \epsilon)_i(ee) \cdot \Delta x_i \\ N_i^{unfolded}(\mu\mu) &= L \cdot (\tfrac{d\sigma}{dx_{t\bar{t}}})_i \cdot Br \cdot (A \cdot \epsilon)_i(\mu\mu) \cdot \Delta x_i \\ N_i^{unfolded}(e\mu) &= L \cdot (\tfrac{d\sigma}{dx_{t\bar{t}}})_i \cdot Br \cdot (A \cdot \epsilon)_i(e\mu) \cdot \Delta x_i \end{aligned} \tag{11.1}$$

for each of the dilepton channels at a variable's bin x_i. If we sum the number of events N_i for all individual channels to a combined dilepton channel, we can obtain

$$N_i^{unfolded}(ll) = L \cdot (\frac{d\sigma}{dx_{t\bar{t}}})_i \cdot Br \cdot (A \cdot \epsilon)_i(ll) \cdot \Delta x_i \tag{11.2}$$

where

$$N_i^{unfolded}(ll) = N_i^{unfolded}(ee) + N_i^{unfolded}(\mu\mu) + N_i^{unfolded}(e\mu) \tag{11.3}$$

and

$$(A \cdot \epsilon)_i(ll) = (A \cdot \epsilon)_i(ee) + (A \cdot \epsilon)_i(\mu\mu) + (A \cdot \epsilon)_i(e\mu) \tag{11.4}$$

from both sides of (11.1) and (11.2). Note that this is true only when L, $(\frac{d\sigma}{dx_{t\bar{t}}})_i$, Br and Δx_i are same for all the dilepton channels. In this analysis, we have Br the same in each case of ee, $\mu\mu$ and $e\mu$ channels since it is the branching ratio of the $t\bar{t}$ default MC sample, which is common for all dilepton channels.

Both (11.3) and (11.4) can be evaluated from the event histograms both for the nominal as well as the systematics. All statistical information (e.g. statistical weights for each channel) and systematic information (e.g. shape) are preserved.

Therefore, the absolute differential cross section of the *combined* dilepton channel is

$$(\frac{d\sigma}{dx_{t\bar{t}}})_i = \frac{N_i^{unfolded}(ll)}{L \cdot Br \cdot (A \cdot \epsilon)_i(ll) \cdot \Delta x_i} \tag{11.5}$$

From this, the inclusive cross section $\sigma_{t\bar{t}}^{int}$ can be obtained by integration and thus the normalized differential cross section $\frac{1}{\sigma_{t\bar{t}}}\frac{d\sigma}{dx_{t\bar{t}}}$ can be calculated in the same manner as in the individual channel case.

Uncertainties (statistical and systematic) and the corresponding covariance matrices in the combined channel are also treated in the same way as in the individual channel. Each systematic component is shifted in the MC in each channel and the number of unfolded events of each channel are summed to obtain the total shift in the combined channel for the systematic component. The statistical covariance matrix simply adds:

$$\mathrm{cov}_(i,j)(ll) = \mathrm{cov}_(i,j)(ee) + \mathrm{cov}_(i,j)(\mu\mu) + \mathrm{cov}_(i,j)(e\mu) \tag{11.6}$$

as the ee, $\mu\mu$ and $e\mu$ channels are statistically uncorrelated.

This event-level combination procedure is preferred over the often-used Best Linear Unbiased Estimation (BLUE) method [48, 49] in this analysis. The BLUE method is formulated (thus far) to combine different measurements with correlated systematic uncertainties to *one* single number. In our differential measurements, the bin-to-bin correlations are introduced due to unfolding, and the BLUE method or its respective software/tool thus far does not handle these bin-to-bin correlations (or correlations among each combined measurement) within the combination algorithm.

The combined results for the absolute and normalized differential cross section as a function of $m_{t\bar{t}}$, $p_{\mathrm{T}}^{t\bar{t}}$, $y_{t\bar{t}}$ and $|y_{t\bar{t}}|$ are shown in sections 11.1,11.2,11.3 and 11.4, respectively. The results are summarized in 11.5 with a consistency check with the channel results, a comparison with the ATLAS lepton+jet measurements with full 7TeV data [22] and a χ^2 comparison of the combined measurements with various MCs.

11.1 Combined results for $m_{t\bar{t}}$

Combined dilepton channel results of absolute and normalized differential cross sections are presented in Tables 11.1 and 11.2, respectively and are summarized in Figure 11.1. The contributions of each systematic uncertainty are shown in Tables 11.3 and 11.4. The bin-to-bin correlations in $m_{t\bar{t}}$ are shown in Table 11.5.

$m_{t\bar{t}}$ [GeV]	$d\sigma/dm_{t\bar{t}}$ [pb/GeV]	Stat. [%]	Syst. [%]
250-450	$0.435^{+0.029}_{-0.029}$	± 2.2	$^{+6.3}_{-6.2}$
450-550	$0.502^{+0.036}_{-0.035}$	± 1.9	$^{+6.9}_{-6.7}$
550-700	$0.197^{+0.020}_{-0.020}$	± 3.2	$^{+9.7}_{-9.6}$
700-950	$0.045^{+0.006}_{-0.006}$	± 5.5	$^{+12}_{-12}$
950-2700	$0.0012^{+0.0003}_{-0.0003}$	± 17	$^{+15}_{-17}$
$\sigma_{t\bar{t}}^{int}$ [pb]	$180.1^{+7.6}_{-7.5}$	± 1.4	$^{+4.0}_{-3.9}$

Table 11.1: Combined result of $d\sigma/dm_{t\bar{t}}$ in the dilepton channel

$m_{t\bar{t}}$ [GeV]	$(1/\sigma)d\sigma/dm_{t\bar{t}}$ [TeV^{-1}]	Stat. [%]	Syst. [%]
250-450	$2.41^{+0.09}_{-0.09}$	± 2.2	$^{+3.0}_{-3.1}$
450-550	$2.79^{+0.09}_{-0.09}$	± 1.9	$^{+2.8}_{-2.7}$
550-700	$1.09^{+0.06}_{-0.06}$	± 3.2	$^{+4.7}_{-4.6}$
700-950	$0.25^{+0.02}_{-0.02}$	± 5.5	$^{+7.7}_{-7.4}$
950-2700	$0.0066^{+0.0013}_{-0.0014}$	± 17	$^{+12}_{-14}$
Integrated	$1^{+0.02}_{-0.02}$	± 1.4	$^{+1.9}_{-1.9}$

Table 11.2: Combined result of $\frac{1}{\sigma_{t\bar{t}}}\frac{d\sigma}{dm_{t\bar{t}}}$ in the dilepton channel

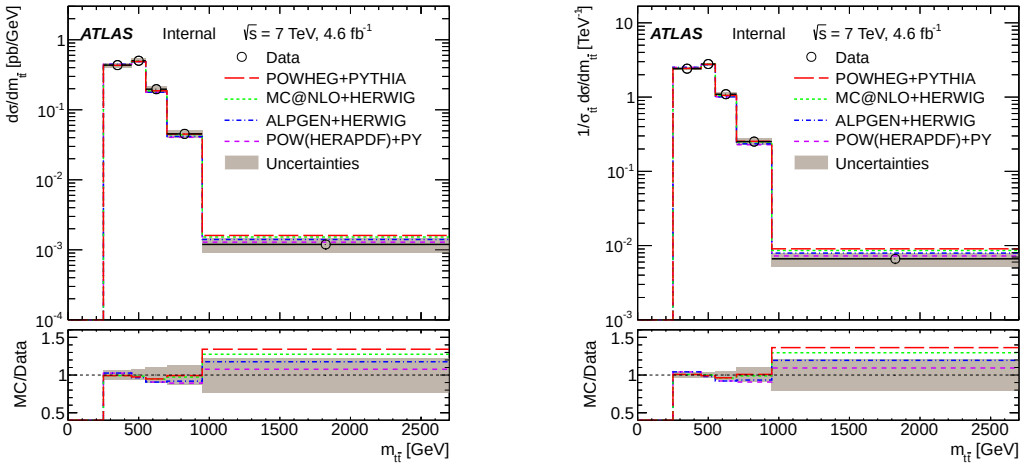

Figure 11.1: Combined unfolded $d\sigma/dm_{t\bar{t}}$ (left) and $\frac{1}{\sigma_{t\bar{t}}}\frac{d\sigma}{dm_{t\bar{t}}}$ (right) in the dilepton channel. The hatched error bands include all statistical and systematic uncertainties.

$d\sigma/dm_{t\bar{t}}$	Bins [GeV]				
Uncertainties [%]	250-450	450-550	550-700	700-950	950-2700
Total	6.65 / -6.57	7.14 / -6.97	10.23 / -10.08	13.17 / -12.80	22.63 / -23.75
Stat. only	2.19 / -2.19	1.90 / -1.90	3.17 / -3.17	5.50 / -5.50	16.53 / -16.53
Syst. only	6.28 / -6.19	6.89 / -6.71	9.73 / -9.57	11.97 / -11.56	15.45 / -17.05
Lepton energy/momentum scale	0.05 / -0.06	0.21 / -0.21	0.46 / -0.51	0.65 / -0.60	1.10 / -1.38
Lepton energy/momentum resolution	0.04 / -0.12	0.02 / -0.09	0.03 / -0.01	0.31 / -0.08	0.15 / -0.09
Lepton reco-id/trigger scale factor	2.80 / -2.68	2.99 / -2.86	3.15 / -3.01	3.35 / -3.20	3.40 / -3.24
Jet energy scale	1.66 / -1.86	1.97 / -1.84	4.69 / -4.65	6.38 / -6.03	7.83 / -9.69
Jet energy resolution	1.43 / -1.40	0.51 / -0.53	0.80 / -0.82	1.67 / -1.69	2.79 / -2.75
Jet reconstruction efficiency	0.05 / -0.05	0.01 / -0.01	0.03 / -0.03	0.04 / -0.04	0.83 / -0.83
Jet vertex fraction scale factor	0.95 / -0.77	0.97 / -0.75	1.00 / -0.77	1.08 / -0.82	0.35 / -1.97
Tagging	1.78 / -1.65	1.93 / -1.78	2.40 / -2.20	3.71 / -3.27	5.16 / -6.61
$E_{\mathrm{T}}^{\mathrm{miss}}$	0.05 / -0.07	0.10 / -0.16	0.26 / -0.31	0.36 / -0.30	0.99 / -1.51
Fake leptons	0.67 / -0.69	0.67 / -0.69	0.89 / -0.87	0.98 / -0.96	3.83 / -3.69
Other backgrounds	0.29 / -0.28	0.28 / -0.27	0.31 / -0.30	0.45 / -0.44	1.19 / -1.15
PDF	1.42 / -1.38	1.55 / -1.50	1.79 / -1.72	2.05 / -1.97	2.76 / -2.62
ISR/FSR	2.57	4.36	5.75	7.09	9.31
MC generator (POW+PY vs MC@NLO+HW)	-0.04	0.26	0.90	2.36	-1.51
POW+PY vs ALPGEN+HW	-3.79	-8.65	-9.00	-7.62	-7.14
Parton shower (POW+PY vs POW+HW)	-2.35	1.16	-3.25	-1.92	1.03
Underlying event	0.06	-0.18	-0.28	1.65	-0.13
Color reconnection	-2.05	-1.54	-1.50	0.51	1.03
Ren./Fac. scale	0.39	-0.02	-1.97	-2.15	-6.00
MC stat.	0.35 / -0.35	0.46 / -0.46	0.66 / -0.66	1.10 / -1.10	2.90 / -2.90
Luminosity	1.93 / -1.87	1.92 / -1.86	1.94 / -1.87	2.00 / -1.93	2.30 / -2.22

Table 11.3: Contribution of each systematic uncertainty to $d\sigma/dm_{t\bar{t}}$ as percentage of the cross section in each bin in the combined dilepton channel.

$(1/\sigma)d\sigma/dm_{t\bar{t}}$	Bins [GeV]				
Uncertainties [%]	250-450	450-550	550-700	700-950	950-2700
Total	3.69 / -3.76	3.34 / -3.32	5.65 / -5.60	9.48 / -9.23	20.28 / -21.39
Stat. only	2.19 / -2.19	1.90 / -1.90	3.17 / -3.17	5.48 / -5.48	16.52 / -16.52
Syst. only	2.97 / -3.05	2.75 / -2.72	4.68 / -4.62	7.73 / -7.42	11.77 / -13.59
Lepton energy/momentum scale	0.22 / -0.21	0.05 / -0.04	0.31 / -0.33	0.49 / -0.43	0.94 / -1.21
Lepton energy/momentum resolution	0.03 / -0.06	0.01 / -0.03	0.06 / -0.04	0.37 / -0.09	0.20 / -0.08
Lepton reco-id/trigger scale factor	0.16 / -0.16	0.04 / -0.05	0.22 / -0.22	0.42 / -0.42	0.49 / -0.47
Jet energy scale	2.20 / -2.31	0.65 / -0.52	3.51 / -3.42	5.32 / -4.95	6.87 / -8.80
Jet energy resolution	0.86 / -0.85	0.03 / -0.05	1.37 / -1.37	2.24 / -2.24	3.37 / -3.30
Jet reconstruction efficiency	0.04 / -0.04	0.02 / -0.02	0.04 / -0.04	0.03 / -0.03	0.84 / -0.84
Jet vertex fraction scale factor	0.01 / -0.01	0.03 / 0.00	0.03 / 0.01	0.11 / -0.04	-0.61 / -1.19
Tagging	0.29 / -0.30	0.15 / -0.15	0.32 / -0.28	1.60 / -1.36	3.05 / -4.91
$E_{\mathrm{T}}^{\mathrm{miss}}$	0.11 / -0.10	0.05 / -0.05	0.20 / -0.17	0.30 / -0.15	1.05 / -1.37
Fake leptons	0.10 / -0.11	0.10 / -0.10	0.15 / -0.14	0.29 / -0.28	3.23 / -3.15
Other backgrounds	0.02 / -0.02	0.03 / -0.03	0.00 / -0.00	0.14 / -0.14	0.87 / -0.85
PDF	0.14 / -0.15	0.02 / -0.02	0.21 / -0.20	0.47 / -0.45	1.17 / -1.11
ISR/FSR	-1.35	0.44	1.84	3.18	5.42
MC generator (POW+PY vs MC@NLO+HW)	-0.37	-0.07	0.57	2.02	-1.83
POW+PY vs ALPGEN+HW	2.66	-2.53	-2.91	-1.43	-0.92
Parton shower (POW+PY vs POW+HW)	-0.88	2.57	-1.77	-0.46	2.45
Underlying event	0.02	-0.21	-0.31	1.62	-0.16
Color reconnection	-0.44	0.08	0.12	2.17	2.70
Ren./Fac. scale	0.76	0.34	-1.61	-1.79	-5.64
MC stat.	0.34 / -0.34	0.47 / -0.47	0.66 / -0.66	1.10 / -1.10	2.94 / -2.94
Luminosity	0.01 / -0.01	0.01 / -0.01	0.00 / -0.00	0.06 / -0.06	0.35 / -0.35

Table 11.4: Contribution of each systematic uncertainty to $(1/\sigma) \cdot d\sigma/dm_{t\bar{t}}$ as percentage of the cross section in each bin in the combined dilepton channel.

$m_{t\bar{t}}$ [GeV]	250-450	450-550	550-700	700-950	950-2700
250-450	1.00	0.28	−0.36	−0.19	0.00
450-550	0.28	1.00	0.44	−0.23	−0.10
550-700	−0.36	0.44	1.00	0.37	−0.18
700-950	−0.19	−0.23	0.37	1.00	0.25
950-2700	0.00	−0.10	−0.18	0.25	1.00

Table 11.5: Bin-to-bin correlations in unfolded $d\sigma/dm_{t\bar{t}}$ and $\frac{1}{\sigma_{t\bar{t}}}\frac{d\sigma}{dm_{t\bar{t}}}$ in the combined dilepton channel. These correlations are present due to bin migrations in unfolding.

11.2 Combined results for $p_{\mathrm{T}}^{t\bar{t}}$

Combined dilepton channel results of absolute and normalized differential cross sections are presented in Tables 11.6 and 11.7, respectively and are summarized in Figure 11.2. The contributions of each systematic uncertainty are shown in Tables 11.8 and 11.9. The bin-to-bin correlations in $p_{\mathrm{T}}^{t\bar{t}}$ are shown in Table 11.10.

$p_{\mathrm{T}}^{t\bar{t}}$ [GeV]	$d\sigma/dp_{T,t\bar{t}}$ [pb/GeV]	Stat. [%]	Syst. [%]
0-40	$2.44^{+0.20}_{-0.20}$	±1.9	$^{+8.0}_{-7.9}$
40-170	$0.57^{+0.06}_{-0.06}$	±2.0	$^{+10}_{-10}$
170-340	$0.049^{+0.008}_{-0.008}$	±6.2	$^{+15}_{-15}$
340-1000	$0.0016^{+0.0005}_{-0.0005}$	±19	$^{+26}_{-26}$
$\sigma_{t\bar{t}}^{int}$ [pb]	$180.6^{+11.2}_{-11.1}$	±1.4	$^{+6.1}_{-6.0}$

Table 11.6: Combined result of $d\sigma/dp_{\mathrm{T}}^{t\bar{t}}$ in the dilepton channel

$p_{\mathrm{T}}^{t\bar{t}}$ [GeV]	$(1/\sigma)d\sigma/dp_{T,t\bar{t}}$ [TeV^{-1}]	Stat. [%]	Syst. [%]
0-40	$13.5^{+0.8}_{-0.8}$	±1.9	$^{+5.6}_{-5.5}$
40-170	$3.14^{+0.19}_{-0.19}$	±2.0	$^{+5.7}_{-5.8}$
170-340	$0.269^{+0.040}_{-0.039}$	±6.2	$^{+13}_{-13}$
340-1000	$0.0088^{+0.0027}_{-0.0027}$	±19	$^{+24}_{-24}$
Integrated	$1^{+0.04}_{-0.04}$	±1.4	$^{+3.9}_{-3.9}$

Table 11.7: Combined result of $\frac{1}{\sigma_{t\bar{t}}}\frac{d\sigma}{dp_{\mathrm{T}}^{t\bar{t}}}$ in the dilepton channel

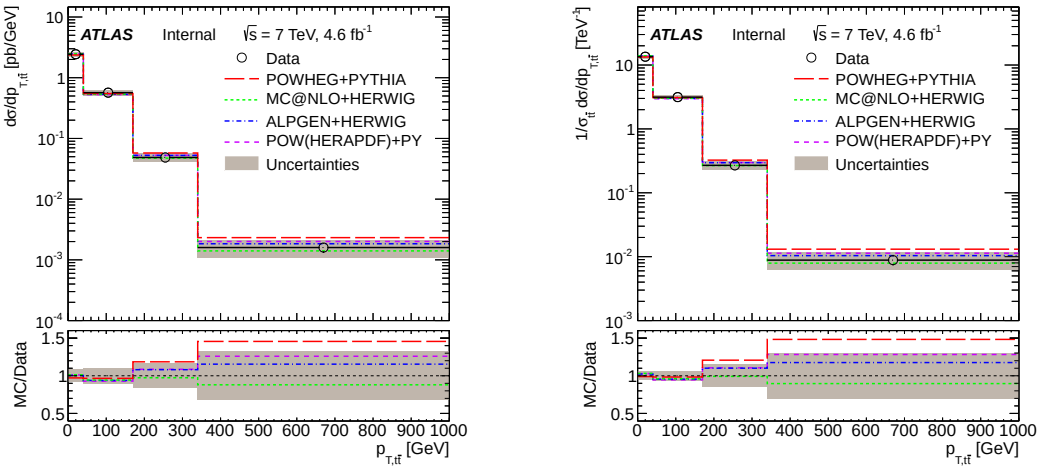

Figure 11.2: Combined unfolded $d\sigma/dp_{\mathrm{T}}^{t\bar{t}}$ (left) and $\frac{1}{\sigma_{t\bar{t}}}\frac{d\sigma}{dp_{\mathrm{T}}^{t\bar{t}}}$ (right) in the dilepton channel. The hatched error bands include all statistical and systematic uncertainties.

$d\sigma/dp_{T,t\bar{t}}$	Bins [GeV]			
Uncertainties [%]	0-40	40-170	170-340	340-1000
Total	8.26 / -8.11	10.43 / -10.45	16.31 / -16.06	31.99 / -32.00
Stat. only	1.93 / -1.93	2.01 / -2.01	6.18 / -6.18	18.70 / -18.70
Syst. only	8.03 / -7.88	10.23 / -10.25	15.10 / -14.83	25.96 / -25.97
Lepton energy/momentum scale	0.19 / -0.20	0.18 / -0.20	0.10 / -0.06	0.17 / -0.26
Lepton energy/momentum resolution	0.01 / -0.09	0.03 / -0.04	0.05 / -0.04	0.14 / -0.07
Lepton reco-id/trigger scale factor	2.99 / -2.87	2.94 / -2.81	2.85 / -2.74	2.89 / -2.79
Jet energy scale	1.42 / -1.42	2.88 / -3.08	6.80 / -6.40	7.68 / -8.08
Jet energy resolution	0.89 / -0.87	0.19 / -0.19	0.38 / -0.39	2.45 / -2.50
Jet reconstruction efficiency	0.04 / -0.04	0.05 / -0.05	0.05 / -0.05	0.14 / -0.24
Jet vertex fraction scale factor	0.73 / -0.54	1.13 / -0.95	1.53 / -1.35	1.80 / -1.65
Tagging	2.15 / -2.01	2.02 / -1.87	2.22 / -2.00	3.53 / -3.20
$E_{\mathrm{T}}^{\mathrm{miss}}$	1.67 / -1.52	1.73 / -2.06	1.12 / -1.11	0.96 / -1.05
Fake leptons	0.71 / -0.74	0.83 / -0.82	1.79 / -1.72	4.28 / -4.15
Other backgrounds	0.37 / -0.35	0.26 / -0.25	0.24 / -0.23	0.29 / -0.28
PDF	1.60 / -1.55	1.32 / -1.29	1.14 / -1.11	3.65 / -3.41
ISR/FSR	1.49	8.12	6.85	9.75
MC generator (POW+PY vs MC@NLO+HW)	2.87	-2.17	-7.26	-18.82
POW+PY vs ALPGEN+HW	-2.40	-10.01	-14.58	-18.73
Parton shower (POW+PY vs POW+HW)	-4.92	0.89	7.03	7.73
Underlying event	0.16	-0.31	1.03	2.59
Color reconnection	-1.76	-1.23	-2.35	-5.30
Ren./Fac. scale	-0.15	-0.19	-4.58	-6.22
MC stat.	0.24 / -0.24	0.28 / -0.28	0.90 / -0.90	2.08 / -2.08
Luminosity	1.94 / -1.87	1.94 / -1.87	1.97 / -1.90	2.04 / -1.97

Table 11.8: Contribution of each systematic uncertainty to $d\sigma/dp_{\mathrm{T}}^{t\bar{t}}$ as percentage of the cross section in each bin in the combined dilepton channel.

$(1/\sigma)d\sigma/dp_{T,t\bar{t}}$	Bins [GeV]			
Uncertainties [%]	0-40	40-170	170-340	340-1000
Total	5.92 / -5.85	6.06 / -6.17	14.72 / -14.54	30.47 / -30.54
Stat. only	1.92 / -1.92	1.99 / -1.99	6.22 / -6.22	18.59 / -18.59
Syst. only	5.60 / -5.53	5.73 / -5.85	13.34 / -13.14	24.13 / -24.22
Lepton energy/momentum scale	0.01 / -0.01	0.01 / -0.01	0.17 / -0.14	0.12 / -0.16
Lepton energy/momentum resolution	0.01 / -0.03	0.02 / -0.02	0.10 / -0.03	0.20 / -0.08
Lepton reco-id/trigger scale factor	0.03 / -0.04	0.04 / -0.03	0.11 / -0.12	0.19 / -0.20
Jet energy scale	1.82 / -1.79	1.68 / -1.79	5.78 / -5.33	7.02 / -7.39
Jet energy resolution	0.36 / -0.36	0.33 / -0.33	0.90 / -0.91	2.98 / -3.01
Jet reconstruction efficiency	0.04 / -0.04	0.05 / -0.05	0.05 / -0.05	0.14 / -0.23
Jet vertex fraction scale factor	0.21 / -0.21	0.19 / -0.20	0.58 / -0.60	0.86 / -0.90
Tagging	0.05 / -0.08	0.11 / -0.09	0.18 / -0.13	1.40 / -1.27
$E_{\mathrm{T}}^{\mathrm{miss}}$	1.67 / -1.45	1.80 / -2.06	1.19 / -1.11	0.90 / -1.04
Fake leptons	0.10 / -0.13	0.16 / -0.15	1.02 / -0.97	3.56 / -3.49
Other backgrounds	0.05 / -0.05	0.05 / -0.05	0.08 / -0.08	0.03 / -0.03
PDF	0.12 / -0.12	0.15 / -0.15	0.33 / -0.34	2.15 / -2.00
ISR/FSR	-3.06	3.58	2.31	5.22
MC generator (POW+PY vs MC@NLO+HW)	2.65	-2.39	-7.46	-19.00
POW+PY vs ALPGEN+HW	4.01	-4.10	-8.97	-13.40
Parton shower (POW+PY vs POW+HW)	-2.93	2.77	8.80	9.48
Underlying event	0.14	-0.33	1.00	2.56
Color reconnection	-0.17	0.37	-0.77	-3.77
Ren./Fac. scale	0.24	0.20	-4.19	-5.83
MC stat.	0.25 / -0.25	0.28 / -0.28	0.89 / -0.89	2.12 / -2.12
Luminosity	0.00 / -0.00	0.00 / -0.00	0.03 / -0.03	0.10 / -0.10

Table 11.9: Contribution of each systematic uncertainty to $(1/\sigma) \cdot d\sigma/dp_{\mathrm{T}}^{t\bar{t}}$ as percentage of the cross section in each bin in the combined dilepton channel.

$p_{\mathrm{T}}^{t\bar{t}}$ [GeV]	0-40	40-170	170-340	340-1000
0-40	1.00	0.04	−0.07	−0.01
40-170	0.04	1.00	0.04	−0.02
170-340	−0.07	0.04	1.00	0.04
340-1000	−0.01	−0.02	0.04	1.00

Table 11.10: Bin-to-bin correlations in unfolded $d\sigma/dp_{\mathrm{T}}^{t\bar{t}}$ and $\frac{1}{\sigma_{t\bar{t}}}\frac{d\sigma}{dp_{\mathrm{T}}^{t\bar{t}}}$ in the combined dilepton channel. These correlations are present due to bin migrations in unfolding.

11.3 Combined results for $y_{t\bar{t}}$

Combined dilepton channel results of absolute and normalized differential cross sections are presented in Tables 11.11 and 11.12, respectively and are summarized in Figure 11.3. The contributions of each systematic uncertainty are shown in Tables 11.13 and 11.14. The bin-to-bin correlations in $y_{t\bar{t}}$ are shown in Table 11.15.

$y_{t\bar{t}}$	$d\sigma/dy_{t\bar{t}}$ [pb]	Stat. [%]	Syst. [%]
-2.5–1	$16.6^{+1.8}_{-1.8}$	±4.8	$^{+9.7}_{-9.5}$
-1–0.5	$58.3^{+4.6}_{-4.6}$	±3.3	$^{+7.2}_{-7.1}$
-0.5-0	$78.2^{+5.4}_{-5.4}$	±2.9	$^{+6.3}_{-6.2}$
0-0.5	$69.9^{+5.7}_{-5.6}$	±3.1	$^{+7.5}_{-7.4}$
0.5-1	$57.1^{+4.5}_{-4.4}$	±3.3	$^{+7.1}_{-6.9}$
1-2.5	$15.1^{+1.6}_{-1.5}$	±5.0	$^{+8.9}_{-8.7}$
$\sigma^{int}_{t\bar{t}}$ [pb]	$179.3^{+6.2}_{-6.1}$	±1.5	$^{+3.1}_{-3.1}$

Table 11.11: Combined result of $d\sigma/dy_{t\bar{t}}$ in the dilepton channel

$y_{t\bar{t}}$	$(1/\sigma)d\sigma/dy_{t\bar{t}}$ [$\times 10^{-3}$]	Stat. [%]	Syst. [%]
-2.5–1	$92.6^{+6.5}_{-6.5}$	±4.8	$^{+5.1}_{-5.1}$
-1–0.5	325^{+15}_{-15}	±3.2	$^{+3.2}_{-3.2}$
-0.5-0	436^{+18}_{-18}	±2.9	$^{+2.8}_{-2.8}$
0-0.5	390^{+17}_{-17}	±3.1	$^{+3.0}_{-3.0}$
0.5-1	318^{+12}_{-12}	±3.3	$^{+1.6}_{-1.6}$
1-2.5	$84.2^{+5.8}_{-5.7}$	±5.0	$^{+4.7}_{-4.6}$
Integrated	$1^{+0.02}_{-0.02}$	±1.5	$^{+1.4}_{-1.4}$

Table 11.12: Combined result of $\frac{1}{\sigma_{t\bar{t}}}\frac{d\sigma}{dy_{t\bar{t}}}$ in the dilepton channel

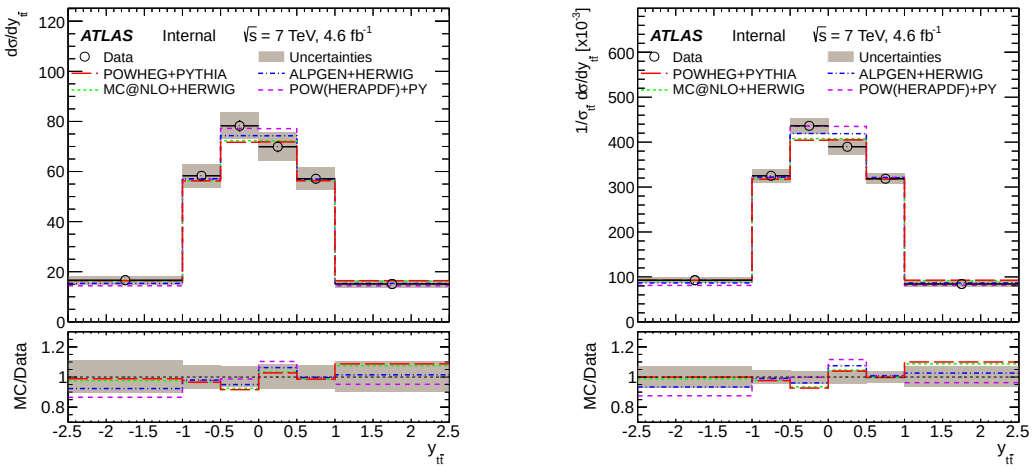

Figure 11.3: Combined unfolded $d\sigma/dy_{t\bar{t}}$ (left) and $\frac{1}{\sigma_{t\bar{t}}}\frac{d\sigma}{dy_{t\bar{t}}}$ (right) in the dilepton channel. The hatched error bands include all statistical and systematic uncertainties.

$d\sigma/dy_{t\bar{t}}$	Bins					
Uncertainties [%]	-2.5–1.0	-1.0–0.5	-0.5-0.0	0.0-0.5	0.5-1.0	1.0-2.5
Total	10.80 / -10.65	7.94 / -7.82	6.90 / -6.84	8.14 / -8.00	7.80 / -7.69	10.27 / -10.07
Stat. only	4.82 / -4.82	3.25 / -3.25	2.91 / -2.91	3.10 / -3.10	3.32 / -3.32	5.04 / -5.04
Syst. only	9.67 / -9.50	7.24 / -7.11	6.26 / -6.19	7.53 / -7.37	7.06 / -6.93	8.95 / -8.72
Lepton energy/momentum scale	0.11 / -0.15	0.17 / -0.18	0.21 / -0.17	0.14 / -0.14	0.19 / -0.23	0.29 / -0.32
Lepton energy/momentum resolution	0.05 / -0.05	0.08 / -0.05	0.01 / -0.07	0.02 / -0.03	0.04 / -0.09	0.01 / -0.24
Lepton reco-id/trigger scale factor	3.00 / -2.87	3.09 / -2.95	2.75 / -2.65	2.73 / -2.63	3.17 / -3.02	3.42 / -3.20
Jet energy scale	2.26 / -2.18	1.57 / -1.64	1.39 / -1.69	1.70 / -1.56	1.82 / -1.81	1.81 / -1.56
Jet energy resolution	0.44 / -0.43	0.86 / -0.85	0.18 / -0.18	0.56 / -0.56	0.72 / -0.71	0.96 / -0.93
Jet reconstruction efficiency	0.02 / -0.02	0.02 / -0.02	0.04 / -0.04	0.03 / -0.03	0.06 / -0.06	0.03 / -0.03
Jet vertex fraction scale factor	0.92 / -0.71	0.97 / -0.78	0.99 / -0.80	1.00 / -0.80	0.96 / -0.82	0.89 / -0.73
Tagging	2.33 / -2.17	2.17 / -2.00	2.06 / -1.90	2.15 / -1.97	2.01 / -1.90	2.05 / -1.95
$E_{\mathrm{T}}^{\mathrm{miss}}$	0.20 / -0.07	0.05 / -0.19	0.15 / -0.20	0.20 / -0.26	0.06 / -0.29	0.13 / -0.23
Fake leptons	1.06 / -1.05	0.68 / -0.70	0.80 / -0.82	0.82 / -0.82	0.93 / -0.91	1.64 / -1.60
Other backgrounds	0.25 / -0.24	0.30 / -0.29	0.32 / -0.31	0.36 / -0.34	0.31 / -0.30	0.27 / -0.26
PDF	2.72 / -2.58	0.20 / -0.20	0.13 / -0.13	0.13 / -0.13	0.22 / -0.22	2.63 / -2.50
ISR/FSR	4.53	4.09	3.85	4.21	4.01	4.37
MC generator (POW+PY vs MC@NLO+HW)	1.20	-2.35	-0.83	2.79	0.21	3.96
POW+PY vs ALPGEN+HW	-10.56	-5.46	-5.09	-4.73	-5.01	-3.62
Parton shower (POW+PY vs POW+HW)	-5.05	-2.05	-0.35	-1.17	-2.57	-3.10
Underlying event	3.53	0.57	-0.66	-0.65	-0.90	0.48
Color reconnection	-0.28	-1.60	-1.89	-2.84	-1.52	0.62
Ren./Fac. scale	-0.57	-0.62	-0.63	-0.24	0.84	-1.22
MC stat.	0.74 / -0.74	0.62 / -0.62	0.48 / -0.48	0.52 / -0.52	0.58 / -0.58	0.75 / -0.75
Luminosity	1.94 / -1.87	1.93 / -1.86	1.93 / -1.86	1.95 / -1.89	1.95 / -1.88	1.95 / -1.88

Table 11.13: Contribution of each systematic uncertainty to $d\sigma/dy_{t\bar{t}}$ as percentage of the cross section in each bin in the combined dilepton channel.

$(1/\sigma)d\sigma/dy_{t\bar{t}}$	Bins					
Uncertainties [%]	-2.5–1.0	-1.0–0.5	-0.5-0.0	0.0-0.5	0.5-1.0	1.0-2.5
Total	7.05 / -7.01	4.55 / -4.55	4.02 / -4.06	4.38 / -4.37	3.66 / -3.67	6.88 / -6.81
Stat. only	4.83 / -4.83	3.23 / -3.23	2.90 / -2.90	3.14 / -3.14	3.29 / -3.29	5.04 / -5.04
Syst. only	5.14 / -5.08	3.20 / -3.21	2.78 / -2.84	3.04 / -3.03	1.60 / -1.62	4.69 / -4.59
Lepton energy/momentum scale	0.06 / -0.07	0.01 / -0.01	0.05 / -0.02	0.06 / -0.06	0.05 / -0.06	0.13 / -0.14
Lepton energy/momentum resolution	0.03 / -0.03	0.13 / -0.04	0.01 / -0.01	0.04 / -0.03	0.02 / -0.03	0.02 / -0.18
Lepton reco-id/trigger scale factor	0.11 / -0.08	0.12 / -0.12	0.22 / -0.24	0.25 / -0.28	0.20 / -0.20	0.45 / -0.39
Jet energy scale	1.09 / -1.01	0.24 / -0.23	0.41 / -0.67	0.63 / -0.54	0.30 / -0.30	1.06 / -0.68
Jet energy resolution	0.07 / -0.06	0.35 / -0.36	0.68 / -0.68	0.05 / -0.06	0.21 / -0.21	0.45 / -0.43
Jet reconstruction efficiency	0.02 / -0.02	0.02 / -0.02	0.04 / -0.04	0.03 / -0.03	0.06 / -0.06	0.03 / -0.03
Jet vertex fraction scale factor	0.07 / -0.04	0.01 / -0.00	0.03 / -0.02	0.04 / -0.02	-0.00 / -0.04	0.04 / -0.07
Tagging	0.21 / -0.20	0.06 / -0.04	0.11 / -0.08	0.04 / -0.01	0.09 / -0.15	0.05 / -0.11
$E_{\mathrm{T}}^{\mathrm{miss}}$	0.32 / -0.10	0.04 / -0.07	0.11 / -0.07	0.15 / -0.13	0.02 / -0.18	0.25 / -0.28
Fake leptons	0.14 / -0.13	0.27 / -0.28	0.12 / -0.16	0.23 / -0.22	0.09 / -0.08	0.75 / -0.74
Other backgrounds	0.05 / -0.05	0.00 / -0.00	0.01 / -0.01	0.05 / -0.05	0.00 / -0.00	0.03 / -0.03
PDF	1.88 / -1.80	0.60 / -0.62	0.67 / -0.70	0.67 / -0.69	0.58 / -0.61	1.78 / -1.71
ISR/FSR	0.39	-0.05	-0.29	0.07	-0.13	0.23
MC generator (POW+PY vs MC@NLO+HW)	0.52	-3.01	-1.50	2.09	-0.47	3.26
POW+PY vs ALPGEN+HW	-5.21	0.19	0.58	0.96	0.67	2.14
Parton shower (POW+PY vs POW+HW)	-2.86	0.08	1.74	0.94	-0.43	-0.95
Underlying event	3.31	0.36	-0.87	-0.86	-1.11	0.27
Color reconnection	1.18	-0.17	-0.46	-1.42	-0.08	2.09
Ren./Fac. scale	-0.19	-0.24	-0.25	0.14	1.22	-0.83
MC stat.	0.73 / -0.73	0.62 / -0.62	0.49 / -0.49	0.51 / -0.51	0.60 / -0.60	0.77 / -0.77
Luminosity	0.00 / -0.00	0.01 / -0.01	0.01 / -0.01	0.01 / -0.01	0.01 / -0.01	0.01 / -0.01

Table 11.14: Contribution of each systematic uncertainty to $(1/\sigma)\cdot d\sigma/dy_{t\bar{t}}$ as percentage of the cross section in each bin in the combined dilepton channel.

$y_{t\bar{t}}$	-2.5–1.0	-1.0–0.5	-0.5-0.0	0.0-0.5	0.5-1.0	1.0-2.5
-2.5–1.0	1.00	0.09	−0.20	−0.02	0.02	0.00
-1.0–0.5	0.09	1.00	0.12	−0.14	−0.04	0.02
-0.5-0.0	−0.20	0.12	1.00	0.02	−0.14	−0.02
0.0-0.5	−0.02	−0.14	0.02	1.00	0.13	−0.20
0.5-1.0	0.02	−0.04	−0.14	0.13	1.00	0.09
1.0-2.5	0.00	0.02	−0.02	−0.20	0.09	1.00

Table 11.15: Bin-to-bin correlations in unfolded $d\sigma/dy_{t\bar{t}}$ and $\frac{1}{\sigma_{t\bar{t}}}\frac{d\sigma}{dy_{t\bar{t}}}$ in the combined dilepton channel. These correlations are present due to bin migrations in unfolding.

11.4 Combined results for $|y_{t\bar{t}}|$

Combined dilepton channel results of absolute and normalized differential cross sections are presented in Tables 11.16 and 11.17, respectively and are summarized in Figure 11.4. The contributions of each systematic uncertainty are shown in Tables 11.18 and 11.19. The bin-to-bin correlations in $|y_{t\bar{t}}|$ are shown in Table 11.20.

$\lvert y_{t\bar{t}}\rvert$	$d\sigma/d\lvert y_{t\bar{t}}\rvert$ [pb]	Stat. [%]	Syst. [%]
0-0.5	148^{+10}_{-10}	± 2.1	$^{+6.6}_{-6.5}$
0.5-1	115^{+8}_{-8}	± 2.3	$^{+7.0}_{-6.9}$
1-2.5	$31.8^{+3.1}_{-3.0}$	± 3.4	$^{+9.0}_{-8.8}$
$\sigma^{int}_{t\bar{t}}$ [pb]	$179.4^{+8.1}_{-7.9}$	± 1.5	$^{+4.3}_{-4.2}$

Table 11.16: Combined result of $d\sigma/d|y_{t\bar{t}}|$ in the dilepton channel

$\lvert y_{t\bar{t}}\rvert$	$(1/\sigma)d\sigma/d\lvert y_{t\bar{t}}\rvert$ [$\times 10^{-3}$]	Stat. [%]	Syst. [%]
0-0.5	826^{+25}_{-25}	± 2.1	$^{+2.1}_{-2.1}$
0.5-1	643^{+20}_{-20}	± 2.3	$^{+2.0}_{-2.0}$
1-2.5	177^{+10}_{-10}	± 3.5	$^{+4.3}_{-4.3}$
Integrated	$1^{+0.02}_{-0.02}$	± 1.5	$^{+1.6}_{-1.6}$

Table 11.17: Combined result of $\frac{1}{\sigma_{t\bar{t}}}\frac{d\sigma}{d|y_{t\bar{t}}|}$ in the dilepton channel

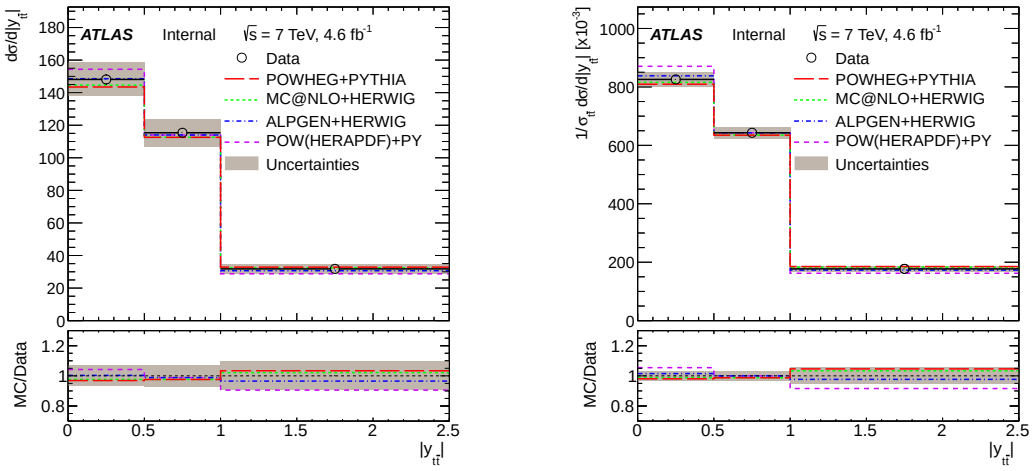

Figure 11.4: Combined unfolded $d\sigma/d|y_{t\bar{t}}|$ (left) and $\frac{1}{\sigma_{t\bar{t}}}\frac{d\sigma}{d|y_{t\bar{t}}|}$ (right) in the dilepton channel. The hatched error bands include all statistical and systematic uncertainties.

$d\sigma/d\lvert y_{t\bar{t}}\rvert$	Bins		
Uncertainties [%]	0.0-0.5	0.5-1.0	1.0-2.5
Total	6.91 / -6.80	7.35 / -7.23	9.63 / -9.44
Stat. only	2.13 / -2.13	2.26 / -2.26	3.45 / -3.45
Syst. only	6.57 / -6.45	6.99 / -6.87	8.99 / -8.79
Lepton energy/momentum scale	0.18 / -0.16	0.18 / -0.21	0.19 / -0.23
Lepton energy/momentum resolution	0.01 / -0.05	0.02 / -0.04	0.03 / -0.14
Lepton reco-id/trigger scale factor	2.74 / -2.64	3.13 / -2.99	3.21 / -3.03
Jet energy scale	1.54 / -1.61	1.68 / -1.73	2.02 / -1.84
Jet energy resolution	0.18 / -0.18	0.77 / -0.77	0.71 / -0.69
Jet reconstruction efficiency	0.03 / -0.03	0.02 / -0.02	0.03 / -0.03
Jet vertex fraction scale factor	0.99 / -0.80	0.96 / -0.80	0.91 / -0.72
Tagging	2.10 / -1.93	2.09 / -1.95	2.19 / -2.06
$E_{\mathrm{T}}^{\mathrm{miss}}$	0.17 / -0.23	0.05 / -0.24	0.16 / -0.14
Fake leptons	0.74 / -0.76	0.73 / -0.73	0.95 / -0.94
Other backgrounds	0.34 / -0.33	0.30 / -0.29	0.26 / -0.25
PDF	0.12 / -0.12	0.20 / -0.20	2.67 / -2.54
ISR/FSR	4.02	4.09	4.43
MC generator (POW+PY vs MC@NLO+HW)	0.86	-1.11	2.60
POW+PY vs ALPGEN+HW	-4.96	-5.20	-7.26
Parton shower (POW+PY vs POW+HW)	-0.75	-2.25	-4.15
Underlying event	-0.64	-0.22	2.09
Color reconnection	-2.33	-1.63	0.22
Ren./Fac. scale	-0.42	0.08	-0.83
MC stat.	0.27 / -0.27	0.44 / -0.44	0.55 / -0.55
Luminosity	1.94 / -1.87	1.94 / -1.87	1.94 / -1.87

Table 11.18: Contribution of each systematic uncertainty to $d\sigma/d|y_{t\bar{t}}|$ as percentage of the cross section in each bin in the combined dilepton channel.

$(1/\sigma)d\sigma/d\lvert y_{t\bar{t}}\rvert$	Bins		
Uncertainties [%]	0.0-0.5	0.5-1.0	1.0-2.5
Total	2.99 / -3.01	3.03 / -3.05	5.56 / -5.50
Stat. only	2.13 / -2.13	2.25 / -2.25	3.48 / -3.48
Syst. only	2.09 / -2.12	2.03 / -2.05	4.34 / -4.26
Lepton energy/momentum scale	0.04 / -0.04	0.02 / -0.03	0.03 / -0.04
Lepton energy/momentum resolution	0.03 / -0.01	0.05 / -0.03	0.01 / -0.07
Lepton reco-id/trigger scale factor	0.24 / -0.26	0.15 / -0.15	0.24 / -0.21
Jet energy scale	0.51 / -0.58	0.18 / -0.23	0.96 / -0.77
Jet energy resolution	0.33 / -0.33	0.26 / -0.27	0.20 / -0.19
Jet reconstruction efficiency	0.03 / -0.03	0.02 / -0.02	0.03 / -0.03
Jet vertex fraction scale factor	0.03 / -0.02	0.00 / -0.02	0.06 / -0.05
Tagging	0.06 / -0.03	0.02 / -0.04	0.07 / -0.10
$E_{\mathrm{T}}^{\mathrm{miss}}$	0.12 / -0.10	0.01 / -0.12	0.29 / -0.19
Fake leptons	0.04 / -0.05	0.10 / -0.10	0.17 / -0.16
Other backgrounds	0.03 / -0.03	0.00 / -0.00	0.04 / -0.05
PDF	0.67 / -0.70	0.60 / -0.62	1.84 / -1.77
ISR/FSR	-0.13	-0.06	0.28
MC generator (POW+PY vs MC@NLO+HW)	0.17	-1.79	1.90
POW+PY vs ALPGEN+HW	0.73	0.47	-1.71
Parton shower (POW+PY vs POW+HW)	1.35	-0.12	-1.98
Underlying event	-0.85	-0.43	1.88
Color reconnection	-0.91	-0.20	1.69
Ren./Fac. scale	-0.05	0.45	-0.46
MC stat.	0.27 / -0.27	0.44 / -0.44	0.55 / -0.55
Luminosity	0.00 / -0.00	0.00 / -0.00	0.00 / -0.00

Table 11.19: Contribution of each systematic uncertainty to $(1/\sigma) \cdot d\sigma/d|y_{t\bar{t}}|$ as percentage of the cross section in each bin in the combined dilepton channel.

$\lvert y_{t\bar{t}}\rvert$	0.0-0.5	0.5-1.0	1.0-2.5
0.0-0.5	1.00	−0.02	−0.21
0.5-1.0	−0.02	1.00	0.11
1.0-2.5	−0.21	0.11	1.00

Table 11.20: Bin-to-bin correlations in unfolded $d\sigma/d|y_{t\bar{t}}|$ and $\frac{1}{\sigma_{t\bar{t}}}\frac{d\sigma}{d|y_{t\bar{t}}|}$ in the combined dilepton channel. These correlations are present due to bin migrations in unfolding.

11.5 Summary

The combined results are summarized in a comparison with the channel results (Figures 11.5,11.6,11.7,11.8) and with the lepton+jets measurements in full 7 TeV data [22] in the normalized differential cross sections (Figures 11.9,11.10,11.11). The levels of agreement between the combined data results and the various MCs of interest in this analysis are also summarized in their respective χ^2/NDF (χ^2 per number of degrees of freedom) in Tables 11.21 and 11.22. The χ^2's are calculated using the measured value of data (y) and predicted MCs ($\bar{y}$), and the statistical covariance matrix of data (cov), as $\chi^2 = (y - \bar{y})^T \mathrm{cov}^{-1} (y - \bar{y})$.

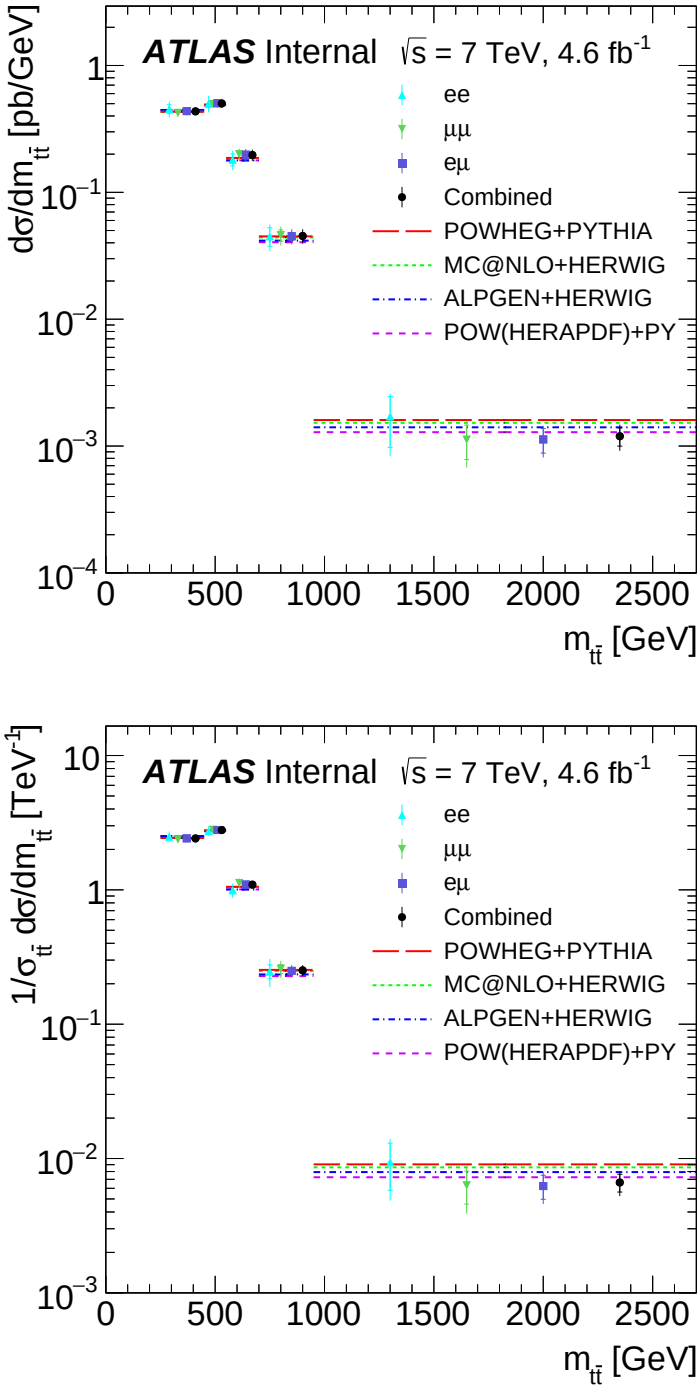

Figure 11.5: Summary of the dilepton ee, $\mu\mu$, $e\mu$ and combined ll channels of the unfolded $d\sigma/dm_{t\bar{t}}$ (top) and $\frac{1}{\sigma_{t\bar{t}}}\frac{d\sigma}{dm_{t\bar{t}}}$ (bottom). The error bars on measured data represent total (stat.+syst.) uncertainties, while the statistical uncertainties are shown with the small horizontal lines in the error bars.

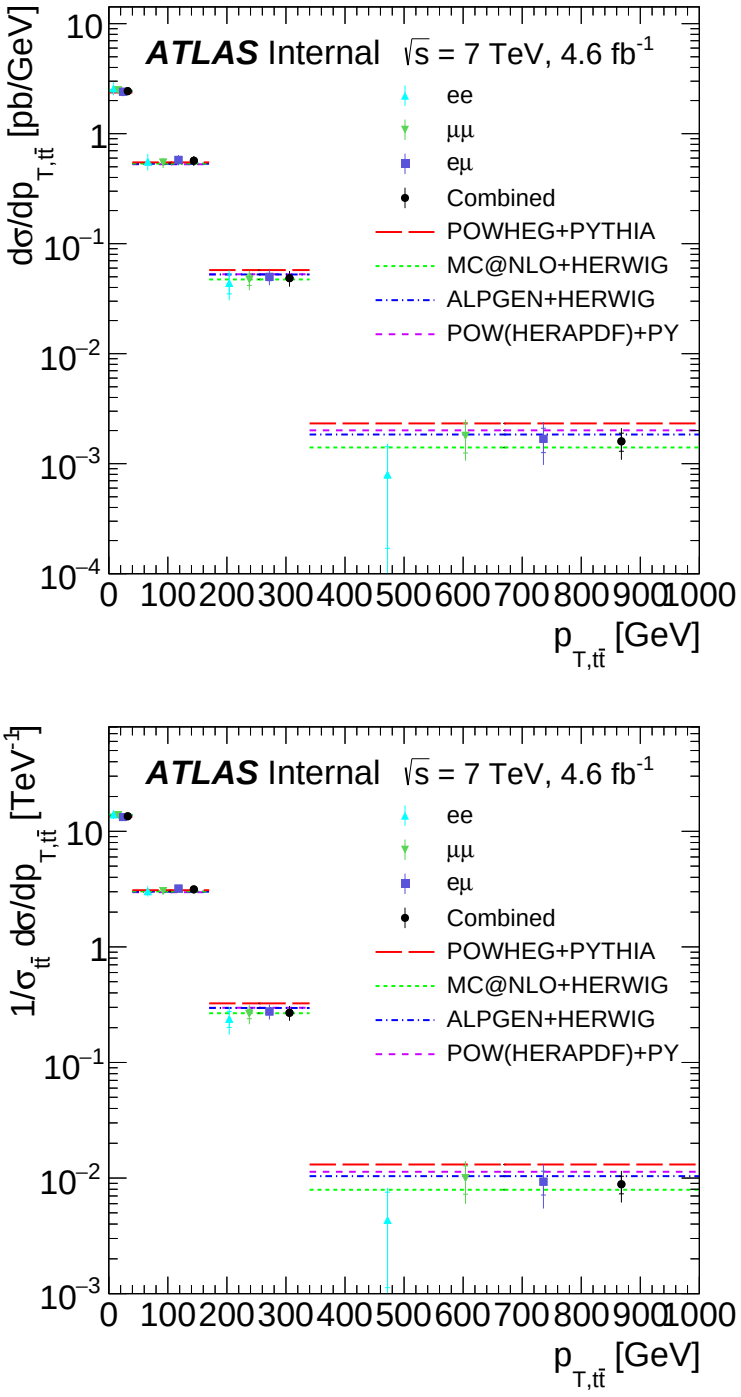

Figure 11.6: Summary of the dilepton ee, $\mu\mu$, $e\mu$ and combined ll channels of the unfolded $d\sigma/dp_{\mathrm{T}}^{t\bar{t}}$ (top) and $\frac{1}{\sigma_{t\bar{t}}}\frac{d\sigma}{dp_{\mathrm{T}}^{t\bar{t}}}$ (bottom). The error bars on measured data represent total (stat.+syst.) uncertainties, while the statistical uncertainties are shown with the small horizontal lines in the error bars.

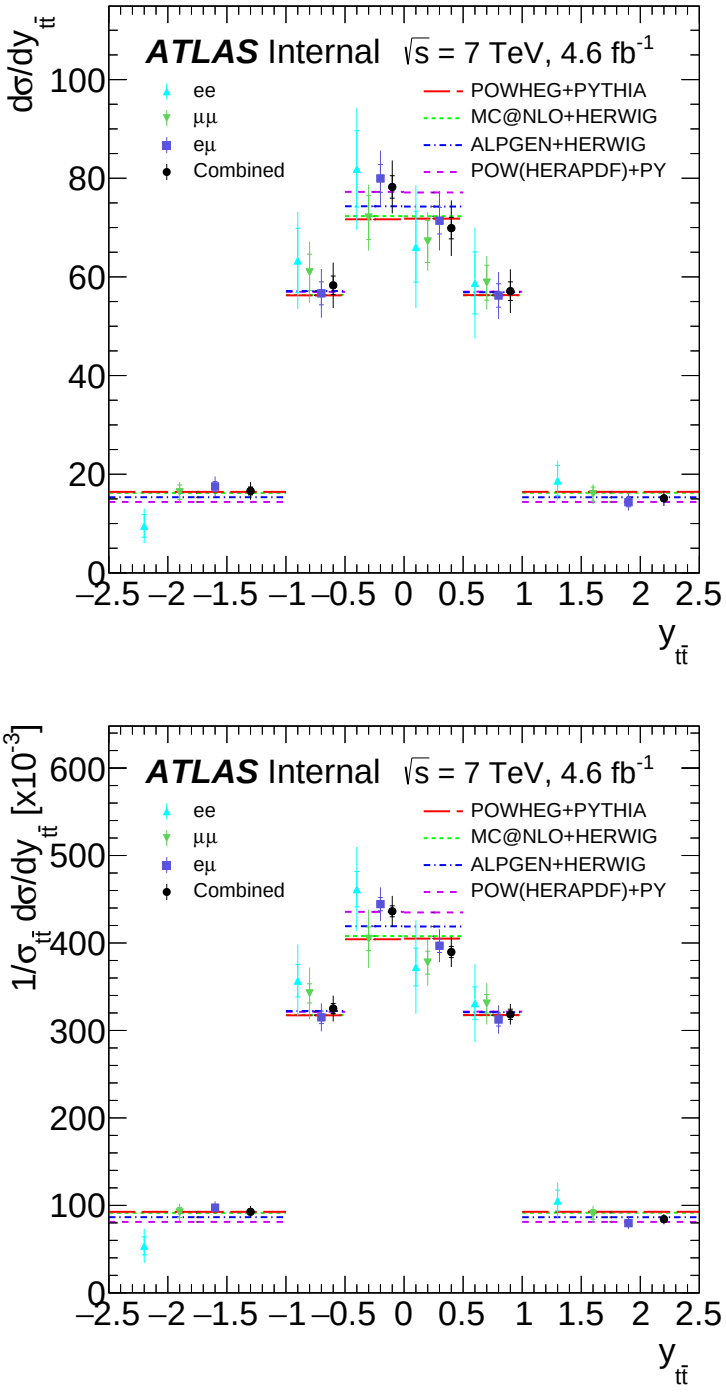

Figure 11.7: Summary of the dilepton ee, $\mu\mu$, $e\mu$ and combined ll channels of the unfolded $d\sigma/dy_{t\bar{t}}$ (top) and $\frac{1}{\sigma_{t\bar{t}}}\frac{d\sigma}{dy_{t\bar{t}}}$ (bottom). The error bars on measured data represent total (stat.+syst.) uncertainties, while the statistical uncertainties are shown with the small horizontal lines in the error bars.

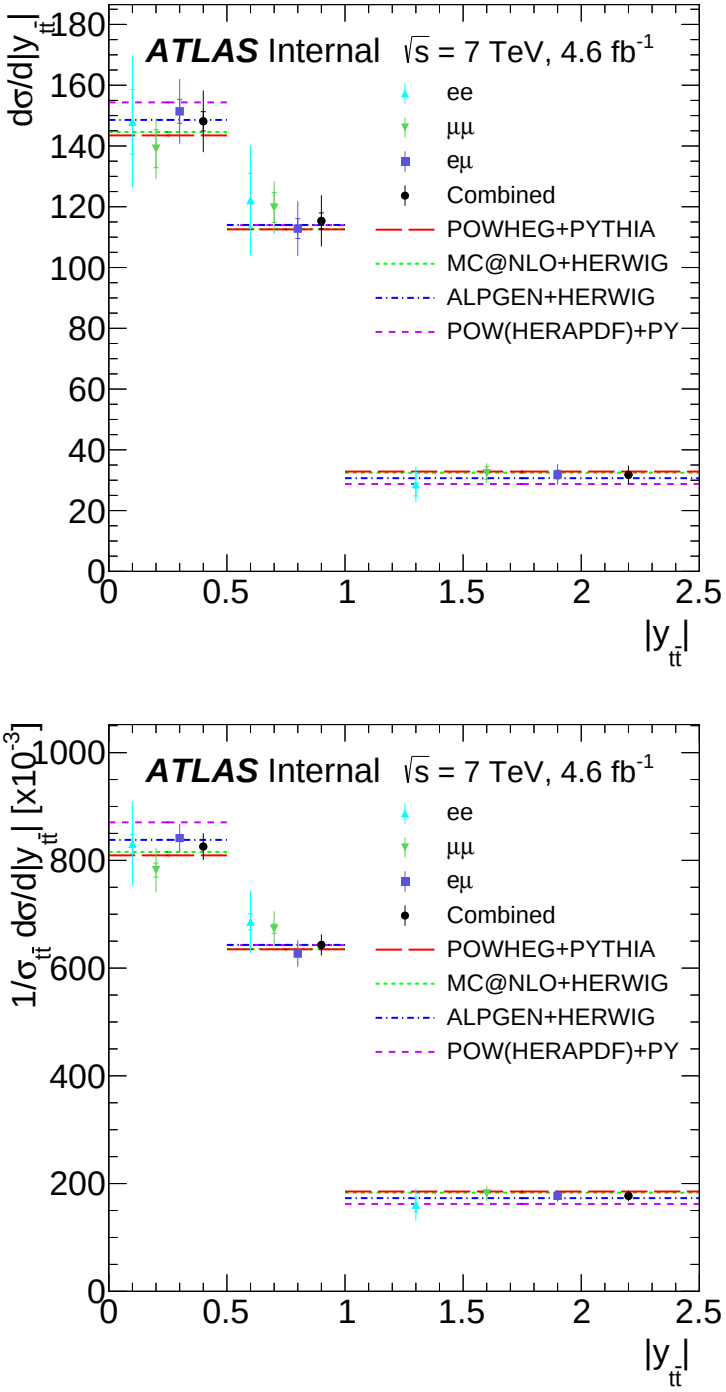

Figure 11.8: Summary of the dilepton ee, $\mu\mu$, $e\mu$ and combined ll channels of the unfolded $d\sigma/d|y_{t\bar{t}}|$ (top) and $\frac{1}{\sigma_{t\bar{t}}}\frac{d\sigma}{d|y_{t\bar{t}}|}$ (bottom). The error bars on measured data represent total (stat.+syst.) uncertainties, while the statistical uncertainties are shown with the small horizontal lines in the error bars.

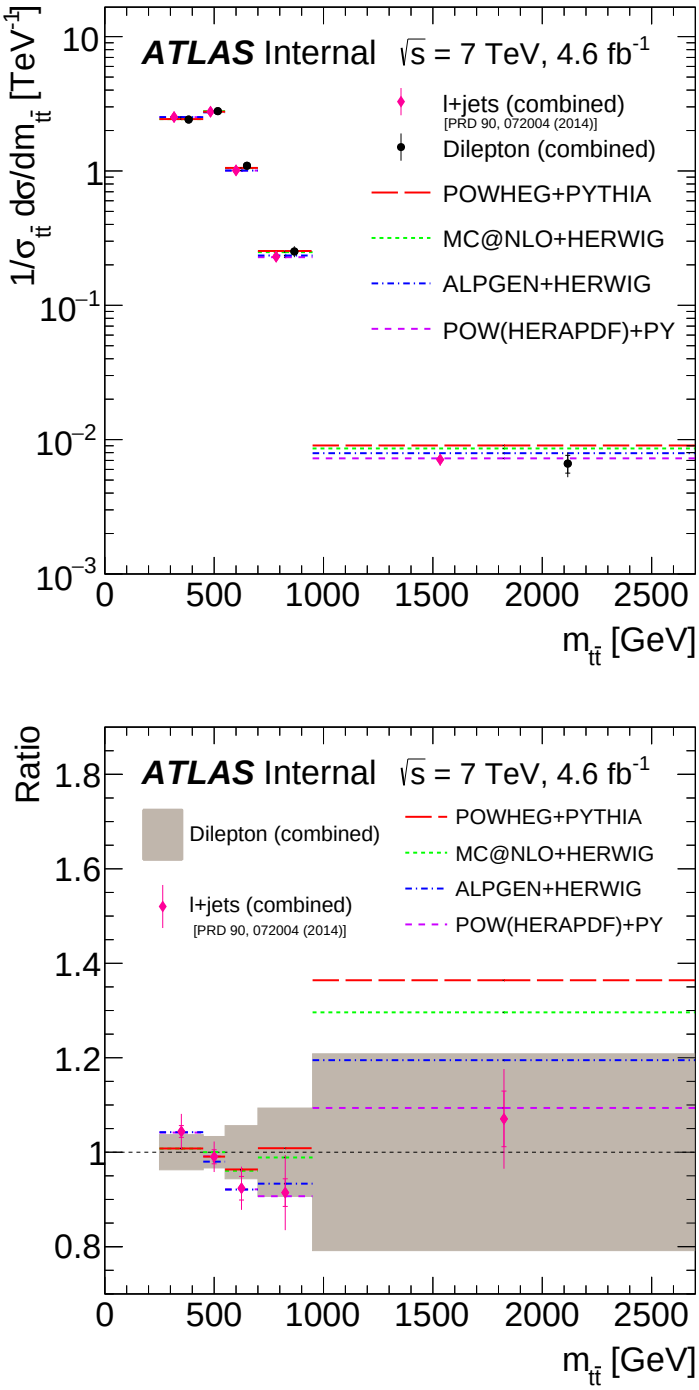

Figure 11.9: Summary of the lepton+jets combined [22] and dilepton combined measurements of the unfolded $\frac{1}{\sigma_{t\bar{t}}}\frac{d\sigma}{dm_{t\bar{t}}}$. The error bars on measured data represent total (stat.+syst.) uncertainties, while the statistical uncertainties are shown with the small horizontal lines in the error bars. The bottom plot shows the ratio of the lepton+jets measurement and the various MC predictions relative to the dilepton measurement.

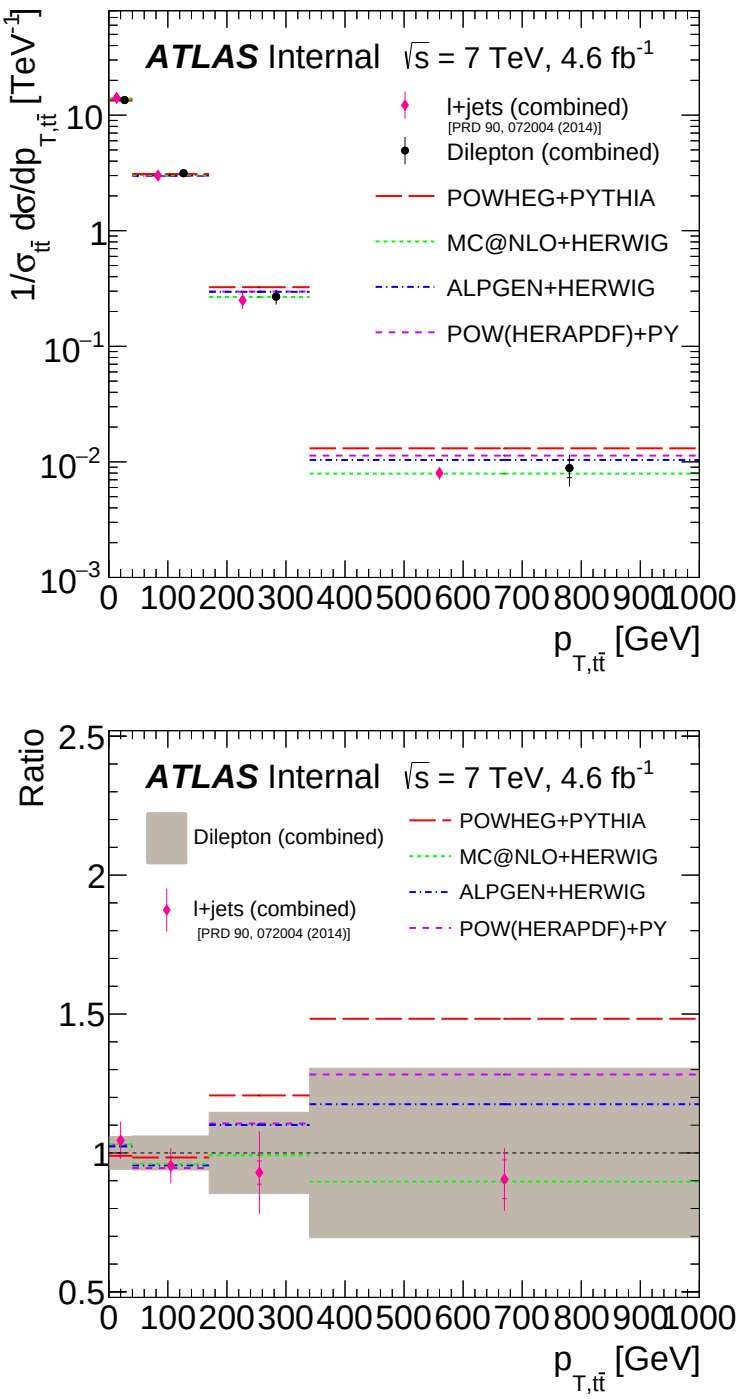

Figure 11.10: Summary of the lepton+jets combined [22] and dilepton combined measurements of the unfolded $\frac{1}{\sigma_{t\bar{t}}}\frac{d\sigma}{dp_{\mathrm{T}}^{t\bar{t}}}$. The error bars on measured data represent total (stat.+syst.) uncertainties, while the statistical uncertainties are shown with the small horizontal lines in the error bars. The bottom plot shows the ratio of the lepton+jets measurement and the various MC predictions relative to the dilepton measurement.

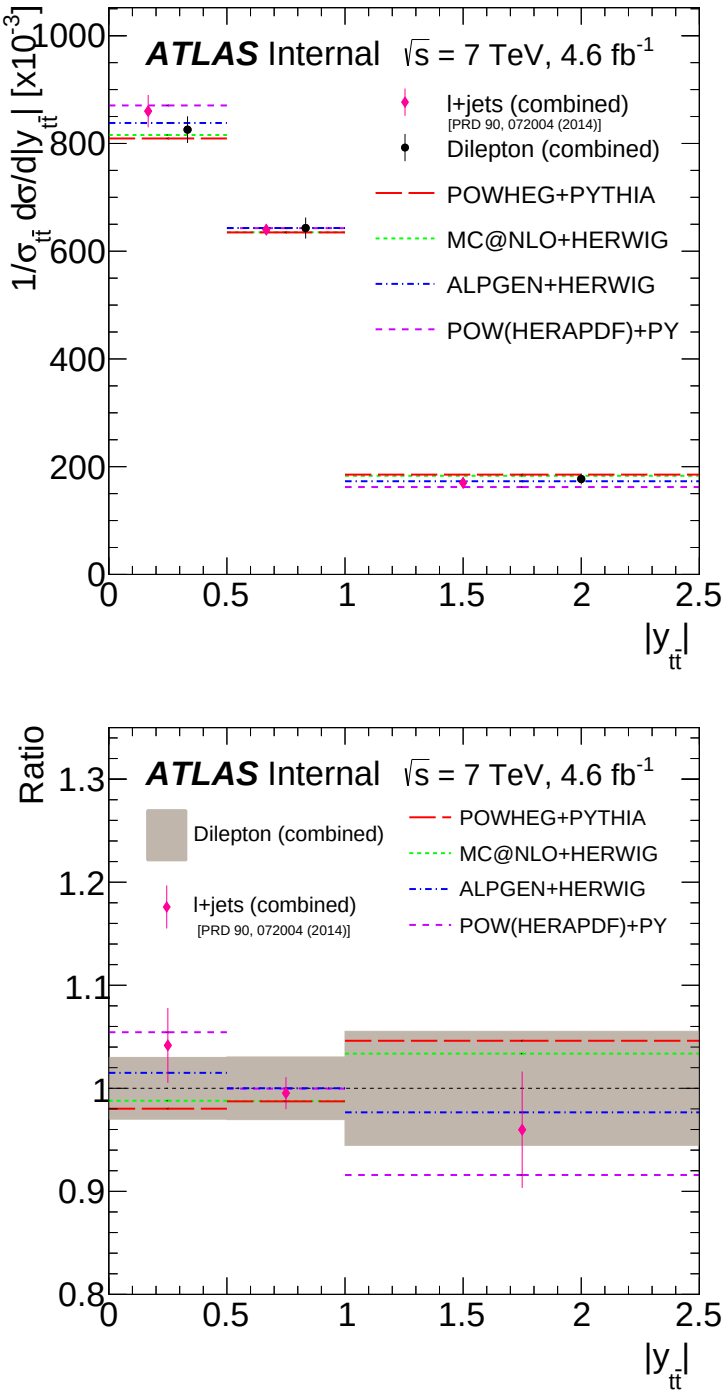

Figure 11.11: Summary of the lepton+jets combined [22] and dilepton combined measurements of the unfolded $\frac{1}{\sigma_{t\bar{t}}}\frac{d\sigma}{d|y_{t\bar{t}}|}$. The error bars on measured data represent total (stat.+syst.) uncertainties, while the statistical uncertainties are shown with the small horizontal lines in the error bars. The bottom plot shows the ratio of the lepton+jets measurement and the various MC predictions relative to the dilepton measurement.

Variable	POWHEG +PYTHIA	ALPGEN +HERWIG	MC@NLO +HERWIG	POWHEG (HERAPDF)+PYTHIA
	χ^2/NDF	χ^2/NDF	χ^2/NDF	χ^2/NDF
$m_{t\bar{t}}$	6.8/4	11.3/4	6.1/4	10.0/4
$p_{\mathrm{T}}^{t\bar{t}}$	19.0/3	12.3/3	9.1/3	17.3/3
$y_{t\bar{t}}$	15.1/5	11.9/5	13.6/5	20.2/5
$\lvert y_{t\bar{t}}\rvert$	4.0/2	1.2/2	2.7/2	9.6/2

Table 11.21: χ^2 values in the comparison of measured absolute differential cross sections of $t\bar{t}$ in the combined channel and predictions from different MC generators. The number of degree of freedom (NDF) is $n_{bins} - 1$ where n_{bins} is the number of bins in each measured variable.

Variable	POWHEG +PYTHIA	ALPGEN +HERWIG	MC@NLO +HERWIG	POWHEG (HERAPDF)+PYTHIA
	χ^2/NDF	χ^2/NDF	χ^2/NDF	χ^2/NDF
$m_{t\bar{t}}$	5.4/4	9.7/4	4.7/4	8.3/4
$p_{\mathrm{T}}^{t\bar{t}}$	18.1/3	10.8/3	7.3/3	15.9/3
$y_{t\bar{t}}$	14.1/5	11.6/5	12.7/5	20.7/5
$\lvert y_{t\bar{t}}\rvert$	2.7/2	0.8/2	1.5/2	10.3/2

Table 11.22: χ^2 values in the comparison of measured normalized differential cross sections of $t\bar{t}$ in the combined channel and predictions from different MC generators. The number of degrees of freedom (NDF) is $n_{bins} - 1$ where n_{bins} is the number of bins in each measured variable.

Chapter 12

Conclusions

Measurement of the differential cross sections of $t\bar{t}$ as a function of $m_{t\bar{t}}$, $p_{\mathrm{T}}^{t\bar{t}}$, $y_{t\bar{t}}$ and $|y_{t\bar{t}}|$ in $\sqrt{s} = 7$ TeV in the dilepton channel is presented. Both the absolute and normalized differential cross sections are measured. The total uncertainty is dominated by systematic uncertainties in the absolute differential measurement for all $t\bar{t}$ system variables, while in the normalized measurement the systematic uncertainty is reduced to the level of statistical uncertainty. The individual channel results are in good agreement with each other, and are combined to total dilepton channel results. The measured differential cross sections are consistent with the SM predictions and the measurements in lepton+jets channel [22] using the same full 7 TeV dataset.

Both the absolute and normalized differential cross-sections are compared with various Monte Carlo models. The comparison in hard regions (high $m_{t\bar{t}}$, high $p_{\mathrm{T}}^{t\bar{t}}$) suggests that POWHEG + PYTHIA with HERAPDF describes the measured data best in $m_{t\bar{t}}$, while MC@NLO + HERWIG describes the $p_{\mathrm{T}}^{t\bar{t}}$ best in these regions. In the same region POWHEG + PYTHIA seems to show most deviations from the measured spectra, in both $m_{t\bar{t}}$ and $p_{\mathrm{T}}^{t\bar{t}}$ cases. The differences among the MC models in comparison are small in the $t\bar{t}$ rapidity distributions. Both absolute and normalized results show similar behaviors in the data-MC comparisons. These observations are consistent with the observed behaviors in data versus the various MCs in the lepton+jets results [22].

Chapter 13

Outlook

During Run II (2015-2017), LHC will deliver pp collisions at $\sqrt{s}$ =13-14 TeV at $10^{34}\text{cm}^{-2}\text{s}^{-1}$ for a total integrated luminosity $\int \mathcal{L}dt \approx 100\text{fb}^{-1}$. This will be about 20 (4) times the data collected in Run I at 7TeV (7+8TeV). The total production cross section of $t\bar{t}$ $\sigma_{t\bar{t}}$ will also be higher at the new energies, at about 800-950pb, as shown in table 2.2. About 90M of top-antitop pairs will be produced during Run II, which is ~ 90 times the $t\bar{t}$ production in 7TeV in this analysis. With this increased new data, the precision of measurements of $t\bar{t}$ total and differential cross sections will be enhanced by a factor of almost 10. In view of the highest bins in $d\sigma/dm_{t\bar{t}}$ $(950 - 2700$ GeV) and $d\sigma/dp_{\text{T}}^{t\bar{t}}$ $(340 - 1000$ GeV) in this analysis, the statistical uncertainty will be reduced from the current $\sim 20\%$ to $\sim 2\%$ in the combined dilepton channel. The statistical uncertainty of other bins in $d\sigma/dm_{t\bar{t}}$ and $d\sigma/dp_{\text{T}}^{t\bar{t}}$ will also be reduced from about percent to sub-percent level, as well as measurements in $d\sigma/dy_{t\bar{t}}$ and $d\sigma/d|y_{t\bar{t}}|$. The measurements will be well-dominated by systematic uncertainty, which will also be much improved with more data especially due to more advanced understanding of the modeling of $t\bar{t}$ production, QCD scales and PDFs.

At an almost doubled center-of-mass energy $\sqrt{s}$ at 13-14 TeV, $t\bar{t}$ will also be produced at an ever higher invariant mass $m_{t\bar{t}}$ and transverse momentum $p_{\text{T}}^{t\bar{t}}$ in the TeV range (above 2.7 TeV and 1 TeV, respectively). The measurement of $d\sigma/dm_{t\bar{t}}$ and $d\sigma/dp_{\text{T}}^{t\bar{t}}$ will continue to be particularly useful handles to detect distortions in the spectra due to resonances that couple strongly in the BSM physics. However, many BSM scenarios predict the effects of these particles in the $m_{t\bar{t}}$ and $p_{\text{T}}^{t\bar{t}}$ distributions are not more than few percents [50]. Thus the more precise measurement of $d\sigma/dm_{t\bar{t}}$ and $d\sigma/dp_{\text{T}}^{t\bar{t}}$ in Run II will elevate the sensitivity to the BSM physics in the top sector. The high statistics will enable the construction of finer bins in the high-end tail regions of $m_{t\bar{t}}$ and $p_{\text{T}}^{t\bar{t}}$, which is required to show local structures clearly and detect deviations from the SM in the spectra. In this high-energy region, the top quarks are also highly Lorentz-boosted, which leads to overlapping or merging of jets and/or leptons from the decay products of $t\bar{t}$. Therefore, special criteria for identification and reconstruction of the $t\bar{t}$ system will be essential for this measurement in Run II.

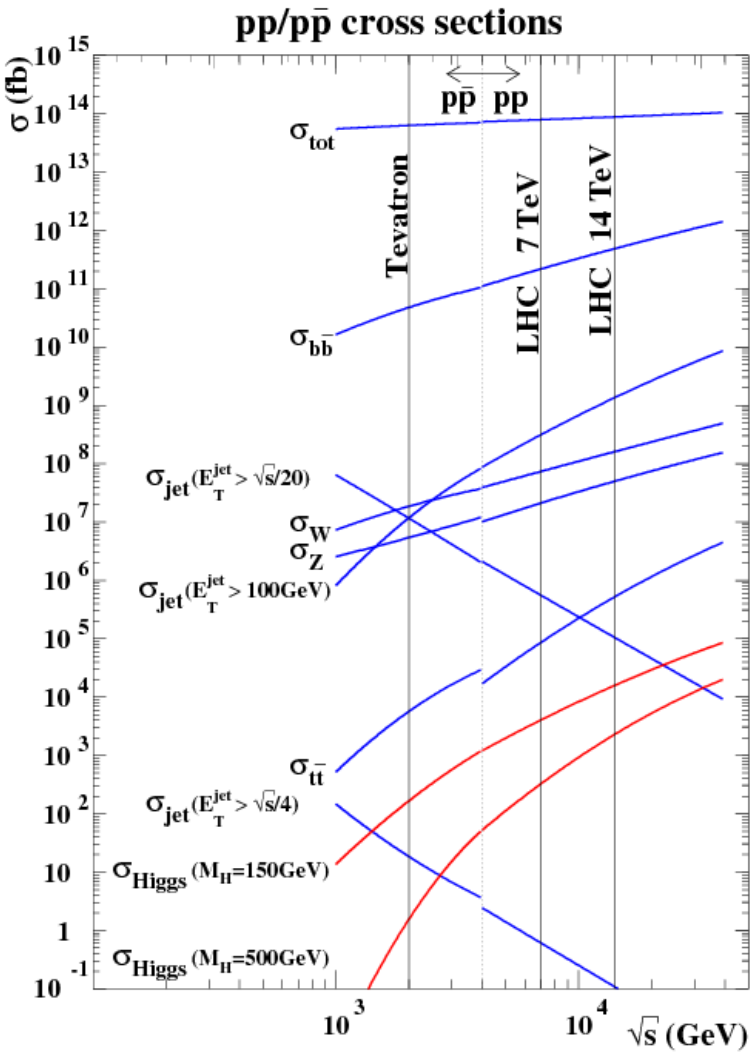

Figure 13.1: Proton-(anti)proton cross sections for various processes as a function of the center-of-mass energy $\sqrt{s}$. The LHC will deliver pp collisions at $\sqrt{s} = 13 - 14$ TeV in Run II (2015-2017).

Appendix A

List of Monte Carlo Simulation Samples

ID	Process	Generator	PDF	$\sigma[pb]$	k-factor
117050	$t\bar{t}$ no full-had	POWHEG+PYTHIA P2011C	CT10	80.07	1.202
110141	Single top (Wt-chan) dilepton	POWHEG+PYTHIA	CT10	1.506	1.092
107650	$Z(\rightarrow ee) + 0$p	ALPGEN+HERWIG/JIMMY	CTEQ6L1	668.32	1.25
107651	$Z(\rightarrow ee) + 1$p	ALPGEN+HERWIG/JIMMY	CTEQ6L1	134.36	1.25
107652	$Z(\rightarrow ee) + 2$p	ALPGEN+HERWIG/JIMMY	CTEQ6L1	40.54	1.25
107653	$Z(\rightarrow ee) + 3$p	ALPGEN+HERWIG/JIMMY	CTEQ6L1	11.16	1.25
107654	$Z(\rightarrow ee) + 4$p	ALPGEN+HERWIG/JIMMY	CTEQ6L1	2.88	1.25
107655	$Z(\rightarrow ee) + 5$p	ALPGEN+HERWIG/JIMMY	CTEQ6L1	0.83	1.25
107660	$Z(\rightarrow \mu\mu) + 0$p	ALPGEN+HERWIG/JIMMY	CTEQ6L1	668.68	1.25
107661	$Z(\rightarrow \mu\mu) + 1$p	ALPGEN+HERWIG/JIMMY	CTEQ6L1	134.14	1.25
107662	$Z(\rightarrow \mu\mu) + 2$p	ALPGEN+HERWIG/JIMMY	CTEQ6L1	40.325	1.25
107663	$Z(\rightarrow \mu\mu) + 3$p	ALPGEN+HERWIG/JIMMY	CTEQ6L1	11.19	1.25
107664	$Z(\rightarrow \mu\mu) + 4$p	ALPGEN+HERWIG/JIMMY	CTEQ6L1	2.75	1.25
107665	$Z(\rightarrow \mu\mu) + 5$p	ALPGEN+HERWIG/JIMMY	CTEQ6L1	0.77	1.25
107670	$Z(\rightarrow \tau\tau) + 0$p	ALPGEN+HERWIG/JIMMY	CTEQ6L1	668.40	1.25
107671	$Z(\rightarrow \tau\tau) + 1$p	ALPGEN+HERWIG/JIMMY	CTEQ6L1	134.81	1.25
107672	$Z(\rightarrow \tau\tau) + 2$p	ALPGEN+HERWIG/JIMMY	CTEQ6L1	40.36	1.25
107673	$Z(\rightarrow \tau\tau) + 3$p	ALPGEN+HERWIG/JIMMY	CTEQ6L1	11.25	1.25
107674	$Z(\rightarrow \tau\tau) + 4$p	ALPGEN+HERWIG/JIMMY	CTEQ6L1	2.79	1.25
107670	$Z(\rightarrow \tau\tau) + 5$p	ALPGEN+HERWIG/JIMMY	CTEQ6L1	0.77	1.25
107100	$WWlnulnu + 0$p	ALPGEN+HERWIG/JIMMY	CTEQ6L1	2.0950	1.26
107101	$WWlnulnu + 1$p	ALPGEN+HERWIG/JIMMY	CTEQ6L1	0.9962	1.26
107102	$WWlnulnu + 2$p	ALPGEN+HERWIG/JIMMY	CTEQ6L1	0.4547	1.26
107103	$WWlnulnu + 3$p	ALPGEN+HERWIG/JIMMY	CTEQ6L1	0.1758	1.26
107104	$WZincll + 0$p	ALPGEN+HERWIG/JIMMY	CTEQ6L1	0.6718	1.28
107105	$WZincll + 1$p	ALPGEN+HERWIG/JIMMY	CTEQ6L1	0.4138	1.28
107106	$WZincll + 2$p	ALPGEN+HERWIG/JIMMY	CTEQ6L1	0.2249	1.28
107107	$WZincll + 3$p	ALPGEN+HERWIG/JIMMY	CTEQ6L1	0.0950	1.28
107108	$ZZincll + 0$p	ALPGEN+HERWIG/JIMMY	CTEQ6L1	0.5086	1.30
107109	$ZZincll + 1$p	ALPGEN+HERWIG/JIMMY	CTEQ6L1	0.2342	1.30
107110	$ZZincll + 2$p	ALPGEN+HERWIG/JIMMY	CTEQ6L1	0.0886	1.30
107111	$ZZincll + 3$p	ALPGEN+HERWIG/JIMMY	CTEQ6L1	0.0314	1.30

Table A.1: Summary of the dataset number, process, generator, PDF, cross-section, and k-factor for each Monte Carlo sample used in default signal and backgrounds. All the samples listed are processed using the full simulation of the ATLAS detector.

ID	Process	Generator	PDF	$\sigma[pb]$	k-factor	Simulation
117050	$t\bar{t}$ no full-had	POWHEG+PYTHIA P2011C	CT10	80.07	1.202	FullSim
117050	$t\bar{t}$ no full-had	POWHEG+PYTHIA P2011C	CT10	80.07	1.202	ALTFASTII
105200	$t\bar{t}$ no full-had	MC@NLO+HERWIG/JIMMY	CT10	79.01	1.219	FullSim
105860	$t\bar{t}$ no full-had	POWHEG+HERWIG/JIMMY	CTEQ6L1	80.85	1.191	ALTFASTII
105890	$t\bar{t}lnln$ + 0p	ALPGEN+HERWIG/JIMMY	CTEQ6L1	3.47	1.793	FullSim
105891	$t\bar{t}lnln$ + 1p	ALPGEN+HERWIG/JIMMY	CTEQ6L1	3.40	1.793	FullSim
105892	$t\bar{t}lnln$ + 2p	ALPGEN+HERWIG/JIMMY	CTEQ6L1	2.11	1.793	FullSim
117897	$t\bar{t}lnln$ + 3p	ALPGEN+HERWIG/JIMMY	CTEQ6L1	0.94	1.793	FullSim
117898	$t\bar{t}lnln$ + 4p	ALPGEN+HERWIG/JIMMY	CTEQ6L1	0.325	1.793	FullSim
117899	$t\bar{t}lnln$ + 5+p	ALPGEN+HERWIG/JIMMY	CTEQ6L1	0.13	1.793	FullSim
105894	$t\bar{t}lnqq$ + 0p	ALPGEN+HERWIG/JIMMY	CTEQ6L1	13.86	1.865	FullSim
105895	$t\bar{t}lnqq$ + 1p	ALPGEN+HERWIG/JIMMY	CTEQ6L1	13.69	1.865	FullSim
105896	$t\bar{t}lnqq$ + 2p	ALPGEN+HERWIG/JIMMY	CTEQ6L1	8.47	1.865	FullSim
117887	$t\bar{t}lnqq$ + 3p	ALPGEN+HERWIG/JIMMY	CTEQ6L1	3.78	1.865	FullSim
117888	$t\bar{t}lnqq$ + 4p	ALPGEN+HERWIG/JIMMY	CTEQ6L1	1.34	1.865	FullSim
117889	$t\bar{t}lnqq$ + 5+p	ALPGEN+HERWIG/JIMMY	CTEQ6L1	0.50	1.865	FullSim
117428	$t\bar{t}$ no full-had	POWHEG+PYTHIA P2011	CTEQ5L	80.07	1.202	ALTFASTII
117429	$t\bar{t}$ no full-had	POWHEG+PYTHIA P2011 noCR	CTEQ5L	80.07	1.202	ALTFASTII
117430	$t\bar{t}$ no full-had	POWHEG+PYTHIA P2011 mpiHi	CTEQ5L	80.06	1.203	ALTFASTII
117525	$t\bar{t}lnln$ + 0p IFSR	ALPGEN+PYTHIA P2011 radHi KTFac05	CTEQ5L	2.50	2.120	ALTFASTII
117526	$t\bar{t}lnln$ + 1p IFSR	ALPGEN+PYTHIA P2011 radHi KTFac05	CTEQ5L	2.71	2.120	ALTFASTII
117527	$t\bar{t}lnln$ + 2p IFSR	ALPGEN+PYTHIA P2011 radHi KTFac05	CTEQ5L	1.93	2.120	ALTFASTII
117528	$t\bar{t}lnln$ + 3p IFSR	ALPGEN+PYTHIA P2011 radHi KTFac05	CTEQ5L	0.99	2.120	ALTFASTII
117529	$t\bar{t}lnln$ + 4+p IFSR	ALPGEN+PYTHIA P2011 radHi KTFac05	CTEQ5L	0.65	2.120	ALTFASTII
117535	$t\bar{t}lnln$ + 0p IFSR	ALPGEN+PYTHIA P2011 radLo KTFac2	CTEQ5L	3.16	2.190	ALTFASTII
117536	$t\bar{t}lnln$ + 1p IFSR	ALPGEN+PYTHIA P2011 radLo KTFac2	CTEQ5L	2.79	2.190	ALTFASTII
117537	$t\bar{t}lnln$ + 2p IFSR	ALPGEN+PYTHIA P2011 radLo KTFac2	CTEQ5L	1.58	2.190	ALTFASTII
117538	$t\bar{t}lnln$ + 3p IFSR	ALPGEN+PYTHIA P2011 radLo KTFac2	CTEQ5L	0.65	2.190	ALTFASTII
117539	$t\bar{t}lnln$ + 4+p IFSR	ALPGEN+PYTHIA P2011 radLo KTFac2	CTEQ5L	0.31	2.190	ALTFASTII
110006	$t\bar{t}$ no full-had	MC@NLO+HERWIG/JIMMY mudown	CT10	89.47	1.076	ALTFASTII
110007	$t\bar{t}$ no full-had	MC@NLO+HERWIG/JIMMY muup	CT10	68.51	1.405	ALTFASTII
117001	$t\bar{t}$ no full-had	POWHEG+PYTHIA P2011C	HERAPDF15NLO	73.10	1.317	FullSim

Table A.2: Summary of the dataset number, process, generator, PDF, cross-section, and k-factor for each Monte Carlo sample used in the $t\bar{t}$ modelling systematics.

Appendix B

Data and Monte Carlo Comparisons

The kinematic variables of the selected objects in $t\bar{t}$ dilepton channels are studied to validate the modelling of our chosen MC in comparison to data. The objects listed and defined in section 5.1 (jets, b-tagging variable, leptons, missing transverse energy) are used in this comparison. Some event cuts variables like m_{ll} and H_{T} are also shown. All events selected in the following plots are in the signal region after all selection cuts defined in section 5.2. The ratio of data over MC prediction is included to magnify the comparison. POWHEG interfaced with PYTHIA is chosen to be the default $t\bar{t}$ signal simulated sample. K-factors are applied to normalize $t\bar{t}$ to the NNLO+NNLL calculations. All systematic uncertainties, except the $t\bar{t}$ modeling uncertainties, are considered for the simulated samples and the statistical uncertainty in data are shown.

B.1 Data/MC plots of primary vertices and μ

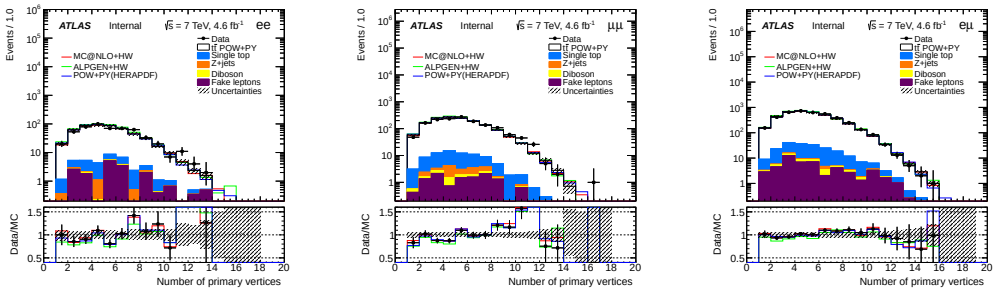

Figure B.1: The number of primary vertices in the ee (left), $\mu\mu$ (center) and $e\mu$ (right) channels. The error band includes all systematic uncertainties except $t\bar{t}$ modeling uncertainties. Simulated $t\bar{t}$ sample is normalized to NNLO+NNLL calculations.

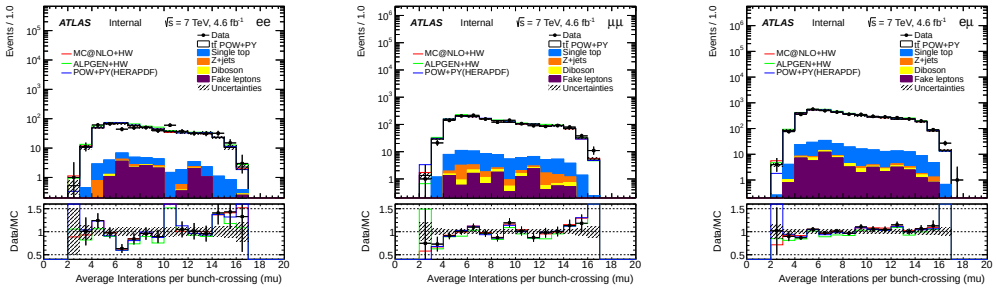

Figure B.2: The number of interactions per bunch-crossing μ in the ee (left), $\mu\mu$ (center) and $e\mu$ (right) channels. The error band includes all systematic uncertainties except $t\bar{t}$ modeling uncertainties. Simulated $t\bar{t}$ sample is normalized to NNLO+NNLL calculations.

B.2 Data/MC plots of jets

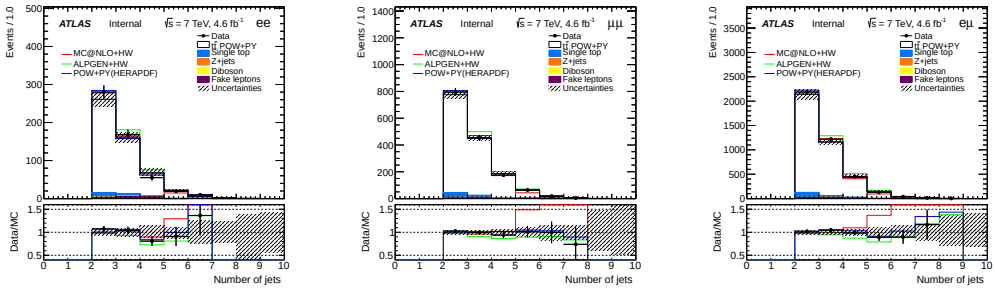

(a) Number of jets

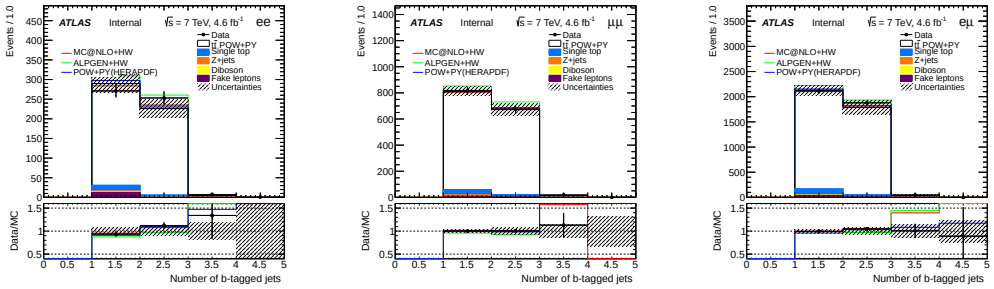

(b) Number of b-tagged jets

Figure B.3: The number of all jets and b-tagged jets in the ee (left), $\mu\mu$ (center) and $e\mu$ (right) channels. The error band includes all systematic uncertainties except $t\bar{t}$ modeling uncertainties. Simulated $t\bar{t}$ sample is normalized to NNLO+NNLL calculations.

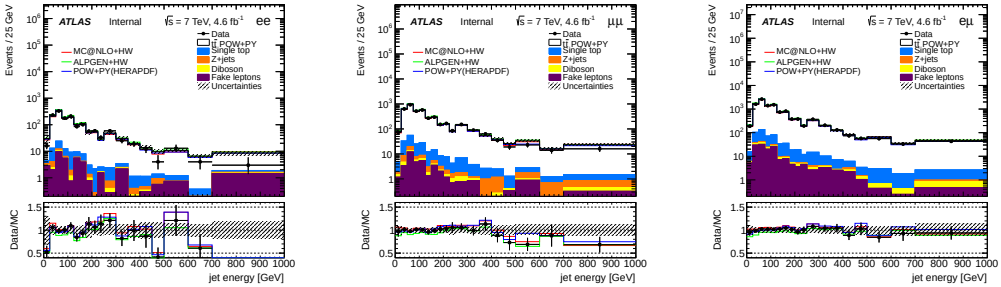

(a) Jet energy

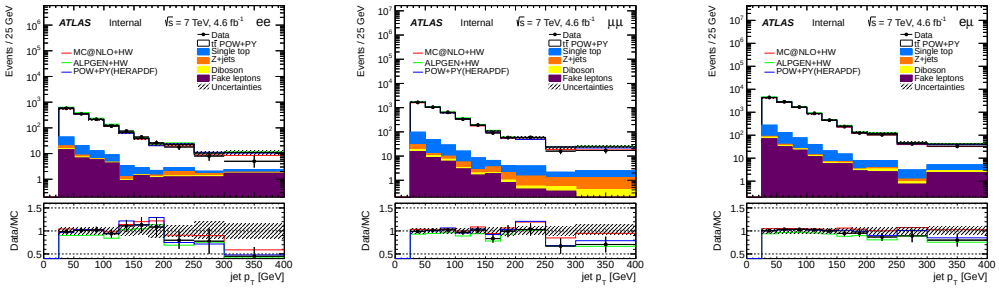

(b) Jet p_{T}

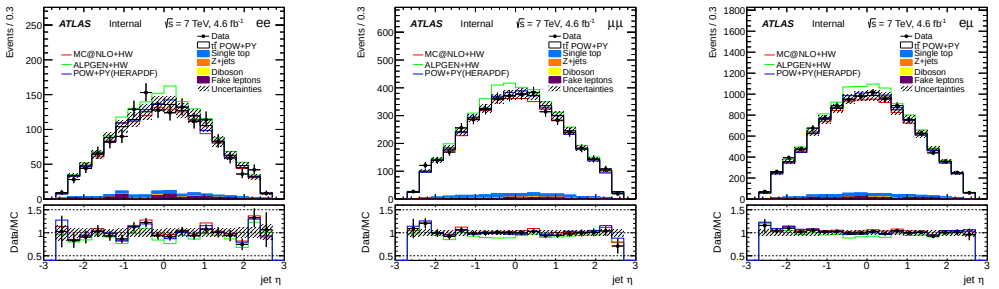

(c) Jet η

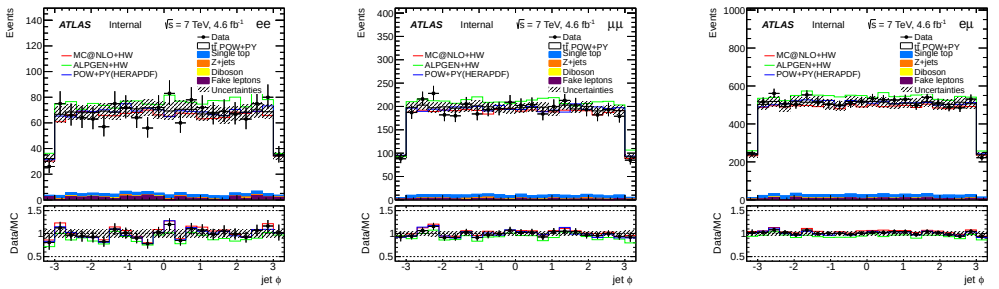

(d) Jet ϕ

Figure B.4: The 4-vector of all jets in the ee (left), $\mu\mu$ (center) and $e\mu$ (right) channels. The error band includes all systematic uncertainties except $t\bar{t}$ modeling uncertainties. Simulated $t\bar{t}$ sample is normalized to NNLO+NNLL calculations.

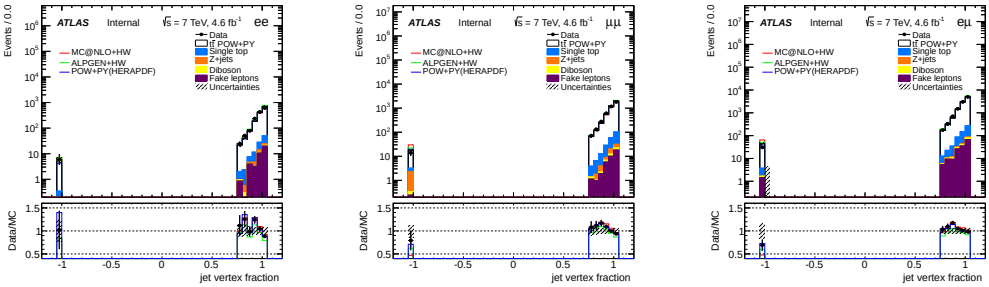

(a) Jet vertex fraction

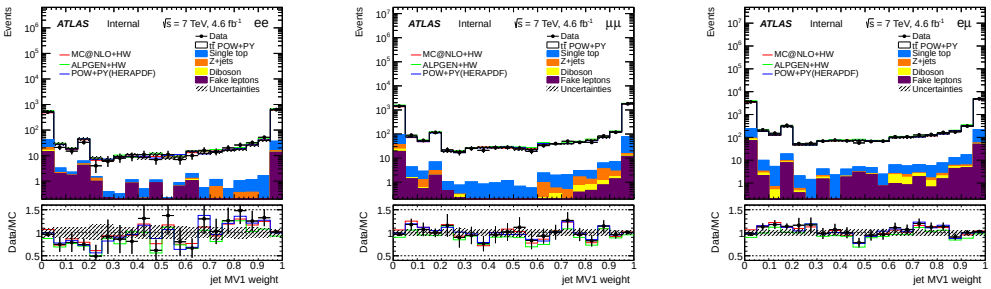

(b) Jet MV1

Figure B.5: The jet vertex fraction and MV1 distribution of all jets in the ee (left), $\mu\mu$ (center) and $e\mu$ (right) channels. The error band includes all systematic uncertainties except $t\bar{t}$ modeling uncertainties. Simulated $t\bar{t}$ sample is normalized to NNLO+NNLL calculations.

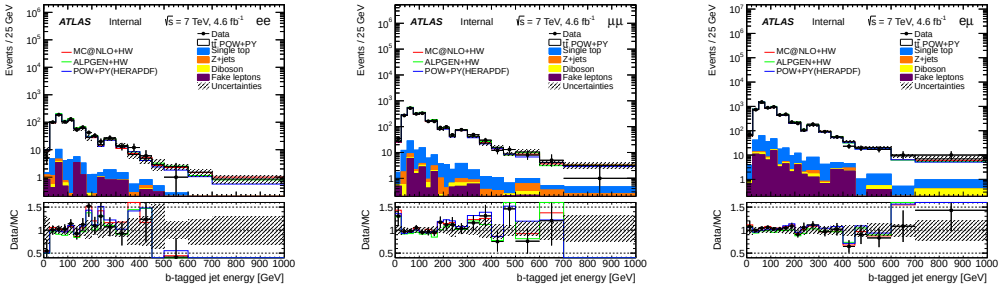

(a) b-tagged jet energy

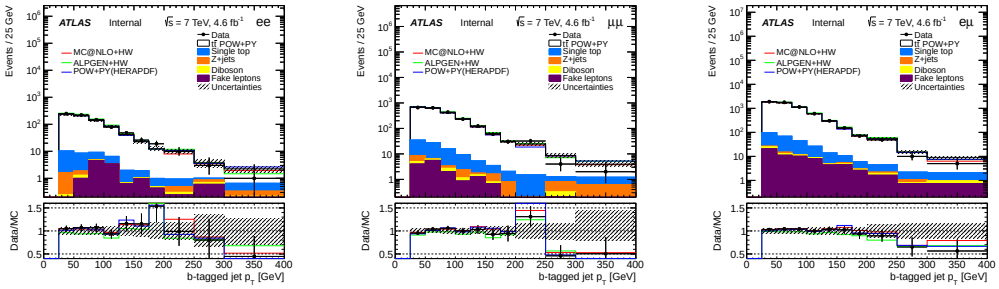

(b) b-tagged jet p_{T}

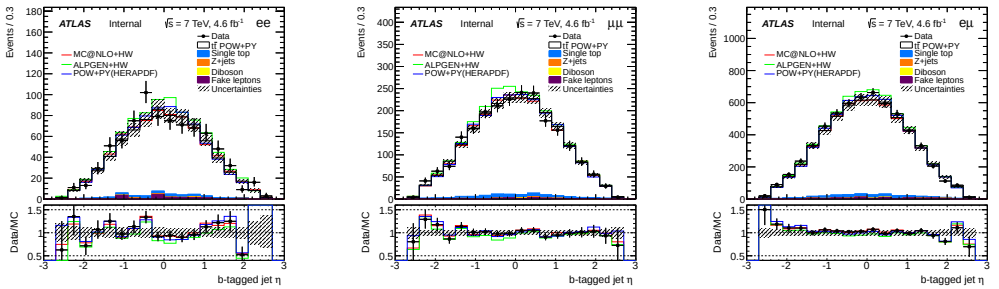

(c) b-tagged jet η

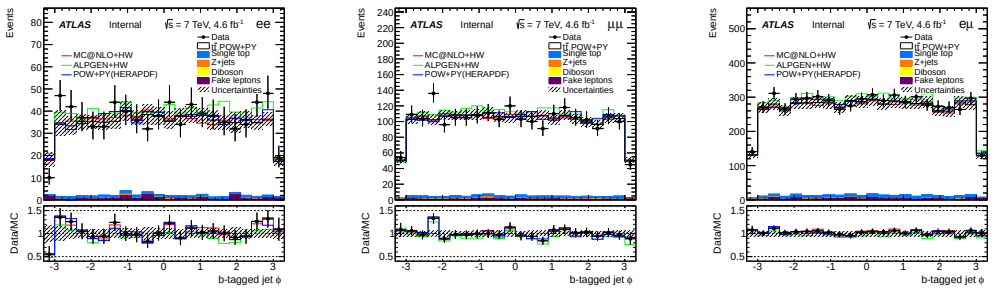

(d) b-tagged jet ϕ

Figure B.6: The 4-vector of b-tagged jets in the ee (left), $\mu\mu$ (center) and $e\mu$ (right) channels. The error band includes all systematic uncertainties except $t\bar{t}$ modeling uncertainties. Simulated $t\bar{t}$ sample is normalized to NNLO+NNLL calculations.

B.3 Data/MC plots of selected jets

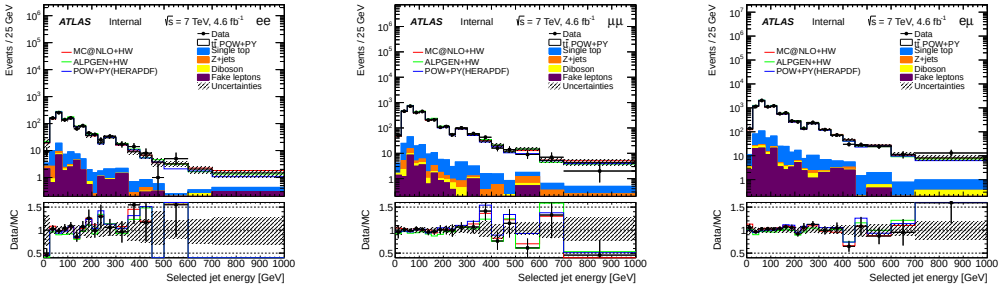

(a) Selected jet energy

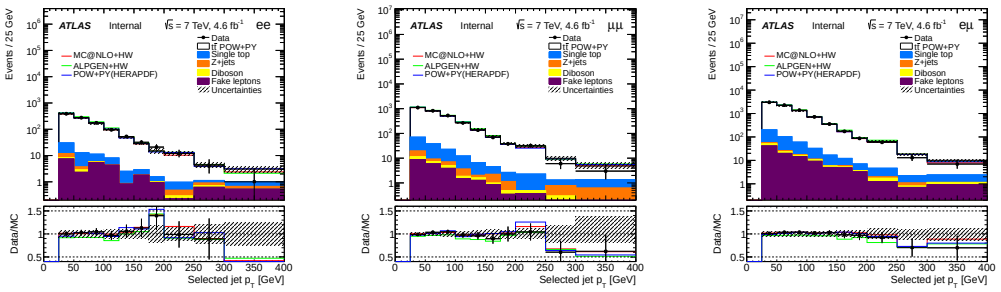

(b) Selected jet p_{T}

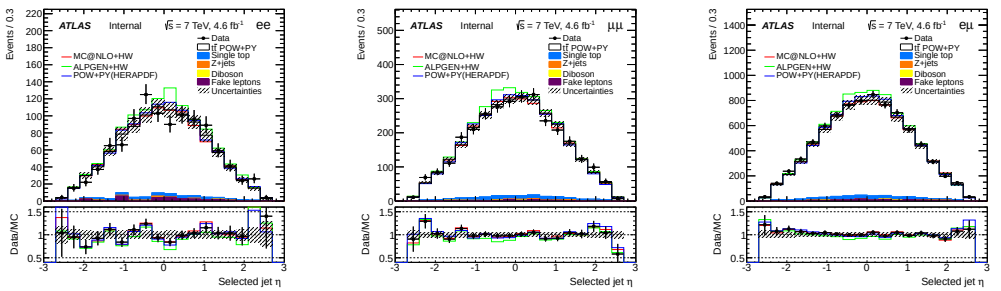

(c) Selected jet η

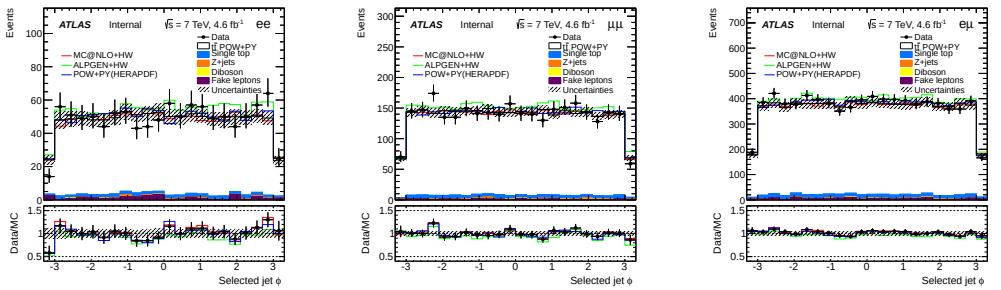

(d) Selected jet ϕ

Figure B.7: The 4-vector of selected jets in the ee (left), $\mu\mu$ (center) and $e\mu$ (right) channels. The error band includes all systematic uncertainties except $t\bar{t}$ modeling uncertainties. Simulated $t\bar{t}$ sample is normalized to NNLO+NNLL calculations.

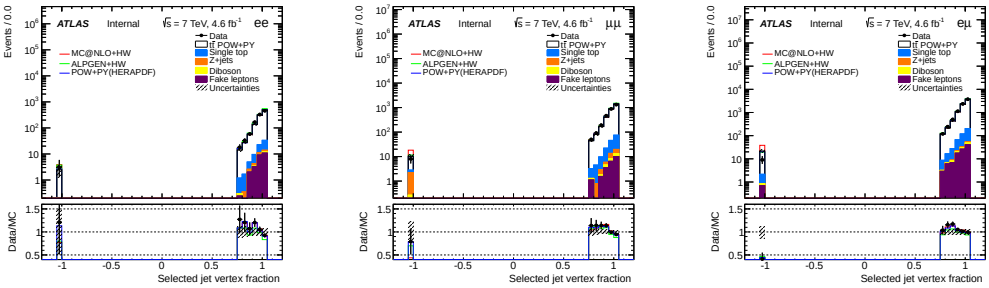

(a) Selected jet vertex fraction

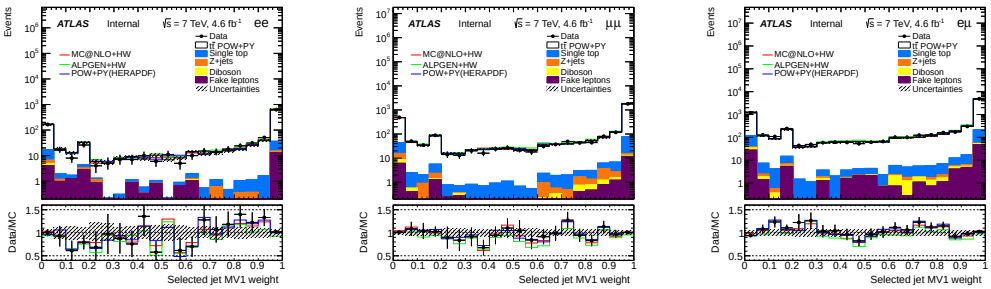

(b) Selected jet MV1

Figure B.8: The jet vertex fraction and MV1 distribution of selected jets in the ee (left), $\mu\mu$ (center) and $e\mu$ (right) channels. The error band includes all systematic uncertainties except $t\bar{t}$ modeling uncertainties. Simulated $t\bar{t}$ sample is normalized to NNLO+NNLL calculations.

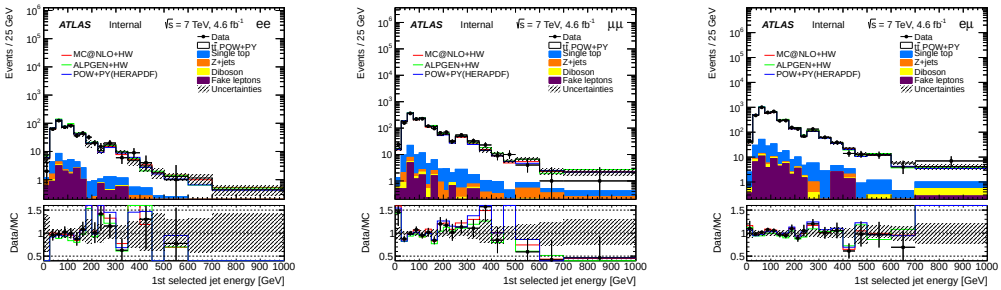

(a) Leading-MV1 jet energy

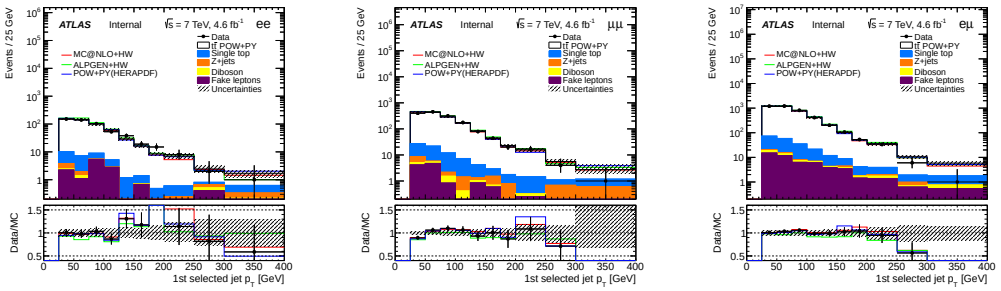

(b) Leading-MV1 jet p_{T}

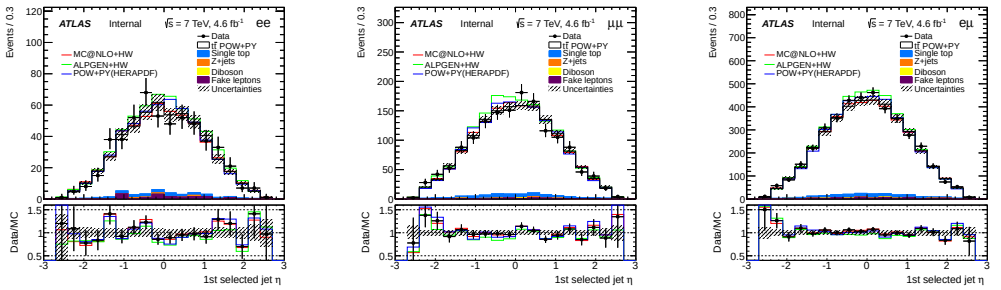

(c) Leading-MV1 jet η

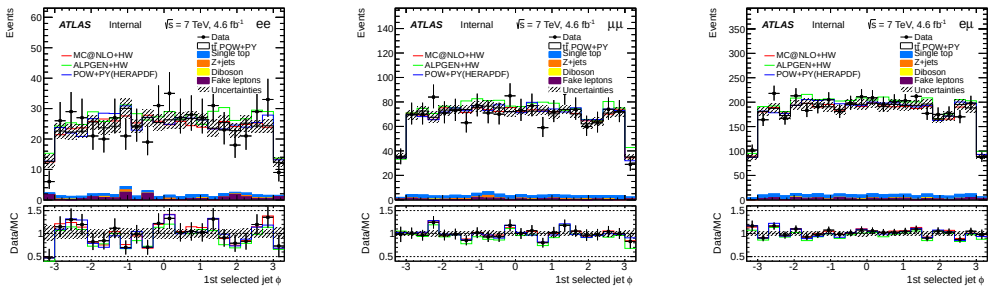

(d) Leading-MV1 jet ϕ

Figure B.9: The 4-vector of leading-MV1 jets in the ee (left), $\mu\mu$ (center) and $e\mu$ (right) channels. The error band includes all systematic uncertainties except $t\bar{t}$ modeling uncertainties. Simulated $t\bar{t}$ sample is normalized to NNLO+NNLL calculations.

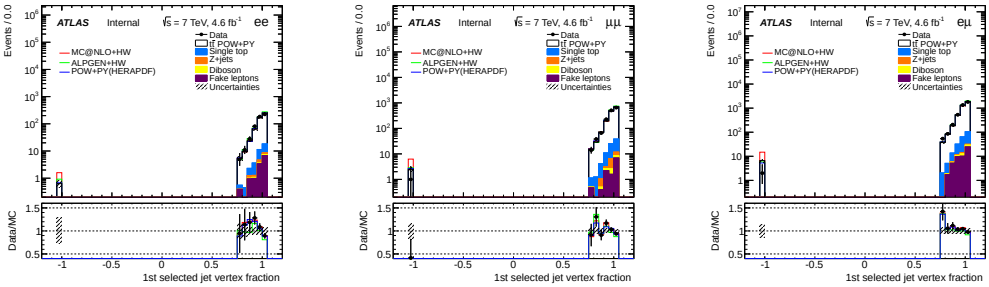

(a) Leading-MV1 jet vertex fraction

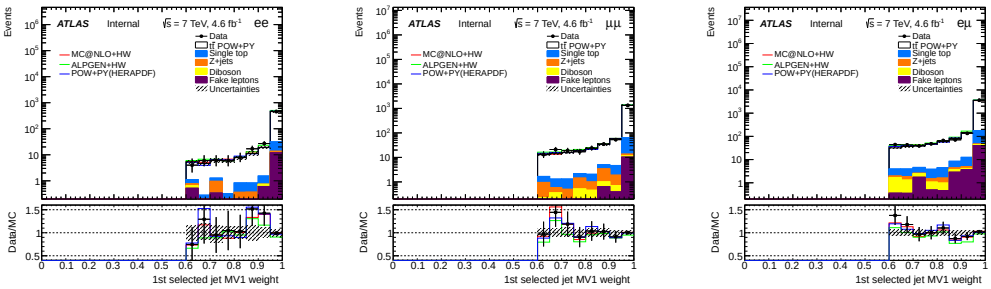

(b) Leading-MV1 jet MV1

Figure B.10: The jet vertex fraction and MV1 distribution of leading-MV1 jets in the ee (left), $\mu\mu$ (center) and $e\mu$ (right) channels. The error band includes all systematic uncertainties except $t\bar{t}$ modeling uncertainties. Simulated $t\bar{t}$ sample is normalized to NNLO+NNLL calculations.

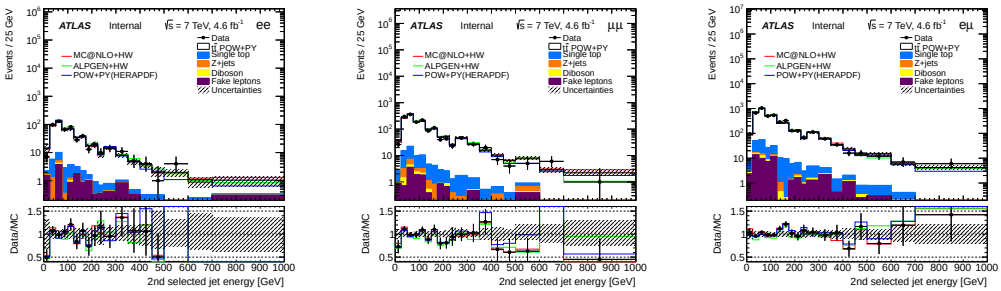

(a) 2nd-leading-MV1 jet energy

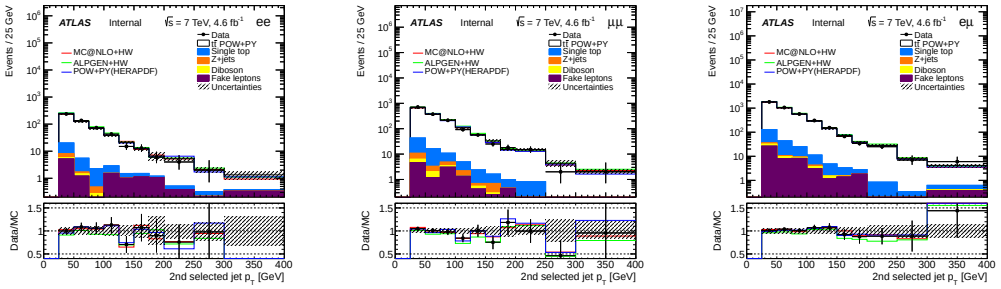

(b) 2nd-leading-MV1 jet p_{T}

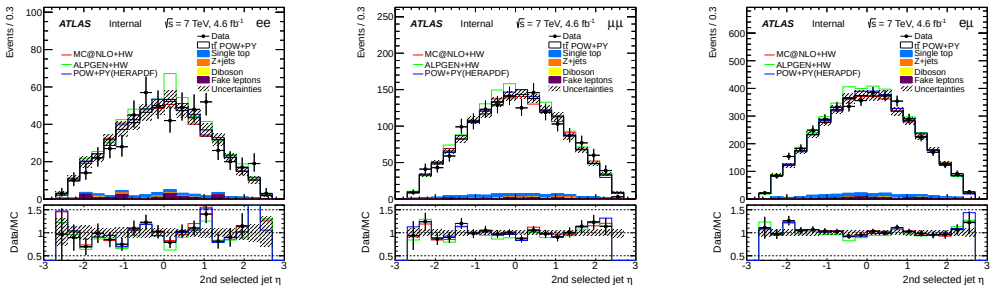

(c) 2nd-leading-MV1 jet η

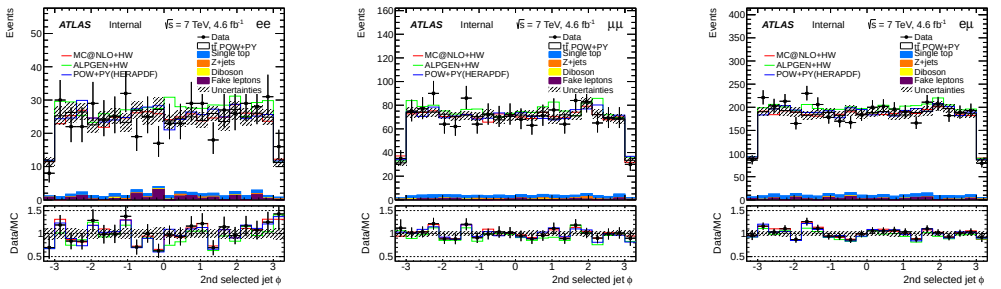

(d) 2nd-leading-MV1 jet ϕ

Figure B.11: The 4-vector of 2nd-leading-MV1 jets in the ee (left), $\mu\mu$ (center) and $e\mu$ (right) channels. The error band includes all systematic uncertainties except $t\bar{t}$ modeling uncertainties. Simulated $t\bar{t}$ sample is normalized to NNLO+NNLL calculations.

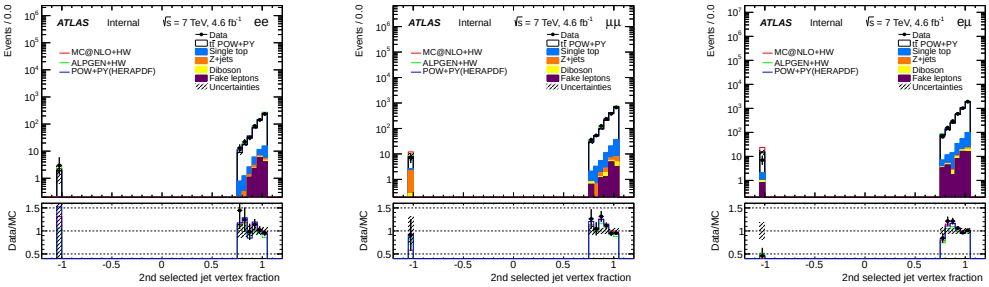

(a) 2nd-leading-MV1 jet vertex fraction

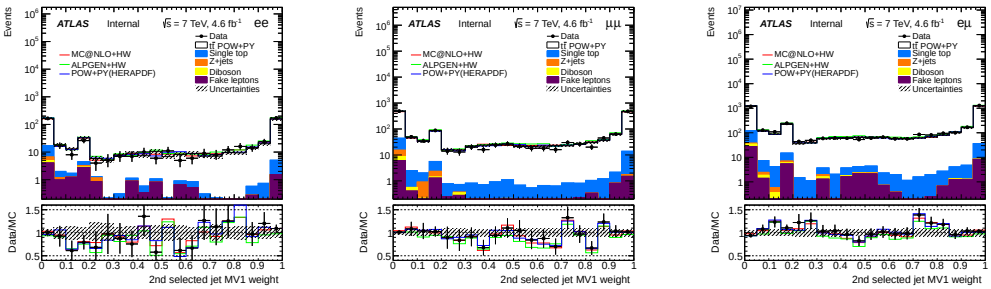

(b) 2nd-leading-MV1 jet MV1

Figure B.12: The jet vertex fraction and MV1 distribution of 2nd-leading-MV1 jets in the ee (left), $\mu\mu$ (center) and $e\mu$ (right) channels. The error band includes all systematic uncertainties except $t\bar{t}$ modeling uncertainties. Simulated $t\bar{t}$ sample is normalized to NNLO+NNLL calculations.

B.4 Data/MC plots of leptons

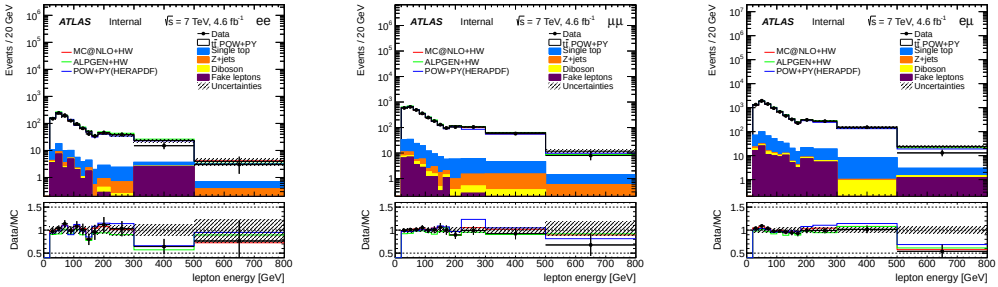

(a) Both leptons' energy

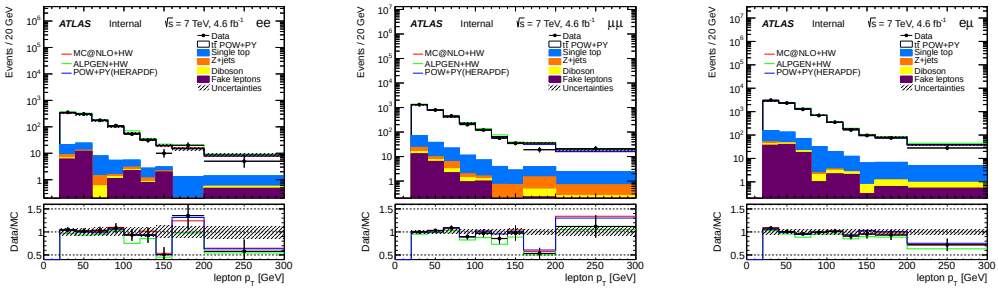

(b) Both leptons p_{T}

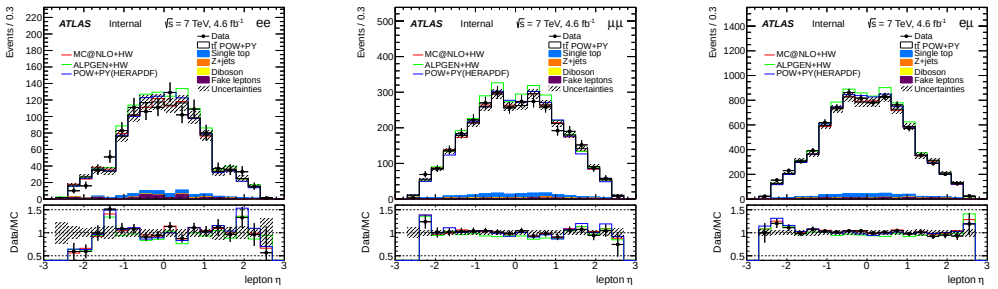

(c) Both leptons η

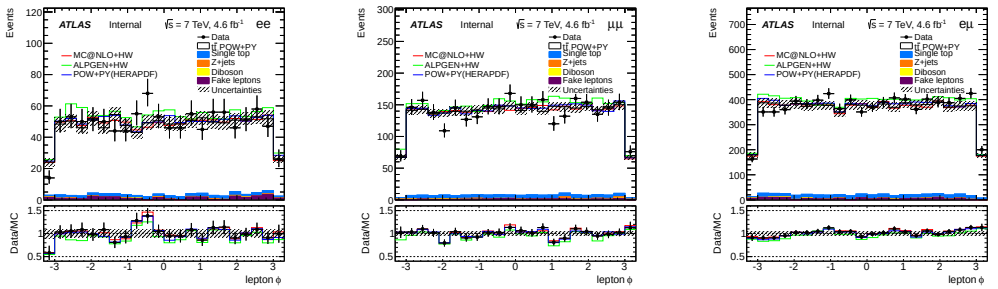

(d) Both leptons ϕ

Figure B.13: The 4-vector of both leptons in the ee (left), $\mu\mu$ (center) and $e\mu$ (right) channels. The error band includes all systematic uncertainties except $t\bar{t}$ modeling uncertainties. Simulated $t\bar{t}$ sample is normalized to NNLO+NNLL calculations.

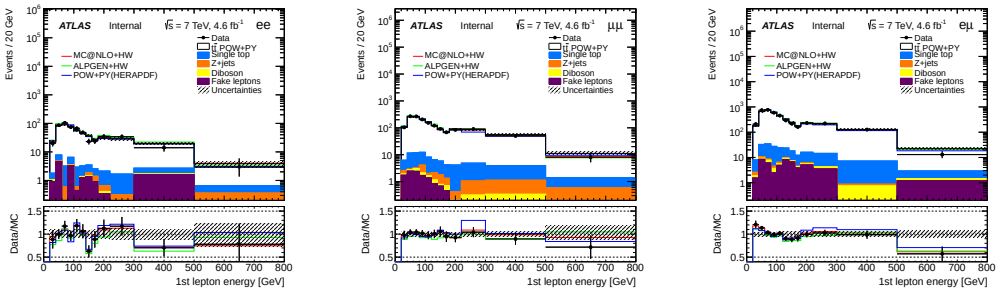

(a) Leading-p_{T} lepton energy

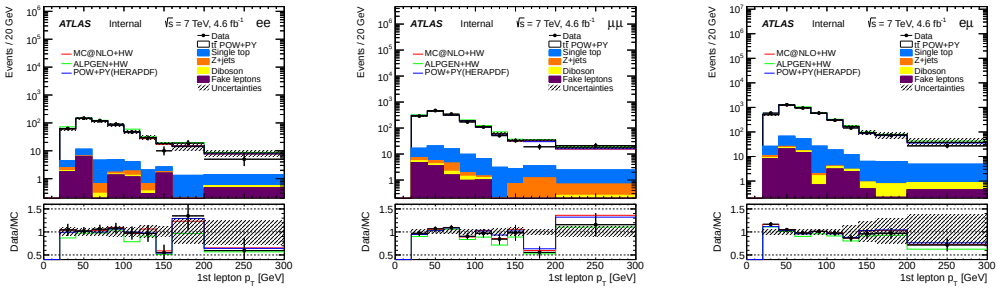

(b) Leading-p_{T} lepton p_{T}

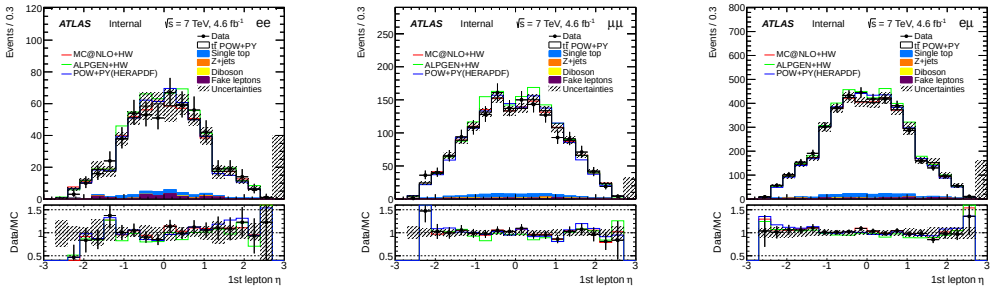

(c) Leading-p_{T} lepton η

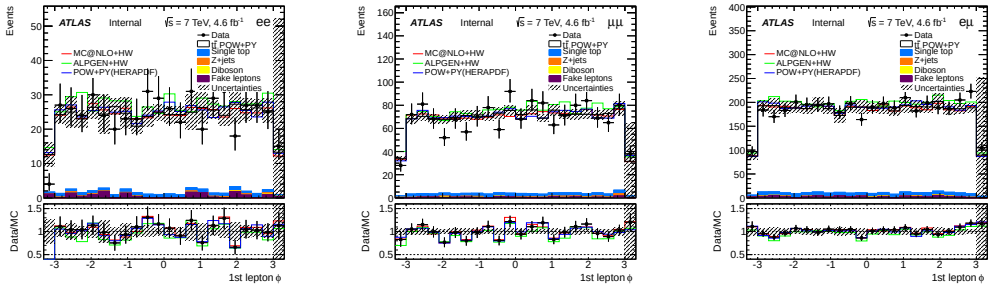

(d) Leading-p_{T} lepton ϕ

Figure B.14: The 4-vector of leading-p_{T} lepton in the ee (left), $\mu\mu$ (center) and $e\mu$ (right) channels. The error band includes all systematic uncertainties except $t\bar{t}$ modeling uncertainties. Simulated $t\bar{t}$ sample is normalized to NNLO+NNLL calculations.

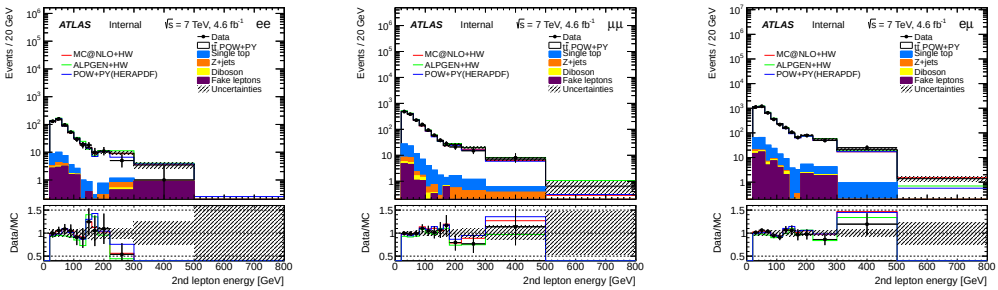

(a) 2nd-leading-p_{T} lepton energy

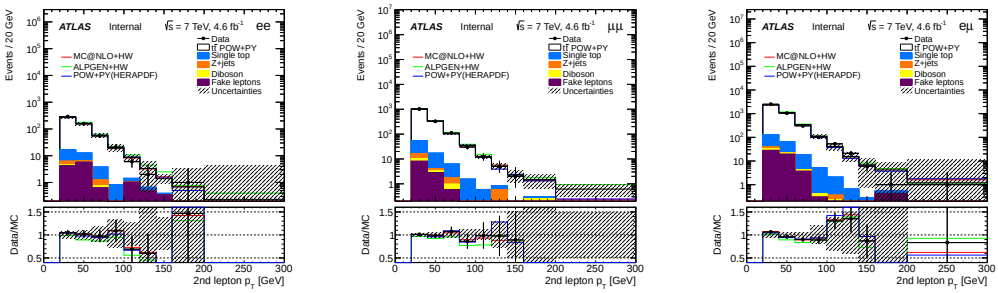

(b) 2nd-leading-p_{T} lepton p_{T}

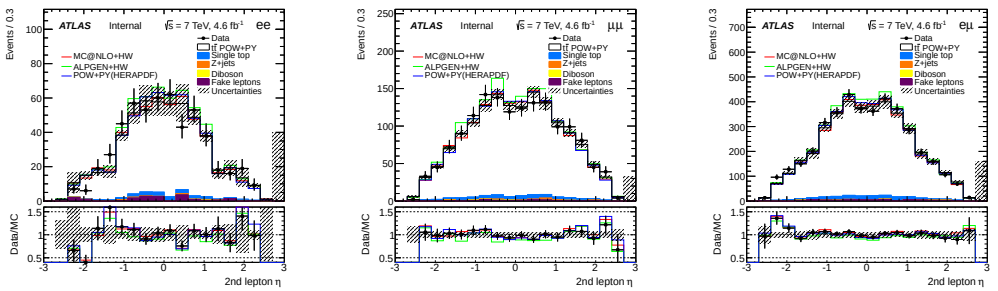

(c) 2nd-leading-p_{T} lepton η

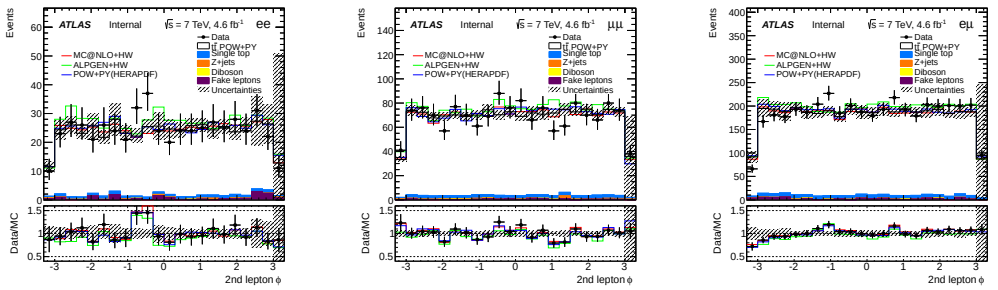

(d) 2nd-leading-p_{T} lepton ϕ

Figure B.15: The 4-vector of 2nd-leading-p_{T} lepton in the ee (left), $\mu\mu$ (center) and $e\mu$ (right) channels. The error band includes all systematic uncertainties except $t\bar{t}$ modeling uncertainties. Simulated $t\bar{t}$ sample is normalized to NNLO+NNLL calculations.

B.5 Data/MC plots of event cut variables

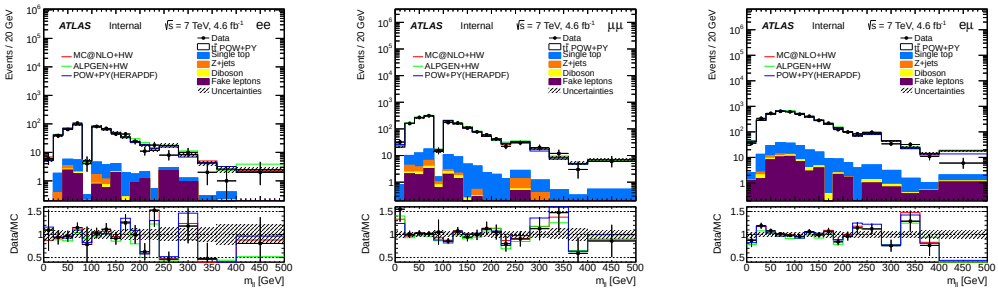

(a) m_{ll}

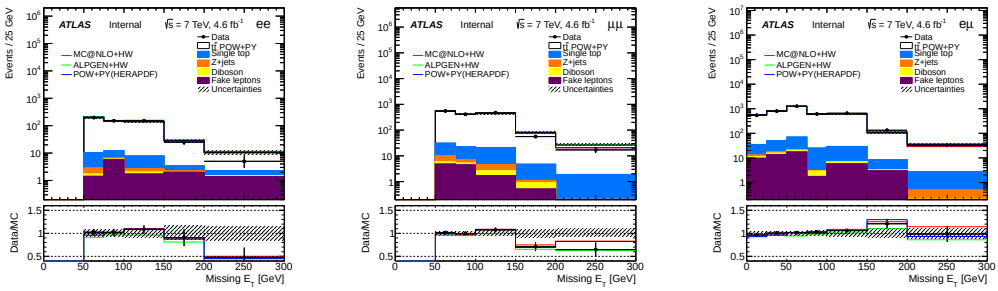

(b) $E_{\mathrm{T}}^{\mathrm{miss}}$

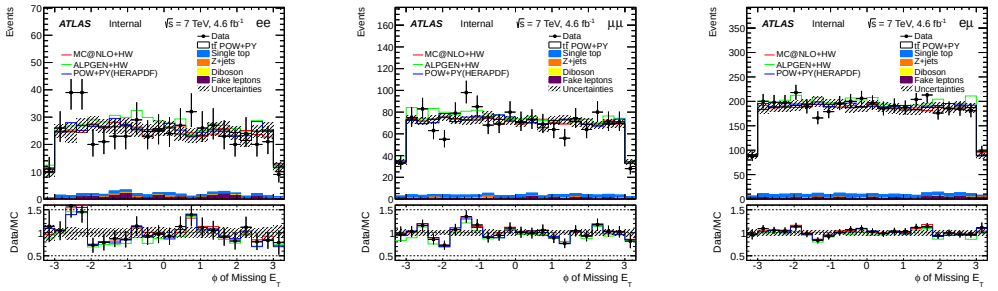

(c) $E_{\mathrm{T}}^{\mathrm{miss}}$ ϕ

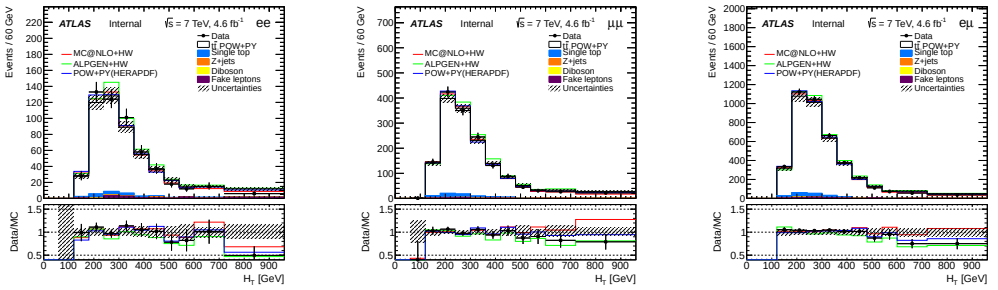

(d) H_{T}

Figure B.16: The dilepton invariant mass m_{ll}, missing tranverse energy $E_{\mathrm{T}}^{\mathrm{miss}}$ and ϕ, and H_{T} in the ee (left), $\mu\mu$ (center) and $e\mu$ (right) channels. The error band includes all systematic uncertainties except $t\bar{t}$ modeling uncertainties. Simulated $t\bar{t}$ sample is normalized to NNLO+NNLL calculations.

B.6 Data/MC plots of jet-lepton mass

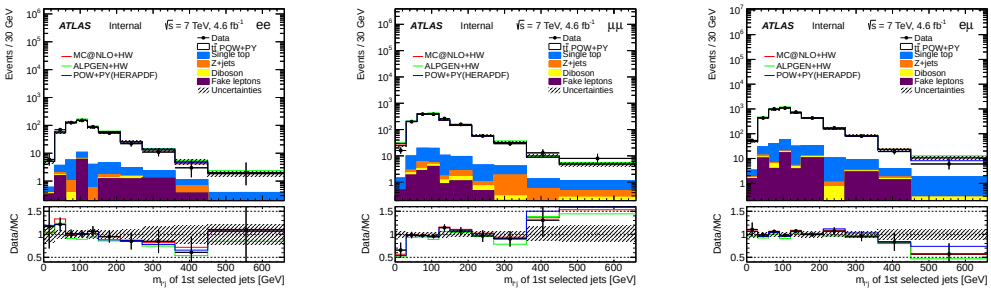

(a) $m_{j_1 l+}$

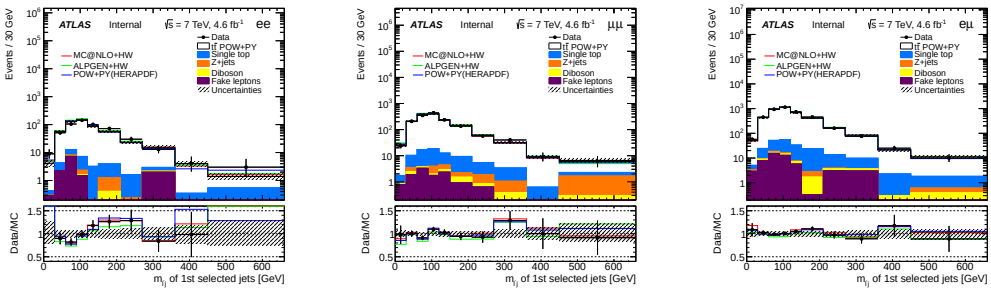

(b) $m_{j_1 l-}$

Figure B.17: The jet-lepton invariant mass of the leading-MV1 jet and B.17a positively-charged lepton and B.17b negatively-charged lepton in the ee (left), $\mu\mu$ (center) and $e\mu$ (right) channels. The error band includes all systematic uncertainties except $t\bar{t}$ modeling uncertainties. Simulated $t\bar{t}$ sample is normalized to NNLO+NNLL calculations.

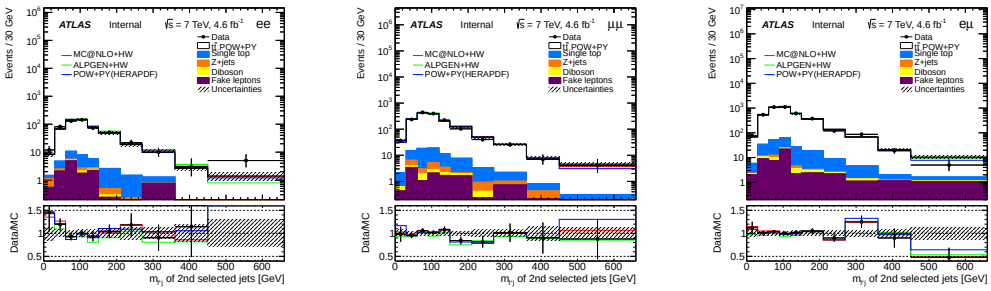

(a) $m_{j_2 l^+}$

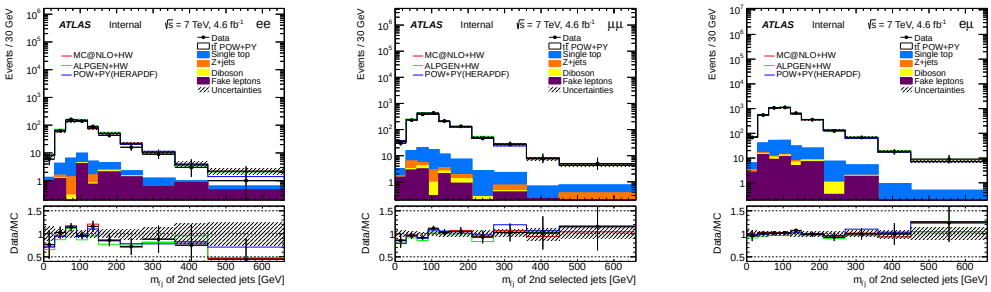

(b) $m_{j_2 l^-}$

Figure B.18: The jet-lepton invariant mass of the 2nd-leading-MV1 jet and B.18a positively-charged lepton and B.18b negatively-charged lepton in the ee (left), $\mu\mu$ (center) and $e\mu$ (right) channels. The error band includes all systematic uncertainties except $t\bar{t}$ modeling uncertainties. Simulated $t\bar{t}$ sample is normalized to NNLO+NNLL calculations.

Appendix C

Unfolding Studies

In section C.1, figures C.1-C.3 show the relative bias ((unfolded-true)/true) of each of the first 5 iterations of unfolded spectra in the cases of half POWHEG+PYTHIA, MC@NLO+HERWIG and ALPGEN+HERWIG samples. Figures C.4-C.7 show the same for the stressed test-data samples, in $m_{t\bar{t}}$, $p_{\mathrm{T}}^{t\bar{t}}$, $y_{t\bar{t}}$ and $|y_{t\bar{t}}|$ respectively. The relative bias shows visually how much an unfolded spectrum deviates from the true one. The uncertainty of each bias value shows the statistical uncertainty estimated in each iteration of the unfolding.

In section C.2, figure C.8-C.14 shows the χ^2 as a function of number of iterations for each $t\bar{t}$ system variable in each dilepton channel. In the closure tests, the total χ^2, the χ^2's of the 2nd last and the last bins are shown and studied, while the total χ^2 and the χ^2's of the most stressed bin are studied in the stress tests. The total χ^2 is a generalized χ^2, taking the covariances across bins into account and calculated using the covariance matrix derived from the unfolding as: $\chi^2 = (x - \bar{x})^T V^{-1} (x - \bar{x})$, where V^{-1} is the inverse of the covariance matrix and x and $\bar{x}$ are the unfolded and true values, respectively. The χ^2 for individual bins cannot include the covariance terms, thus is calculated in the usual way as the sum of (residuals/uncertainty)-squared (and thus is independent from the neighboring bins): $\sum_i \frac{(x_i - \bar{x}_i)^2}{\sigma_i^2}$, where x_i and $\bar{x}_i$ are the unfolded and true values respectively at bin i, and σ_i is the statistical uncertainty of bin i (taken as the square root of the i-th diagonal element of the covariance matrix from unfolding).

The summary of the number of iterations with minimum χ^2 ($n_{\min.\chi^2}$) for the closure (stress) tests are shown in table 8.1 (8.2) in section 8.3.1.

The differences of the relative bias of the unfolded spectrum at the optimal n_{opt} (as discussed in section 8.3.2) and the neighboring values of n_{opt} are seen to be small from section C.1, for each $t\bar{t}$ system variable in each dilepton channel. The central values of the unfolded spectrum at the neighboring-n from n_{opt} differs from that at the optimal iteration no larger than 3% for overall variables and bins and are around or less than 1% in most cases. In all cases, these differences are well-covered by the statistical uncertainty of the unfolded spectrum at the optimal iteration for each variable.

C.1 Dependence of relative bias on the unfolding parameter

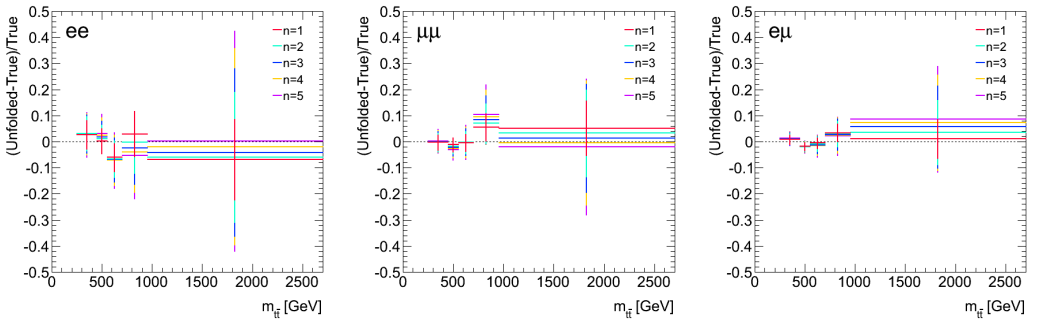

(a) $m_{t\bar{t}}$

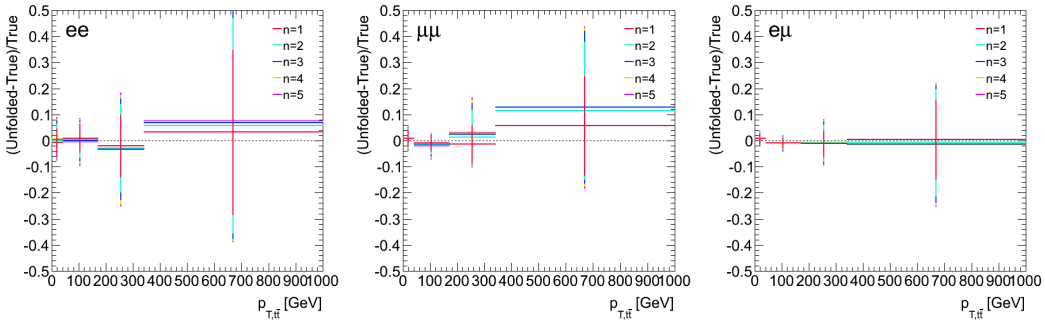

(b) $p_{\mathrm{T}}^{t\bar{t}}$

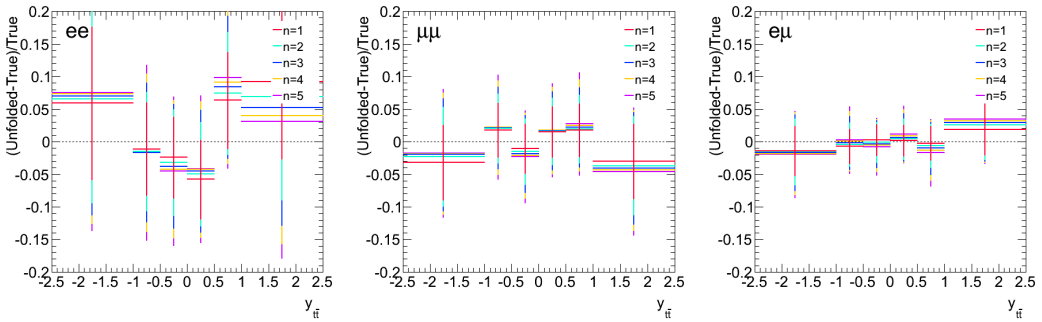

(c) $y_{t\bar{t}}$

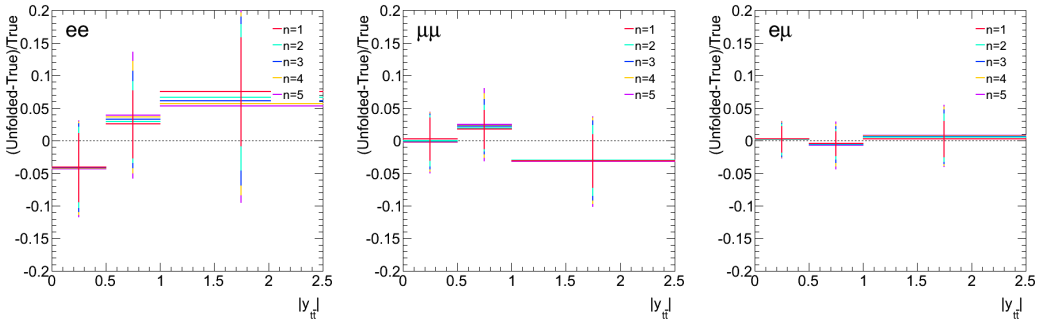

(d) $|y_{t\bar{t}}|$

Figure C.1: Unfolded spectra of the $t\bar{t}$ system variables in the ee, $\mu\mu$ and $e\mu$ channels with 1-5 number of iterations. Test data uses 2nd half (half1) of the POWHEG +PYTHIA $t\bar{t}$ samples as input. The other half of the POWHEG +PYTHIA $t\bar{t}$ is used as the training sample.

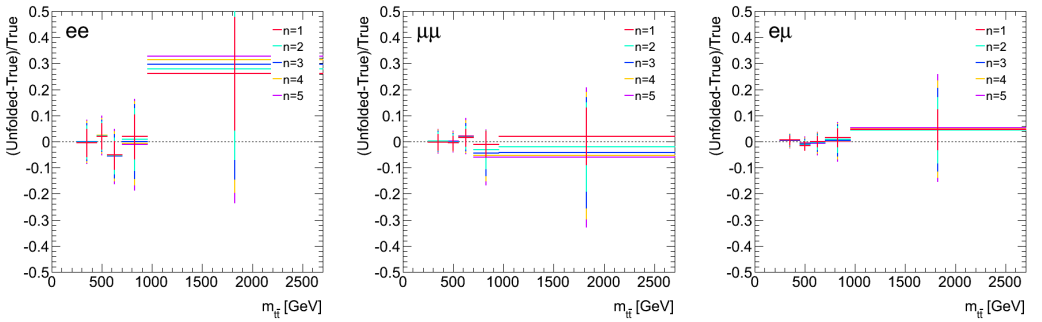

(a) $m_{t\bar{t}}$

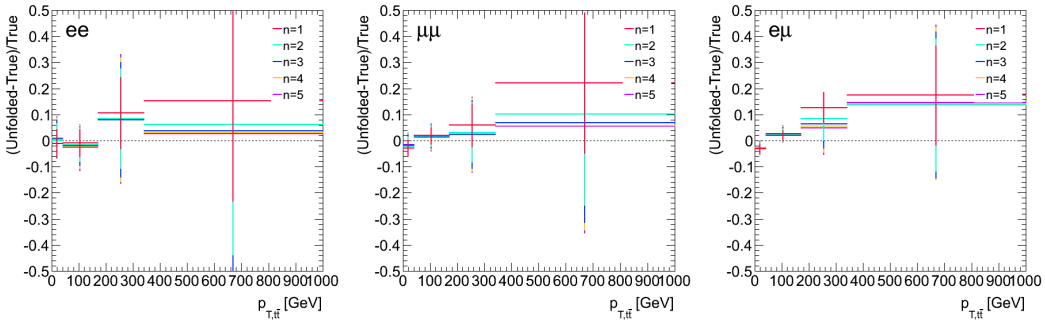

(b) $p_{\mathrm{T}}^{t\bar{t}}$

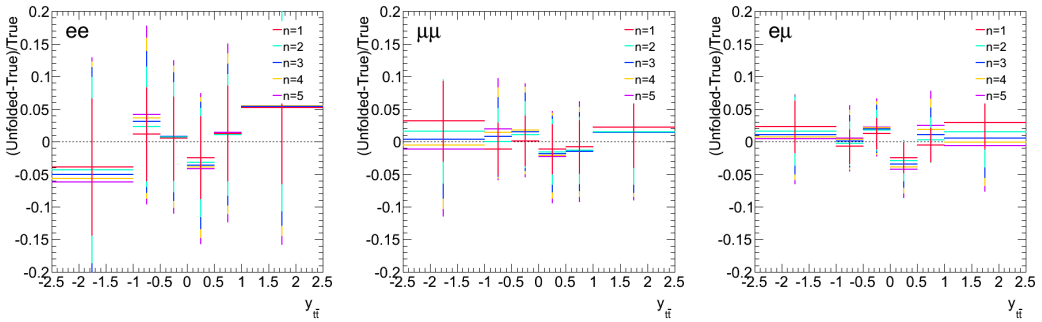

(c) $y_{t\bar{t}}$

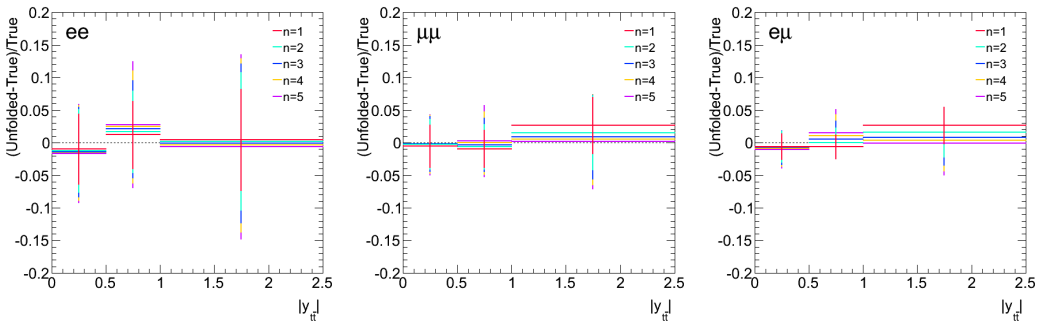

(d) $|y_{t\bar{t}}|$

Figure C.2: Unfolded spectra of the $t\bar{t}$ system variables in the ee, $\mu\mu$ and $e\mu$ channels with 1-5 number of iterations. Test data uses MC@NLO +Herwig $t\bar{t}$ samples as input. The default Powheg +Pythia $t\bar{t}$ is used as the training sample.

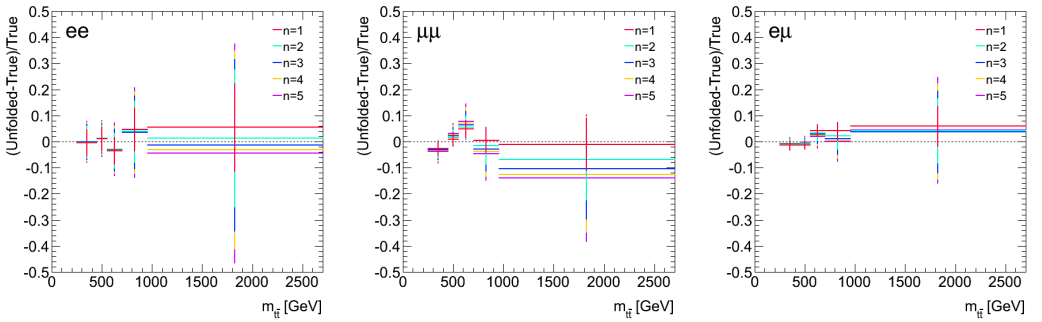

(a) $m_{t\bar{t}}$

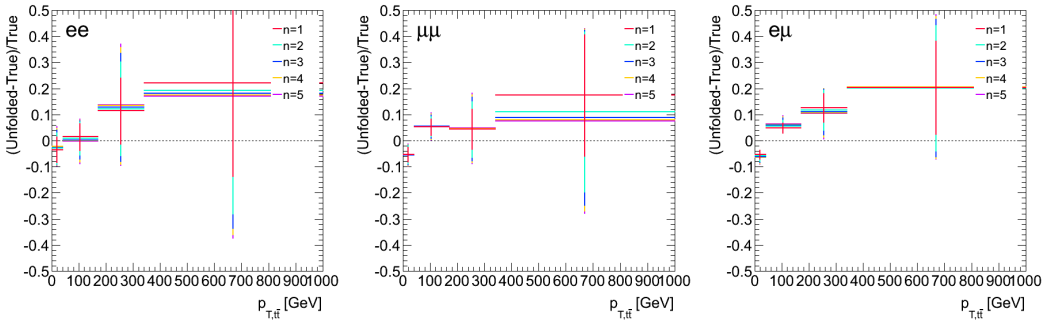

(b) $p_{\mathrm{T}}^{t\bar{t}}$

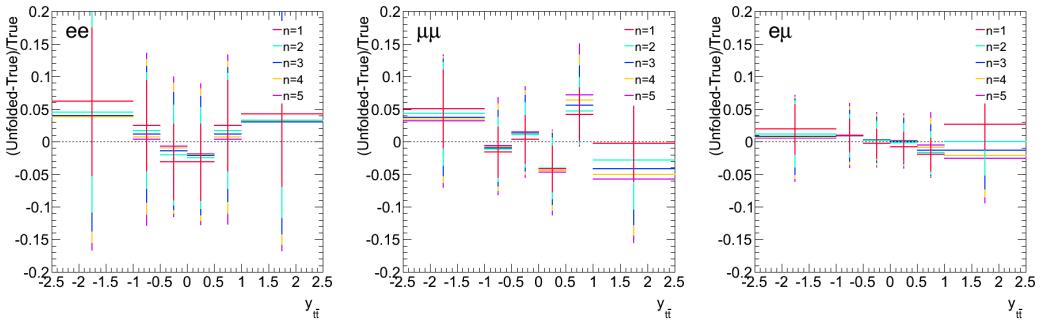

(c) $y_{t\bar{t}}$

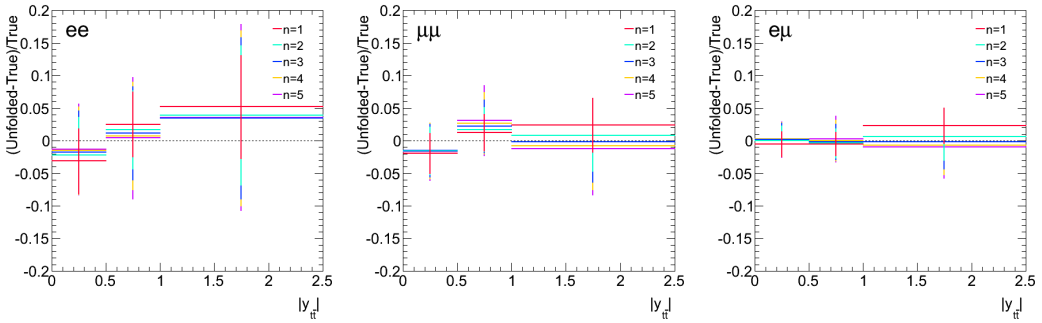

(d) $|y_{t\bar{t}}|$

Figure C.3: Unfolded spectra of the $t\bar{t}$ system variables in the ee, $\mu\mu$ and $e\mu$ channels with 1-5 number of iterations. Test data uses ALPGEN +HERWIG $t\bar{t}$ samples as input. The default POWHEG +PYTHIA $t\bar{t}$ is used as the training sample.

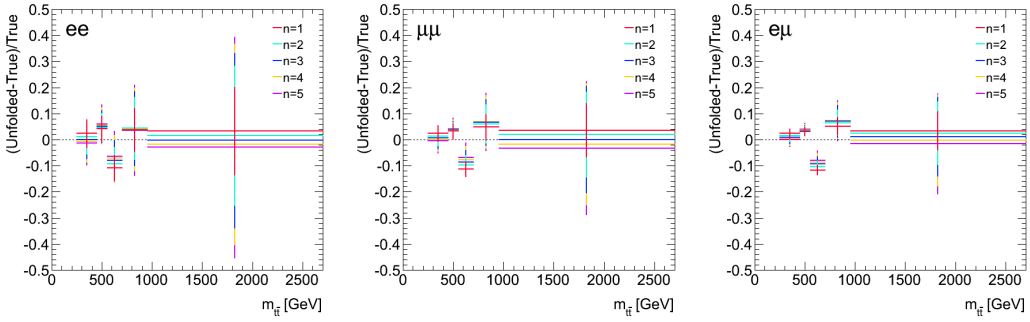

(a) $m_{t\bar{t}}$ with $m_{Z'} = 0.6$ TeV

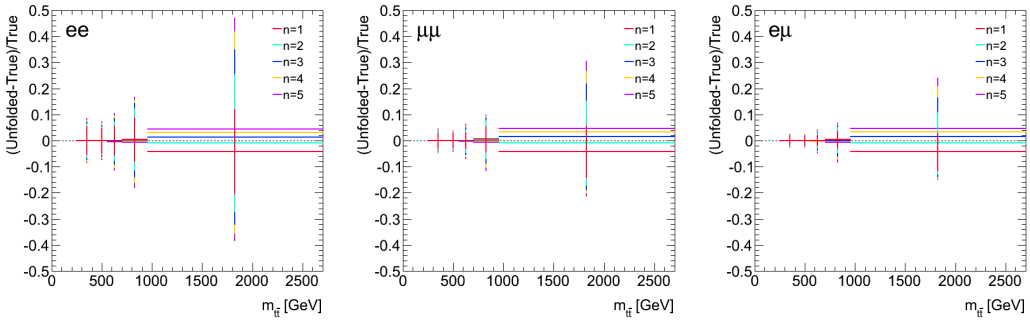

(b) $m_{t\bar{t}}$ with $m_{Z'} = 1.6$ TeV

Figure C.4: Unfolded spectra of the $m_{t\bar{t}}$ in the ee, $\mu\mu$ and $e\mu$ channels with 1-5 number of iterations. Stressed test data uses (a)$m_{Z'} = 0.6$ TeV and (b)$m_{Z'} = 1.6$ TeVsamples as input. The default POWHEG +PYTHIA $t\bar{t}$ is used as the training sample.

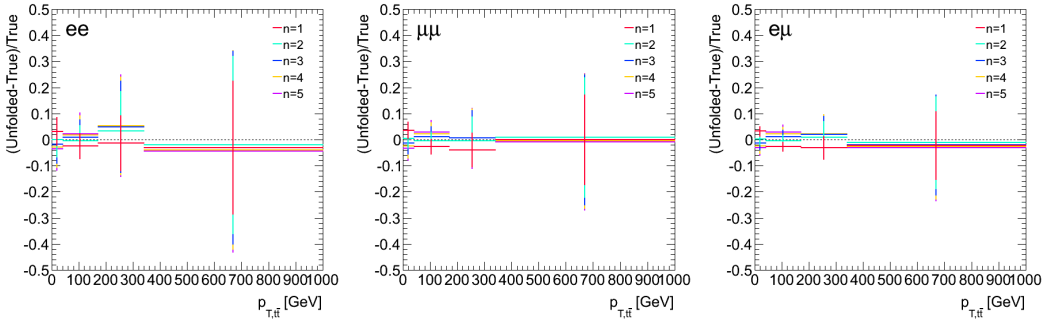

(a) $p_{\mathrm{T}}^{t\bar{t}}$ with Alpgen+HW Np3 lnln

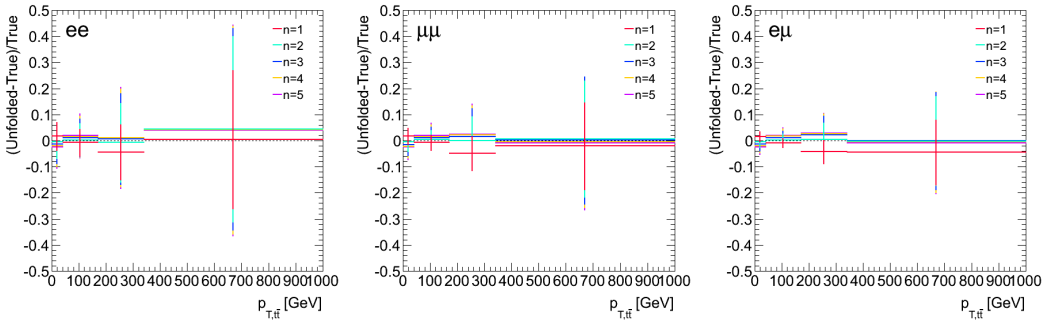

(b) $p_{\mathrm{T}}^{t\bar{t}}$ with Alpgen+HW Np4 lnln

Figure C.5: Unfolded spectra of the $p_{\mathrm{T}}^{t\bar{t}}$ in the ee, $\mu\mu$ and $e\mu$ channels with 1-5 number of iterations. Stressed test data uses (a)Alpgen+HW Np3 lnln and (b)Alpgen+HW Np4 lnln samples as input. The default POWHEG +PYTHIA $t\bar{t}$ is used as the training sample.

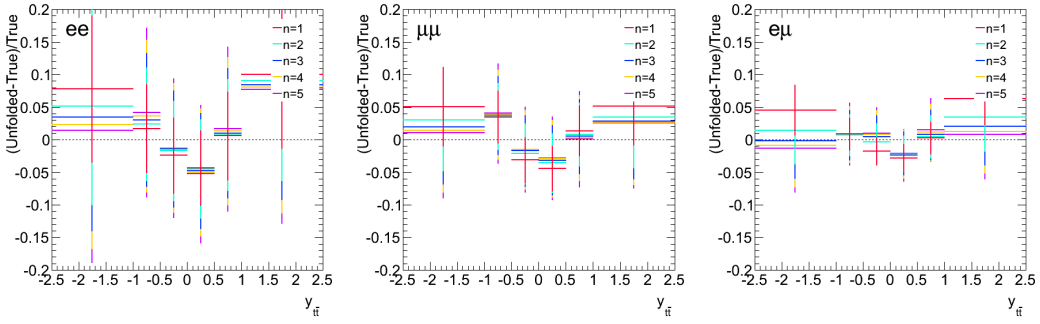

(a) $y_{t\bar{t}}$ with $m_{Z'} = 1.6$ TeV

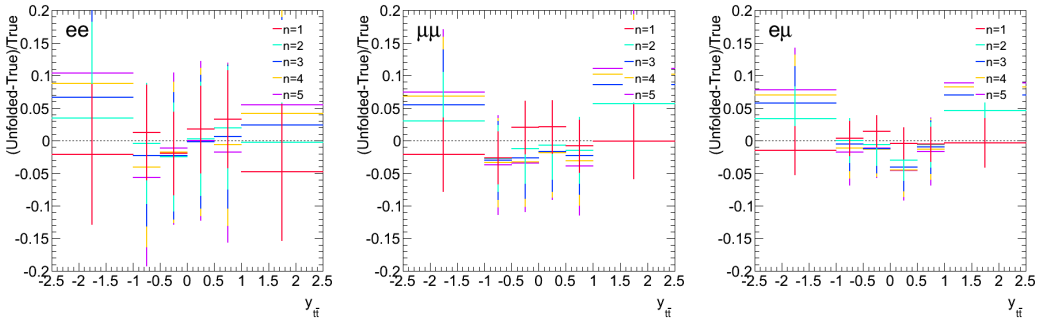

(b) $y_{t\bar{t}}$ with Alpgen+HW Np0 lnln

Figure C.6: Unfolded spectra of the $y_{t\bar{t}}$ in the ee, $\mu\mu$ and $e\mu$ channels with 1-5 number of iterations. Stressed test data uses (a)$m_{Z'} = 1.6$ TeV and (b)Alpgen+HW Np0 lnln samples as input. The default POWHEG +PYTHIA $t\bar{t}$ is used as the training sample.

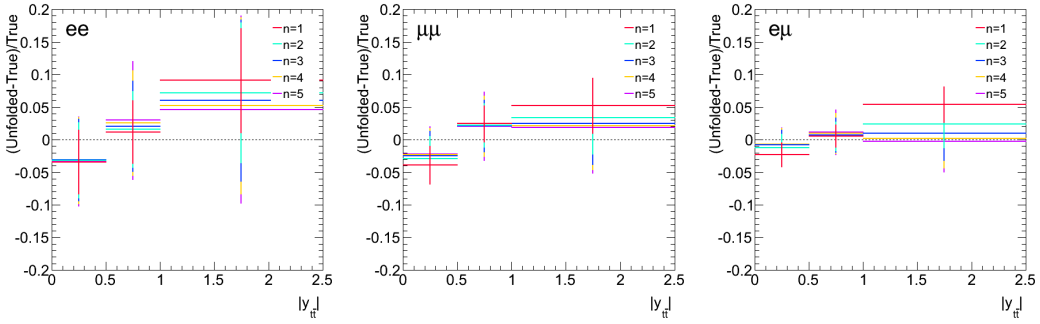

(a) $|y_{t\bar{t}}|$ with $m_{Z'} = 1.6$ TeV

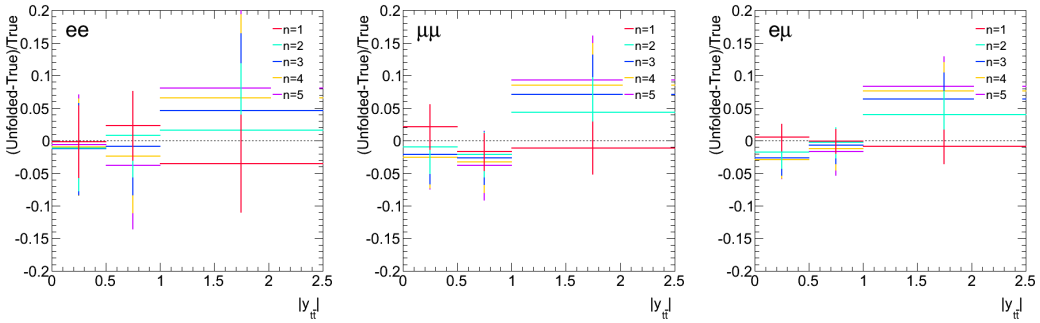

(b) $|y_{t\bar{t}}|$ with Alpgen+HW Np0 lnln

Figure C.7: Unfolded spectra of the $|y_{t\bar{t}}|$ in the ee, $\mu\mu$ and $e\mu$ channels with 1-5 number of iterations. Stressed test data uses (a)$m_{Z'} = 1.6$ TeV and (b)Alpgen+HW Np0 lnln samples as input. The default POWHEG +PYTHIA $t\bar{t}$ is used as the training sample.

C.2 Dependence of χ^2 on the unfolding parameter

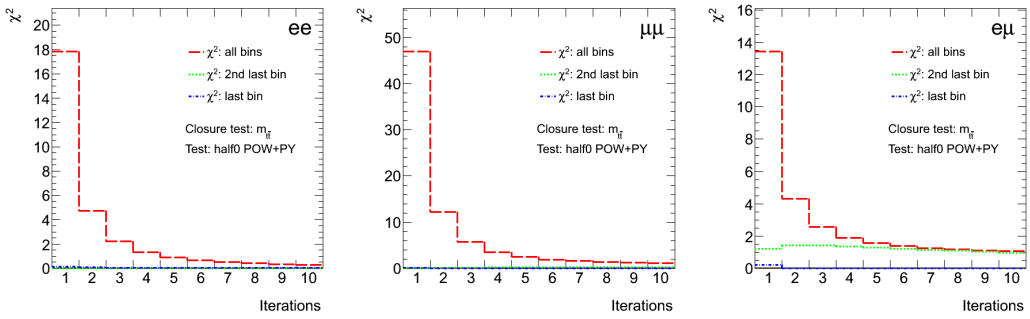

(a) $m_{t\bar{t}}$

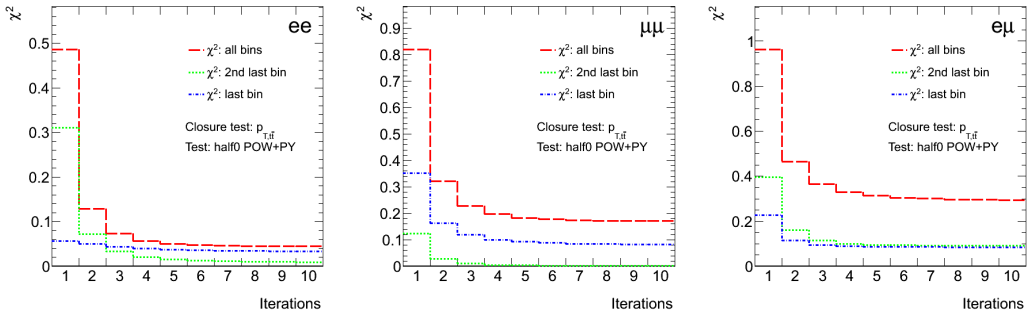

(b) $p_{\mathrm{T}}^{t\bar{t}}$

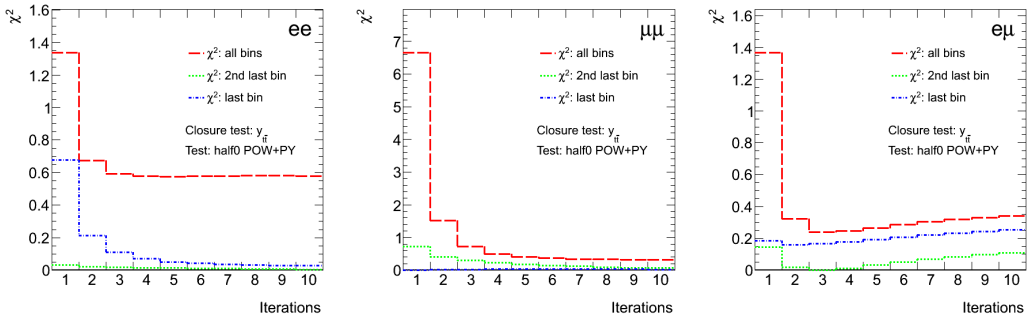

(c) $y_{t\bar{t}}$

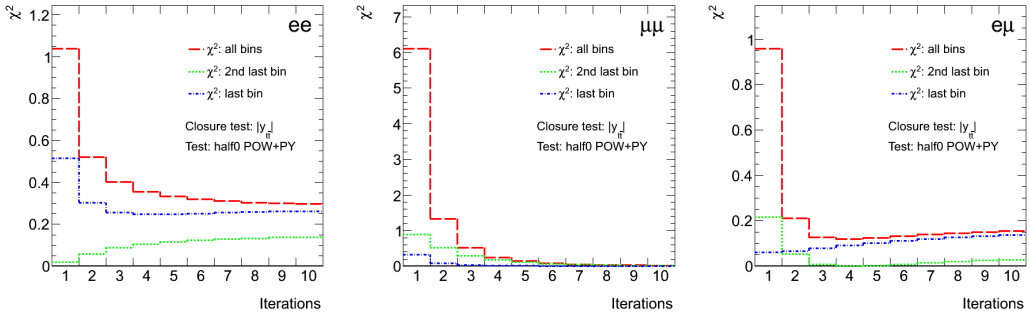

(d) $|y_{t\bar{t}}|$

Figure C.8: χ^2 of all bins, 2nd last bin and the last bin as number of iterations in Bayesian unfolding of (a)$m_{t\bar{t}}$, (b)$p_{\mathrm{T}}^{t\bar{t}}$, (c)$y_{t\bar{t}}$ and (d)$|y_{t\bar{t}}|$ in the ee (left), $\mu\mu$ (center) and $e\mu$ (right) channels. Test data using half of the POWHEG +PYTHIA $t\bar{t}$ sample as input is compared. The other half of the POWHEG +PYTHIA $t\bar{t}$ is used as the training sample.

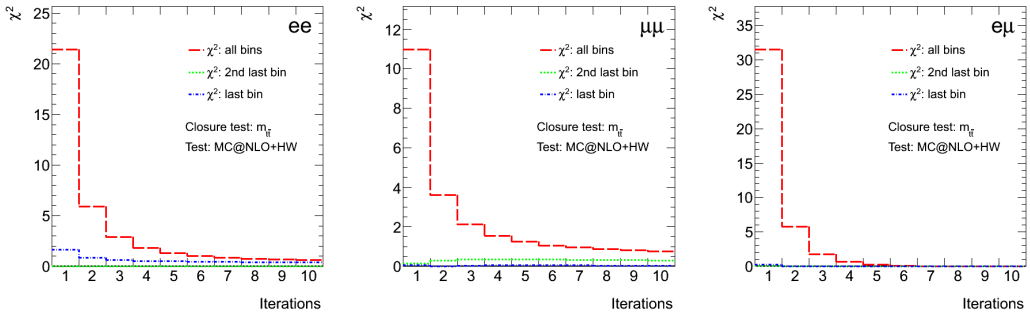

(a) $m_{t\bar{t}}$

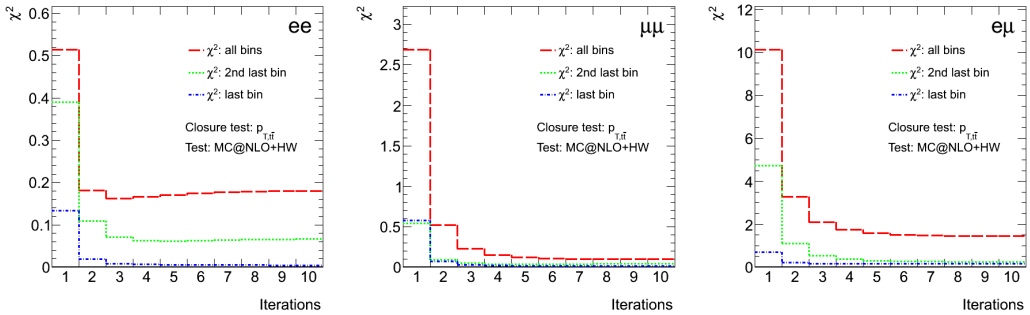

(b) $p_{\mathrm{T}}^{t\bar{t}}$

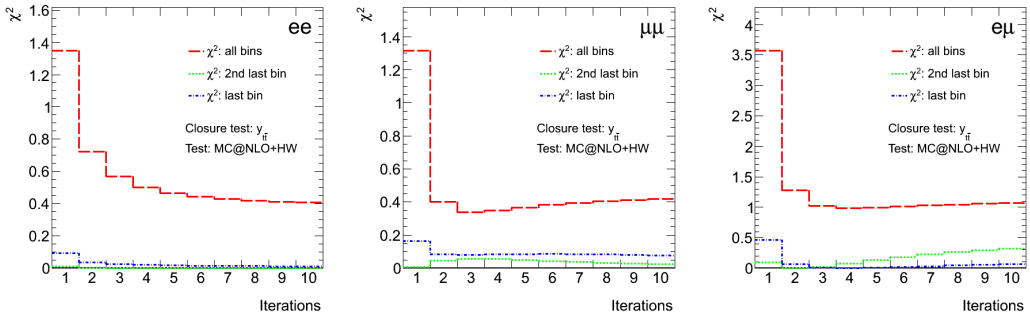

(c) $y_{t\bar{t}}$

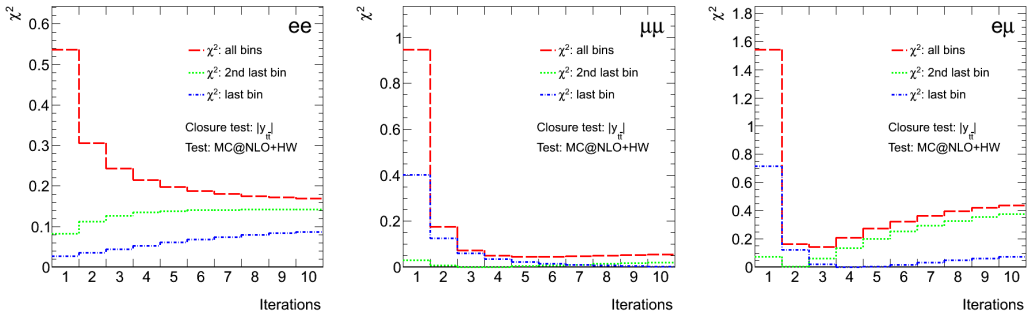

(d) $|y_{t\bar{t}}|$

Figure C.9: χ^2 of all bins, 2nd last bin and the last bin as number of iterations in Bayesian unfolding of (a)$m_{t\bar{t}}$, (b)$p_{\mathrm{T}}^{t\bar{t}}$, (c)$y_{t\bar{t}}$ and (d)$|y_{t\bar{t}}|$ in the ee (left), $\mu\mu$ (center) and $e\mu$ (right) channels. Test data using MC@NLO +Herwig $t\bar{t}$ sample as input is compared. Powheg +Pythia $t\bar{t}$ is used as the training sample.

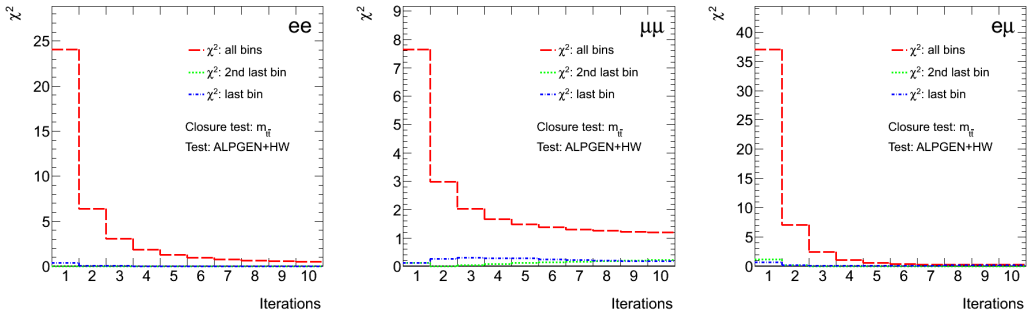

(a) $m_{t\bar{t}}$

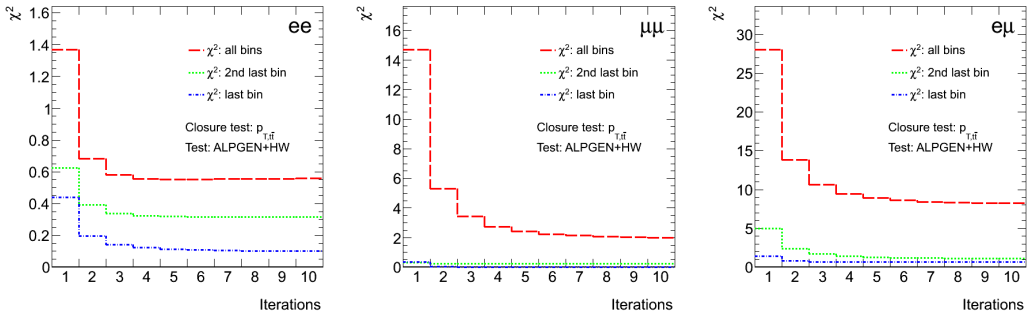

(b) $p_{\mathrm{T}}^{t\bar{t}}$

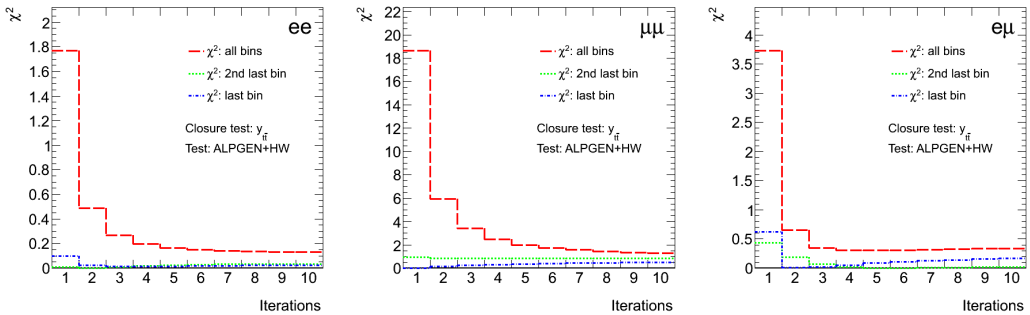

(c) $y_{t\bar{t}}$

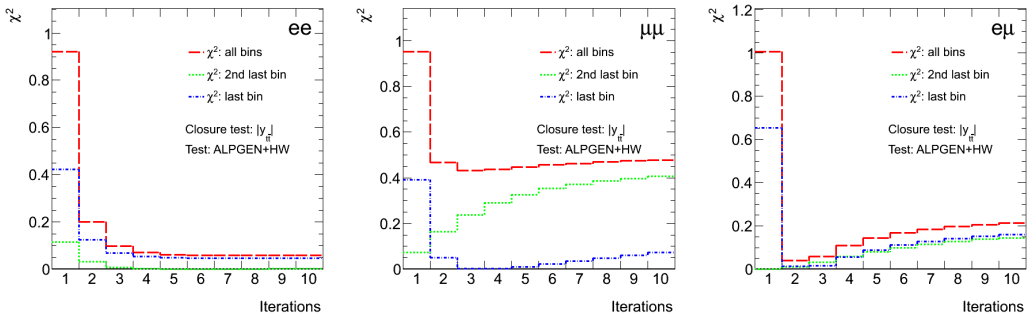

(d) $|y_{t\bar{t}}|$

Figure C.10: χ^2 of all bins, 2nd last bin and the last bin as number of iterations in Bayesian unfolding of (a)$m_{t\bar{t}}$, (b)$p_{\mathrm{T}}^{t\bar{t}}$, (c)$y_{t\bar{t}}$ and (d)$|y_{t\bar{t}}|$ in the ee (left), $\mu\mu$ (center) and $e\mu$ (right) channels. Test data using ALPGEN +HERWIG $t\bar{t}$ sample as input is compared. POWHEG +PYTHIA $t\bar{t}$ is used as the training sample.

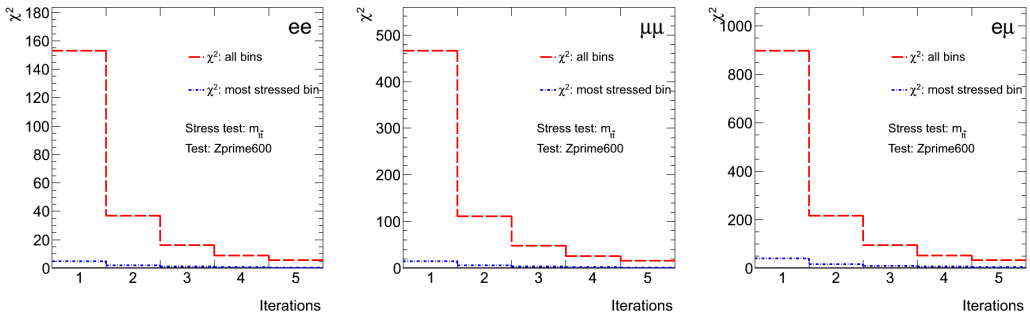

(a) $m_{t\bar{t}}$ with $m_{Z'} = 0.6$ TeV

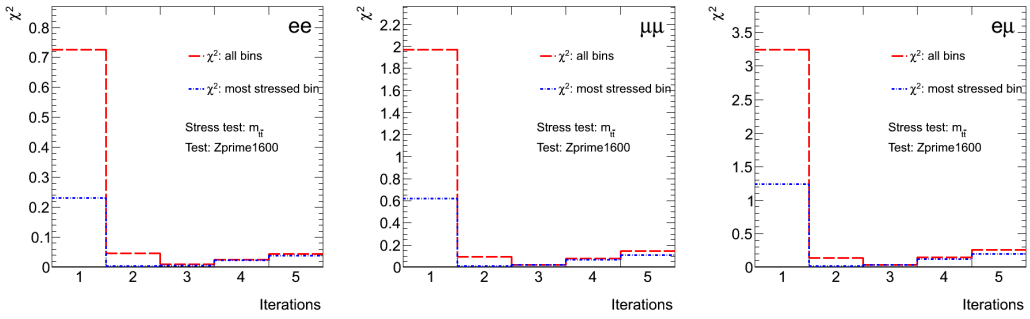

(b) $m_{t\bar{t}}$ with $m_{Z'} = 1.6$ TeV

Figure C.11: χ^2 of all bins of the $m_{t\bar{t}}$ in the ee, $\mu\mu$ and $e\mu$ channels with 1-5 number of iterations. Test data uses $m_{Z'} = 0.6$ TeV and $m_{Z'} = 1.6$ TeV as input stress samples. The default POWHEG +PYTHIA $t\bar{t}$ is used as the training sample.

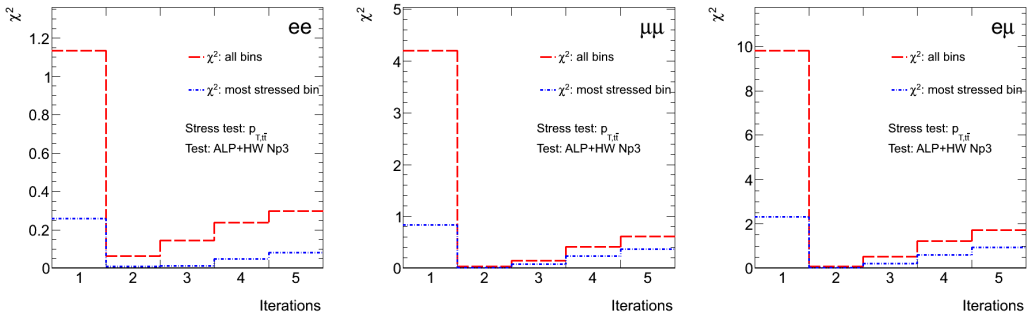

(a) $p_{\mathrm{T}}^{t\bar{t}}$ with Alpgen+HW Np3 lnln

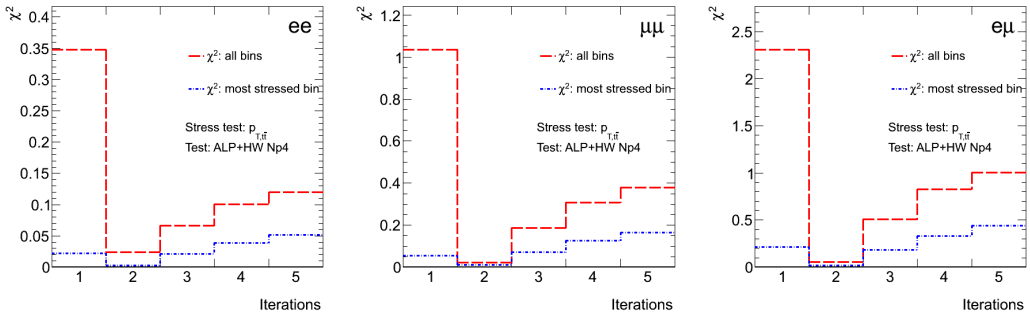

(b) $p_{\mathrm{T}}^{t\bar{t}}$ with Alpgen+HW Np4 lnln

Figure C.12: χ^2 of all bins of the $p_{\mathrm{T}}^{t\bar{t}}$ in the ee, $\mu\mu$ and $e\mu$ channels with 1-5 number of iterations. Test data uses Alpgen+HW Np3 lnln and Alpgen+HW Np4 lnln as input stress samples. The default POWHEG +PYTHIA $t\bar{t}$ is used as the training sample.

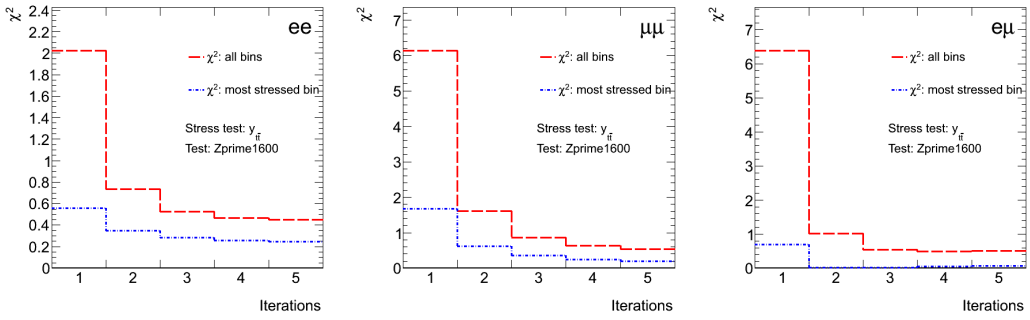

(a) $y_{t\bar{t}}$ with $m_{Z'} = 1.6$ TeV

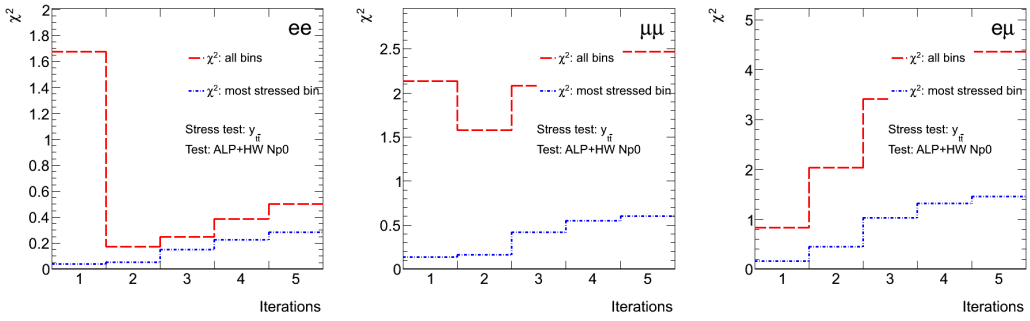

(b) $y_{t\bar{t}}$ with Alpgen+HW Np0 lnln

Figure C.13: χ^2 of all bins of the $y_{t\bar{t}}$ in the ee, $\mu\mu$ and $e\mu$ channels with 1-5 number of iterations. Test data uses $m_{Z'} = 1.6$ TeV and Alpgen+HW Np0 lnln as input stress samples. The default POWHEG +PYTHIA $t\bar{t}$ is used as the training sample.

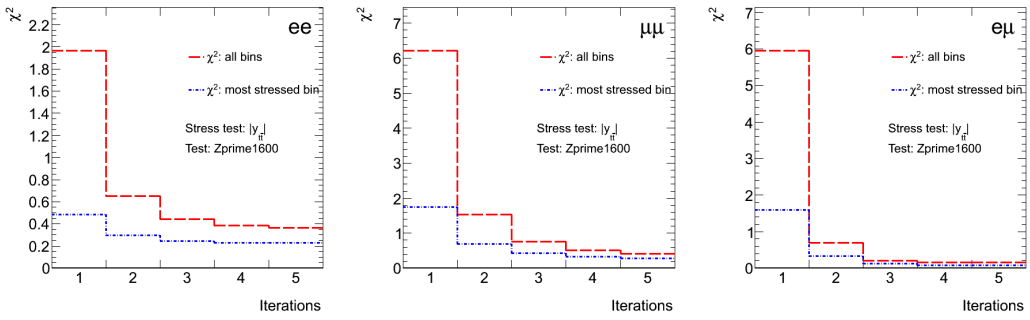

(a) $|y_{t\bar{t}}|$ with $m_{Z'} = 1.6$ TeV

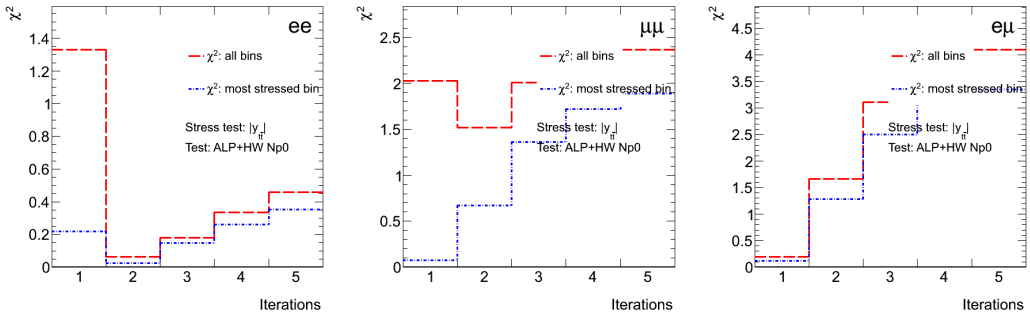

(b) $|y_{t\bar{t}}|$ with Alpgen+HW Np0 lnln

Figure C.14: χ^2 of all bins of the $|y_{t\bar{t}}|$ in the ee, $\mu\mu$ and $e\mu$ channels with 1-5 number of iterations. Test data uses $m_{Z'} = 1.6$ TeV and Alpgen+HW Np0 lnln as input stress samples. The default POWHEG +PYTHIA $t\bar{t}$ is used as the training sample.

Appendix D

Selection Efficiency in $t\bar{t}$ events

The differential efficiency with respect to $m_{t\bar{t}}$, $p_{\mathrm{T}}^{t\bar{t}}$, $y_{t\bar{t}}$ and $|y_{t\bar{t}}|$, or $(A{\cdot}\epsilon)_i$ where i is the i-th bin of the $t\bar{t}$ system variable, is measured using the baseline $t\bar{t}$ POWHEG +PYTHIA P2011C 117050 sample. It is measured by dividing the number of generated events passing all selection cuts and the total number of generated events in each bin i. The highest bins include overflow events outside the ranges defined for $m_{t\bar{t}}$, $p_{\mathrm{T}}^{t\bar{t}}$, $y_{t\bar{t}}$ and $|y_{t\bar{t}}|$. The bin ranges are determined such that there is no event passing all selection cuts outside these ranges in the simulated $t\bar{t}$ sample, and are kept identical with the previous measurements in ATLAS [**?**, 22] when possible. The generator-level events are chosen and defined at the top-parton level (as described in 5.1.1).

D.1 Selection efficiency in differential $t\bar{t}$

Table D.1 shows the differential efficiency $(A \cdot \epsilon)_i$ of $m_{t\bar{t}}$, $p_{\mathrm{T}}^{t\bar{t}}$, $y_{t\bar{t}}$ and $|y_{t\bar{t}}|$ in the ee, $\mu\mu$ and $e\mu$ channels. Figure D.1 illustrates the same graphically. The uncertainty shown in Figure D.1 includes all statistical and systematic errors associated with the MC $t\bar{t}$ sample described in Section **??**, including the PDF uncertainties.

The differential efficiency measures the acceptance and efficiency relative to all $t\bar{t}$ events (i.e. not just the dileptonic ones). Therefore, the acceptances for $\mu\mu$ events are $\sim$ half of the $e\mu$ events, as expected from their branching ratios from the top quark decay. The lower acceptances of ee events is mainly due to the higher cut in lepton transverse momentum for selecting the electrons and the muons: $p_{\mathrm{T}} > 25$ GeV for electrons and $p_{\mathrm{T}} > 20$ GeV for muons. The difference in the shape of $(A \cdot \epsilon)_i$ in the $ee/\mu\mu$ and the $e\mu$ channels is also attributed to the non-identical kinematic cuts defined in the dilepton channels. For example, a $E_{\mathrm{T}}^{\mathrm{miss}}$ cut of 60 GeV is required in ee and $\mu\mu$ channels, while in $e\mu$ channel there is no $E_{\mathrm{T}}^{\mathrm{miss}}$ requirement, leading to the apparent shape difference in $(A \cdot \epsilon)_i$ in $m_{t\bar{t}}$ and $p_{\mathrm{T}}^{t\bar{t}}$ between $e\mu$ and the other two channels.

$m_{t\bar{t}}$ [GeV]	$(A \cdot \epsilon)$		
	ee	$\mu\mu$	$e\mu$
250-450	0.000 88	0.0028	0.0080
450-550	0.0012	0.0033	0.0088
550-700	0.0014	0.0037	0.0092
700-950	0.0016	0.0041	0.0087
950-2700	0.0015	0.0040	0.0073

(a) $m_{t\bar{t}}$

p_{T}^{tt} [GeV]	$(A \cdot \epsilon)$		
	ee	$\mu\mu$	$e\mu$
0-40	0.000 96	0.0028	0.0079
40-170	0.0012	0.0036	0.0092
170-340	0.0015	0.0040	0.0090
340-1000	0.0019	0.0045	0.0073

(b) $p_{\mathrm{T}}^{t\bar{t}}$

$y_{t\bar{t}}$	$(A \cdot \epsilon)$		
	ee	$\mu\mu$	$e\mu$
-2.5–1	0.000 67	0.0025	0.0060
-1–0.5	0.0012	0.0033	0.0090
-0.5-0	0.0014	0.0035	0.0099
0-0.5	0.0013	0.0036	0.0098
0.5-1	0.0012	0.0034	0.0088
1-2.5	0.000 67	0.0026	0.0060

(c) $y_{t\bar{t}}$

$\lvert y_{t\bar{t}} \rvert$	$(A \cdot \epsilon)$		
	ee	$\mu\mu$	$e\mu$
0-0.5	0.0013	0.0036	0.0098
0.5-1	0.0012	0.0034	0.0089
1-2.5	0.000 67	0.0026	0.0060

(d) $|y_{t\bar{t}}|$

$t\bar{t}$	$(A \cdot \epsilon)$		
	ee	$\mu\mu$	$e\mu$
inclusive	0.0011	0.0032	0.0085

(e) $t\bar{t}$

Table D.1: The differential efficiency in $m_{t\bar{t}}$, $p_{\mathrm{T}}^{t\bar{t}}$, $y_{t\bar{t}}$ and $|y_{t\bar{t}}|$ and the total efficiency in ee, $\mu\mu$ and $e\mu$ channels. Note that the total efficiency cannot be calculated from the differential efficiencies of all bins in a variable. POWHEG+PYTHIA $t\bar{t}$ sample is used to extract these efficiencies.

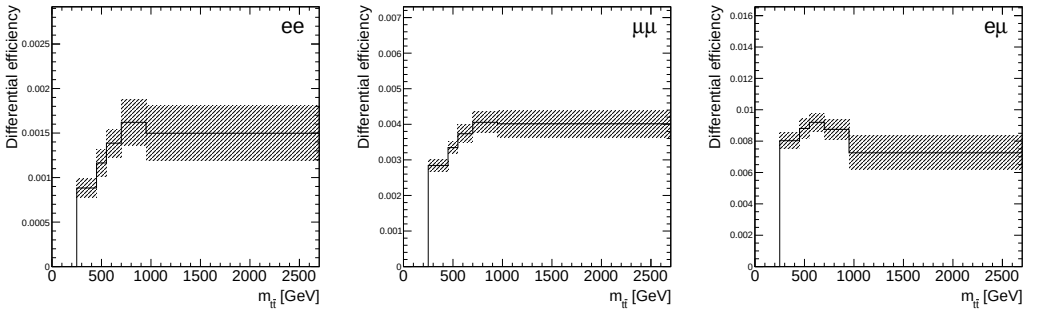

(a) $m_{t\bar{t}}$

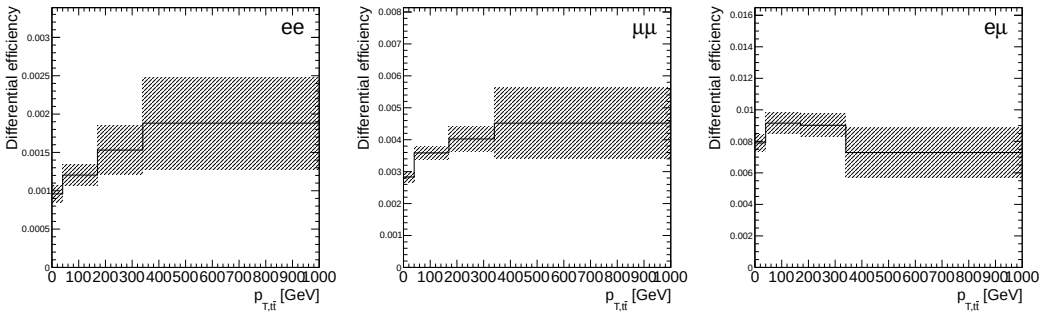

(b) $p_{\mathrm{T}}^{t\bar{t}}$

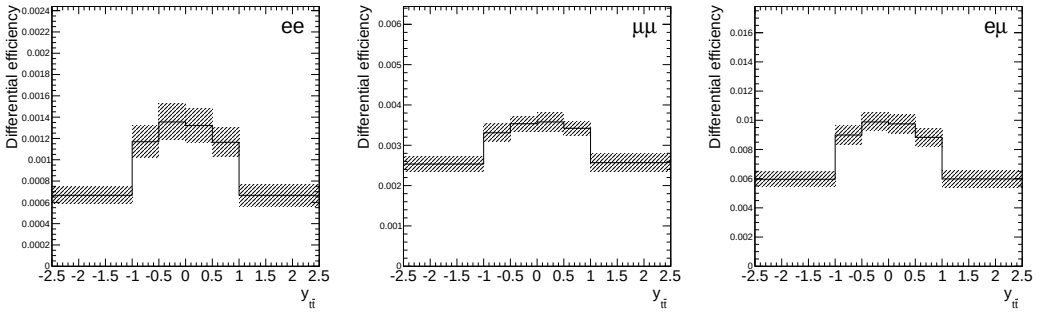

(c) $y_{t\bar{t}}$

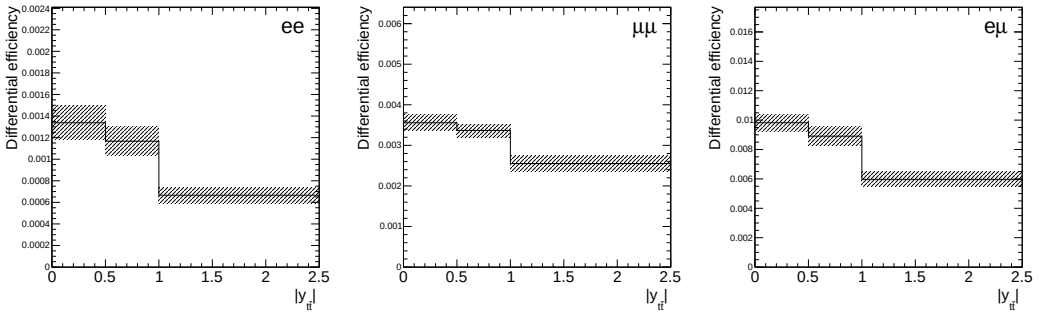

(d) $|y_{t\bar{t}}|$

Figure D.1: Differential efficiency in true (a)$m_{t\bar{t}}$, (b)$p_{\mathrm{T}}^{t\bar{t}}$, (c)$y_{t\bar{t}}$ and (d)$|y_{t\bar{t}}|$ in the ee (left), $\mu\mu$ (center) and $e\mu$ (right) channels. POWHEG+PYTHIA $t\bar{t}$ sample is used to extract these efficiencies.

Appendix E

Inclusive $\sigma_{t\bar{t}}$ Measurement

Using equation 2.5, an inclusive $t\bar{t}$ cross-section $\sigma_{t\bar{t}}^{inc}$ can be measured by a cut-and-count method in each dilepton channel. The results are summarized in table E.1 in the ee, $\mu\mu$ and $e\mu$ channels. The break-down of the systematic uncertainties is shown in tables E.2 and E.3.

Channel	$\sigma_{t\bar{t}}$ [pb]
ee	$181.4 \pm 8.4(\text{stat.})^{+21.1}_{-20.4}(\text{syst.})$
$\mu\mu$	$178.1 \pm 4.8(\text{stat.})^{+9.9}_{-9.9}(\text{syst.})$
$e\mu$	$181.0 \pm 3.0(\text{stat.})^{+13.0}_{-12.6}(\text{syst.})$

Table E.1: Measured inclusive $t\bar{t}$ cross section $\sigma_{t\bar{t}}^{inc}$ by the cut-and-count method in this analysis. The selection cuts are defined in section 5.2, the same as in the differential cross section measurement.

	ee	$\mu\mu$	$e\mu$
Uncertainties	$\Delta\sigma/\sigma$ [%]		
Total	12.51 / -12.17	6.19 / -6.20	7.37 / -7.14
Stat. only	4.65 / -4.65	2.72 / -2.72	1.66 / -1.66
Syst. only	11.61 / -11.25	5.56 / -5.57	7.18 / -6.94
Electron energy scale	0.50 / -0.70	0.00 / 0.00	0.14 / -0.14
Electron energy resolution	0.06 / -0.26	0.00 / 0.00	-0.01 / -0.05
Electron trigger scale factor	-0.01 / -0.10	0.00 / 0.00	0.14 / -0.17
Electron reco-id scale factor	6.78 / -6.18	0.00 / 0.00	3.38 / -3.18
Muon momentum scale	0.00 / -0.03	0.01 / -0.22	0.01 / -0.08
Muon momentum resolution	0.00 / -0.00	0.01 / -0.01	0.00 / 0.00
Muon trigger scale factor	0.00 / 0.00	0.54 / -0.51	0.02 / -0.02
Muon reco-id scale factor	0.00 / 0.00	1.66 / -1.62	0.82 / -0.81
Jet energy resolution	0.02 / -0.61	0.25 / 0.21	0.74 / -0.01
Jet energy scale	2.94 / -2.99	2.19 / -2.44	1.19 / -1.20
Jet reconstruction efficiency	0.00 / -0.02	0.04 / -0.03	0.02 / -0.00
Jet vertex fraction scale factor	0.98 / -0.79	0.97 / -0.82	0.96 / -0.77
E_T^{miss} pileup	0.11 / -0.13	0.12 / -0.28	0.00 / 0.00
E_T^{miss} cellout	0.16 / -0.23	0.19 / -0.47	0.00 / 0.00
b-tag efficiency	2.08 / -1.91	2.11 / -1.99	2.11 / -1.95
Mis-tag	0.20 / -0.20	0.20 / -0.24	0.14 / -0.14
c-tag	0.04 / -0.04	0.04 / -0.07	0.04 / -0.04
Fake leptons (normalisation)	1.48 / -1.48	0.33 / -0.33	0.68 / -0.71
Single top (normalisation)	0.32 / -0.31	0.31 / -0.30	0.31 / -0.30
PDF	1.42 / -1.38	1.19 / -1.16	1.59 / -1.54
ISR/FSR	5.75 / -5.75	3.28 / -3.28	4.09 / -4.09
MC generator (POWHEG+PY vs MC@NLO+HW)	0.16 / -0.16	0.37 / -0.37	0.47 / -0.47
POWHEG+PY vs ALPGEN+HW	9.89 / -9.89	6.01 / -6.01	5.75 / -5.75
Parton shower (POWHEG+PY vs POWHEG+HW)	1.86 / -1.86	0.94 / -0.94	2.25 / -2.25
Underlying event	1.55 / -1.55	0.36 / -0.36	0.10 / -0.10
Color reconnection	5.15 / -5.15	0.02 / -0.02	1.71 / -1.71
Ren./Fac. scale	0.70 / -0.70	0.06 / -0.06	0.37 / -0.37
MC stat.	0.97 / -0.97	0.58 / -0.58	0.35 / -0.35
Luminosity	1.97 / -1.90	1.94 / -1.87	1.94 / -1.87

Table E.2: Contribution of each systematic uncertainty to the total $\sigma_{t\bar{t}}^{inc}$ as percentage of the cross-section $\Delta\sigma/\sigma$ for each of the dilepton channels. The grayed items are shown only for the purpose of detailed comparisons and are not included in the total systematic uncertainty.

	ee	$\mu\mu$	$e\mu$
Uncertainties	$\Delta\sigma/\sigma$ [%]		
Combined JES	2.94 / -2.99	2.19 / -2.44	1.19 / -1.20
Backgrounds JES	0.37 / -0.28	0.24 / -0.48	0.19 / -0.20
EffectiveNP STAT1	0.57 / -0.56	0.40 / -0.37	0.35 / -0.40
EffectiveNP STAT2	0.04 / -0.04	0.05 / -0.04	0.01 / -0.01
EffectiveNP STAT3	0.13 / -0.17	0.16 / -0.18	0.02 / -0.00
EffectiveNP MODEL1	1.19 / -1.24	0.83 / -0.89	0.56 / -0.61
EffectiveNP MODEL2	0.06 / -0.17	0.12 / -0.12	0.07 / -0.06
EffectiveNP MODEL3	0.06 / -0.22	0.15 / -0.12	0.06 / -0.05
EffectiveNP MODEL4	0.03 / -0.07	0.05 / -0.08	0.01 / -0.01
EffectiveNP DET1	0.72 / -0.86	0.66 / -0.61	0.14 / -0.14
EffectiveNP DET2	0.04 / -0.06	0.07 / -0.06	0.01 / -0.01
EffectiveNP MIXED1	0.08 / -0.09	0.07 / -0.10	0.01 / -0.01
EffectiveNP MIXED2	0.18 / -0.15	0.17 / -0.14	0.12 / -0.11
EtaIntercalibration TotalStat	0.22 / -0.31	0.24 / -0.20	0.14 / -0.15
EtaIntercalibration Theory	1.01 / -1.07	0.71 / -0.75	0.25 / -0.24
SingleParticle HighPt	0.00 / 0.00	0.00 / 0.00	-0.00 / -0.00
RelativeNonClosure MC11b	0.13 / -0.14	0.09 / -0.13	0.08 / -0.10
Pileup OffsetMu	0.06 / -0.17	0.08 / -0.09	0.04 / -0.05
Pileup OffsetNPV	0.19 / -0.22	0.06 / -0.04	0.04 / -0.03
closeby	1.27 / -1.10	0.72 / -0.71	0.39 / -0.30
flavor comp	0.08 / -0.12	0.05 / -0.09	0.02 / -0.05
flavor response	0.46 / -0.53	0.16 / -0.24	0.09 / -0.15
BJesUnc	1.17 / -1.32	1.13 / -1.10	0.53 / -0.45

Table E.3: Contribution of each component in jet energy scale uncertainty to the $\sigma_{t\bar{t}}^{inc}$ as percentage of the cross-section $\Delta\sigma/\sigma$ for each of the dilepton channels.

Appendix F

Evaluation of Systematic uncertainties

F.1 Systematic uncertainties from parton distribution functions

Three NLO PDF sets, CT10, MWST2008nlo68cl and NNPDF2.3, are used to evaluate the PDF uncertainty in the inclusive and differential $t\bar{t}$ cross sections. $t\bar{t}$ events in MC@NLO +Herwig (105200) sample are re-weighted with respect to these PDF sets (and their respective error sets) and the relative uncertainty of the 'envelope' is used to calculate the uncertainty on the central value of the observable.

The uncertainty of each individual PDF sets (intra-PDF uncertainty) is calculated based on their errors sets (52 for CT10, 42 for MWST and 100 for NNPDF) as follows. For an observable X, the uncertainty ΔX in each case is:

- CT10 (symmetric Hessian and reduced the uncertainty by 1.645 to correspond to 68 % C.L. errors):

$$\Delta X = (1/1.645) * 0.5 * \sqrt{\sum_i ((X_{i+} - X_{i-})^2)} \tag{F.1}$$

  where $X_{i+/-}$ is the $+/-$ 1-sigma variation of the i-th parameter ($i = 1, ..., 52/2$)

- MWST2008nlo68cl (asymmetric Hessian):

  For each pair varied with the i-th parameter (X_{2i} and X_{2i-1}), assign the variation to be up or down according to its direction with respect to the central value X_0. When both X_{2i} and X_{2i-1} are in the same direction, take the largest, as below:

$$\begin{aligned} \Delta X_{\text{up}} &= \sqrt{\sum_i (\max(0, X_{2i} - X_0, X_{2i-1} - X_0)^2} \\ \Delta X_{\text{down}} &= \sqrt{\sum_i (\max(0, X_0 - X_{2i}, X_0 - X_{2i-1})^2} \end{aligned} \tag{F.2}$$

  for $i = 1, ..., 42/2$.

- NNPDF2.3 (sample standard deviation):

For the i-th error set,

$$\Delta X = \sqrt{(1/(N-1)) * \sum((X_i - X_0)^2)} \tag{F.3}$$

for $i = 1, ...100$.

The total PDF uncertainty (envelope, or inter-PDF uncertainty) is taken as half of the the extremum (minimum and maximum) of all variations of the three PDF sets calculated from above.

The re-weighted selected events passing cuts are corrected by the normalisation of all events re-weighted. This keeps the normalisation of a distribution of all events the same and ensures that the PDF uncertainty accounts only for the acceptance and shape variation of the distribution, since the PDF normalisation uncertainty is already accounted for in the theory uncertainty. Without applying this renormalisation would lead to an overestimation of the PDF uncertainty.

It is also seen that in CT10 PDF set, error set number 48 has large weights (up to ~ 1400). It also contains most of the large weights (> 10) of all the 52 error sets in the CT10 PDF set. The effect of this was seen in $p_{\mathrm{T}}^{t\bar{t}}$, where in the last bin ($p_{\mathrm{T}}^{t\bar{t}} = 340 - 1000$ GeV), the re-weighted acceptance of this particular error set is significantly different from the other error sets, by up to $20 - 30\%$, and contributes to an unexpectedly large PDF uncertainty overall (6.8% in $\mu\mu$ and 9% in $e\mu$) in the last bin of $p_{\mathrm{T}}^{t\bar{t}}$ acceptance. To avoid the bias attributed to unrealistically large weights, this error set (48) and its associated set in the pair with the same parameter (47) are therefore removed while estimating the uncertainties for the CT10 PDF set, as the calculation is based on the difference between the error set pair.

F.1.1 PDF uncertainties in inclusive $t\bar{t}$

The PDF envelopes of inclusive $t\bar{t}$ in ee, $\mu\mu$ and $e\mu$ channels and the corresponding uncertainties of individual PDF sets are summarized in Table F.1 and Figure F.1.

$t\bar{t}$	CT10 [%]	MWST2008nlo68cl [%]	NNPDF2.3 [%]	Total PDF uncertainty [%]
ee	0.79	+0.26/-0.06	0.49	1.39
$\mu\mu$	0.65	+0.18/-0.04	0.39	1.17
$e\mu$	0.89	+0.30/-0.12	0.59	1.56

Table F.1: Summary of PDF uncertainties of inclusive $t\bar{t}$. Relative uncertainties are shown for each PDF set (CT10, MWST2008nlo68cl and NNPDF2.3) and the total PDF uncertainty, in the ee, $\mu\mu$ and $e\mu$ channels.

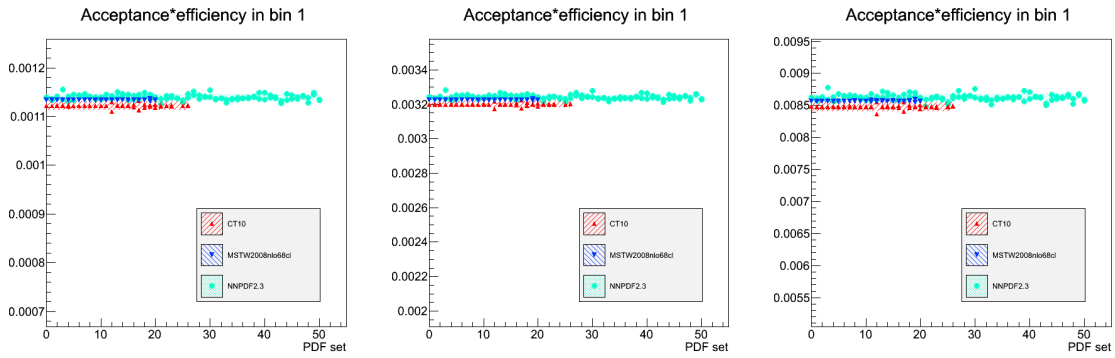

Figure F.1: Reweighted differential efficiency of inclusive $t\bar{t}$ with respect to the 3 different PDF sets, *CT10*, *MWST2008nlo68cl* and *NNPDF2.3*, in the ee (left), $\mu\mu$ (center) and $e\mu$ (right) channels. The total PDF uncertainty (the envelope) is evaluated as the half of the extremum of all the variations.

F.1.2 PDF uncertainties in $m_{t\bar{t}}$

	$m_{t\bar{t}}$ [GeV]	CT10 [%]	MWST2008nlo68cl [%]	NNPDF2.3 [%]	Total PDF uncertainty [%]
ee	inclusive	0.79	$+0.26\,/-0.06$	0.49	1.40
	250 - 450	0.90	$+0.37\,/-0.09$	0.60	1.67
	450 - 550	1.01	$+0.34\,/-0.15$	0.68	1.80
	550 - 700	1.08	$+0.32\,/-0.18$	0.71	1.76
	700 - 950	1.25	$+0.38\,/-0.30$	0.93	1.92
	950 - 2700	1.16	$+0.29\,/-0.31$	0.90	1.59
$\mu\mu$	inclusive	0.65	$+0.18\,/-0.04$	0.39	1.17
	250 - 450	0.65	$+0.22\,/-0.06$	0.38	1.18
	450 - 550	0.73	$+0.22\,/-0.09$	0.46	1.27
	550 - 700	0.93	$+0.26\,/-0.13$	0.63	1.68
	700 - 950	1.15	$+0.33\,/-0.16$	1.03	2.00
	950 - 2700	1.02	$+0.20\,/-0.15$	0.84	1.78
$e\mu$	inclusive	0.89	$+0.30\,/-0.12$	0.59	1.56
	250 - 450	0.82	$+0.31\,/-0.11$	0.54	1.46
	450 - 550	0.91	$+0.30\,/-0.14$	0.61	1.58
	550 - 700	1.05	$+0.31\,/-0.16$	0.71	1.78
	700 - 950	1.20	$+0.32\,/-0.20$	0.87	2.03
	950 - 2700	1.98	$+0.44\,/-0.30$	1.56	3.42

Table F.2: Summary of PDF uncertainties of $m_{t\bar{t}}$. Relative uncertainties are shown for each PDF set (CT10, MWST2008nlo68cl and NNPDF2.3) and the total PDF uncertainty, in the ee, $\mu\mu$ and $e\mu$ channels. PDF uncertainties for inclusive $t\bar{t}$ are also shown for comparison.

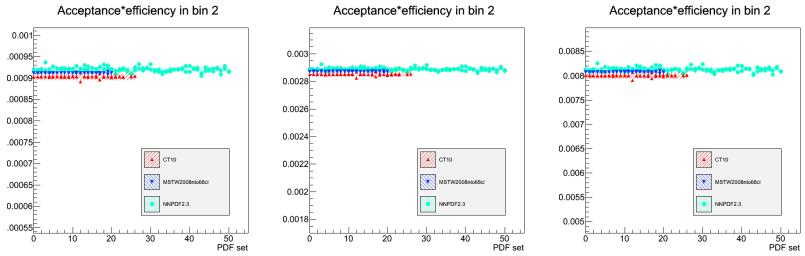

(a) 250 GeV $< m_{t\bar{t}} <$ 450 GeV

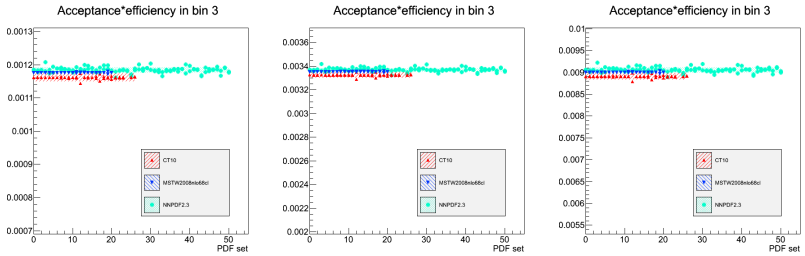

(b) 450 GeV $< m_{t\bar{t}} <$ 550 GeV

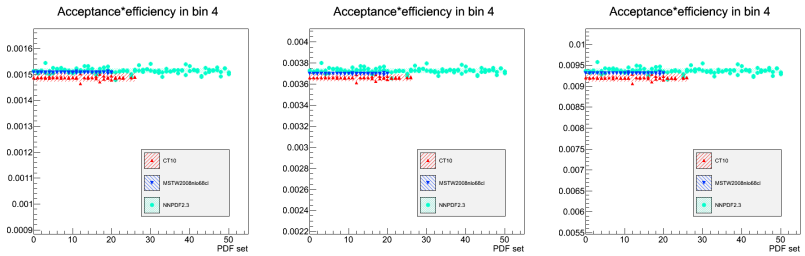

(c) 550 GeV $< m_{t\bar{t}} <$ 700 GeV

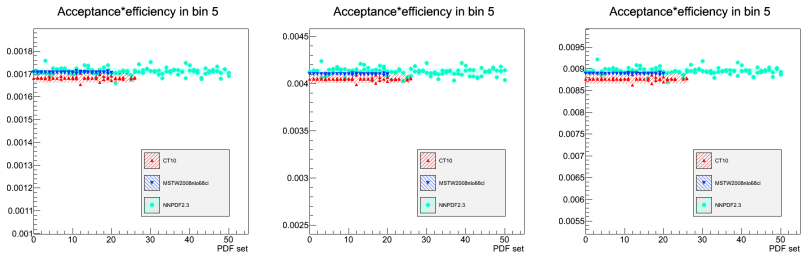

(d) 700 GeV $< m_{t\bar{t}} <$ 950 GeV

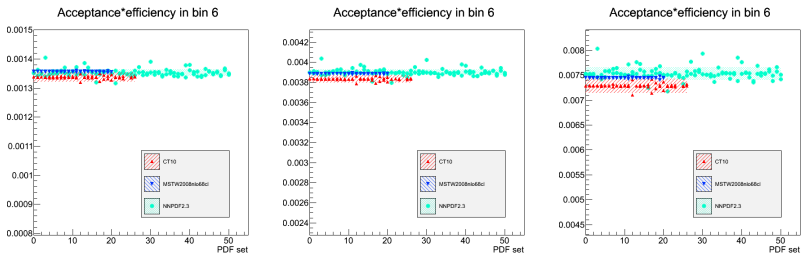

(e) 950 GeV $< m_{t\bar{t}} <$ 2700 GeV

Figure F.2: Reweighted differential efficiency of $m_{t\bar{t}}$ with respect to the 3 different PDF sets, *CT10*, *MWST2008nlo68cl* and *NNPDF2.3*, for each bin in the ee (left), $\mu\mu$ (center) and $e\mu$ (right) channels. The total PDF uncertainty (the envelope) is evaluated as the half of the extremum of all the variations.

F.1.3 PDF uncertainties in $p_{\mathrm{T}}^{t\bar{t}}$

	$p_{\mathrm{T}}^{t\bar{t}}$ [GeV]	CT10 [%]	MWST2008nlo68cl [%]	NNPDF2.3 [%]	Total PDF uncertainty [%]
	inclusive	0.79	$+0.26\,/{-0.06}$	0.49	1.40
	0 - 40	0.82	$+0.27\,/{-0.07}$	0.52	1.40
ee	40 - 170	0.76	$+0.27\,/{-0.09}$	0.51	1.36
	170 - 340	0.56	$+0.21\,/{-0.11}$	0.40	1.01
	340 - 1000	1.62	$+0.40\,/{-0.32}$	0.72	3.41
	inclusive	0.65	$+0.18\,/{-0.04}$	0.39	1.17
	0 - 40	0.74	$+0.22\,/{-0.05}$	0.46	1.32
$\mu\mu$	40 - 170	0.53	$+0.14\,/{-0.05}$	0.32	0.91
	170 - 340	0.56	$+0.20\,/{-0.10}$	0.42	1.18
	340 - 1000	2.00	$+0.59\,/{-0.54}$	5.32	5.45
	inclusive	0.89	$+0.30\,/{-0.12}$	0.59	1.56
	0 - 40	0.98	$+0.33\,/{-0.14}$	0.65	1.68
$e\mu$	40 - 170	0.84	$+0.28\,/{-0.13}$	0.57	1.46
	170 - 340	0.59	$+0.20\,/{-0.08}$	0.40	1.12
	340 - 1000	0.52	$+0.16\,/{-0.30}$	0.58	2.36

Table F.3: Summary of PDF uncertainties of $p_{\mathrm{T}}^{t\bar{t}}$. Relative uncertainties are shown for each PDF set (CT10, MWST2008nlo68cl and NNPDF2.3) and the total PDF uncertainty, in the ee, $\mu\mu$ and $e\mu$ channels. PDF uncertainties for inclusive $t\bar{t}$ are also shown for comparison.

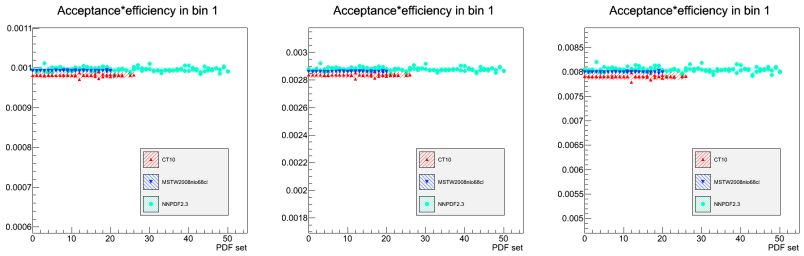

(a) 0 GeV $< p_{\mathrm{T}}^{t\bar{t}} <$ 40 GeV

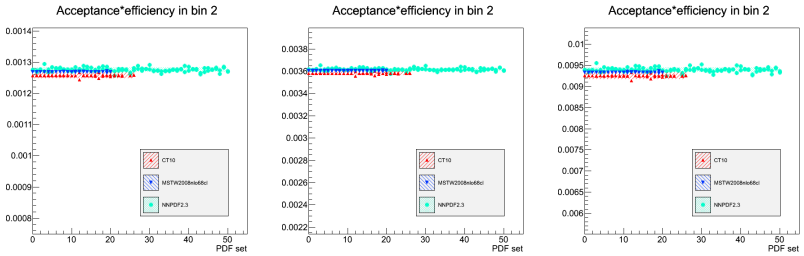

(b) 40 GeV $< p_{\mathrm{T}}^{t\bar{t}} <$ 170 GeV

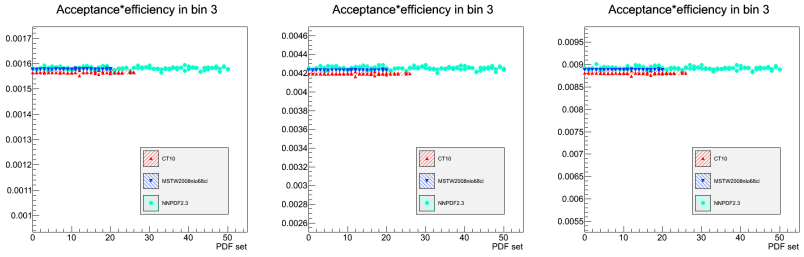

(c) 170 GeV $< p_{\mathrm{T}}^{t\bar{t}} <$ 340 GeV

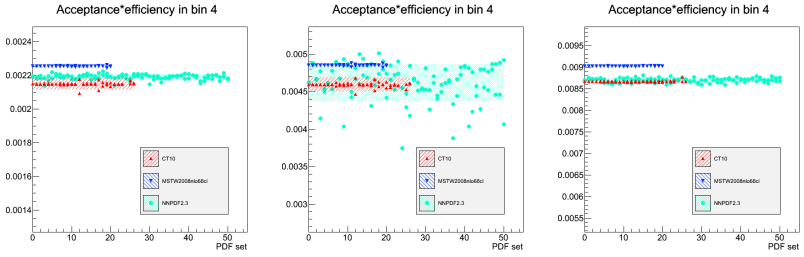

(d) 340 GeV $< p_{\mathrm{T}}^{t\bar{t}} <$ 1000 GeV

Figure F.3: Reweighted differential efficiency of $p_{\mathrm{T}}^{t\bar{t}}$ with respect to the 3 different PDF sets, *CT10*, *MWST2008nlo68cl* and *NNPDF2.3*, for each bin in the ee (left), $\mu\mu$ (center) and $e\mu$ (right) channels. The total PDF uncertainty (the envelope) is evaluated as the half of the extremum of all the variations.

F.1.4 PDF uncertainties in $y_{t\bar{t}}$

	$y_{t\bar{t}}$ [GeV]	CT10 [%]	MWST2008nlo68cl [%]	NNPDF2.3 [%]	Total PDF uncertainty [%]
	inclusive	0.79	+0.26 /−0.06	0.49	1.40
	-2.5 - -1.0	1.28	+0.33 /−0.18	0.93	2.21
	-1.0 - -0.5	0.35	+0.10 /−0.15	0.28	0.52
ee	-0.5 - 0	0.30	+0.09 /−0.12	0.24	0.31
	0 - 0.5	0.23	+0.08 /−0.09	0.19	0.23
	0.5 - 1.0	0.28	+0.11 /−0.13	0.26	0.45
	1.0 - 2.5	1.24	+0.29 /−0.13	0.77	1.93
	inclusive	0.65	+0.18 /−0.04	0.39	1.17
	-2.5 - -1.0	1.36	+0.32 /−0.14	0.95	2.41
	-1.0 - -0.5	0.09	+0.04 /−0.04	0.07	0.12
$\mu\mu$	-0.5 - 0	0.25	+0.08 /−0.11	0.27	0.28
	0 - 0.5	0.26	+0.09 /−0.11	0.21	0.29
	0.5 - 1.0	0.11	+0.05 /−0.04	0.10	0.15
	1.0 - 2.5	1.29	+0.29 /−0.10	0.89	2.28
	inclusive	0.89	+0.30 /−0.12	0.59	1.56
	-2.5 - -1.0	1.62	0.37 /−0.18	1.13	2.81
	-1.0 - -0.5	0.11	+0.05 /−0.03	0.09	0.19
$e\mu$	-0.5 - 0	0.03	+0.01 /−0.01	0.02	0.05
	0 - 0.5	0.05	+0.03 /−0.02	0.05	0.06
	0.5 - 1.0	0.13	+0.05 /−0.03	0.09	0.21
	1.0 - 2.5	1.64	+0.38 /−0.19	1.15	2.75

Table F.4: Summary of PDF uncertainties of $y_{t\bar{t}}$. Relative uncertainties are shown for each PDF set (CT10, MWST2008nlo68cl and NNPDF2.3) and the total PDF uncertainty, in the ee, $\mu\mu$ and $e\mu$ channels. PDF uncertainties for inclusive $t\bar{t}$ are also shown for comparison.

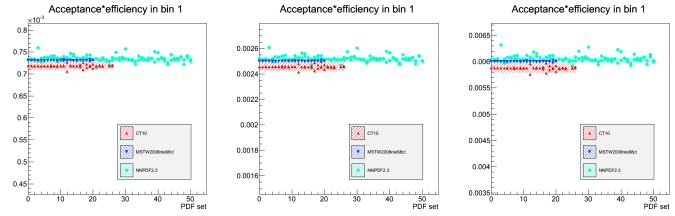

(a) $-2.5 < y_{t\bar{t}} < -1.0$

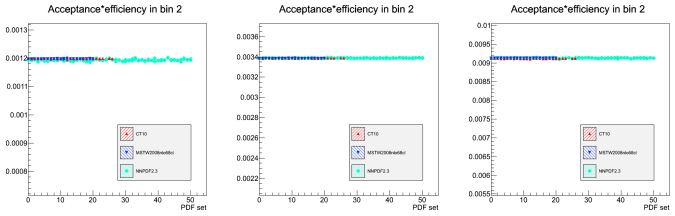

(b) $-1.0 < y_{t\bar{t}} < -0.5$

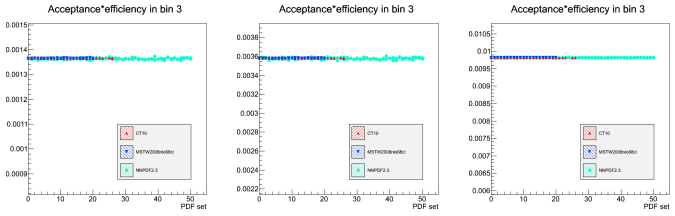

(c) $-0.5 < y_{t\bar{t}} < 0$

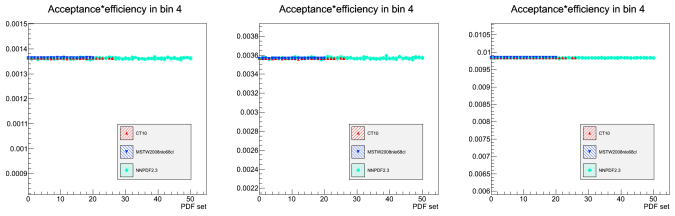

(d) $0 < y_{t\bar{t}} < 0.5$

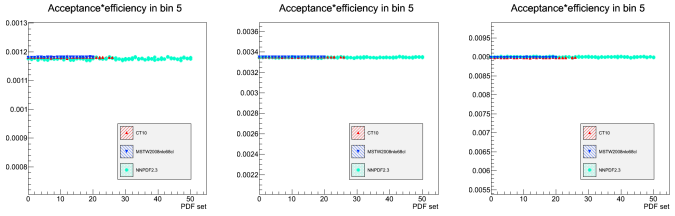

(e) $0.5 < y_{t\bar{t}} < 1.0$

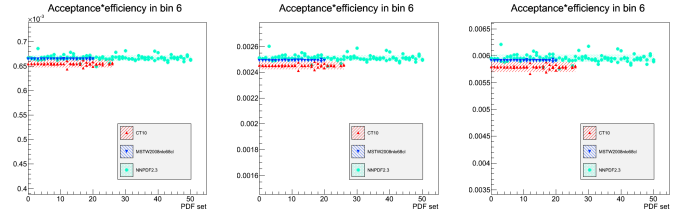

(f) $1.0 < y_{t\bar{t}} < 2.5$

Figure F.4: Reweighted differential efficiency of $y_{t\bar{t}}$ with respect to the 3 different PDF sets, *CT10*, *MWST2008nlo68cl* and *NNPDF2.3*, for each bin in the ee (left), $\mu\mu$ (center) and $e\mu$ (right) channels. The total PDF uncertainty (the envelope) is evaluated as the half of the extremum of all the variations.

F.1.5 PDF uncertainties in $|y_{t\bar{t}}|$

	$\lvert y_{t\bar{t}}\rvert$ [GeV]	CT10 [%]	MWST2008nlo68cl [%]	NNPDF2.3 [%]	Total PDF uncertainty [%]
ee	inclusive	0.79	+0.26 /−0.06	0.49	1.40
	0 - 0.5	0.26	+0.08 /−0.11	0.21	0.27
	0.5 - 1.0	0.31	+0.10 /−0.14	0.27	0.48
	1.0 - 2.5	1.26	+0.31 /−0.15	0.85	2.07
$\mu\mu$	inclusive	0.65	+0.18 /−0.04	0.39	1.17
	0 - 0.5	0.25	+0.09 /−0.11	0.23	0.26
	0.5 - 1.0	0.09	+0.04 /−0.03	0.08	0.09
	1.0 - 2.5	1.32	+0.30 /−0.12	0.92	2.34
$e\mu$	inclusive	0.89	+0.30 /−0.12	0.59	1.56
	0 - 0.5	0.03	+0.02 /−0.01	0.03	0.05
	0.5 - 1.0	0.11	+0.04 /−0.03	0.09	0.20
	1.0 - 2.5	1.63	+0.37 /−0.18	1.14	2.78

Table F.5: Summary of PDF uncertainties of $|y_{t\bar{t}}|$. Relative uncertainties are shown for each PDF set (CT10, MWST2008nlo68cl and NNPDF2.3) and the total PDF uncertainty, in the ee, $\mu\mu$ and $e\mu$ channels. PDF uncertainties for inclusive $t\bar{t}$ are also shown for comparison.

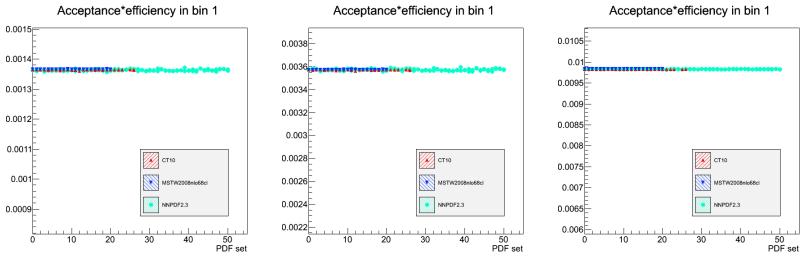

(a) $0 < |y_{t\bar{t}}| < 0.5$

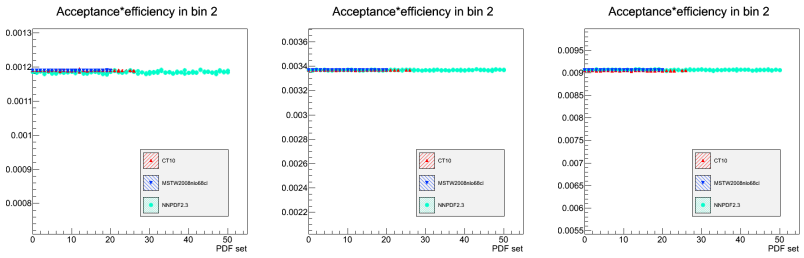

(b) $0.5 < |y_{t\bar{t}}| < 1.0$

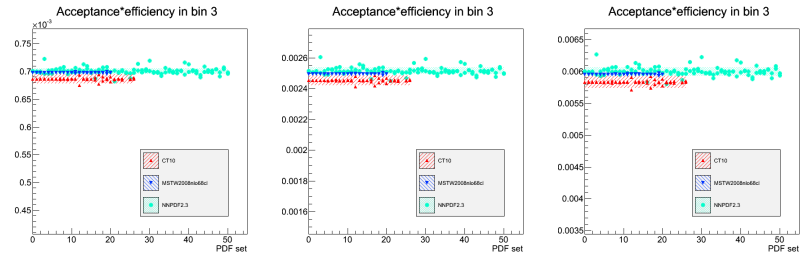

(c) $1.0 < |y_{t\bar{t}}| < 2.5$

Figure F.5: Reweighted differential efficiency of $|y_{t\bar{t}}|$ with respect to the 3 different PDF sets, *CT10*, *MWST2008nlo68cl* and *NNPDF2.3*, for each bin in the ee (left), $\mu\mu$ (center) and $e\mu$ (right) channels. The total PDF uncertainty (the envelope) is evaluated as the half of the extremum of all the variations.

F.2 Comparison of uncertainty evaluation methods in $t\bar{t}$ modeling systematics

This section shows the comparison of the results of these two methods of evaluating the $t\bar{t}$ modelling systematic uncertainties in measured and unfolded $t\bar{t}$ differential cross section $d\sigma/dm_{t\bar{t}}$, $d\sigma/dp_{\mathrm{T}}^{t\bar{t}}$, $d\sigma/dy_{t\bar{t}}$ and $d\sigma/d|y_{t\bar{t}}|$ for the channel (section F.2.1) and combined (section F.2.2) results. The comparisons are done for both absolute and normalized results.

F.2.1 Comparisons for channel results

Absolute results

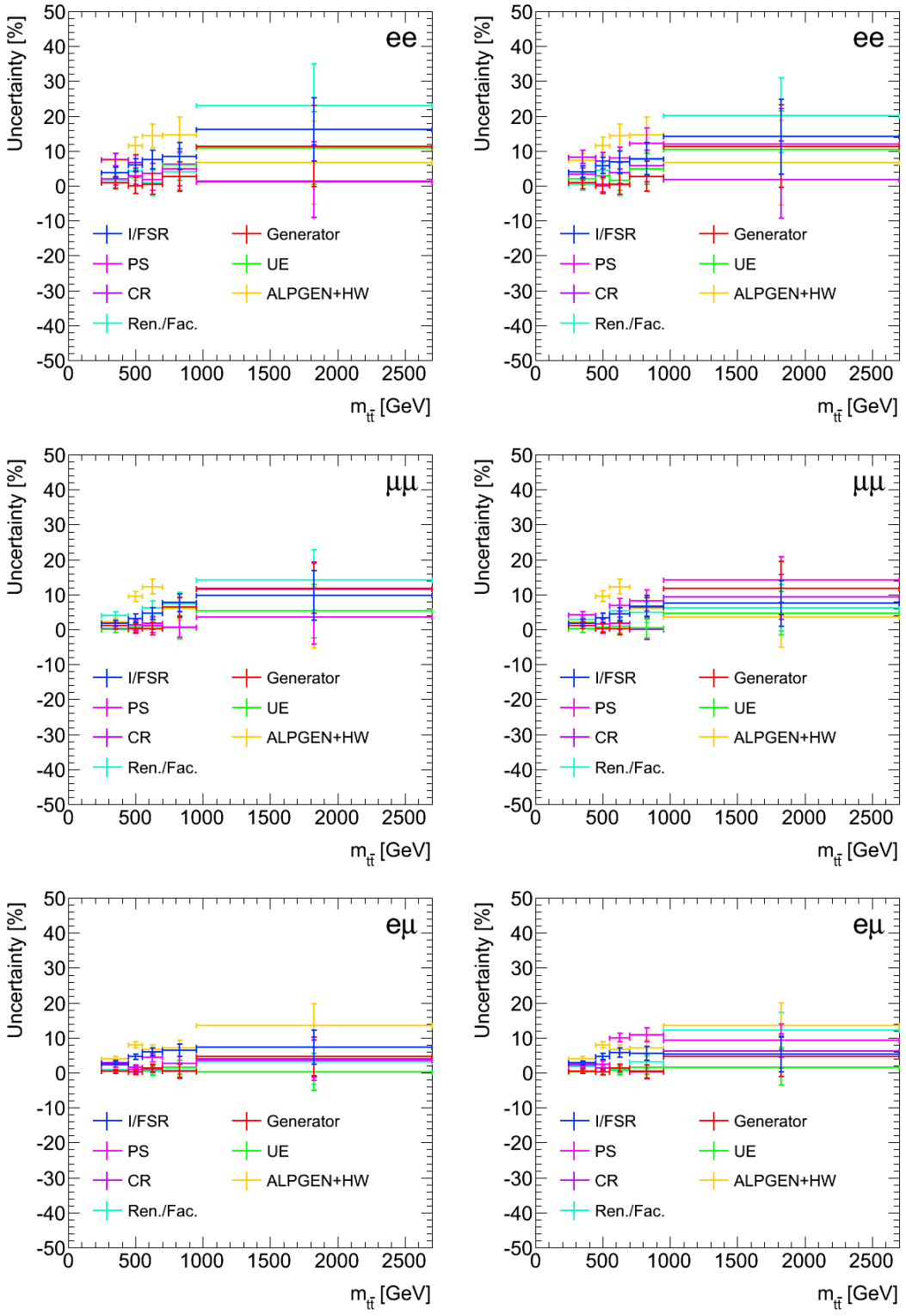

Figure F.6: Comparison of $t\bar{t}$ modelling systematics in $d\sigma/dm_{t\bar{t}}$ in the ee, $\mu\mu$ and $e\mu$ channels evaluated using data-based (left) and MC-based (right) methods.

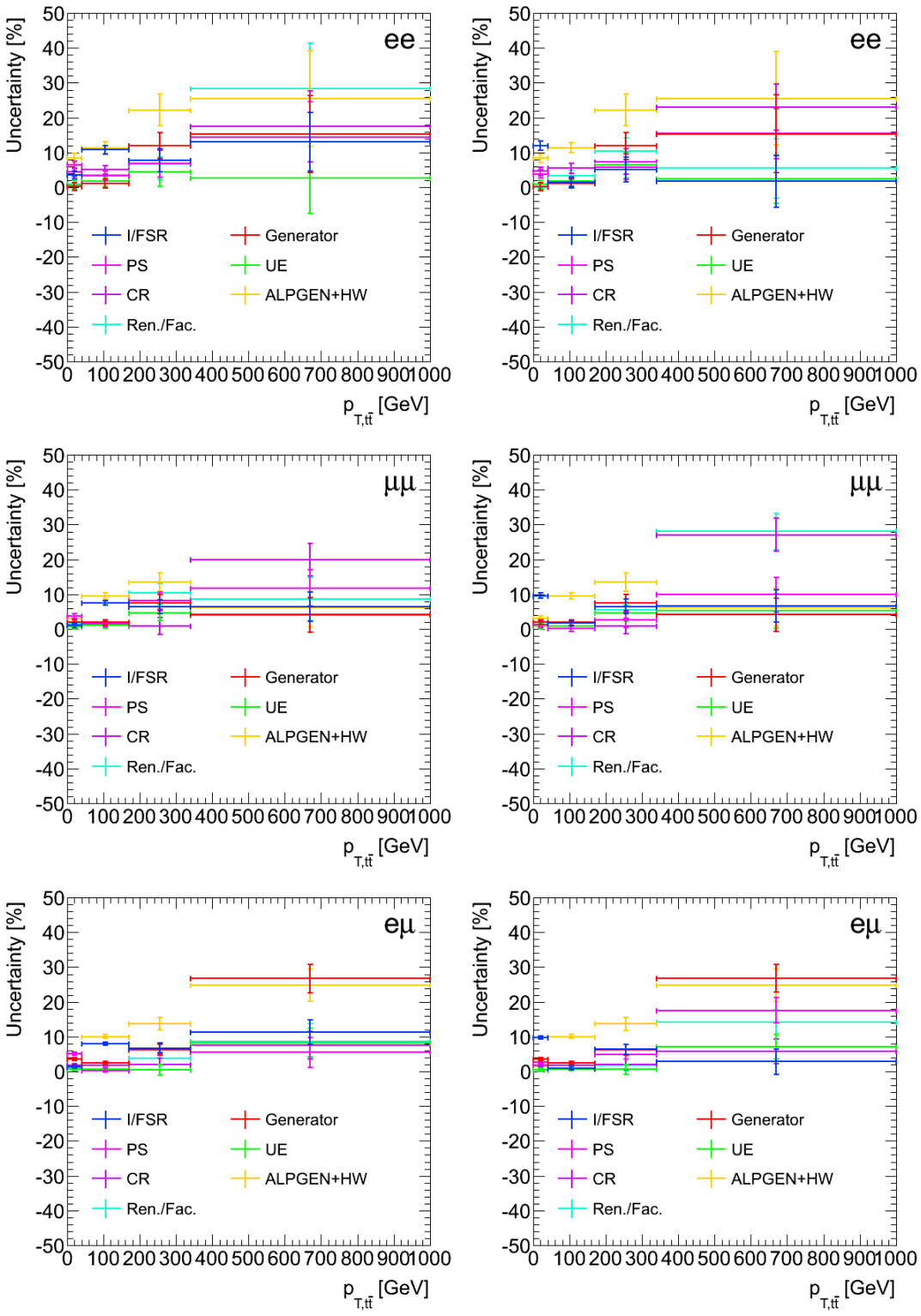

Figure F.7: Comparison of $t\bar{t}$ modelling systematics in $d\sigma/dp_{\mathrm{T}}^{t\bar{t}}$ in the ee, $\mu\mu$ and $e\mu$ channels evaluated using data-based (left) and MC-based (right) methods.

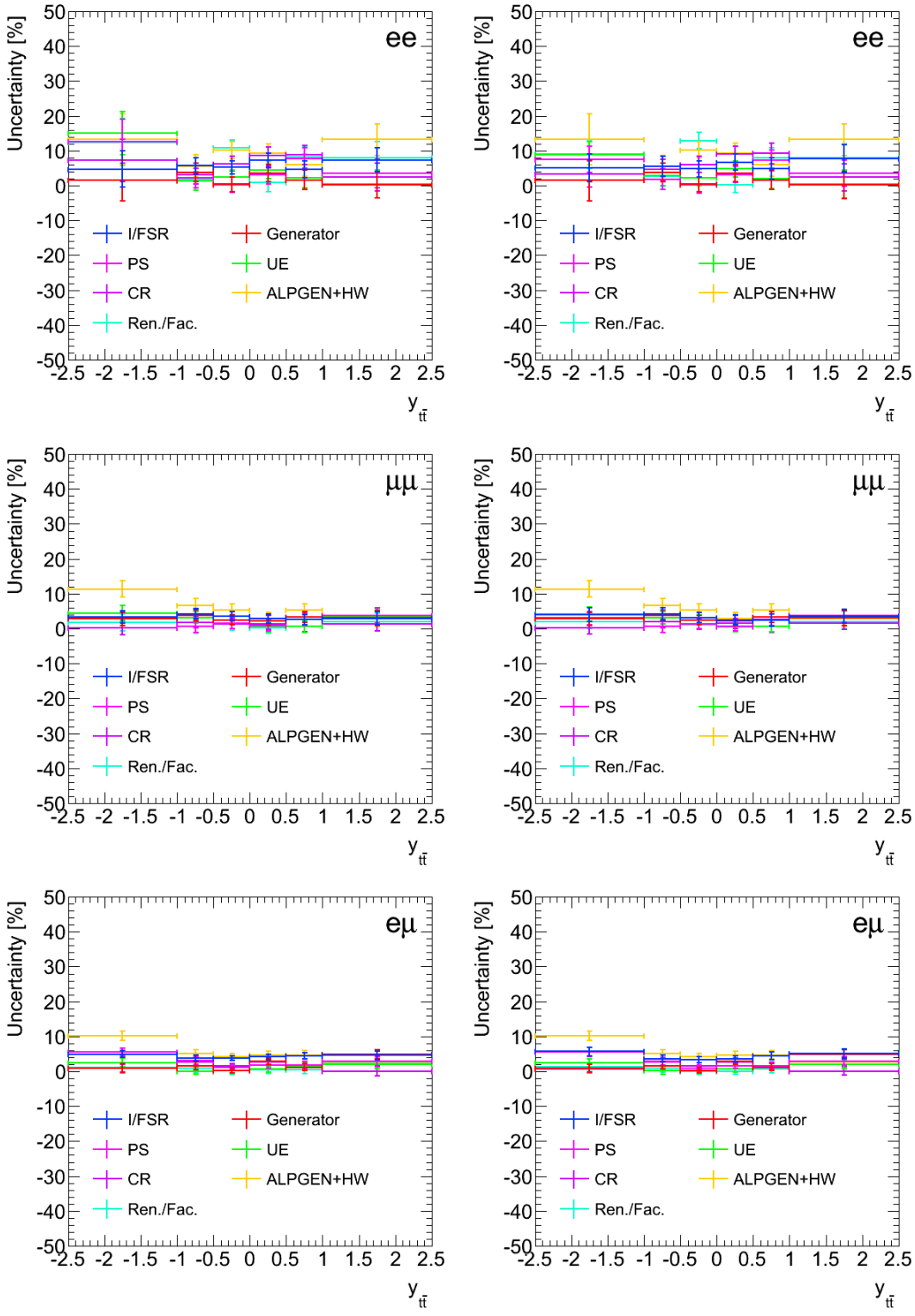

Figure F.8: Comparison of $t\bar{t}$ modelling systematics in $d\sigma/dy_{t\bar{t}}$ in the ee, $\mu\mu$ and $e\mu$ channels evaluated using data-based (left) and MC-based (right) methods.

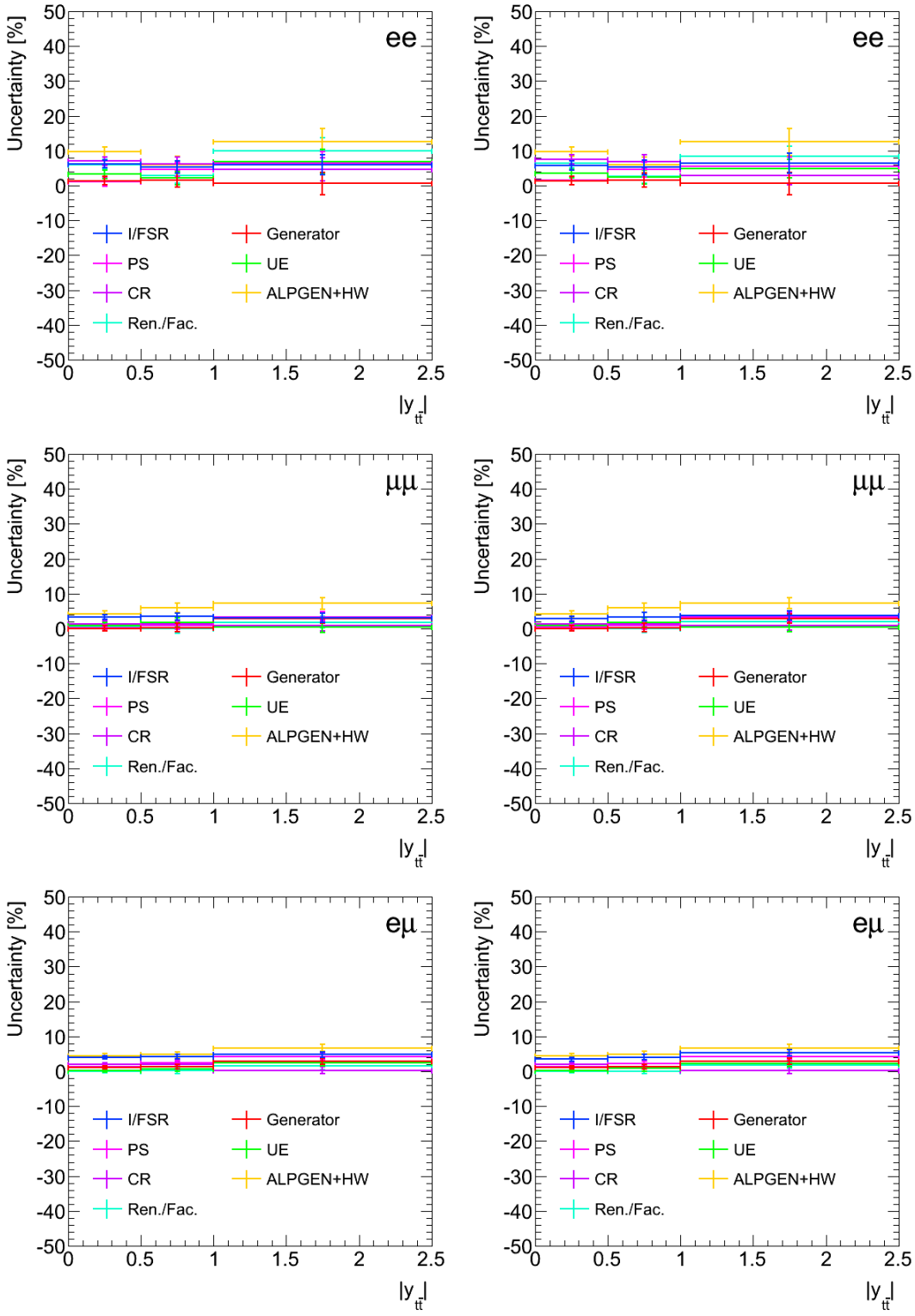

Figure F.9: Comparison of $t\bar{t}$ modelling systematics in $d\sigma/d|y_{t\bar{t}}|$ in the ee, $\mu\mu$ and $e\mu$ channels evaluated using data-based (left) and MC-based (right) methods.

Normalized results

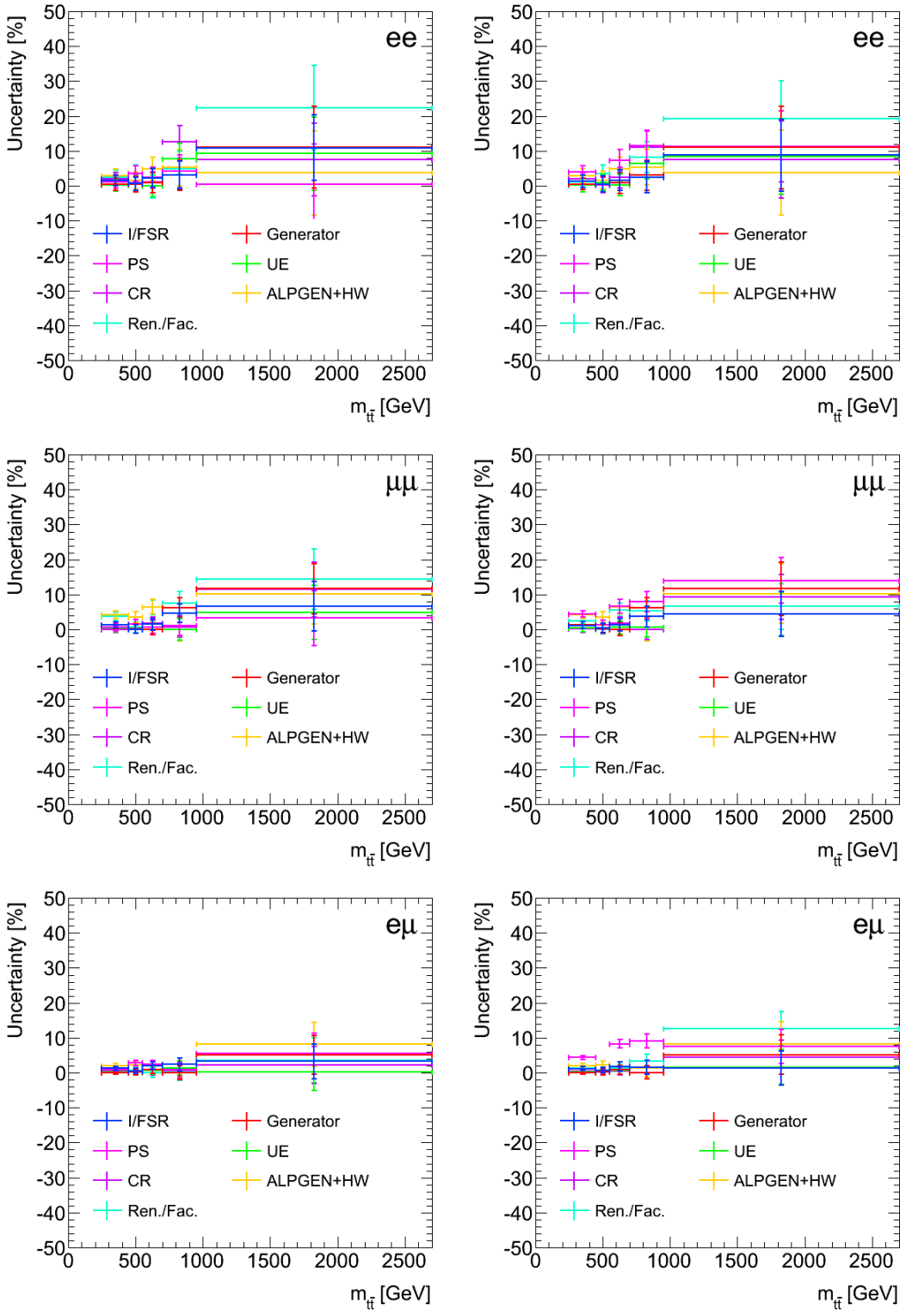

Figure F.10: Comparison of $t\bar{t}$ modelling systematics in $(1/\sigma_{t\bar{t}})d\sigma/dm_{t\bar{t}}$ in the ee, $\mu\mu$ and $e\mu$ channels evaluated using data-based (left) and MC-based (right) methods.

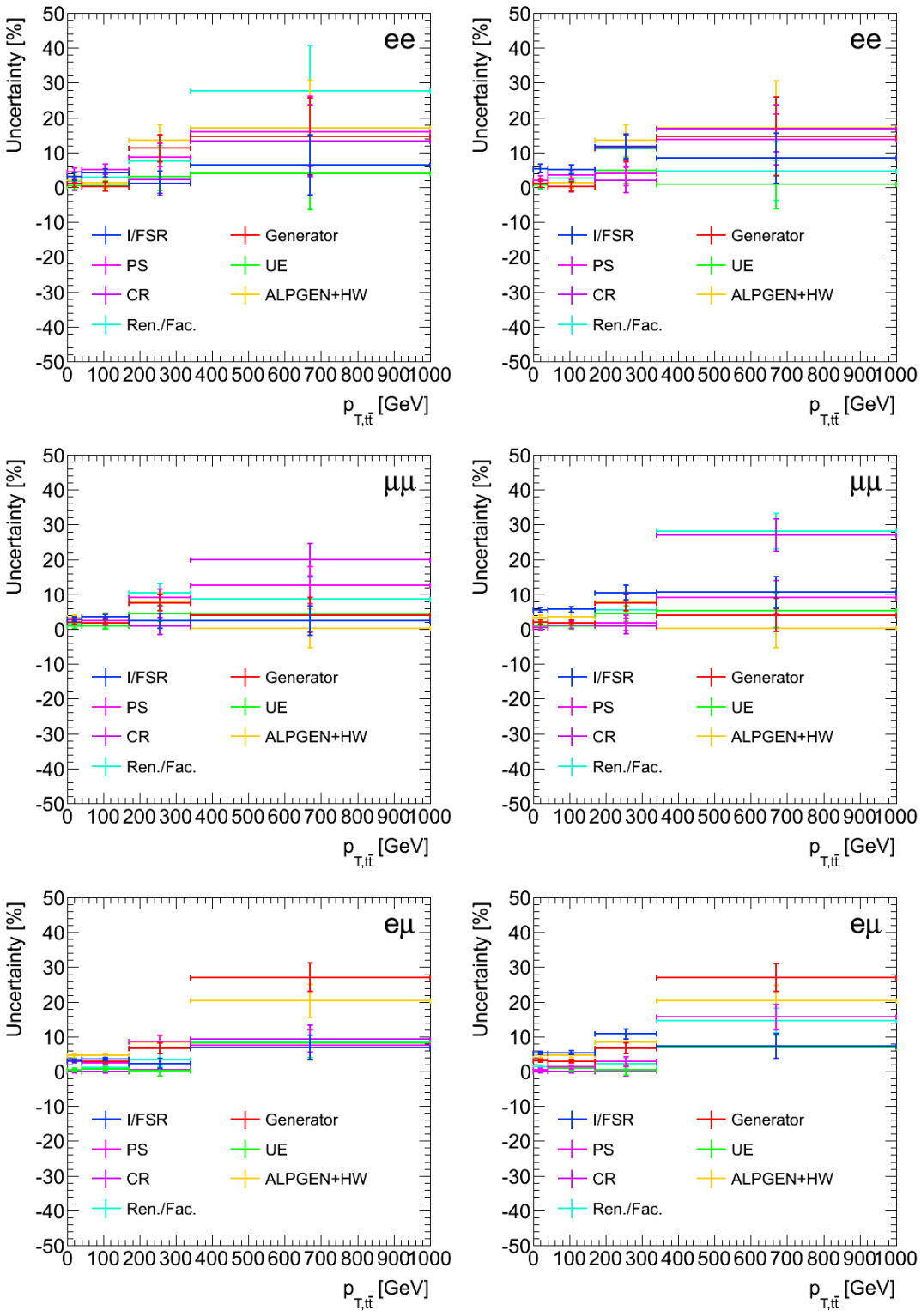

Figure F.11: Comparison of $t\bar{t}$ modelling systematics in $(1/\sigma_{t\bar{t}})d\sigma/dp_{\mathrm{T}}^{t\bar{t}}$ in the ee, $\mu\mu$ and $e\mu$ channels evaluated using data-based (left) and MC-based (right) methods.

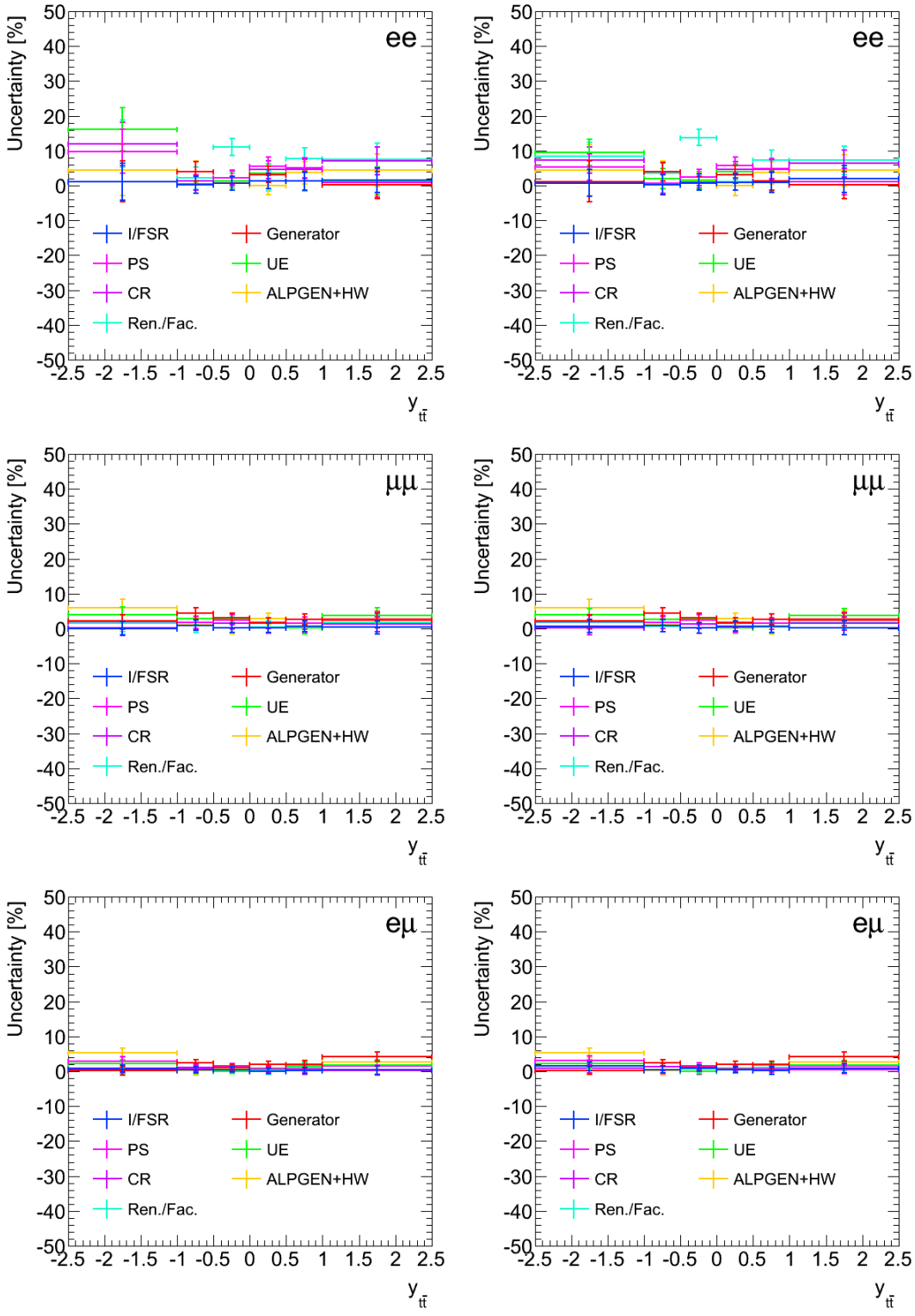

Figure F.12: Comparison of $t\bar{t}$ modelling systematics in $(1/\sigma_{t\bar{t}})d\sigma/dy_{t\bar{t}}$ in the ee, $\mu\mu$ and $e\mu$ channels evaluated using data-based (left) and MC-based (right) methods.

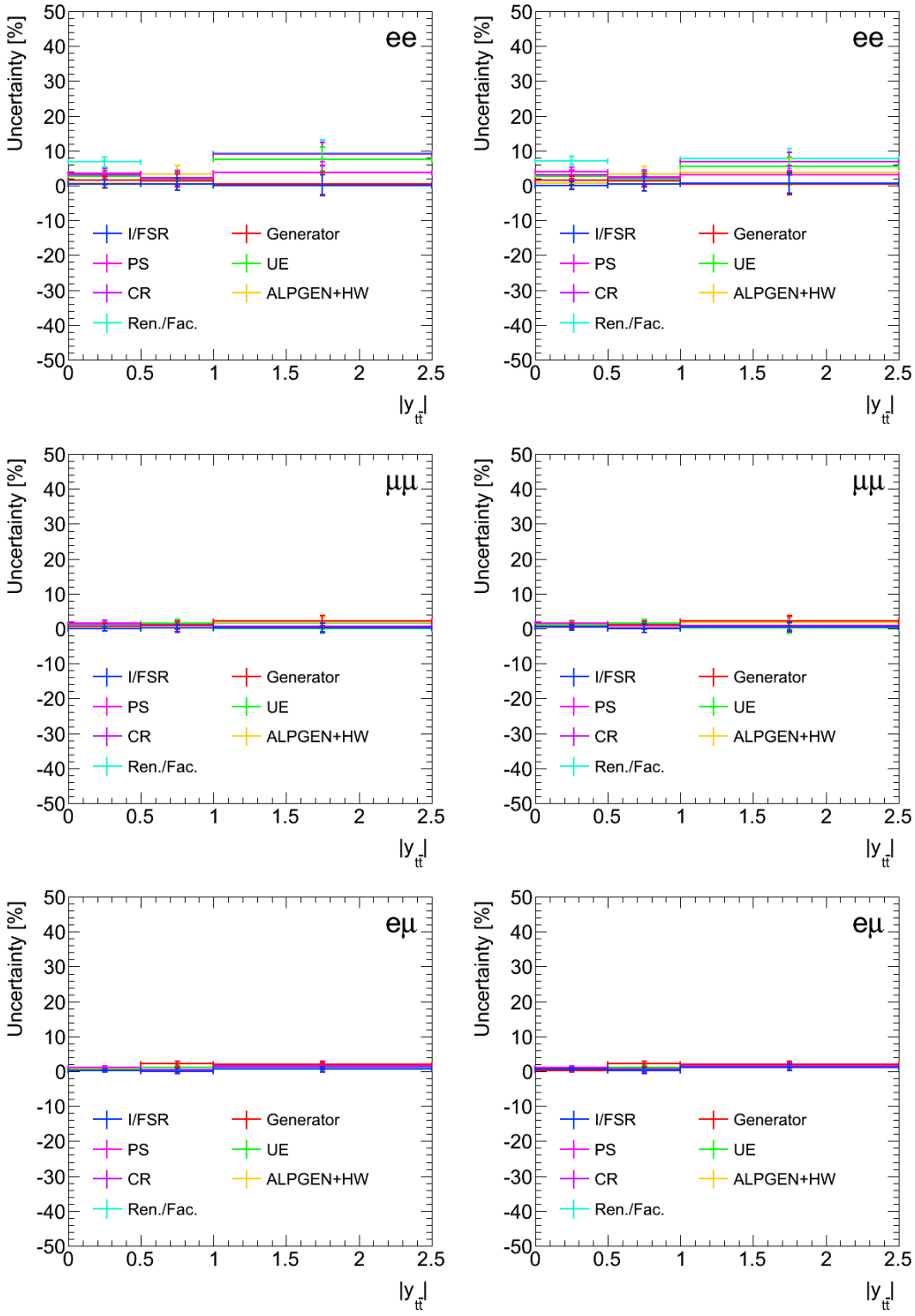

Figure F.13: Comparison of $t\bar{t}$ modelling systematics in $(1/\sigma_{t\bar{t}})d\sigma/d|y_{t\bar{t}}|$ in the ee, $\mu\mu$ and $e\mu$ channels evaluated using data-based (left) and MC-based (right) methods.

F.2.2 Comparisons for combined results

Absolute results

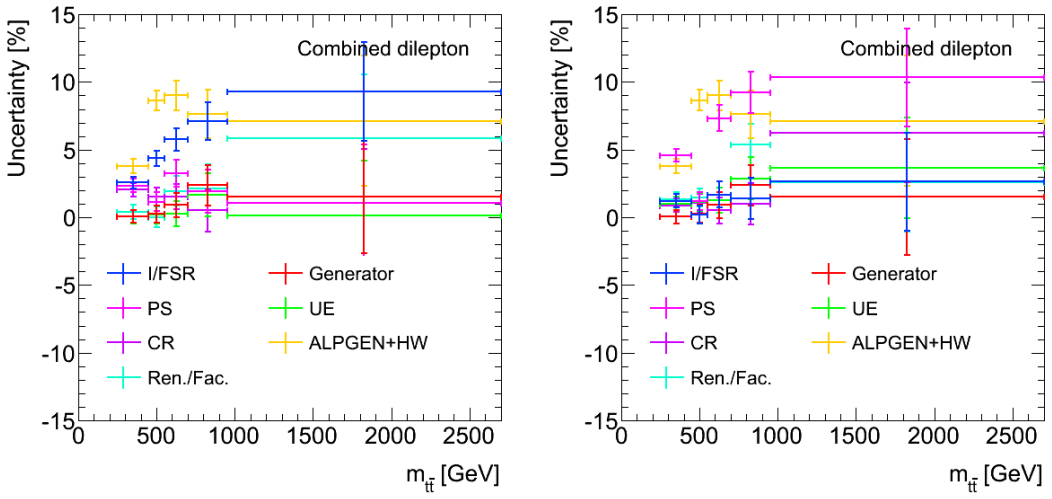

Figure F.14: Comparison of $t\bar{t}$ modelling systematics in $d\sigma/dm_{t\bar{t}}$ in the combined dilepton channel evaluated using data-based (left) and MC-based (right) methods.

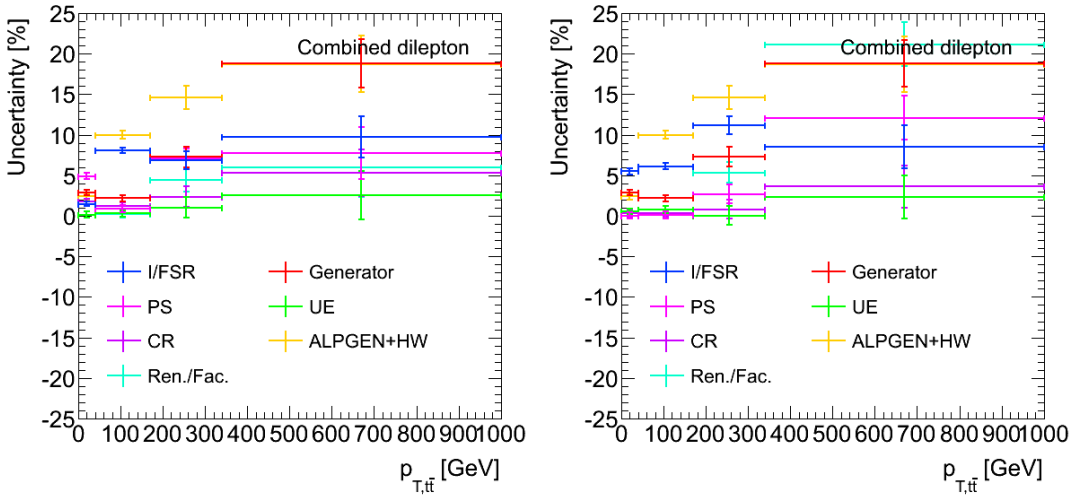

Figure F.15: Comparison of $t\bar{t}$ modelling systematics in $d\sigma/dp_{\mathrm{T}}^{t\bar{t}}$ in the combined dilepton channel evaluated using data-based (left) and MC-based (right) methods.

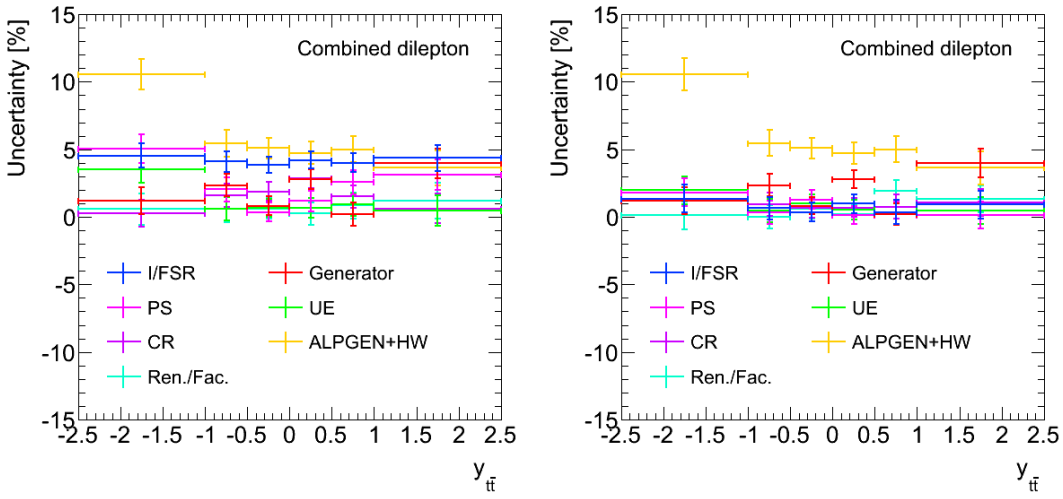

Figure F.16: Comparison of $t\bar{t}$ modelling systematics in $d\sigma/dy_{t\bar{t}}$ in the combined dilepton channel evaluated using data-based (left) and MC-based (right) methods.

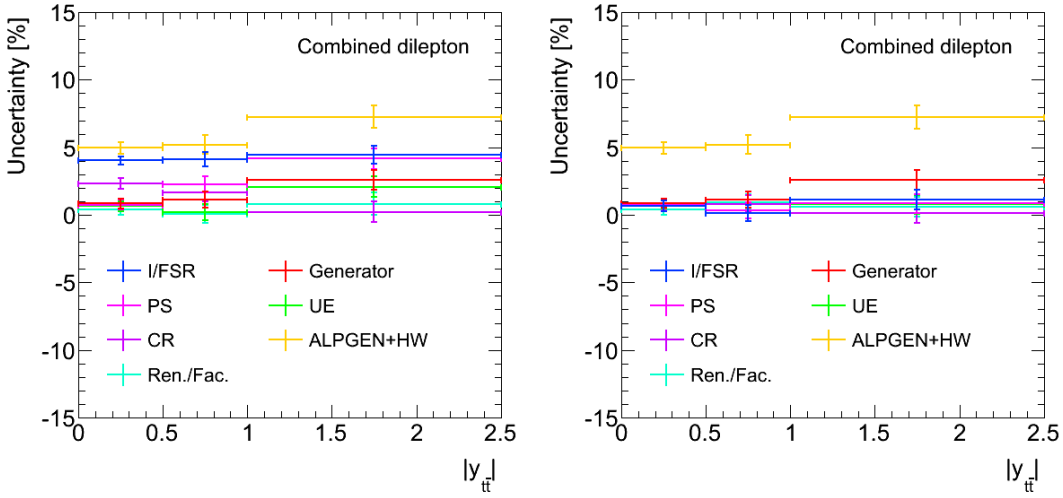

Figure F.17: Comparison of $t\bar{t}$ modelling systematics in $d\sigma/d|y_{t\bar{t}}|$ in the combined dilepton channel evaluated using data-based (left) and MC-based (right) methods.

Normalized results

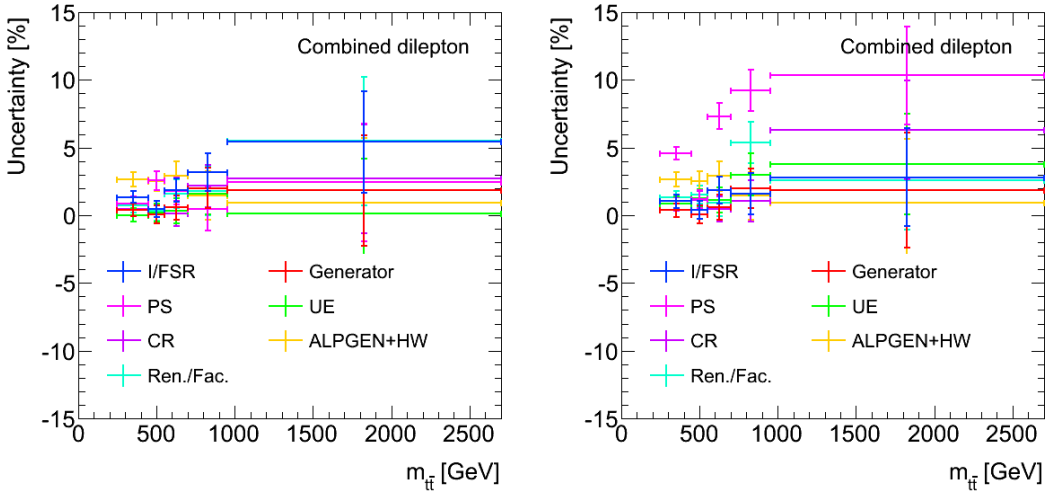

Figure F.18: Comparison of $t\bar{t}$ modelling systematics in $(1/\sigma_{t\bar{t}})d\sigma/dm_{t\bar{t}}$ in the combined dilepton channel evaluated using data-based (left) and MC-based (right) methods.

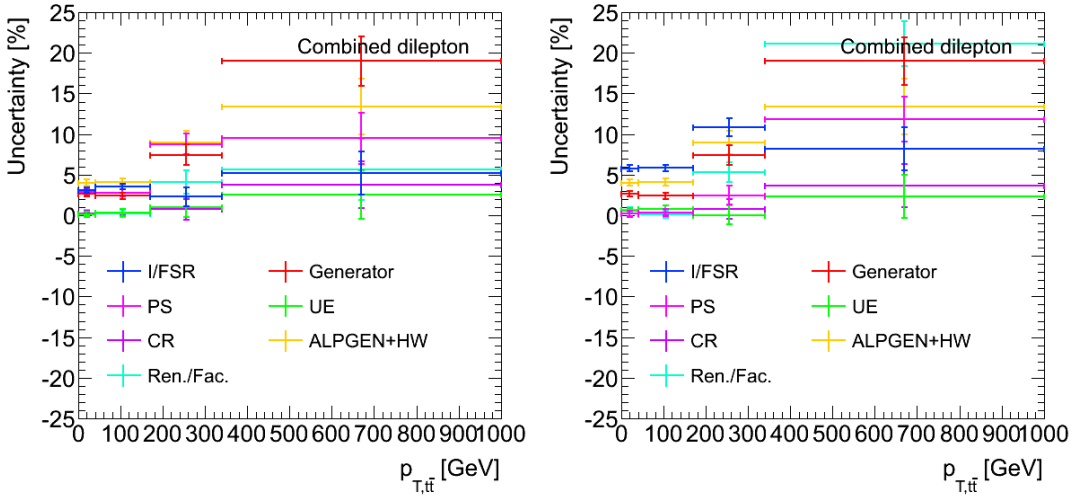

Figure F.19: Comparison of $t\bar{t}$ modelling systematics in $(1/\sigma_{t\bar{t}})d\sigma/dp_{\mathrm{T}}^{t\bar{t}}$ in the combined dilepton channel evaluated using data-based (left) and MC-based (right) methods.

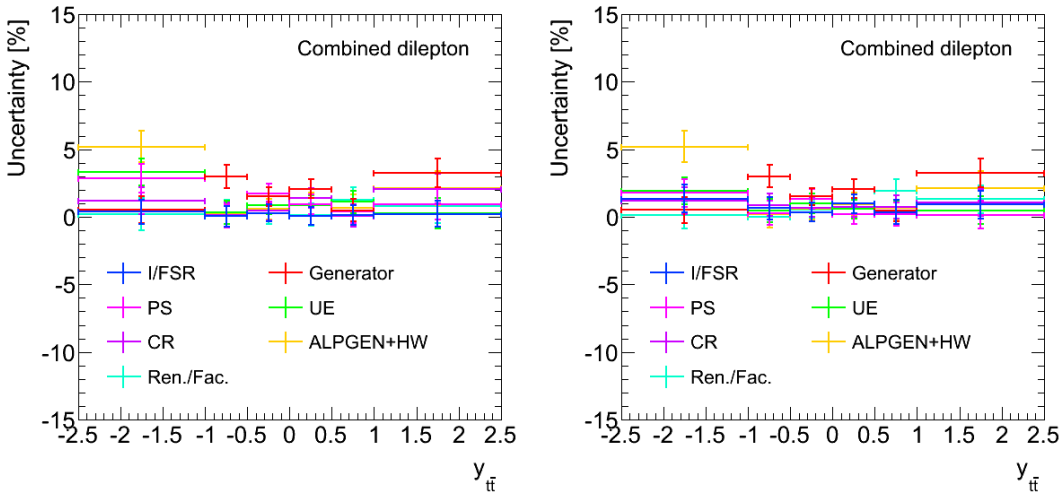

Figure F.20: Comparison of $t\bar{t}$ modelling systematics in $(1/\sigma_{t\bar{t}})d\sigma/dy_{t\bar{t}}$ in the combined dilepton channel evaluated using data-based (left) and MC-based (right) methods.

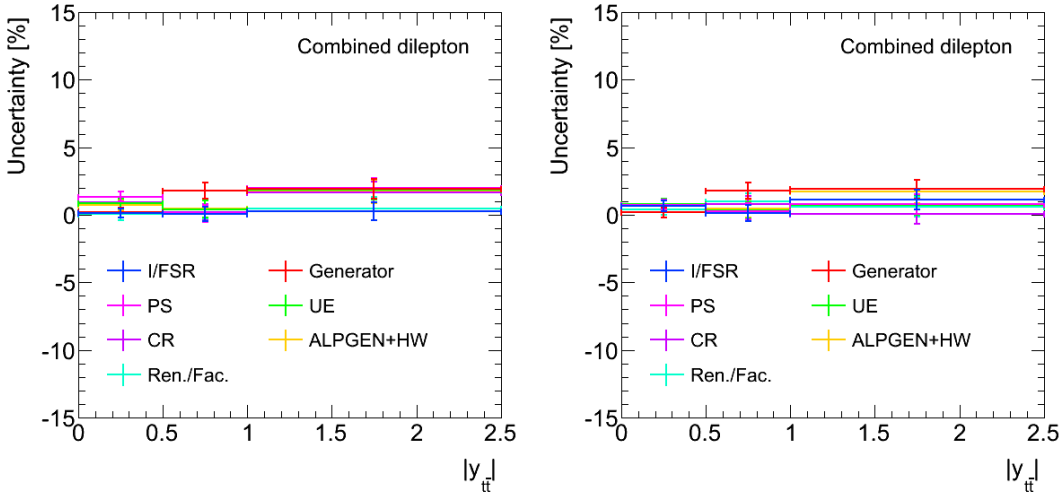

Figure F.21: Comparison of $t\bar{t}$ modelling systematics in $(1/\sigma_{t\bar{t}})d\sigma/d|y_{t\bar{t}}|$ in the combined dilepton channel evaluated using data-based (left) and MC-based (right) methods.

References

[1] V. D. Barger and R. J. N. Phillips, *Collider Physics*. Addison-Wesley Reading, 1987.

[2] D. J. Griffiths, *Introduction to Elementary Particles*. John Wiley & Sons, New York, USA, 1987.

[3] F. Halzen and A. D. Martin, *Quarks and Leptons: An Introductory Course in Modern Particle Physics*. John Wiley & Sons, New York, USA, 1984.

[4] M. Peskin and D. Schroeder, *An Introduction to Quantum Field Theory*. Advanced book classics. Addison-Wesley Publishing Company, 1995. http://books.google.com/books?id=i35LALN0GosC.

[5] Particle Data Group Collaboration, K. O. et al., *Review of Particle Physics*, Chin. Phys. C **38** (2014) 090001.

[6] ATLAS Collaboration, *Observation of a new particle in the search for the Standard Model Higgs boson with the ATLAS detector at the LHC*, Phys.Lett. **B716** (2012) 1–29, arXiv:1207.7214 [hep-ex].

[7] C. Collaboration, *Observation of a new boson at a mass of 125 GeV with the CMS experiment at the LHC*, Phys.Lett. **B716** (2012) 30–61, arXiv:1207.7235 [hep-ex].

[8] ATLAS and CMS Collaborations, *Combined Measurement of the Higgs Boson Mass in pp Collisions at $\sqrt{s} = 7$ and 8 TeV with the ATLAS and CMS Experiments*, arXiv:1503.07589 [hep-ex].

[9] ATLAS Collaboration, *Measurements of Higgs boson production and couplings in diboson final states with the ATLAS detector at the LHC*, Phys.Lett. **B726** (2013) 88–119, arXiv:1307.1427 [hep-ex].

[10] ATLAS Collaboration, *Evidence for the spin-0 nature of the Higgs boson using ATLAS data*, Phys.Lett. **B726** (2013) 120–144, arXiv:1307.1432 [hep-ex].

[11] C. Collaboration, *Precise determination of the mass of the Higgs boson and tests of compatibility of its couplings with the standard model predictions using proton collisions at 7 and 8 TeV*, arXiv:1412.8662 [hep-ex].

[12] C. Collaboration, *Constraints on the spin-parity and anomalous HVV couplings of the Higgs boson in proton collisions at 7 and 8 TeV*, arXiv:1411.3441 [hep-ex].

[13] ALEPH, CDF, D0, DELPHI, L3, OPAL, SLD, LEP Electroweak Working Group, Tevatron Electroweak Working Group, SLD Electroweak and Heavy Flavour Groups, *Precision Electroweak Measurements and Constraints on the Standard Model*, arXiv:1012.2367 [hep-ex].

[14] Gfitter Group Collaboration, M. Baak et al., *The global electroweak fit at NNLO and prospects for the LHC and ILC*, Eur.Phys.J. **C74** (2014) 3046, arXiv:1407.3792 [hep-ph].

[15] M. Cacciari, M. Czakon, M. Mangano, A. Mitov, and P. Nason, *Top-pair production at hadron colliders with next-to-next-to-leading logarithmic soft-gluon resummation*, Phys.Lett. **B710** (2012) 612–622, arXiv:1111.5869 [hep-ph].

[16] P. Baernreuther, M. Czakon, and A. Mitov, *Percent Level Precision Physics at the Tevatron: First Genuine NNLO QCD Corrections to $q\bar{q} \to t\bar{t} + X$*, Phys.Rev.Lett. **109** (2012) 132001, arXiv:1204.5201 [hep-ph].

[17] M. Czakon and A. Mitov, *NNLO corrections to top pair production at hadron colliders: the quark-gluon reaction*, JHEP **1301** (2013) 080, arXiv:1210.6832 [hep-ph].

[18] M. Czakon and A. Mitov, *NNLO corrections to top-pair production at hadron colliders: the all-fermionic scattering channels*, JHEP **1212** (2012) 054, arXiv:1207.0236 [hep-ph].

[19] M. Czakon, P. Fiedler, and A. Mitov, *The total top quark pair production cross-section at hadron colliders through O(alpha$_S^4$)*, arXiv:1303.6254 [hep-ph].

[20] M. Czakon and A. Mitov, *Top++: A Program for the Calculation of the Top-Pair Cross-Section at Hadron Colliders*, arXiv:1112.5675 [hep-ph].

[21] A. Martin, W. Stirling, R. Thorne, and G. Watt, *Parton distributions for the LHC*, Eur. Phys. J. **C63** (2009) 189–285, arXiv:0901.0002 [hep-ph].

[22] ATLAS Collaboration, *Measurements of normalized differential cross-sections for ttbar production in pp collisions at sqrt(s) = 7 TeV using the ATLAS detector*, Phys.Rev. **D90** no. 7, (2014) 072004, arXiv:1407.0371 [hep-ex].

[23] ATLAS Collaboration, *The ATLAS Experiment at the CERN Large Hadron Collider*, JINST **3** (2008) S08003, arXiv:0901.0512 [hep-ex].

[24] S. Frixione, P. Nason, and C. Oleari, *Matching NLO QCD computations with Parton Shower simulations: the POWHEG method*, JHEP **0711** (2007) 070.

[25] H.-L. Lai, M. Guzzi, J. Huston, Z. Li, P. M. Nadolsky, et al., *New parton distributions for collider physics*, Phys. Rev. **D82** (2010) 074024, arXiv:1007.2241 [hep-ph].

[26] T. Sjostrand, S. Mrenna, and P. Z. Skands, *PYTHIA 6.4 Physics and Manual*, JHEP **0605** (2006) 026.

[27] ATLAS Collaboration, The ATLAS Collaboration, "ATLAS tunes of PYTHIA 6 and Pythia 8 for MC11." ATL-PHYS-PUB-2011-009, 2011.

[28] N. Kidonakis, *Two-loop soft anomalous dimensions for single top quark associated production with a W- or H-*, Phys.Rev. **D82** (2010) 054018, arXiv:1005.4451 [hep-ph].

[29] J. Butterworth, E. Dobson, U. Klein, B. Mellado Garcia, T. Nunnemann, J. Qian, D. Rebuzzi, and R. Tanaka, *Single Boson and Diboson Production Cross Sections in pp Collisions at sqrts=7 TeV*, Tech. Rep. ATL-COM-PHYS-2010-695, CERN, Geneva, Aug, 2010.

[30] G. Corcella, I. Knowles, G. Marchesini, S. Moretti, K. Odagiri, et al., *HERWIG 6: An Event generator for hadron emission reactions with interfering gluons (including supersymmetric processes)*, JHEP **0101** (2001) 010.

[31] J. Butterworth, J. R. Forshaw, and M. Seymour, *Multiparton interactions in photoproduction at HERA*, Z.Phys. **C72** (1996) 637–646.

[32] ATLAS Collaboration, The ATLAS Collaboration, "New ATLAS event generator tunes to 2010 data." ATL-PHYS-PUB-2011-008, 2011.

[33] "Web page: Herwig 6.5." http://webber.home.cern.ch/webber/hw65_manual.html.

[34] ATLAS Collaboration, *Electron reconstruction and identification efficiency measurements with the ATLAS detector using the 2011 LHC proton-proton collision data*, Eur.Phys.J. **C74** no. 7, (2014) 2941, arXiv:1404.2240 [hep-ex].

[35] ATLAS Muon Combined Performance, "Twiki page: Guidelines of 2011 data in release 17." https://twiki.cern.ch/twiki/bin/viewauth/AtlasProtected/MCPAnalysisGuidelinesRel17MC11a.

[36] ATLAS Collaboration, *Muon reconstruction efficiency and momentum resolution of the ATLAS experiment in proton-proton collisions at* $\sqrt{s}$ *= 7 TeV in 2010*, Eur.Phys.J. **C74** no. 9, (2014) 3034, arXiv:1404.4562 [hep-ex].

[37] M. Cacciari, G. P. Salam, and G. Soyez, *The Anti-k(t) jet clustering algorithm*, JHEP **0804** (2008) 063.

[38] ATLAS Collaboration, B. Acharya et al., "Object selection and calibration, background estimations and MC samples for the Autumn 2012 Top Quark analyses with 2011 data." ATL-COM-PHYS-2012-1197, 2012.

[39] ATLAS Collaboration, *Measuring the b-tag efficiency in a top-pair sample with 4.7* fb^{-1} *of data from the ATLAS detector*, Tech. Rep. ATLAS-CONF-2012-097, CERN, Geneva, Jul, 2012.

[40] G. D'Agostini, *A Multidimensional unfolding method based on Bayes' theorem*, Nucl.Instrum.Meth. **A362** (1995) 487–498.

[41] "Web page: Roounfold." http://hepunx.rl.ac.uk/ adye/software/unfold/RooUnfold.html.

[42] T. Adye, *Unfolding algorithms and tests using RooUnfold*,. Comments: 6 pages, 5 figures, presented at PHYSTAT 2011, CERN, Geneva, Switzerland, January 2011, to be published in a CERN Yellow Report.

[43] W. Bell, L. Bellagamba, C. Bernard, P. Berta, K. Bilsback, K. Black, T. Childers, R. Di Sipio, L. DellAsta, M. Franchini, C. Gabaldon, M. Yamada, J. Kanzaki, J. Kvita, R. Romano, A. Sady, J. Schovancova, F. Spano', R. Spighi, J. Sjolin, M. Talby, N. Tannoury, and I. Watson, *Measurement of top quark pair differential cross section with ATLAS in pp collisions at sqrt(s)=7 TeV*, Tech. Rep. ATL-COM-PHYS-2012-1137, CERN, Geneva, Jul, 2012.

[44] M. Botje, J. Butterworth, A. Cooper-Sarkar, A. de Roeck, J. Feltesse, et al., *The PDF4LHC Working Group Interim Recommendations*, arXiv:1101.0538 [hep-ph].

[45] P. Z. Skands, *Tuning Monte Carlo generators: The Perugia tunes*, Phys. Rev. **D82** (2010) 074018, arXiv:1005.3457 [hep-ph].

[46] "Atlas twiki page: Topsystematicuncertainties for winter 2012 (rel17) 5 fb-1 analyses." https://twiki.cern.ch/twiki/bin/viewauth/AtlasProtected/TopSystematicUncertainties2011.

[47] "Atlas twiki page: Flavour tagging calibration results in 2014." https://twiki.cern.ch/twiki/bin/viewauth/AtlasProtected/BTagCalib2014.

[48] L. Lyons, D. Gibaut, and P. Clifford, *How to Combine Correlated Estimates of a Single Physical Quantity*, Nucl.Instrum.Meth. **A270** (1988) 110.

[49] A. Valassi, *Combining correlated measurements of several different physical quantities*, Nucl.Instrum.Meth. **A500** (2003) 391–405.

[50] W. Bernreuther, *Top quark physics at the LHC*, J.Phys. **G35** (2008) 083001, arXiv:0805.1333 [hep-ph].